UNIVERSITY OF LEEDS

Controlling quantum chaos: new platforms for many-body scars and weak ergodicity breaking in synthetic quantum matter

Jean-Yves Marc Desaules

University of Leeds

School of Physics and Astronomy

Submitted in accordance with the requirements for the degree of

Doctor of Philosophy

September, 2023

Intellectual Property Statement

The candidate confirms that the work submitted is his own, except where work which has formed part of jointly-authored publications has been included. The contribution of the candidate and the other authors to this work has been explicitly indicated below. The candidate confirms that appropriate credit has been given within the thesis where reference has been made to the work of others.

Chapter 3 contains work from the following publications (Refs. [1–3]):

Extensive Multipartite Entanglement from su(2) Quantum Many-Body Scars
Jean-Yves Desaules, Francesca Pietracaprina, Zlatko Papić, John Goold, and Silvia Pappalardi
Phys. Rev. Lett. 129, 020601 (2022)
Contributions of the candidate: Computation of all numerical results. Derivation of all results relating to the PXP model. Analytical derivations and original derivation for quantum Fisher information at infinite time. Analysis of results. Redaction of the manuscript
Contribution of other authors: Analytical derivations and original derivation of the proof of quantum Fisher information values for thermal and scarred eigenstates. Analysis of results. Redaction of the manuscript.

Superdiffusive Energy Transport in Kinetically Constrained Models, Marko Ljubotina*, Jean-Yves Desaules*, Maksym Serbyn, and Zlatko Papić
* These authors contributed equally
Phys. Rev. X 13, 011033 (2023)
Contributions of the candidate: Preliminary results. Exact diagonalisation computations. Results at short time and all results relating to the multiple su(2) representations. Analysis of results. Redaction of the manuscript.
Contribution of other authors: Large scale TEBD simulations. Analysis of results. Redaction of the manuscript.

Ergodicity Breaking Under Confinement in Cold-Atom Quantum Simulators
Jean-Yves Desaules, Guo-Xian Su, Ian P. McCulloch, Bing Yang, Zlatko Papić, Jad C. Halimeh
arXiv:2301.07717 (2023)

Contributions of the candidate: All analytical derivations. Numerical simulations using both exact diagonalisation and TEBD. Analysis of results. Redaction of the manuscript.
Contribution of other authors: Preliminary TEBD simulation. Analysis of results. Redaction of the manuscript.

Chapter 4 contains work from the following publications (Refs. [4, 5]):

Observation of many-body scarring in a Bose-Hubbard quantum simulator, Guo-Xian Su, Hui Sun, Ana Hudomal, Jean-Yves Desaules, Zhao-Yu Zhou, Bing Yang, Jad C. Halimeh, Zhen-Sheng Yuan, Zlatko Papić, and Jian-Wei Pan
Phys. Rev. Research 5, 023010 (2023)
Contributions of the candidate: Study of the resonance condition and computation of the effective Hamiltonian and higher order perturbations. Development of the theoretical explanation behind revivals from the polarised states. Large scale exact diagonalisation results for the PXP model. Numerical simulation of the Bose-Hubbard and PXP models. Analysis of results. Redaction of the manuscript.
Contribution of other authors: Design and operation of the experiment. Numerical simulation of the Bose-Hubbard and PXP models. Analysis of results. Redaction of the manuscript.

Bridging quantum criticality via many-body scarring
Aiden Daniel, Andrew Hallam, Jean-Yves Desaules, Ana Hudomal, Guo-Xian Su, Jad C. Halimeh, and Zlatko Papić
Phys. Rev. B 107, 235108 (2023)
Contributions of the candidate: Derivation of the TDVP description of the dynamics for the polarised state. Computation and analysis of the quasiparticle picture of revivals from the critical ground state. Numerical simulations of the PXP model. Analysis of results. Redaction of the manuscript.
Contribution of other authors: Large-scale numerical simulations using matrix product states techniques. Derivation of the ramping procedure for state preparation. Numerical simulations of the PXP model. Analysis of results. Redaction of the manuscript.

Chapter 5 contains work from the following publication (Ref. [6]):

Proposal for Realizing Quantum Scars in the Tilted 1D Fermi-Hubbard Model
Jean-Yves Desaules, Ana Hudomal, Christopher J. Turner, and Zlatko Papić
Phys. Rev. Lett. 126, 210601 (2021)
Contribution of the candidate: Study of the resonance condition and computation of the effective Hamiltonian and higher order perturbations. Development of the theoretical explanation behind scarring. Numerical simu-

lation of model. Analysis of results. Redaction of the manuscript.
Contribution of other authors: Numerical simulation of the model. Analysis of results. Redaction of the manuscript.

Chapter 6 contains work from the following publication (Refs. [7, 8]):

Many-body Hilbert space scarring on a superconducting processor
Pengfei Zhang, Hang Dong, Yu Gao, Liangtian Zhao, Jie Hao, Jean-Yves Desaules, Qiujiang Guo, Jiachen Chen, Jinfeng Deng, Bobo Liu, Wenhui Ren, Yunyan Yao, Xu Zhang, Shibo Xu, Ke Wang, Feitong Jin, Xuhao Zhu, Bing Zhang, Hekang Li, Chao Song, Zhen Wang, Fangli Liu, Zlatko Papić, Lei Ying, H. Wang and Ying-Cheng Lai
Nature Physics 19, 120-125 (2023)
Contribution of the candidate: Development of the theory. Large-scale numerical simulation. Analysis of results. Redaction of the manuscript.
Contribution of other authors: Development of the theory. Numerical simulation. Design and operation of the superconducting sample. Analysis of results. Redaction of the manuscript.

Robust rainbow entanglement in disordered quantum circuits at infinite temperature
Hang Dong*, Jean-Yves Desaules*, Yu Gao*, Ning Wang, Zexian Guo, Jiachen Chen, Yiren Zou, Feitong Jin, Xuhao Zhu, Pengfei Zhang, Hekang Li, Zhen Wang, Qiujiang Guo, Junxiang Zhang, Lei Ying, and Zlatko Papić
* These authors contributed equally
In preparation
Contribution of the candidate: Development of the theory. Analytical derivation of all properties of scarred states. Numerical simulation, both using exact diagonalisation and variational methods. Analysis of results. Redaction of the manuscript.
Contribution of other authors: Development of the theory. Numerical simulation. Design and operation of the superconducting sample. Analysis of results. Redaction of the manuscript.

Abstract

Quantum-many body scarring is a recently discovered paradigm of weak ergodicity breaking that allows specific states to evade thermalisation in chaotic quantum systems. Since its discovery in a Rydberg atom quantum simulator, signatures of quantum many-body scarring have been predicted in numerous theoretical models. However, most of these models do not lend themselves to implementation on the current generation of quantum simulators. In this thesis, we develop theoretical blueprints for realising many-body scarring phenomena in three types of quantum devices beyond Rydberg atom arrays. We start by providing an introduction to quantum thermalisation and weak ergodicity breaking in Chapter 2, focusing on the PXP model – an effective kinetically-constrained model describing Rydberg atoms. In Chapter 3, we illustrate anomalous dynamical properties of the PXP model, such as superdiffusive energy transport, and its possible applications as a resource for quantum metrology. In Chapter 4, we demonstrate how the PXP model can be emulated by ultracold bosonic atoms in a tilted optical lattice. The realisation of quantum many-body scarring in a new experimental platform will allow us to identify a larger set of initial configurations that lead to scarring. In Chapter 5, we employ similar techniques to implement a different type of quantum many-body scarring in a Fermi–Hubbard chain. We explain the distinct scarring mechanism in this model using a graph-based approach. Finally, in Chapter 6 we demonstrate how to create tunable scars in a quantum processor based on superconducting qubits. Overall, these results expand the realm of many-body scarring phenomena to a greater variety of experimental systems and they demonstrate that scarring is a powerful tool for protection of quantum information and entanglement engineering in out-of-equilibrium many-body systems.

Contents

1 Introduction **1**

2 Quantum thermalisation, weak ergodicity breaking and many-body scars **5**

2.1 Thermalisation and ergodicity 5
2.1.1 Ergodicity and the Eigenstate Thermalisation Hypothesis 5
2.1.2 Chaos and random matrix theory 9
2.1.3 Non-ergodic quantum systems 10
2.2 Quantum scars of a single particle 11
2.3 PXP model of Rydberg atom arrays 12
2.3.1 Rydberg atom experiments 12
2.3.2 PXP model 14
2.4 Quantum many-body scars in the PXP model 16
2.4.1 Semi-classical limit for many-body scarred dynamics 19
2.4.2 Algebraic structure of scarred eigenstates 23
2.4.3 Spin-1 interpretation 26
2.4.4 Beyond the original PXP model 30
2.5 Mechanisms of weak ergodicity breaking 30
2.5.1 Projector embedding 31
2.5.2 Restricted spectrum generating algebra 32
2.5.3 Rainbow scars 34
2.5.4 Other constructions 36
2.6 Summary 37

3 Algebraic structure of many-body scars and implications for transport and metrology **39**

3.1 Multipartite entanglement of eigenstates 39
3.1.1 Multipartite entanglement and quantum Fisher information . . . 40
3.1.2 QFI for chaotic eigenstates 41
3.1.3 QFI for scarred eigenstates 43
3.2 Multipartite entanglement in the PXP model 45
3.2.1 Effect of perturbations 48

3.3 Multiple su(2) representations and spectral properties of the PXP model 49
3.4 Superdiffusive energy transport in the PXP model 53
3.4.1 Stability of superdiffusion to perturbations 56
3.4.2 Origin of superdiffusion 59
3.5 Summary 60

4 Realising many-body scars in Bose-Hubbard quantum simulators 61
4.1 The tilted Bose-Hubbard model 62
4.1.1 Mapping the PXP model onto the tilted Bose-Hubbard model . . 63
4.1.2 Higher-order terms in the mapping 65
4.2 Observation of $\mathbb{Z}_2$ quantum many-body scars 67
4.3 Unravelling the details of scarred dynamics via quantum interference . . 69
4.4 Emergence of detuned scarring in the polarised state 72
4.5 Mechanism of scarring in the polarised state 74
4.5.1 Semi-classical limit 74
4.5.2 Algebraic picture 77
4.6 Summary 80

5 Graph-theoretic approach to quantum many-body scarring in tilted Fermi-Hubbard chains 81
5.1 The tilted Fermi-Hubbard model 82
5.1.1 Largest connected component of the Hilbert space 83
5.1.2 Symmetries of the model and level statistics 84
5.2 Embedded hypergrid subgraph 86
5.3 Scarred dynamics 88
5.4 Eigenstate properties 91
5.5 Algebraic structure and scar-enhancing perturbation 93
5.6 Experimental implications 94
5.7 Scarring at half-filling in the large-tilt limit 96
5.8 Summary 98

6 Tunable many-body scars on a superconducting quantum processor 101
6.1 Experimental device and the effective XY model 102
6.2 One-dimensional XY model 104
6.2.1 Embedded hypercubic subgraph and signatures of scarring 104
6.2.2 Integrability-breaking perturbations 107
6.2.3 Population dynamics 110
6.3 XY model on a ladder with tunable couplings 113
6.3.1 Symmetries of the model and level statistics 115
6.3.2 Two families of rainbow scars 117
6.3.3 Dynamical signatures of the two scar families 121
6.3.4 Experimental realisation of the two scar families 127
6.4 Summary 128

7 Conclusions and outlook **131**

A Infinite-time average of the quantum Fisher information **135**

B Effect of staggered magnetisation on the PXP model **137**

C Single-site fidelity **147**

D Derivation of TDVP equations of motion and quantum leakage in the PXP model **151**
D.1 Equations of motion 151
D.2 Instantaneous leakage 153

E Structure of rainbow scars **157**
E.1 Building scarred states of the second family 157
E.2 Proof that rainbow scars are eigenstates 160
E.2.1 $n = 0$ and $n = M$ scarred states 160
E.2.2 $n = 1$ scarred states 160
E.2.3 Other values of n 162

F Entanglement entropy of rainbow scars **165**

References **170**

List of Figures

2.1 Chaotic billiard hosting single-particle scars . . . 12
2.2 Ground state phase diagram and quench dynamics in a chain of Rydberg atoms. . . . 14
2.3 Hilbert space structure of the PXP model. . . . 15
2.4 Signatures of ergodicity breaking in the PXP model. . . . 17
2.5 Violation of the strong ETH in the PXP model. . . . 19
2.6 TDVP Ansatz used for the PXP model . . . 20
2.7 Classical trajectory of the Néel state in the PXP model . . . 22
2.8 Large-spin precession picture of scarring in the PXP model . . . 23
2.9 Scar-enhancing perturbations in the PXP model. . . . 27
2.10 Schematic illustration of the Hamiltonian matrix structure for the main mechanisms to engineer QMBSs . . . 31

3.1 Quantum Fisher information of eigenstates in the PXP model. . . . 45
3.2 Scaling of Quantum Fisher information with system size in the PXP model. 46
3.3 Quantum Fisher information after quenches in the PXP model. . . . 47
3.4 QFI density of PXP eigenstates with an algebra-enhancing perturbation. 48
3.5 Effect of staggered magnetisation in the PXP model . . . 50
3.6 Signatures of multiple su(2) representations in the PXP model. . . . 51
3.7 Fidelity and period of revivals for two eigenstates of the spin-1 S^z paramagnet projected into the PXP Hilbert space. . . . 53
3.8 Time evolution of the various global spin operators projected to the constrained PXP space. . . . 54
3.9 Energy transport in the PXP model at infinite temperature. . . . 55
3.10 Energy transport in the PXP model with the PXPZ perturbation. . . . 57
3.11 Energy transport in the PXP model with chemical potential. . . . 58

4.1 Realising the PXP model in a Bose-Hubbard quantum simulator. . . . 62
4.2 Comparison between the full Bose-Hubbard model at the resonance and the PXP model. . . . 65
4.3 Observation of $\mathbb{Z}_2$ quantum many-body scars in a Bose-Hubbard quantum simulator. . . . 68

LIST OF FIGURES

4.4 Probing many-body scarred dynamics in a Bose-Hubbard simulator via quantum interference. . . . 70
4.5 Emergence of many-body scarring in the polarised state . . . 72
4.6 Difference between the expectation values of the diagonal and canonical ensembles for the average number of excitations in the PXP model. . . . 75
4.7 Comparison between exact quantum dynamics and the semi-classical prediction for a quench from the polarised state. . . . 76
4.8 Leakage from the TDVP manifold after a quench from the polarised state in the PXP model. . . . 78
4.9 Bloch sphere representation of scarring from the polarised state. . . . 79

5.1 Level-spacing statistics for the effective Fermi-Hubbard model. . . . 85
5.2 Adjacency graph of the effective model of the tilted Fermi-Hubbard chain. 87
5.3 Dynamics in the effective model of the tilted Fermi-Hubbard chain. . . . 89
5.4 Signatures of the non-trivial embedding of the hypergrid in the effective tilted Fermi-Hubbard model. . . . 90
5.5 Properties of eigenstates of the effective model of the tilted Fermi-Hubbard chain. . . . 91
5.6 Expectation value of the projector onto the hypergrid for the eigenstates of the effective tilted Fermi-Hubbard model. . . . 92
5.7 Fidelity after a quench in the effective tilted Fermi-Hubbard model with a perturbation enhancing the scarring. . . . 94
5.8 Signatures of scarring in fidelity after quenches in the full Fermi-Hubbard model. . . . 95
5.9 Signatures of scarring in imbalance in the full tilted Fermi-Hubbard chain at the resonance. . . . 96
5.10 Mapping between the $\nu = 1/2$ and $\nu = 1$ sectors of the tilted Fermi-Hubbard model. . . . 98

6.1 Experimental setup with superconducting qubits . . . 103
6.2 Quantum state tomography on four superconducting qubits. . . . 106
6.3 Cross coupling in the experimental setup. . . . 107
6.4 Average level spacing ratio in the SSH chain with cross-couplings . . . 108
6.5 Scarring in the SSH chain with a regular integrability breaking perturbation. . . . 109
6.6 Experimental results of superconducting qubit population dynamics. . . . 111
6.7 Scaling of the revival fidelity with superconducting qubits. . . . 112
6.8 Superconducting processor with ladder geometry. . . . 114
6.9 Properties of the tunable XY model on a ladder. . . . 116
6.10 Entanglement structure of eigenstates in the XY ladder. . . . 120
6.11 Entropy of eigenstates in the XY ladder for two different cuts. . . . 121
6.12 Properties of special initial states in the XY ladder. . . . 124
6.13 Improvement of the revivals in the XY ladder by tuning of the couplings. 125

6.14 Experimental observation of the dynamical signatures of scars in the superconducting XY ladder. 126

B.1 Effect of staggered magnetisation on the Néel state in the PXP model. . 138
B.2 Effect of staggered magnetisation on entanglement in the PXP model. . 139
B.3 Ergodicity of the PXP model with staggered magnetisation. 140
B.4 Energy variance of the projected spin-1 eigenstates in the PXP model. . 141

C.1 Comparison between global and local fidelity and entanglement in the Bose-Hubbard model 150

F.1 Entanglement entropy of scarred states in the XY ladder. 167
F.2 Entanglement entropy of scarred states of the second kind in the XY ladder. 168

Abbreviations

QMBS	Quantum many-body scar
ETH	Eigenstate thermalisation hypothesis
MBL	Many-body localisation
MPS	Matrix product state
TDVP	Time-dependent variational principle
FSA	Forward scattering approximation
SGA	Spectrum-generating algebra
RSGA	Restricted spectrum-generating algebra
AKLT	Affleck-Kennedy-Lieb-Tasaki
QFI	Quantum Fisher information
QI	Quantum information
GHZ	Greenberger-Horne-Zeilinger
ODLRO	Off-diagonal long-range order
DOS	Density of states
sDOS	Smoothened density of states
SFF	Spectral form factor
TEBD	Time-evolving block decimation
KPZ	Kardar-Parisi-Zhang
SC	Superconducting
SSH	Su-Schrieffer-Heeger

Chapter 1

Introduction

When compared to their classical counterparts, many-body quantum systems display a plethora of intriguing properties due to quantum superposition and entanglement. Notably, the number of possible configurations in such systems grows exponentially with the number of particles, which makes their classical simulation unfeasible due to the sheer amount of memory and computing power required. In particular, one of the challenging tasks is predicting the properties of the system after letting it evolve from a specific initial state. Moreover, even a basic understanding of quantum dynamics via classical terms turns out to be a challenge, due to the quantum dynamics being *unitary*. In simple terms, this means that it is always possible to "rewind" the quantum evolution of a state backwards in time. Consequently, a specific state at a given time can only be obtained from one single initial state. Since thermalisation in classical physics embodies the idea that many states will end up in the same configuration at late times, this makes the notion of quantum thermalisation subtle to define.

Empirically, however, it is well-established that in many physically relevant cases, accurate predictions for the expectation values of local observable quantities can be obtained, even after the system has evolved for long times. This provides a way to define a quantum equivalent to thermalisation, in the sense that the observable properties depend only on the effective temperature, dictated by the energy of the initial state. This independence on details of the initial state has been distilled into a powerful conjecture called the Eigenstate Thermalisation Hypothesis (ETH). The ETH conjectures that all eigenstates around a given energy have similar properties, leading to the same expectations value for local observables. Thus, the exact distribution of the initial configuration on the eigenstates does not matter, as they will all lead to the same thermal value. While this is undeniably an advantage for predicting long-time values of observables, it also implies that recovering any information about the initial state beyond its average energy is essentially impossible from observables alone.

The ETH implications are problematic for devices such as quantum memories and

quantum computers, where it is necessary to robustly store and retrieve quantum states. Recent flurry of research efforts has aimed at understanding the conditions for ETH to break down. Finely-tuned integrable models and many-body localised systems with strong disorder both evade the fate of thermalisation due to an extensive number of conserved quantities. These effectively separate the Hilbert space in a multitude of isolated sectors, confining the system's wave-function into a small part of it. From the eigenstates point of view, it means that eigenstates in different sectors need not have similar properties. This is an example of a "strong" ETH violation, as generically all eigenstates at a similar energy will have widely different characteristics. As such, for any initial state the long-time value of observables will heavily depend on microscopic properties of the state, not just its energy.

More recently, in 2017 a new type of ergodicity breaking emerged from experiments on large-scale Rydberg atom quantum simulators. In those systems, the vast majority of initial states indeed lead to thermalisation, as expected from ETH. However, when the atoms are prepared in a specific product state, coherent oscillations can be seen, lasting well beyond the known thermalisation timescales. This puzzling "weak" breaking of ergodicity could not be explained by integrability or localisation, nor was it due to symmetries. Instead, it was found that this phenomenon bears a resemblance to the non-ergodic behaviour of a single particle inside a stadium billiard, where an unstable classical periodic orbit leaves a "scar" upon the particle's quantum eigenfunctions. Hence, the phenomenon was named "quantum many-body scars" (QMBSs), triggering a great deal of theoretical efforts to understand its origin. However, the realisations of QMBS phenomena in other platforms beyond Rydberg atoms have remained very sparse compared to the plethora of theoretical models. Moreover, the potential practical utility of QMBS has not been fully understood or appreciated.

In this thesis, we expand the realm of quantum many-body scarring phenomena to two important classes of synthetic quantum systems: ultracold atoms in optical lattices and superconducting quantum processors. We show that the previously-known QMBS physics from Rydberg atom systems can be successfully emulated in these new platforms. More importantly, the unique properties of these platforms also inspired us to formulate entirely new QMBS models. This not only allows for a deeper fundamental understanding of weak ergodicity breaking due to QMBS, but it also opens the door to their practical applications in quantum control and entanglement engineering in complex many-body systems.

In Chapter 2, we set the stage by reviewing the main concepts of quantum thermalisation, focusing on ETH and its violations. We also introduce the concept of single particle scars and explain its relation to the many-body case. To illustrate the latter, we refer to the so-called PXP model – an effective model describing the Rydberg atom experiments in which QMBSs were first observed – which will play an important role throughout this thesis. We conclude this Chapter by presenting an overview of some of the leading mechanisms known to give rise to QMBS phenomena.

In Chapter 3, we show that scarred eigenstates with a specific su(2) algebraic structure also possess multipartite entanglement, rendering them highly useful for quantum

metrology. We demonstrate that this is the case in the PXP model, despite the fact that the su(2) algebraic structure is not exact in that model. In the second half of this chapter, we study the PXP model in more detail, finding that it contains multiple subspaces with an approximate su(2) structure. We show that this leads to signatures of non-ergodicity in various observable quantities, including energy transport, where the signatures manifest as coherent oscillations at moderate times. Meanwhile, through large-scale numerical simulations we also unveil signs of superdiffusion at long times, which are at odds with the naïve expectations of diffusion for a generic chaotic model.

The results in Chapter 3 highlight the fact that the PXP model exhibits many surprising and still poorly understood properties, calling for development of new experimental probes. To this end, in Chapter 4, we use a tilt potential in resonance with on-site interaction to engineer the PXP model in a Bose-Hubbard chain. This allows us to simulate the PXP model with Rubidium-87 atoms trapped in an two-dimensional optical lattice. Using the unique capabilities of this platform, one can interfere multiple copies of the same chain to access quantum fidelity and entanglement entropy, allowing for new types of probes compared to Rydberg atom systems. These new capabilities will allow us to identify scarring from a new initial state in the presence of chemical potential. We also provide a theoretical explanation for our findings based on the semiclassical picture of the dynamics.

In Chapter 5, we apply a similar mapping to the spinful Fermi-Hubbard model. Using the resonance between tilt and on-site interaction, we create an effective kinetically-constrained model. However, in this case we show that the resulting model is completely different from PXP and it has not been previously explored in the literature. Nevertheless, we show that this new model also hosts QMBSs, with a similar phenomenology to those in Chapter 4, but due to a different mechanism, which we elucidate through a new graph-theoretic approach.

In Chapter 6, we take advantage of the graph approach developed in Chapter 5 to engineer QMBSs on a superconducting (SC) quantum processor. We realise QMBS states both in one-dimensional (1D) chains and beyond 1D geometries. This is made possible by the high tunability of the SC platform, which allows to adjust each coupling individually. We also use the advanced readout capabilities to obtain the fidelity and entanglement entropy for multi-site subsystems. Moreover, utilising a circuit with a ladder geometry, we show that it is possible to create QMBS states that are tunable by disorder in the couplings between qubits, allowing to control entanglement dynamics in a disordered many-body system far from equilibrium.

Finally, in Chapter 7 we will conclude and discuss the different models and experimental platforms, mentioning a few directions for future research. The Appendices contain analytical derivations and numerical simulations that support the results in the main text.

Chapter 2

Quantum thermalisation, weak ergodicity breaking and many-body scars

In that chapter, we present an overview of the main concepts in thermalisation of isolated quantum systems. First of all, we introduce the notion of ergodicity through the lens of the Eigenstate Thermalisation Hypothesis and discuss a few important examples of its violation. Among these, we highlight the case of single-particle quantum scars as an example of *weak* ergodicity breaking. We then move on to introduce a many-body analogue of this phenomenon, first through its original experimental discovery, then followed by theoretical studies of the corresponding effective model. We discuss in detail the origin of ergodicity breaking in that case, drawing parallels with single-particle scarring. Finally, we conclude by providing a broader overview of weak ergodicity breaking mechanisms, along with their physical realisations and experimental relevance.

2.1 Thermalisation and ergodicity

2.1.1 Ergodicity and the Eigenstate Thermalisation Hypothesis

We start by briefly reviewing the notion of ergodicity in the classical case before jumping to quantum mechanics. We will consider a Hamiltonian system with many degrees of freedom, where each point in phase space is characterised by $\vec{x} = (\vec{q}, \vec{p})$, with $\vec{q}$ and $\vec{p}$ the generalised position and momentum, respectively. Let us initialise the system at coordinates $\vec{x}_0$, which corresponds to an energy E_0. The ergodic hypothesis [9] postulates that over a long period of time, the system will explore *all* configurations with the same energy. Due to Liouville's theorem [10], these will then be explored uniformly. This means that for a local observable O, the long-time average is equal to

the microcanonical average on all states with energy E_0:

$$\lim_{T\to\infty}\frac{1}{T}\int_0^T O(t)\mathrm{d}t = O_{\mathrm{MC}} = \frac{\int_{\vec{x}\in\mathrm{MC}} O(\vec{x})\mathrm{d}\vec{x}}{\int_{\vec{x}\in\mathrm{MC}}\mathrm{d}\vec{x}}, \tag{2.1}$$

where MC denotes the microcanonical ensemble. Notably, the right hand side of this equation only depends on E_0 and not on any other detail of the initial configuration $\vec{x}_0$.

A similar statement can be made in quantum systems. Let us consider a quantum system with N degrees of freedom and a Hamiltonian $\hat{H}$ with no symmetries. The state of the system is characterised by the wave-function $|\psi\rangle$ which can be assigned an energy $E_0 = \langle\psi|\hat{H}|\psi\rangle$. This state will evolve in time according to the Schrödinger equation as $|\psi(t)\rangle = e^{-i\hat{H}t}|\psi\rangle$ (here and in the rest of this thesis we will work in natural units $\hbar = 1$). We can once again look at a local operator $\hat{O}$ (or a sum of local operators) over time, now focusing on the expectation value $O(t) = \langle\psi(t)|\hat{O}|\psi(t)\rangle$. If we denote the energy eigenvalues of the Hamiltonian by E_k, with the corresponding eigenvectors $|E_k\rangle$, we can then expand $O(t)$ as

$$O(t) = \sum_j |c_j|^2 O_{jj} + \sum_{j\neq k} c_j^\star c_k O_{jk} e^{i(E_j-E_k)t}, \tag{2.2}$$

with $O_{jk} = \langle E_j|\hat{O}|E_k\rangle$ and $c_k = \langle E_k|\psi\rangle$. If there are no special structures in the spectrum such as clustering of states around certain energies (including, of course, exact degeneracies), then at late time the phases of $e^{i(E_j-E_k)t}$ will essentially cancel out. This only leaves the diagonal contributions and allows to write

$$\lim_{T\to\infty}\frac{1}{T}\int_0^T O(t)\mathrm{d}t = \sum_j |c_j|^2 O_{jj}. \tag{2.3}$$

This weighted average on the right hand side is called the "diagonal ensemble" [11].

The previous scenario holds provided that $|\psi\rangle$ is a "generic" state, i.e., it does not have overlap only on a very small number of eigenstates. This is not a stringent requirement, since it is typically the case for product states (and more generally for states with low entanglement). Notably, for these states the standard deviation of the energy with respect to $\hat{H}$ scales as $\sqrt{N}$ while the the energy range of the system scales as N [12]. Therefore, if $|\psi\rangle$ belongs to this category, it means that it only has strong overlap on eigenstates within a small (relative to the energy range) energy window $[E_0-\Delta, E_0+\Delta]$ with $\Delta\approx\sqrt{N}$. This represents our microcanonical ensemble. Coming back to the ergodic hypothesis, we can now write it in the quantum case as

$$\sum_j |c_j|^2 O_{jj} = \lim_{T\to\infty}\frac{1}{T}\int_0^T O(t)\mathrm{d}t = O_{\mathrm{MC}} = \frac{1}{M}\sum_{j\in\mathrm{MC}} O_{jj}, \tag{2.4}$$

where M is the number of states in the microcanonical ensemble.

The meaning of Eq. (2.4) is pretty straightforward. It implies that the late-time value of any physical observable only depends on the original energy of the state.

Thus, thermalisation occurs as the energy is being spread homogeneously across the entire system. However, for this to hold, the eigenstates themselves must have special properties. Indeed, this requires that the distribution of the $|c_j|^2$ for all E_j in the energy window does not matter. For this to be true, O_{jj} must be identical and equal to O_{MC} for essentially all states in the energy window. Additionally, this must be true as the energy window is moved around by choosing a different initial state. Therefore, O_{MC} (and the O_{jj}) must also be a smooth function of energy. This is the main pillar of the (diagonal) Eigenstate Thermalisation Hypothesis (ETH) [12–14].

The ETH conjecture for the observable matrix elements was put forward by Srednicki [13, 15] to describe the observed thermalisation in isolated quantum systems. With the help of the microcanonical average introduced above, the ansatz for the matrix element can be written as

$$O_{jk} = \delta_{j,k} O_{\mathrm{MC}}(E) + e^{-S(E)/2} f_O(E, \omega) R_{jk}, \tag{2.5}$$

where $\omega = E_j - E_k$ denotes the eigenenergy difference and $E = (E_j + E_k)/2$ is their average. The diagonal contribution is thus the microcanonical value, with some fluctuations around it due to the second (off-diagonal) term. R_{jk} is a pseudo-random number with zero mean and unit variance, while $f_O(E, \Omega)$ is a function smooth with respect to both variables and intensive in system size, which relates to linear response of the system to perturbations. The scale of the off-diagonal fluctuations is dictated by the thermodynamic entropy $S(E)$, which is extensive in system size [11]. This means that the amplitude of off-diagonal terms will vanish in the thermodynamic limit. Note that in the presence of symmetries that split the Hilbert space into multiple sectors, the ETH is expected to hold within each individual sector [11, 12, 16]. While the ETH is still a conjecture with no formal proof, extensive study has shown that its predictions hold for many quantum systems [12, 16].

It is important to note that there are two versions of the ETH. For Eq. (2.4) to hold for all initial states, Eq. (2.5) must also hold for all eigenstates. We will refer to this as *strong* ETH. However, we can also consider the case where both equations are violated for a small number of states, which represent a vanishing fraction of the Hilbert space in the thermodynamic limit. Any randomly selected initial state will thermalise and any randomly selected eigenstate will obey the ETH, however there are still non-thermal eigenstates in the spectrum. In this case, we say that a *weak* ETH holds.

Beyond local observables, the ETH also makes predictions for other properties of eigenstates, in particular their entanglement properties. In most of this thesis, we consider a bipartition of our physical system into a set of sites A and its complement $\bar{A}$, such that $\mathcal{H} = \mathcal{H}_A \otimes \mathcal{H}_{\bar{A}}$. We can then use the Schmidt decomposition [17] to split any pure state of the total system as

$$|\psi\rangle = \sum_{j=1}^{\chi} \lambda_j \, |\phi_j^A\rangle \otimes |\phi_j^{\bar{A}}\rangle \,, \tag{2.6}$$

where the λ_j are the Schmidt coefficients and the $|\phi_j^A\rangle$ and $|\phi_j^{\bar{A}}\rangle$ are the orthonormal Schmidt basis states in $\mathcal{H}_A$ and $\mathcal{H}_{\bar{A}}$, respectively. The number of non-zero coefficients

χ is always between one and $\min\{\dim(\mathcal{H}_A), \dim(\mathcal{H}_{\bar{A}})\}$. The reduced density matrix describing the subsystem A can be built directly from there as

$$\hat{\rho}_A = \mathrm{Tr}_{\bar{A}} \left[|\psi\rangle \langle\psi| \right] = \sum_{j=1}^{\chi} |\lambda_j|^2 \, |\phi_j^A\rangle \langle\phi_j^A| \,. \tag{2.7}$$

In order to quantify the amount of entanglement between A and $\bar{A}$, a commonly used metric is the von Neumann entanglement entropy

$$S_{\mathrm{vN}} = -\mathrm{Tr} \left[\hat{\rho}_A \ln(\hat{\rho}_A) \right] = -\sum_j |\lambda_j|^2 \ln\Big(|\lambda_j|^2 \Big). \tag{2.8}$$

We thus see that the Schmidt coefficients directly determine the amount of bipartite entanglement. With a single nonzero Schmidt coefficient, the state is a product state without any entanglement. On the other hand, if all the Schmidt coefficients λ_j are non-zero and of similar magnitude, we obtain a state that maximises the entanglement entropy.

We note that there are other entropies which are occasionally used, such as the Rényi entropies:

$$S_{\mathrm{R}}^{(n)} = \frac{1}{1-n} \ln \left(\mathrm{Tr} \left[\hat{\rho}_A^n \right] \right). \tag{2.9}$$

with integer $n \geq 2$, although the case $n \to 1$ recovers the von Neumann entropy. The low-order Rényi entropies are much more accessible in experiment as they only require measuring powers of the reduced density matrix, for which a useful proxy exists, as opposed to the logarithm of it. In this thesis, by entanglement entropy we will primarily refer to the von Neumann entanglement entropy, with an exception of Chapter 4 where Rényi entropy will be useful.

In order to intuitively understand the predictions of the ETH for entanglement entropy, it is helpful to consider a simplified picture of thermalisation. As the latter implies that the energy of the system is homogeneously distributed, for a small subsystem A we can consider the rest of the system as a thermal reservoir. From the initial energy E_0, we can then define an inverse temperature β such that $(1/Z)\mathrm{Tr}\left[\hat{H} e^{-\beta \hat{H}}\right] = E_0$, with $Z = \mathrm{Tr}\left[e^{-\beta \hat{H}}\right]$ the partition function. At late time, the density matrix in the subsystem A should then resemble the Gibbs density matrix

$$\hat{\rho}_A \approx \hat{\rho}^\beta = \frac{1}{Z_A} e^{-\beta \hat{H}_A}, \tag{2.10}$$

with $\hat{H}_A$ the Hamiltonian in subsystem A and Z_A its partition function. It is straightforward to see that for $\hat{\rho}^\beta$, the squared Schmidt coefficients are all non-zero and simply given by $e^{-\beta E_a}/Z_A$. Near the middle of the spectrum where $\beta = 0$, they are all equal to $1/\dim(\mathcal{H}_A)$, leading to $S(\rho^{\beta=0}) = \ln[\dim(\mathcal{H}_A)]$. Taking as an example a system of N_A qubits in A, we have $S \propto N_A$, i.e., entanglement entropy scales with the volume of the subsystem. This result is not limited to infinite temperature but generically holds away from the edges of the spectrum. This so-called volume-law scaling of entanglement will

also be present in eigenstates. Indeed, from Eqs. (2.4) and (2.5), the eigenstates of a thermalising system must resemble Gibbs states in the sense of measurable properties on their subsystems. Intuitively, it is useful to think of thermalising eigenstates as random vectors in the Hilbert space, for which entanglement entropy can be analytically computed and shown to obey volume law scaling, the so-called Page entropy in that case [18].

2.1.2 Chaos and random matrix theory

Quantum chaos is closely tied with the notions of thermalisation and ergodicity. While these terms are often used interchangeably, a Hamiltonian is said to be chaotic if correlations in the spectrum match those of random matrices belonging to the same symmetry class [19]. This is tightly linked to properties like repulsion between energy levels of the system [20]. This property is now commonly used as a diagnostic for verifying whether a given system is indeed chaotic.

Let us consider the normalised energy spacing between consecutive eigenstates [21], $s_j = (E_{j+1} - E_j)/\langle s \rangle_{\text{loc}}$, with $\langle s \rangle_{\text{loc}}$ the local mean spacing and where we assume that the eigenstates are sorted such that $E_{j+1} \geq E_j$. For a random matrix, it is possible to compute the probability distribution of the s_j, which is the Wigner-Dyson distribution [19]. This distribution has a free parameter β (the Dyson index) that depends on the symmetries of the random matrix. Three different classes have been introduced by Wigner in the 1950s [22]. To reproduce properties of Hamiltonians that are invariant under time-reversal (meaning they can be written as real matrices), the corresponding ensemble is that of real symmetric matrices with Gaussian entries. This ensemble is called the Gaussian orthogonal ensemble (GOE) as it is invariant under the conjugate action of any orthogonal matrix. If time-reversal symmetry is not present, then the Gaussian unitary ensemble (GUE), consisting of Hermitian matrices, is used instead. Finally, the Gaussian symplectic ensemble (GSE), where matrices are Hermitian but also self-dual, is relevant for the special case of systems with time-reversal symmetry that are not invariant under rotation [19]. These ensembles respectively correspond to a Dyson index $\beta = 1$, $\beta = 2$ and $\beta = 4$. The exact distribution for large matrices does not admit a closed form expression. However it can be well approximated by the Wigner surmise, which gives this spacing for a 2 x 2 random matrix from a given ensemble. This surmise then predicts [23]

$$P_\beta(s) = s^\beta a_\beta e^{-s^2 b_\beta}, \tag{2.11}$$

with $a_1{=}\pi/2$, $a_2 = 32/\pi^2$ and and $a_4 = 2^{18}/(3^6\pi^3)$ and $b_1 = \pi/4$, $b_2 = 4/\pi$ and $b_4 = 64/(9\pi)$.

One problem encountered when numerically checking the match with these results for a realistic Hamiltonian is the need to resolve $\langle s \rangle_{\text{loc}}$ in $s_j = (E_{j+1} - E_j)/\langle s \rangle_{\text{loc}}$. One way to get rid of these influences is to "unfold" the spectrum [19], which allows to have a homogeneous density of states across the whole spectrum. A simpler way to bypass this problem is to use instead a quantity that is insensitive to the local density of states.

A common choice of such a quantity is the level spacing ratio, defined as [24]

$$r_j = \frac{\min\{s_{j+1}, s_j\}}{\max\{s_{j+1}, s_j\}}, \tag{2.12}$$

meaning that r_j is always between 0 and 1. As s_{j+1} and s_j are tied to eigenstates very close in energy, they share the same $\langle s\rangle_{\text{loc}}$ that is cancelled by taking their ratio. The probability distribution of the r_j can be computed from the Wigner surmise, leading to [25]

$$P(r) = \frac{2}{Z_\beta}\frac{(r+r^2)^\beta}{(1+r+r^2)^{1+3\beta/2}}, \quad \text{for} \quad r \in [0,1] \tag{2.13}$$

with $Z_1 = 8/27$, $Z_2 = \frac{4}{81}\frac{\pi}{\sqrt{3}}$ and $Z_4 = \frac{4}{729}\frac{\pi}{\sqrt{3}}$. One can also reduce this test to a single number, by computing the average level spacing ratio $\langle r\rangle$. This makes it much easier to compare with numerical computations of the results for the actual Wigner-Dyson distribution in large systems instead of the surmise. In that case, the predicted outcomes are approximately [24, 25]

$$\langle r\rangle_{\beta=1} = 0.5307, \quad \langle r\rangle_{\beta=2} = 0.5996 \quad \text{and} \quad \langle r\rangle_{\beta=4} = 0.6744. \tag{2.14}$$

These values are very close to the analytical values that can be derived using Eq. (2.13).

2.1.3 Non-ergodic quantum systems

Counterexamples to the ETH have been known for a long time. Obvious counterexamples can be constructed from projectors on individual energy eigenstates, which trivially commute with the Hamiltonian and therefore do not "relax". However, such examples are not physical as they result in highly non-local models with complex structure. An important class of physical counterexamples to ETH are integrable systems [26]. These quantum models are characterised by an extensive number of non-trivial conservation laws which can be expressed in a local form (or as a sum of local terms). The presence of these conservation laws effectively prevents states in the many different symmetry sectors from interacting with each other. More recently, many-body localisation (MBL) has been argued to give rise to a similar effect [27, 28]. This many-body equivalent of Anderson localisation [29] happens in systems where strong disorder leads to the emergence of an extensive number of local integrals of motions that constrain the dynamics in a similar way to integrable systems (see the reviews [30, 31]). The nature of these conserved charges lead to the entanglement entropy of eigenstates scaling with the area of subsystem A instead of with its volume [30, 31]. Similar ETH violations can also occur due to strong "Hilbert space fragmentation" [32–35], where the Hilbert space shatters into exponentially many disconnected sectors, acting similarly as the symmetry sectors in the two cases discussed above. We will address this case in more detail in Sec. 2.5.

These types of ETH breakdown affect all eigenstates, hence they represent strong ETH violation. The lack of interactions between states in the various sectors also has

a profound effect on the energy spacing statistics. Indeed, as there is no repulsion between energies corresponding to eigenstates with different quantum numbers, the energy spacings between consecutive eigenstates obey the Poisson distribution typical of independent events:

$$P(s) = e^{-s}, \quad P(r) = \frac{2}{(1+r)^2}, \quad \text{and} \quad \langle r \rangle = 2\ln(2) - 1 = 0.3863, \tag{2.15}$$

where we recall that $r \in [0, 1]$.

Eq. (2.15) provides a practical means to detect strong ETH violation by comparison with Eqs. (2.13)-(2.14). However, in this thesis, our focus will be on quantum systems with *weak* ergodicity breaking, which still obey Eqs. (2.13)-(2.14) but feature subtler violations of the strong ETH. While we will mainly concentrate on many-body systems in what follows, it is important to keep in mind that analogous phenomena can arise in the context of single-particle or few-body systems. A prominent example of such systems that display a form of weak ergodicity breaking are quantum billiards, which we discuss in the next section.

2.2 Quantum scars of a single particle

A well-known example of weak ergodicity breaking in single-particle systems is the phenomenon of quantum scars in chaotic billiards. This was first observed in the two-dimensional Bunimovich stadium billiard [36], composed of a rectangle capped by two semicircles as shown in Fig. 2.1. We can consider the classical case, where a particle is initialised inside the billiard at the position $\vec{q} = (q_1, q_2)$ and momentum $\vec{p} = (p_1, p_2)$. For most initial configurations of $\vec{q}$ and $\vec{p}$, the classical dynamics is chaotic. This means that small changes in the initial conditions will rapidly evolve into large differences, and the trajectory taken will not have any apparent structure, exploring the entire configuration space at long times in an ergodic fashion. However, there exist a small number of trajectories that *do* lead to periodic orbits. This includes "bouncing ball" trajectories where the particle simply bounces up and down in the rectangular part of the billiard, as well as more complicated trajectories like the "figure-of-eight" trajectory displayed in Fig. 2.1**a** Importantly, such trajectories are "rare", i.e., the measure of the initial conditions leading to regular dynamics is zero [37]. Additionally, these trajectories are unstable, meaning that small deviations away from them will bring the system back to a non-periodic orbit.

We can then look at the equivalent quantum system, where $\vec{q}$ and $\vec{p}$ are now operators and the dynamics in the billiard obeys the time-dependent Schrödinger equation. Instead of a set of coordinates in phase space, we can think of a particle being initially prepared in a localised wave-packet. This wave-packet must have a non-zero width in all coordinates and therefore it will have some support also on the chaotic part of phase space. As a consequence, one would naïvely expect that the wave-packet will quickly deviate away from the periodic trajectory and spread homogeneously across the entire billiard. However, the wave-packet shows a surprisingly long lifetime [37]. It was found

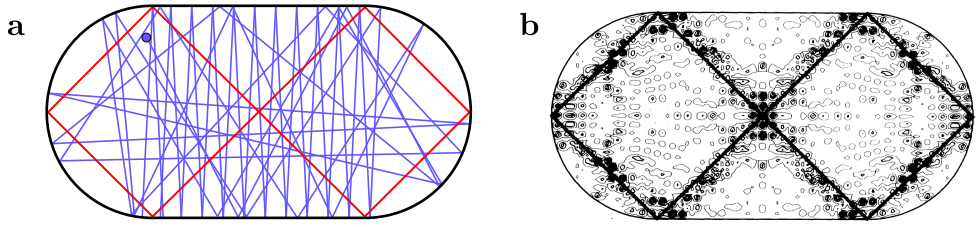

Figure 2.1: Signature of quantum scarring in the Bunimovich billiard. **a** Periodic and chaotic trajectories, respectively in red and blue. **b** Wave-function amplitude for a scarred eigenfunction of the quantum billiard concentrated around the red orbit in **a**. The same orbit is shown as the solid black line. Panel **b** reproduced with permission from Ref. [36], American Physical Society.

that the initial wave-packet has a large overlap with a small number of special eigenfunctions. These special eigenfunctions are highly localised around the classical periodic orbit, unlike other eigenfunctions at the same energy that show a more homogeneous spread in space [36, 38, 39]. This is illustrated in Fig. 2.1**b** for one such eigenfunction that concentrates around the figure-of-eight trajectory. This phenomenon was named "quantum scarring" due to the classical periodic orbit imprinting a "scar" upon the corresponding quantum system.

The scarred eigenfunctions, such as the one in Fig. 2.1**b**, are few and far between, with the majority of eigenfunctions being ergodic. This vanishing fraction of non-ergodic states is a hallmark of weak ergodicity breaking. Despite the rare occurrence of these special eigenfunctions in the spectrum, they can still lead to observable consequences in many physical systems, as seen in numerous experiments during the 1980s and 1990s, e.g., on microwave cavities [40], quantum wells in semiconductors [41] and the hydrogen atom in a magnetic field [42]. However, all these systems can be described in terms of essentially non-interacting particles, and for a long time it has been unknown whether a similar phenomenon can occur in systems where the non-interacting particle description breaks down. As such systems may not have an obvious classical limit, the answer to this question was not apparent. In the next section, we discuss an experiment that kick-started a broad exploration of scarring in many-body systems.

2.3 PXP model of Rydberg atom arrays

2.3.1 Rydberg atom experiments

The many-body equivalent of single-particle quantum scarring was first discovered in a experiment on an array of 51 Rydberg atoms [43]. This array can be modelled as a chain of coupled two-level systems, where each atom can either be in the ground state, denoted $|\circ\rangle$, or the excited Rydberg state $|\bullet\rangle$. The transition between these states is driven by lasers, at a Rabi frequency ω. Additionally, there is detuning Δ between the driving lasers and the energy spacing between the $|\circ\rangle$ and $|\bullet\rangle$ states. Finally, atoms excited into the Rydberg states also interact with each other via van der Waals forces,

which decay with interatomic distance as $1/d^6$. The full Hamiltonian of the system is then given by

$$\hat{H}_{\text{Rydberg}} = \frac{\omega}{2}\sum_j \hat{\sigma}_j^x - \Delta\sum_j \hat{n}_i + \sum_{j<k} V_{j,k}\hat{n}_j\hat{n}_k, \tag{2.16}$$

where $V_{j,k} = C/R_{i,j}^6$ with $R_{j,k}$ the distance between atoms j and k, $\sigma^x = |\circ\rangle\langle\bullet| + |\bullet\rangle\langle\circ|$ is the Pauli X matrix, and $\hat{n} = (\hat{\sigma}^z + 1)/2 = |\bullet\rangle\langle\bullet|$. In a 1D chain with lattice spacing a, we have $R_{j,k} = a|j-k|$ and so $V_{j,k} = V_{|j-k|} = C/(a^6|j-k|^6)$.

Due to the large exponent of the interaction, the difference between V_k and V_{k+1} is also large, with $V_{k+1} = V_k/64$. Thus, it is possible to reach a regime where $V_k \gg \omega > V_{k+1}$. This means that the energy scale of the interaction between excitations at a distance $d \leq k$ is much larger than the energy scale ω of Rabi flips. As such, these neighbouring excitations are heavily suppressed. This regime is called the Rydberg blockade [44], and the blockade radius R_b is defined as the distance such that $V = \omega$.

If the detuning is turned on such that $V_k \gg \Delta \gg \omega > V_{k+1}$, we can also find the atomic ground state by satisfying the constraints in descending energy order. First, very large V_k imposes that excitations are spaced by at least k sites apart. Then, a large Δ requires that as many excitations as possible are present. Neglecting ω for simplicity, this leaves the following crystalline states as ground states:

$$|\mathbb{Z}_k\rangle = |\bullet\underbrace{\circ\cdots\circ}_{k-1}\bullet\underbrace{\circ\cdots\circ}_{k-1}\cdots\bullet\underbrace{\circ\cdots\circ}_{k-1}\rangle\,. \tag{2.17}$$

These states are schematically illustrated in Fig. 2.2**a**. Alternatively, if Δ is large and negative, excitations are suppressed and the ground state is simply the polarised state $|0\rangle = |\circ\circ\circ\ldots\circ\rangle$. As this state is straightforward to prepare, this offers a clear pathway for reaching the $|\mathbb{Z}_k\rangle$ state by starting from the $|0\rangle$ state and slowly ramping Δ from a large negative value to a large positive one. This was experimentally achieved in Ref. [43] to prepare the states $|\mathbb{Z}_2\rangle$, $|\mathbb{Z}_3\rangle$ and $|\mathbb{Z}_4\rangle$.

Beyond probing the equilibrium phase diagram of the Rydberg atom chain, the same experiments also allow to study a global quench of the system by preparing the atoms in a $|\mathbb{Z}_k\rangle$ state and then rapidly setting Δ back to 0. Note that the value of R_b is not changed, meaning that the constraint on close-by excitations remains present throughout the process. In the case $k = 2$ (where only neighbouring excitations are suppressed), the quench is performed from the $|\mathbb{Z}_2\rangle$ initial state, also called the Néel state due to the alternation of excited and unexcited atoms. For $\Delta = 0$ this state is essentially at "infinite temperature", i.e., its energy is exactly in the middle of the spectrum (assuming the Rydberg blockade condition, i.e., no neighbouring excitations). Therefore, the expectation value of any local observable (or a sum of those) should quickly converge towards the thermal value after a quench from the $|\mathbb{Z}_2\rangle$ state. However, when monitoring the domain wall density, which is proportional to the number of consecutive $|\circ\rangle$, Ref. [43] found persistent oscillations instead of the expected decay, see Fig. 2.2**b**. Meanwhile, quenches from other simple initial states, such as the polarised state $|0\rangle$ mentioned above, were found to lead to fast thermalisation, as expected. In order to better understand this phenomenon, it is helpful to consider a simpler effective model for $R_b = 1$, which we introduce next.

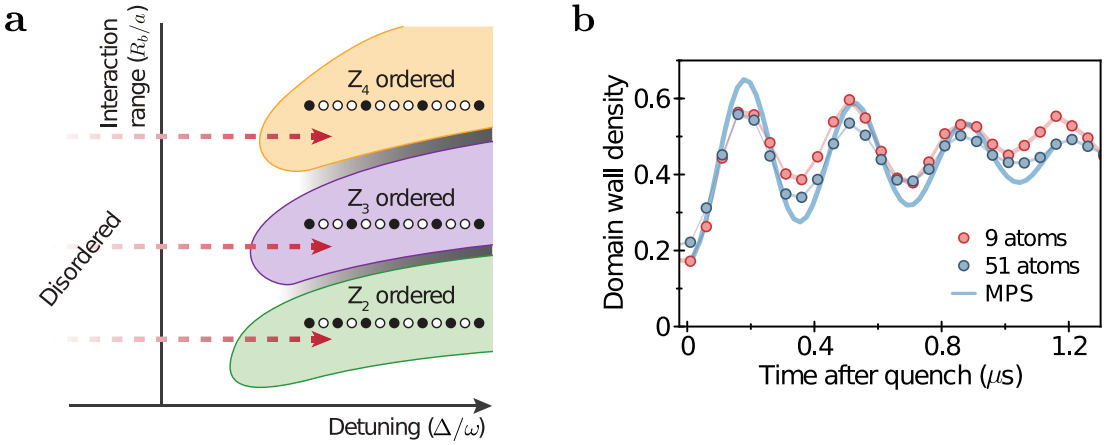

Figure 2.2: **a** Ground state phase diagram of the Rydberg atom chain. **b** Domain wall density after a quench from the $|\mathbb{Z}_2\rangle$ state in the regime where $R_b = 1$ and $\Delta = 0$. The markers indicate experimental results while the thick blue line is numerical simulation using matrix product states (MPS) methods. In all cases, persistent oscillations are seen instead of fast decay towards the thermal value. Panels reproduced with permission from Ref. [43], Springer Nature Ltd.

2.3.2 PXP model

The PXP model [45, 46] derives from the Rydberg chain Hamiltonian (2.16) in the limit of very large interaction strength $V_2 \gg \omega > V_1$. In that case, we can perform a Schrieffer-Wolf transformation [47] and keep the leading term which is of order 1, which results in

$$\hat{H} = \hat{\mathcal{P}} \left(\Omega \sum_{j=1}^{N} \hat{\sigma}_j^x + \mu \sum_{j=1}^{N} \hat{n}_j \right) \hat{\mathcal{P}}, \tag{2.18}$$

where we have introduced $\Omega = \omega/2$ and $\mu = -\Delta$[1]. As a result of the Schrieffer-Wolff transformation, the Rabi term becomes dressed by a global projector $\hat{\mathcal{P}}$ defined as

$$\hat{\mathcal{P}} = \prod_{j=1}^{N} \left(\mathbf{1} - |\bullet\bullet\rangle \langle\bullet\bullet| \right)_{j,j+1}. \tag{2.19}$$

This projector ensures that the dynamics generated by Rabi flipping never generates neighbouring excitations, which are energetically forbidden. Fortunately, the effect of the project can be equivalently recast in a much more convenient local form, resulting in the so-called PXP model:

$$\hat{H} = \Omega \sum_{j=1}^{N} \hat{P}_{j-1} \hat{\sigma}_j^x \hat{P}_{j+1} + \mu \sum_{j=1}^{N} \hat{n}_j, \quad \hat{P}_j = |\circ\rangle \langle\circ| = \frac{\mathbf{1}_j - \hat{\sigma}_j^z}{2}. \tag{2.20}$$

[1] This sign change is simply due to a different convention being used in most theoretical papers on the PXP model.

Throughout this thesis, we will consider both periodic and open boundary conditions. For periodic boundary conditions (PBCs), as implied in the equation above, we simply identify atom $N+1$ with atom labelled 1. In the case of open boundary conditions (OBCs), the boundary terms with $j=1$ and $j=N$ are modified to become $\hat{\sigma}_1^x \hat{P}_2$ and $\hat{P}_{N-1}\hat{\sigma}_N^x$, respectively, as a boundary atom lacks a neighbour to one side. In the rest of this chapter, we will restrict to PBCs, as this choice is more common in the literature. Moreover, we will set $\mu = \Delta = 0$ for the rest of this chapter, as this is the regime in which scarring was initially observed. It is worth noting that, prior to the experiment in Ref. [43], thermalisation in the PXP model was numerically studied in Refs. [48, 49].

The Hamiltonian in Eq. (2.20) only allows a single process $|\circ\,\circ\,\circ\rangle \rightleftarrows |\circ\,\bullet\,\circ\rangle$, i.e., an atom can only flip its state if both neighbouring atoms are in the ground state and it is impossible to create or destroy two neighbouring excitations. As such, most of the literature has focused only on the largest connected sector of the Hilbert space, which is the one containing no neighbouring excitations. This sector also contains the Néel state, from which the anomalous dynamics was observed in experiment. Due to the constraint, for a chain with N atoms, the Hilbert space dimension is no longer equal to 2^N but to $\mathcal{D} = F_{N-1} + F_{N+1}$ with PBC and F_{N+2} for OBC, where F_n is the nth Fibonacci number [50]. This model is thus also known as the Fibonacci chain [51]. This means that, asymptotically, the dimension grows as ϕ^N, where $\phi = (1+\sqrt{5})/2$ is the Golden Ratio. The effect of the constraint on the Hilbert space and the action of the Hamiltonian is shown schematically in Fig. 2.3**a**.

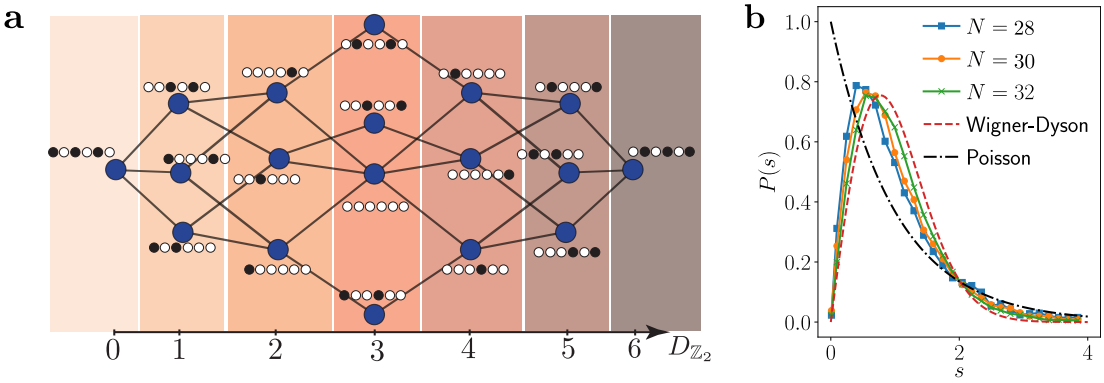

Figure 2.3: **a** Graph representation of the Hilbert space of the PXP model with 6 sites. Each vertex corresponds to a basis state in the Fock basis, and two vertices are linked by an edge if the Hamiltonian matrix element between them is non-zero. The x axis labels the Hamming distance of each state, i.e., the number of Rabi flips needed to reach this state starting from the leftmost $|\mathbb{Z}_2\rangle$ state. **b** Energy level spacing statistics of the PXP model. The statistics are computed in the sector invariant under translation and point group symmetries (see text for details). Panel **a** reproduced with permission from Ref. [50], Springer Nature Ltd

Once the Hilbert space is reduced down to the sector without neighbouring excitations, the constraint does not bring any additional conserved quantities. The Hamiltonian (with PBCs) is only invariant under translation $\hat{T}$ and spatial reflection $\hat{R}$. The

former takes site j to $j+1$, while the latter takes site j to $N+1-j$. Each symmetry sector can then be labelled with a momentum value of k between $-\pi$ and π, e.g., see Ref. [52]. As $\hat{R}$ maps momentum k to $-k$, it only commutes with $\hat{T}$ when $k=0$ and $k=\pi$, when a change of sign maps back to the same sector. Thus, only these sectors are labelled with a value p of ± 1 corresponding to its eigenvalue under $\hat{R}$. Once these symmetries are resolved, one can expect the system to be chaotic. Indeed, the neighbouring terms in Eq. (2.20) do not commute as $\left[\hat{P}, \hat{\sigma}^x\right] \neq 0$. As such the system is not a collection of non-interacting particles and its many-body nature should lead to fast thermalisation. This can be probed by looking at the level spacing statistics in the fully symmetric sector, i.e., the one with $\{k=0, p=+1\}$, as done in Fig. 2.3**b**.

In computing the level statistics for the PXP model, care must be taken to remove "zero modes", i.e., states with energy $E=0$, as there is an exponentially large number of such states, which can impact the level statistics in finite systems. The origin of these states can be explained through symmetry analysis [50, 53]. Indeed, when $\mu=0$, the PXP Hamiltonian *anti-commutes* with the operator

$$\hat{Z} = \prod_{j=1}^{N} \hat{\sigma}_j^z, \tag{2.21}$$

which is directly related to the parity of the number of excitations. As the only dynamical term is $\hat{\sigma}^x$, it always changes the number of excitations by 1, thus changing the parity between $\pm$. This also means that the graph representation of the PXP Hamiltonian in Fig. 2.3**a** is *bipartite*, with states with an even/odd number of excitations being the two classes. The mismatch between the number of states in these two classes then creates an exponential number of zero modes [50, 53]. In order to filter out these states, a common procedure is to only consider states with energy strictly lower than 0, since the spectrum is symmetric between $\pm E$ and no information is lost in doing so. At the same time, this excludes all the degenerate eigenstates at $E=0$. After doing this, the unfolded distribution of level spacing is close to the Wigner-Dyson one, with better agreement as N increases, as seen in Fig. 2.3**b**.

2.4 Quantum many-body scars in the PXP model

Having established that the PXP model shows no traces of strong ergodicity breaking, we come back to the anomalous dynamics observed from the Néel state in Fig. 2.2. The same oscillations that were observed in the full Rydberg model can be reproduced numerically in the PXP model as well, assuming $\mu=0$. Rather than studying different observables, numerics allow us to compute the return fidelity of the wave-function itself, which is more convenient to analyse. The fidelity is defined as

$$\mathcal{F}(t) = |\langle\psi(t)|\psi(0)\rangle|^2, \quad \text{with} \quad |\psi(t)\rangle = e^{-i\hat{H}t}\,|\psi(0)\rangle\,. \tag{2.22}$$

This quantifies the overlap between the initial wave-function $|\psi(0)\rangle$ and the time-evolved wave-function at time t. For a generic state, we expect the wave-function to

spread evenly into the Hilbert space and thus its overlap with any pure state (including the initial wave-function) should be $\approx 1/\mathcal{D}$, where $\mathcal{D}$ is the Hilbert space dimension. The fidelity should therefore vanish rapidly as system size is increased, meaning that there will be negligible probability for a chaotic system to return to its initial state.

Contrary to the previous expectation, as shown in Fig. 2.4**a**, after a quench from the Néel state there are pronounced oscillations in $\mathcal{F}$, with the first peak reaching fidelity of $\mathcal{F} \approx 0.66$ for the system size $N = 30$ and period $T \approx 4.8$. The growth of bipartite entanglement entropy is also highly suppressed, with oscillations visible, Fig. 2.4**b**. Note that the oscillations in entanglement entropy occur at twice the frequency of those in the return fidelity. This is due to the particular trajectory taken by the wave-function. Indeed, at $t = T/2$, the wave-function is almost entirely concentrated on the state $|\mathbb{Z}_2'\rangle = |\circ \bullet \circ \bullet \ldots \circ \bullet\rangle$, also called the anti-Néel state. The dynamics can be thought of as repeated "state transfer" between these two states. As they are product states, the entropy is minimal when close to them. Meanwhile, at $t \approx T/4$ the wave-function is instead spread into large parts of the space, leading to higher values of S.

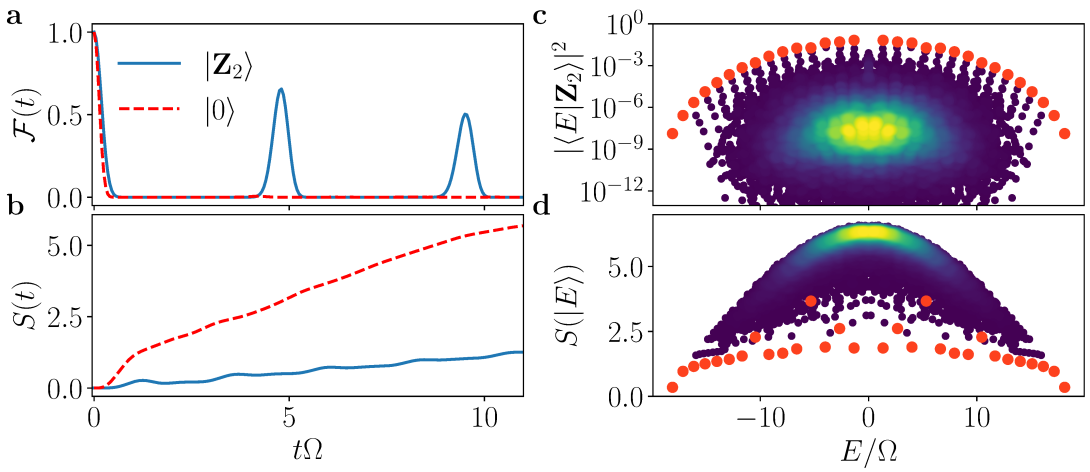

Figure 2.4: Signatures of ergodicity breaking in the PXP model. **a** Return fidelity and **b** half-chain entanglement entropy after quench. There is a stark contrast between the behaviour of the Néel and polarised states, despite both of them being infinite-temperature states. **c** Overlap between the Néel state and the eigenstate and **d** entanglement entropy of the eigenstates. The colour indicates the density of data points, with dark blue being less dense and yellow being the densest. The red markers indicates the state with the highest overlap at the top of each tower of states and highlight the same states in both **c** and **c**. All data is for the PXP model with $N = 30$.

The origin of the oscillations in Fig. 2.4**a-b** is to be found in a set of atypical eigenstates of the PXP model. They can be identified by plotting the overlap of the Néel state with all the eigenstates as shown in Fig. 2.4**c**. Due to the homogeneous properties of thermal eigenstates, one would expect such a plot to be featureless. Instead, a set of $N + 1$ towers of states are visible. The tower at $E = 0$ is less pronounced as numerical diagonalisation leads to strong mixing between all the degenerate eigenstates at this

energy. Importantly, the states at the top of each tower (which we will call the top band) are also approximately equally spaced, with a spacing close to $\Delta E \approx 1.34$ near the middle of the spectrum. This equal spacing is one of the conditions for the persistence of oscillations in large systems. By expressing the Néel state in the eigenbasis of $\hat{H}$ as

$$|\mathbb{Z}_2\rangle = \sum_{n=1}^{\mathcal{D}} c_n |E_n\rangle, \quad \text{with} \quad c_n = \langle E|\mathbb{Z}_2\rangle, \tag{2.23}$$

one can then rewrite

$$|\langle \mathbb{Z}_2|\mathbb{Z}_2(t)\rangle|^2 = \sum_{m=1}^{\mathcal{D}}\sum_{n=1}^{\mathcal{D}} c_m^\star c_n \langle E_m|e^{-i\hat{H}t}|E_n\rangle = \sum_{n=1}^{\mathcal{D}} |c_n|^2 e^{-iE_n t}. \tag{2.24}$$

The overlaps plotted in Fig. 2.4**c** are nothing but the $|c_n|^2$. The states with high overlap will therefore have a dominant impact on the behaviour of the return fidelity. Due to their approximate equal spacing, the phases of their contribution will realign after a time equal to $2\pi/(E_{n+1} - E_n)$. We can check that this is the case here as $2\pi/1.34$ is indeed close to the observed period of 4.8. The slight mismatch between the two is caused by the energy spacing getting smaller (and so the period getting longer) as we move away from the middle of the spectrum.

This anomalously high overlap also has consequences for the eigenstate themselves, as it implies they are much less homogeneously spread across the Hilbert space. This is visible, for example, in the entanglement entropy of eigenstates shown in Fig. 2.4**d**. The eigenstates in the top band have a much lower entropy than other states at the same energy. In fact, the scaling of their entanglement entropy with system size strongly suggests that $S \propto \ln(N)$ instead of the expected $S \propto N$ for thermalising states [54]. A precise quantification of this scaling is somewhat hindered by hybridisation with thermal states. Indeed, the density of states grows exponentially with N, resulting in thermal eigenstates getting closer and closer in energy to the states in the top band. As the latter are not protected by a symmetry, they can hybridise with thermal states. This will render the top band state "less atypical" and the states they hybridise with less thermal. Effects of this can already be seen in Fig. 2.4**d**, where some top band states have much higher entanglement entropy than their neighbours. These same states also display a slightly lower overlap in Fig. 2.4**c** than other top band states close in energy.

Beyond entanglement, violation of the ETH as formulated in Eq. (2.5) can be directly probed by computing expectation values of observables for eigenstates. Let us focus in particular on the normalised density of excitations $\hat{n}_{\text{dens}} = \frac{2}{N}\sum_{j=1}^{N}\hat{n}_j$, which is between 0 and 1 for all states in the constrained PXP Hilbert space. Focusing on the $\{k = 0, p = 1\}$ sector and on an energy window centred on $E = 2\Omega$ with a width of 1.6Ω, Fig. 2.5**a** shows that the states in the top band are far from the microcanonical value. To rule out a finite-size effect, the scaling of ETH violation with system-size can be quantified. Denoting the microcanonical average by n_{MC}, two different metrics can be computed as done in Ref. [55]. On the one hand, the maximum difference between n_{MC} and the expectation value for a state in the energy window will be denoted by

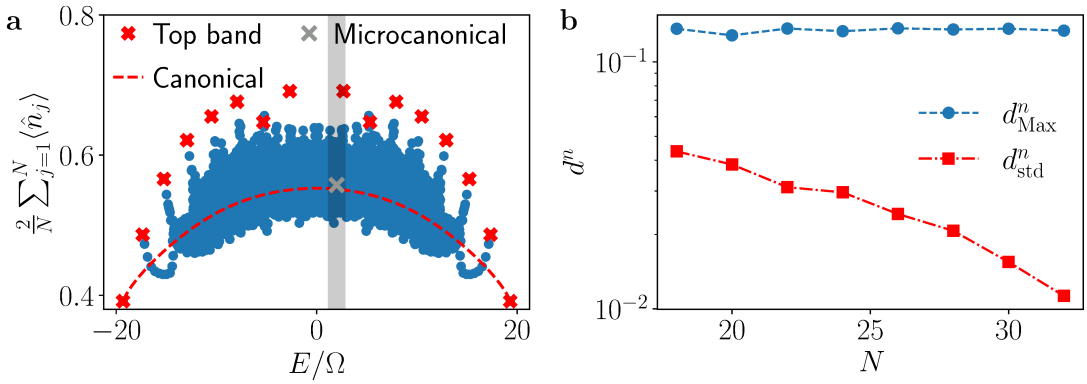

Figure 2.5: Violation of the strong ETH in the $\{k = 0, p = 1\}$ sector of the PXP model, probed by local observables. **a** Expectation value of the normalised excitation density for eigenstates in system size $N = 32$. The states in the top band are highlighted in red. The grey shaded area indicates the energy window used for the microcanonical value. **b** Scaling of the two metrics of ETH violation in a window centred around $E = 2\Omega$ and with width 1.6Ω.

d^n_{Max}. On the other hand, d^n_{std} denotes the standard deviation of the expectation of $\hat{n}_{\mathrm{dens}}$ for all states in the energy window. Fig. 2.5 shows that the former is stable with N, while the latter decays approximately exponentially with N. This means that in the thermodynamic limit, the vast majority of states in the window obey the ETH, but there are some eigenstates that do not. Thus, this is a violation of the strong ETH, but the ETH in the weak sense continues to hold.

In conclusion, the PXP model displays multiple signatures of weak ergodicity breaking. While most of its eigenstates are thermal, there are a few non-thermal eigenstates that show atypical concentration in certain parts of the Hilbert space. Initialising a state with high-overlap on these non-thermal eigenstates leads to regular periodic dynamics, while quenches from other states lead to fast thermalisation. All these phenomena are reminiscent of quantum scarring seen in single-particle billiards. Thus, the atypical eigenstates observed in the PXP model have been dubbed "quantum many-body scars" [50] (QMBSs). However, one piece that is missing to complete the analogy with the single-particle case is the periodic orbit corresponding to the classical limit of the model. We discuss a way to recover this orbit in the next section.

2.4.1 Semi-classical limit for many-body scarred dynamics

In the case of single-particle scarring, the quantum system is directly obtained by quantising a classical system. As such, the quantum-classical relation is clear and it is straightforward to identify any imprint of classical trajectories on the quantum eigenstates. This framework is generally lacking for many-body quantum systems, including the PXP model. While there exists a well-defined classical limit as the spin value goes to infinity, what we are interested in here is instead the thermodynamic limit where the number of sites goes to infinity.

2. QUANTUM THERMALISATION, WEAK ERGODICITY BREAKING AND MANY-BODY SCARS

A semi-classical limit for many-body systems [56] can be obtained by appealing to the notion of the time-dependent variational principle (TDVP) [57, 58]. The idea behind this method is to define a variational manifold $\mathcal{M}$ on which the wave-function is parameterised by a set of classical variables $\mathbf{z}$. TDVP equations of motion for variables $\mathbf{z}$ can be derived as the saddle point equations for the following Lagrangian [56, 57]:

$$\mathcal{L} = \frac{i}{2}\left(\langle\psi|\dot{\psi}\rangle - \langle\dot{\psi}|\psi\rangle\right) - \langle\psi\left|\hat{H}\right|\psi\rangle. \tag{2.25}$$

Essentially, this means that, at each point $\mathbf{z}$ in the manifold, we minimise the difference between the instantaneous evolution within the manifold, $|\dot{\psi}\rangle = \dot{\mathbf{z}}\partial_{\mathbf{z}}|\psi(\mathbf{z})\rangle$, and the full quantum evolution, $-i\hat{H}|\psi(\mathbf{z})\rangle$, generated by the Schrödinger equation. This corresponds to projecting the local quantum evolution onto the manifold, as shown schematically in Fig. 2.6**a**. The difference between the full quantum dynamics and the projected one then quantifies the instantaneous "leakage" of the exact wave-function out of the manifold. We denote this quantity by Λ, which is defined according to

$$\Lambda^2 = N\gamma^2 = \|\dot{\psi}\rangle - i\hat{H}|\psi\rangle\|^2. \tag{2.26}$$

Here γ is the leakage density, which we will find more convenient to use as it removes the system-size dependence and allows extrapolation to the thermodynamic limit.

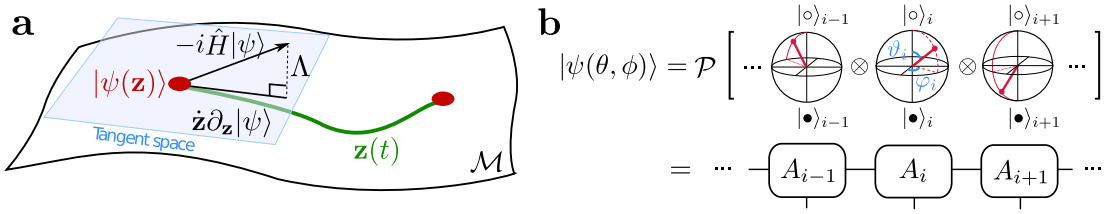

Figure 2.6: **a** Schematic representation of the instantaneous dynamics in the TDVP manifold $\mathcal{M}$, corresponding to the projection of the true instantaneous quantum motion. **b** For the PXP model, states in the manifold can be chosen as product states projected into the constrained space satisfying the Rydberg blockade. In this product state, the configuration of each atom is specified by two angles θ and ϕ that describe its position on the Bloch sphere. States in the manifold can be conveniently described as MPS, as represented graphically on the bottom row. Figure adapted with permission from Ref. [59], American Physical Society.

The Ansatz proposed by Ref. [59] for the PXP model is given by a bond-dimension 2 matrix product state (MPS) [60]. The MPS matrices are given by

$$A^{\bullet}(\theta_j,\phi_j) = \begin{pmatrix} 0 & -ie^{i\phi_j}\sin\left(\frac{\theta_j}{2}\right) \\ 0 & 0 \end{pmatrix}, \quad A^{\circ}(\theta_j,\phi_j) = \begin{pmatrix} \cos\left(\frac{\theta_j}{2}\right) & 0 \\ 1 & 0 \end{pmatrix}, \tag{2.27}$$

where the angles θ_j, ϕ_j play the role of variational parameters $\mathbf{z}$ in the previous discussion. As standard in MPS formalism, the wave-functions belonging to the manifold are constructed via the usual expression [61]

$$|\psi(\theta,\phi)\rangle = \sum_{\vec{\sigma}} \mathrm{Tr}\left[A^{\sigma_1}(\theta_1,\phi_1)A^{\sigma_2}(\theta_2,\phi_2)A^{\sigma_3}(\theta_3,\phi_3)\cdots A^{\sigma_N}(\theta_N,\phi_N)\right]|\vec{\sigma}\rangle\,. \tag{2.28}$$

This Ansatz has a simple interpretation, illustrated in Fig. 2.6**b**. The Ansatz takes a product state of the atoms, where each site is characterised by angles θ and ϕ on the Bloch sphere, and then projects it to the constrained space of the PXP model, akin to the Gutzwiller projection [62].

The MPS bond dimension of 2 allows just enough entanglement between neighbouring sites to guarantee that the Rydberg blockade is never violated. More precisely, the Ansatz can capture states with entanglement entropy of at most $\ln(2)$ between adjacent subsystems ($\ln(4)$ with PBC). This is clearly rather small, especially in large systems – for any state evolving under a chaotic Hamiltonian, the entanglement entropy is expected to exceed this limit very quickly. Thus, in general, this manifold should not be able to capture faithfully the full quantum dynamics and leakage is expected to be high. However, the quench from the Néel state in the PXP model is characterised by a very slow growth of entanglement, and this Ansatz will prove to be very useful.

The $|\mathbb{Z}_2\rangle$ state has a simple structure in that all odd sites are identical and the same is true for even sites. In order to describe quench dynamics from the $|\mathbb{Z}_2\rangle$ state in the crudest possible approximation, it makes sense to restrict the variational manifold to only four degrees of freedom: θ_1 and ϕ_1 for odd sites and θ_2 and ϕ_2 for even sites. This makes the computation of equation of motions for these variables tractable in the thermodynamic $N \to \infty$. The result is a set of 4 non-linear equations that have not been solved analytically to this day. Interestingly, when $\mu = 0$, if ϕ_1 and ϕ_2 are set to 0 initially they will stay at this value at all times. This means that starting from the Néel state at $\theta_1 = \pi$, $\theta_2 = 0$ and $\phi_1 = \phi_2 = 0$ leads to a system with only two degrees of freedom. Numerically integrating the equations of motion from the Néel state leads to a periodic orbit that passes through the anti-Néel state, in a very similar fashion to the true quantum dynamics. This is illustrated in Fig. 2.7**a**, which also shows that this trajectory is confined to the low-leakage region. This means that the full quantum trajectory will be relatively close to the one in the manifold.

Subsequent work explored the consequences of "requantising" this classical dynamical system, in a way that mimics the procedure for single-particle scars [63]. It was shown that this results in a mean-field description of the PXP model, which contains information only about the total numbers of excitations on the odd and even sites, rather than their exact locations. The scarred eigenstates obtained in this mean-field picture displayed high overlap with the exact scarred eigenstates of the PXP model, while the same was no longer the case for thermalising eigenstates. In addition, projecting these scarred eigenstates on the (θ_1, θ_2) phase space showed anomalous concentration around the periodic orbit of the Néel state. This can be seen in Fig. 2.7**b**, which bears a striking resemblance to the results on single-particle billiards.

Nonetheless, there is an important difference between the PXP model and chaotic billiards. Indeed, in the original Bunimovich stadium studied by Heller [36], there are enough degrees of freedom to allow for chaos to develop. The classical trajectories responsible for scarring are rare and unstable. Meanwhile, in the PXP case, the classical limit obtained through TDVP only has two independent degrees of freedom, formally precluding the possibility of chaos. Nevertheless, quantum leakage provides further

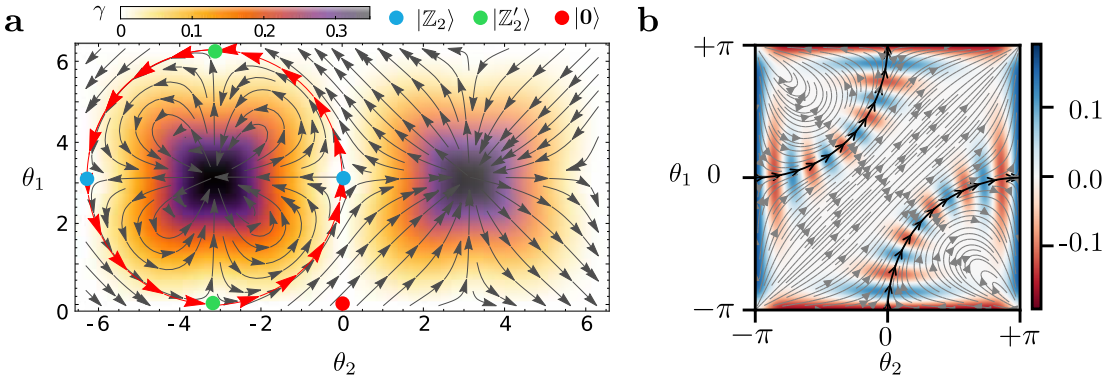

Figure 2.7: **a** Flow diagram in the (θ_1, θ_2) phase space of the PXP model. The Néel state trajectory is highlighted in red. It is periodic, and unlike other trajectories does not flow towards the high-leakage areas at $(\pm\pi, \pm\pi)$. **b** Projection of a scarred eigenstate in a mean-field approximation of the PXP model introduced in Ref. [63]. The concentration around the Néel state trajectory highlighted in black is evident. Panel **a** adapted with permission from Ref. [59], Americal Physical Society. Panel **b** adapted from [63] under a Creative Commons licence CC BY 4.0.

insight that allows us to identify which orbits are more or less prone to chaos. For example, the Néel state trajectory is special as it is the only one that does not flow towards the point $\theta_1 = \theta_2 = \pi$, where leakage is high. As such, it is the only trajectory for which we expect the full quantum trajectory to bear any resemblance to the variational one. The same is true for the eigenstates obtained in the mean-field limit of the PXP model. While for many eigenstates their projection onto the (θ_1, θ_2) space is anomalously localised, only the ones around the Néel periodic orbit are similar to eigenstates of the full model, which turn out to be the scarred ones. Ref. [64] has further explored this paradigm by changing the period of the MPS manifold to 3, allowing chaos to develop. In that case, the TDVP phase space was found to be mixed, with regular islands surrounded by chaotic regions, as expected from weak perturbation to classical integrable systems according to the Kolmogorov-Arnold-Moser theorem [65, 66].

Beyond establishing an additional similarity between quantum many-body scarring and its single-particle equivalent, the accurate description of the dynamics through the simple TDVP Ansatz of Ref. [59] helps us to understand intuitively the scarred dynamics in the PXP model. Indeed, as all angles are the same on odd sites, we can understand these sites are forming a large spin coherent state before the projection into the constrained space. The same is true for even sites. Without projection, we could understand the periodic dynamics as a precession of two uncoupled large spins of magnitude $N/4$. Of course, the Rydberg constraint will couple and generally destroy this picture. However, the Néel state trajectory is special in that when one large spin is maximal along the Z axis, the other spin is minimal. As such, the effect of the constraint is reduced compared to arbitrary configurations and the picture of two large spins approximately holds, however they are now coupled in a complicated way by the constraint. A schematic view of the dynamics using two Bloch spheres is shown in

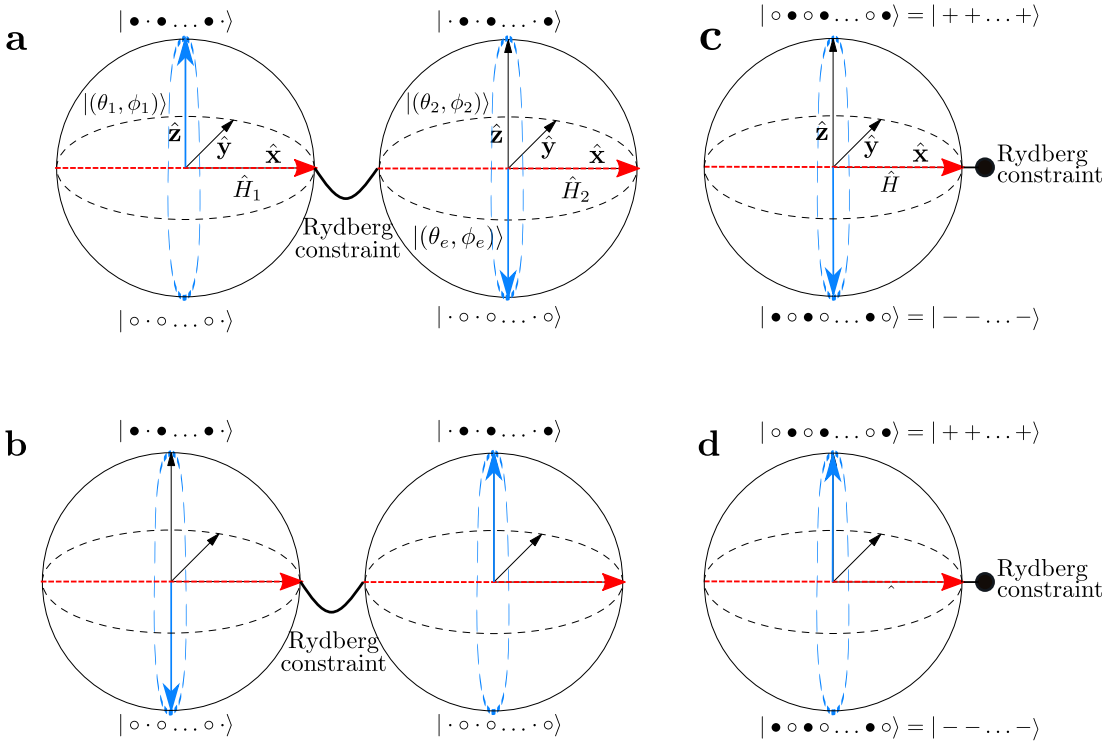

Figure 2.8: Large-spin precession picture of scarring in the PXP model. **a**-**b** Dynamics seen as the precession of two large spins (with total spin $N/4$) corresponding to coherent states on odd and even sites and coupled by the Rydberg constraint. **a** Initial configuration in the Néel state. **b** Configuration after a half-period, where the state is now the anti-Néel. The fact that when one lattice is fully occupied the other is empty greatly reduces the effect of the constraint and allows this large spin picture to hold. **c**-**d** Combining the two spins into a single one with total spin $N/2$ makes apparent the full su(2) algebra in the model. Panels **c** and **d** correspond to the same state as panels **a** and **b** respectively.

Fig. 2.8**a** and **b**. If we instead start in the polarised state $|0\rangle$, this can still be described in the two large spin picture, but they are now both down. As they precess, they will both reach the zenith of the sphere at the same time. This is the regime where the effect of the constraint is the strongest, leading to a complete breakdown of the large spin picture. Logically, it also corresponds to the point with maximum leakage on Fig. 2.7. For other initial configurations of the two large spins, the dynamics is more complicated but the end results is the same. On top of providing a simple picture for visualising the origin of scarring in the PXP model, this large spin picture also hints at the presence of a special su(2) algebraic structure, that we discuss next.

2.4.2 Algebraic structure of scarred eigenstates

The presence of an approximate su(2) algebra in the PXP model was first pointed out by Ref. [67], although the groundwork had already been laid out in Refs. [50] and

[54] through the so-called Forward Scattering Approximation (FSA). The FSA was originally introduced as a scheme to construct approximations to the scarred eigenstates in the PXP model. In this section, we first present an overview of the FSA and explain how it gives rise to su(2) algebra representation in the subspace of scarred PXP eigenstates. As an important piece of evidence in favour of the FSA, we then illustrate that it allows to construct perturbations to the PXP model that "enhance" its scarring behaviour by bringing the structure constants of the algebra closer to su(2). Finally, we discuss a complementary approach, introduced more recently in Ref. [68], which provides a hint to the origin of the algebra: an emergent spin-1 degree of freedom.

The FSA relies on the decomposition of the Hamiltonian into two parts as $\hat{H}_{\mathrm{PXP}} = \hat{H}^+ + \hat{H}^-$. Let us set $\Omega = 1$ to simplify the notation, we then have

$$\hat{H}^{\pm} = \sum_{j \text{ odd}} \hat{P}_{j-1}\hat{\sigma}_j^{\mp}\hat{P}_{j+1} + \sum_{j \text{ even}} \hat{P}_{j-1}\hat{\sigma}_j^{\pm}\hat{P}_{j+1}. \tag{2.29}$$

The structure of these operators mimic the structure of the Néel state. In the graph picture of Fig. 2.3**a**, the action of $\hat{H}^{\pm}$ is easy to visualise as each application of these operators starting from the Néel states simply changes the Hamming distance in units of 1. Moreover, it is easy to see that applying $\hat{H}^-$ to the Néel state annihilates it (similarly, $\hat{H}^+$ annihilates the anti-Néel state). Consequently, starting from the Néel state and applying $\hat{H}^+$ to it, one can construct a closed subspace of $N+1$ states, due to the fact that Hamming distance can be at most N. Within this subspace, a Lanczos-type diagonalisation then produces an effective tight-binding model with $N+1$ sites, which can serve as an approximation to the scarred subspace [50]. The eigenstates of the effective tight-binding model are found to be excellent approximations of the exact scarred eigenstates [54].

From the semiclassical point of view presented above, we can understand why the FSA works well. Essentially, $\hat{H}^+$ acts as a raising operator for the big spin encompassing all even sites and as a lowering one for the odd sites. It is then equivalent to combining these two big spins into a spin of magnitude $N/2$ by taking the one for even sites minus the one for odd sites. The dynamics can be seen as the precession of a single big spin, as illustrated in Fig. 2.8**c** and **d**. In that picture, $\hat{H}^+$ acts as a global raising operator and $\hat{H}^-$ as a lowering one. It is then natural to ask about the diagonal operator $\hat{H}^z$ which, for a true spin, must be equal to $\frac{1}{2}\left[\hat{H}^+, \hat{H}^-\right]$ in order to be consistent with su(2) commutation rules. We proceed to *construct* $\hat{H}^z$ in this way, as this ensures that the commutation relation between $\hat{H}^x$ and $\hat{H}^y$ satisfies $\left[\hat{H}^x, \hat{H}^y\right] = i\hat{H}^z$, as expected

for an su(2) algebra. Thus, we get [67, 69]

$$\begin{aligned}\hat{H}^x &= \frac{\hat{H}^+ + \hat{H}^-}{2} = \frac{1}{2}\hat{H}_{\mathrm{PXP}} = \frac{1}{2}\sum_{j=1}^{N}\hat{P}_{j-1}\hat{\sigma}_j^x\hat{P}_{j+1},\\ \hat{H}^y &= \frac{\hat{H}^+ - \hat{H}^-}{2i} = \frac{1}{2}\hat{H}_{\mathrm{PYP}} = \frac{1}{2}\sum_{j=1}^{N}(-1)^j\hat{P}_{j-1}\hat{\sigma}_j^y\hat{P}_{j+1},\\ \hat{H}^z &= \frac{1}{2}\left[\hat{H}^+,\hat{H}^-\right] = \frac{1}{2}\sum_{j=1}^{N}(-1)^j\hat{P}_{j-1}\hat{\sigma}_j^z\hat{P}_{j+1}.\end{aligned} \tag{2.30}$$

It can be easily verified that the Néel and anti-Néel states are respectively the ground and ceiling state of $\hat{H}^z$. Thus, when acted on with the PXP Hamiltonian (which is directly proportional to $\hat{H}^x$), we would expect a free precession with state transfer from one state to the other if the algebra was exact. This explains why we observe revivals from the $|\mathbb{Z}_2\rangle$ state in the PXP model.

However, if the scarred subspace could simply be interpreted as a free spin, the revivals would be perfect, while in both numerics and experiment they clearly decay in time. The reason is that, by defining the generators according to Eq. (2.30), we are not guaranteed for the algebra to close. For example, we should have $\left[\hat{H}^z,\hat{H}^+\right] = \hat{H}^+$. Directly plugging in the expressions from Eq. (2.30), it can be verified that this relation is not obeyed exactly, but up to a correction term $\left[\hat{H}^z,\hat{H}^+\right] = \hat{H}^+ + \delta^+$, denoted by δ^+. This term is equal to [69]

$$\delta^+ = -\frac{1}{2}\sum_{j\ \mathrm{odd}}\hat{P}_{j-1}\hat{\sigma}_j^-\hat{P}_{j+1}\left(\hat{P}_{j+2}+\hat{P}_{j-2}\right) - \frac{1}{2}\sum_{j\ \mathrm{even}}\hat{P}_{j-1}\hat{\sigma}_j^+\hat{P}_{j+1}\left(\hat{P}_{j+2}+\hat{P}_{j-2}\right). \tag{2.31}$$

Thus, while the algebra formed by $\hat{H}^+$, $\hat{H}^-$ and $\hat{H}^z$ is not closed, it is still resembles an su(2) algebra. It is therefore natural to attempt to close the algebra by incorporating δ^+ into the definition of $\hat{H}^+$ and doing the same with δ^- (obtained from $\left[\hat{H}^z,\hat{H}^-\right] = -\hat{H}^- + \delta^-$) and $\hat{H}^-$. Doing this still does not make the algebra closed, however the "closeness" can be iteratively improved as in each step we can reduce the norm of the operator $\left[\hat{H}^z,\hat{H}^+\right] - \hat{H}^+$ [69].

We illustrate the process of closing the algebra by deriving the first-order perturbation to the model resulting from imposing su(2) structure on it. We can combine δ^+ and δ^- to create a perturbation for the PXP Hamiltonian, as it is directly proportional to $\hat{H}^+ + \hat{H}^-$. The resulting perturbation is Hermitian and equal to

$$\delta\hat{H}_{\mathrm{PXPP}} = \sum_{j=1}^{N}\hat{P}_{j-1}\hat{\sigma}_j^x\hat{P}_{j+1}\left(\hat{P}_{j-2}+\hat{P}_{j+2}\right). \tag{2.32}$$

Since this perturbation brings the algebra closer to the exact su(2), we predict that it will lead to an improvement in revivals from the Néel state. Indeed, for system size $N =$

24, the largest improvement in fidelity is seen with a perturbation strength $\lambda = 0.108$, with the fidelity at the first peak increasing from $1 - 2.85 \times 10^{-1}$ to $1 - 6.76 \times 10^{-4}$ [69].

As the projector $\hat{P}$ can be decomposed into $\hat{\sigma}^z$ and the identity, the PXPP perturbation is equivalent to

$$\delta\hat{H}_{\mathrm{PXPZ}} = -\sum_{j=1}^{N} \hat{P}_{j-1}\hat{\sigma}_j^x\hat{P}_{j+1}\left(\hat{\sigma}_{j-2}^z + \hat{\sigma}_{j+2}^z\right). \tag{2.33}$$

up to a non-linear mapping of the perturbation strength. This corresponds to the perturbation found to enhance the revivals and the algebra for $\lambda = 0.051$ in Ref. [67]. Surprisingly, it was also found to make system nearly integrable for $\lambda = 0.025$, as indicated by the energy level spacing statistics [70]. In addition, Ref. [67] found that even better revivals could be obtained by extending the perturbation range. This is done by adding terms with a similar structure, increasing range, but an exponentially decaying strength. More precisely, the PXP Hamiltonian is deformed using the quasi-local operator

$$\delta\hat{H}_{\mathrm{QL}} = -\sum_{j=1}^{N}\sum_{d=2}^{R} h_d\ \hat{P}_{j-1}\hat{\sigma}_j^x\hat{P}_{j+1}\left(\hat{\sigma}_{j-d}^z + \hat{\sigma}_{j+d}^z\right), \tag{2.34}$$

with the strength given by

$$h_d = h_0\left(\phi^{(d-1)} - \phi^{-(d-1)}\right)^{-2}, \tag{2.35}$$

where $\phi = \left(1+\sqrt{5}\right)/2$ is the golden ratio, and $h_0 \approx 0.051$ is a (numerically determined) strength of the deformation. Finally, we note that the same PXPZ perturbation was also derived by Ref. [71] by considering the dynamics as a scattering problem.

The effects of the PXPZ perturbation and of its longer-range version are illustrated in Fig. 2.9. The improvement in the dynamics of both fidelity and entanglement entropy is very clear. This can be traced back to the scarred eigenstates, as for larger perturbation range R their spacing in energy becomes much closer to equal. The overlap of the Néel state with them also increases, leading to highly reduced influence from thermal states in the dynamics.

2.4.3 Spin-1 interpretation

While the PXPP and PXPZ perturbations were found to be crucial in improving the approximate su(2) algebra of the PXP model, the origin of this structure was not well understood. An alternative explanation was put forward in Ref. [68] using a spin-1 formulation of the PXP Hamiltonian first used in Ref. [72]. Due to the Rydberg constraint, a pair of neighbouring atoms can never be in the configuration $|\bullet\bullet\rangle$ and can be mapped to spin-1 basis states according to

$$|\bullet\circ\rangle \equiv |-\rangle\,, \quad |\circ\circ\rangle \equiv |0\rangle\,, \quad \text{and} \quad |\circ\bullet\rangle \equiv |+\rangle\,. \tag{2.36}$$

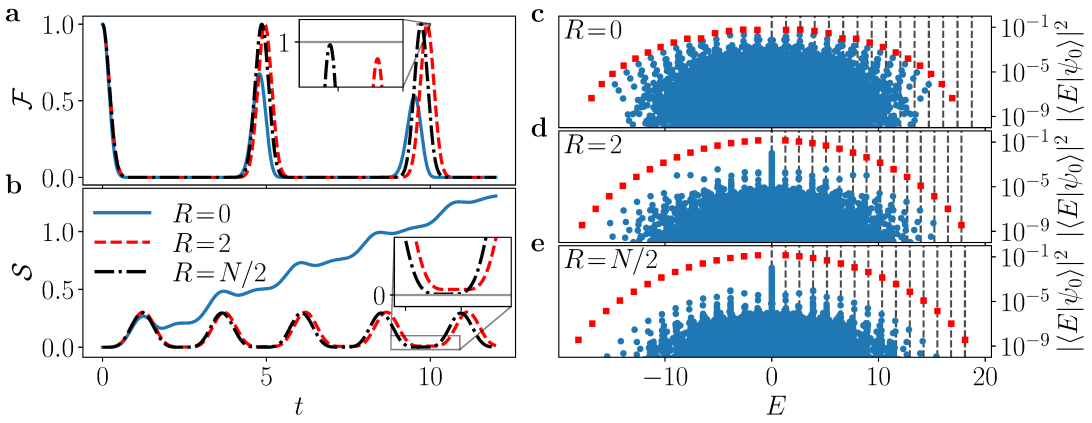

Figure 2.9: Scar-enhancing perturbations in the PXP model. **a-b** Fidelity and entanglement entropy after a quench from the Néel state in the PXP model with $N = 28$. Different curves correspond to different ranges of the perturbation in Eq. (2.34), with $R = 0$ being the unperturbed PXP model, $R = 2$ is the PXPZ perturbation in Eq. (2.33), while $R = N/2$ encompasses all longer-range terms found in Ref. [67]. The insets are zooms of the respective plots and show that for $R = N/2$ the dynamics is almost exactly periodic, with the fidelity coming back to 1 and the entanglement entropy back to 0 up to at least three decimal places. **c-e** Overlap of the Néel state with eigenstates in the cases discussed in panels **a** and **b**. The red squares indicate scarred eigenstates. The vertical dashed lines are equally spaced with an energy separation corresponding to that between scarred states near $E = 0$. As R is increased, the top band becomes more separated from the other eigenstates and the energy spacing in it is also more equal.

Thus, grouping neighbouring atoms in disjoint pairs, this maps each configuration on N sites to a spin-1 chain with $N/2$ sites. However, the spin-1 model is still constrained as neighbouring pairs $|{+}{-}\rangle = |\circ\bullet\bullet\circ\rangle$ are forbidden. The PXP constraint can be rewritten in the spin-1 language, giving

$$\hat{\mathbf{P}} = \prod_{b\in\Lambda_B} \left(1 - |{+}{-}\rangle\langle{+}{-}|_{b,b+1}\right), \tag{2.37}$$

where Λ_B denotes the set of all dimers. To distinguish between operators acting on the full spin-1 Hilbert space and those acting in the restricted PXP subspace, we will write the former in boldface. The full spin-1 Hamiltonian is then

$$\begin{aligned}\hat{\mathbf{H}}_{\Lambda_B} &= \sqrt{2}\sum_{b\in\Lambda_B}\hat{\mathbf{S}}^x_b - \sum_{b\in\Lambda_B}\left(|{+},0\rangle + |0,{-}\rangle\right)\langle{+},{-}|_{b,b+1} - \sum_{b\in\Lambda_B}|{+},{-}\rangle\left(\langle{+},0| + \langle 0,{-}|\right)_{b,b+1}\\ &\equiv \hat{\mathbf{H}}_{\mathrm{FX}} + \hat{\mathbf{H}}_1 + \hat{\mathbf{H}}_2,\end{aligned} \tag{2.38}$$

where $\hat{\mathbf{S}}^x_j$ is the spin-1 X operator acting on site j. We will also denote the global spin operator along the α axis as $\hat{\mathbf{S}}^\alpha = \sum_{b\in\Lambda_B}\hat{\mathbf{S}}^\alpha_b$, with $\alpha = x,\ y,\ z$. This means that $\hat{\mathbf{H}}_{\mathrm{FX}} = \sqrt{2}\hat{\mathbf{S}}^x$ is a free paramagnet along the X direction, and $\hat{\mathbf{H}}_1$ and $\hat{\mathbf{H}}_2$ are

added to cancel the matrix elements violating the constraint. As a consequence, the full Hamiltonian does not connect the PXP constrained space to the rest of the spin-1 Hilbert space, and it must hold that $\left[\hat{\mathbf{P}}, \hat{\mathbf{H}}_{\Lambda_B}\right] = 0$. This allows to write

$$\hat{\mathbf{H}}_{\Lambda_B} = \hat{H}_{\mathrm{PXP}} \oplus \hat{H}_{\perp}, \tag{2.39}$$

where $\hat{H}_{\perp}$ acts on the complement of the PXP subspace in the spin-1 Hilbert space. We then define

$$\hat{\mathbf{H}}'_{\mathrm{PXP}} \equiv \hat{H}_{\mathrm{PXP}} \oplus \hat{0}_{\perp} = \hat{\mathbf{P}}\hat{\mathbf{H}}_{\Lambda_B}\hat{\mathbf{P}} = \hat{\mathbf{P}}^2\hat{\mathbf{H}}_{\Lambda_B} = \hat{\mathbf{P}}\hat{\mathbf{H}}_{\Lambda_B}, \tag{2.40}$$

that acts as PXP in its sector but annihilates any state outside of it. More generally, we will use the prime to denote operators in the PXP subspace "blown up" to the full spin-1 space but acting as the null operator in its complement.

One can also notice that $\hat{\mathbf{P}}\hat{\mathbf{H}}_2 = 0$ but $\hat{\mathbf{P}}\hat{\mathbf{H}}_1 \neq 0$. This means that if we take an eigenstate $|\mathbf{E}\rangle$ of $\hat{\mathbf{H}}_{\mathrm{FX}}$ (with energy E), the only thing preventing its constrained version $|\mathbf{E}'\rangle = \hat{\mathbf{P}}\,|\mathbf{E}\rangle = |E\rangle \oplus 0_{\perp}$ to be an eigenstate of $\hat{H}'$ is $\hat{\mathbf{H}}_1$. However, if there is a perturbation $\delta\hat{\mathbf{H}}$ such that $\hat{\mathbf{P}}\left(\hat{\mathbf{H}}_1 + \delta\hat{\mathbf{H}}\right)|E\rangle = 0$ and $\left[\hat{\mathbf{P}}, \delta\hat{\mathbf{H}}\right] = 0$, then the contribution of $\hat{\mathbf{H}}_1$ is cancelled and $|E'\rangle$ is an eigenstate of $\hat{\mathbf{H}}'_{\mathrm{PXP}} + \delta\hat{\mathbf{H}}'$ with energy E, where $\delta\hat{\mathbf{H}}' = \hat{\mathbf{P}}\delta\hat{\mathbf{H}}$. Indeed, after some simple manipulations

$$\begin{aligned}
\left(\hat{\mathbf{H}}'_{\mathrm{PXP}}+\delta\hat{\mathbf{H}}'\right)|\mathbf{E}'\rangle &= \left(\hat{\mathbf{H}}'_{\mathrm{PXP}} + \delta\hat{\mathbf{H}}'\right)\left(\hat{\mathbf{P}}\,|\mathbf{E}\rangle\right) \\
&= \hat{\mathbf{P}}\left(\hat{\mathbf{H}}_{\Lambda_B} + \delta\hat{\mathbf{H}}\right)|\mathbf{E}\rangle \\
&= \hat{\mathbf{P}}\left(\hat{\mathbf{H}}_{\mathrm{FX}} + \hat{\mathbf{H}}_1 + \hat{\mathbf{H}}_2 + \delta\hat{\mathbf{H}}\right)|\mathbf{E}\rangle \\
&= \hat{\mathbf{P}}\hat{\mathbf{H}}_{\mathrm{FX}}\,|\mathbf{E}\rangle + \hat{\mathbf{P}}\left(\hat{\mathbf{H}}_1 + \hat{\mathbf{H}}_2 + \delta\hat{\mathbf{H}}\right)|\mathbf{E}\rangle \\
&= \hat{\mathbf{P}}\left(\hat{\mathbf{H}}_{\mathrm{FX}}\,|\mathbf{E}\rangle\right) = \hat{\mathbf{P}}\left(E\,|\mathbf{E}\rangle\right) = E\,|\mathbf{E}'\rangle\,.
\end{aligned} \tag{2.41}$$

Equivalently, it means that $|E\rangle$ will be an eigenstate of $\hat{H}_{\mathrm{PXP}}+\delta\hat{H}$ with energy E.

The desired perturbation

$$\delta\hat{\mathbf{H}} = \sum_{\Lambda_B} \frac{1}{2}\left(|+,0\rangle + |0,-\rangle\right)\langle 0,0|_{b,b+1} \tag{2.42}$$

was found in Ref. [68]. However, the condition $\left(\hat{\mathbf{H}}_1 + \delta\hat{\mathbf{H}}\right)|\mathbf{E}\rangle = 0$ does not hold for all states. To work, it requires that neighbouring dimers form a spin-2 quintuplet. The only eigenstates of $\hat{\mathbf{H}}_{\mathrm{FX}}$ that satisfy this for *all* pairs are the ones with maximal total spin, i.e, $N/2$. This means that the spin-1/2 Hamiltonian $\hat{H}_{\mathrm{PXP}}+\delta\hat{H}$ has $N+1$ scarred eigenstates that correspond to the projection of the eigenstates of $\hat{\mathbf{H}}_{\mathrm{FX}}$ with maximal total spin into the constrained space. Unlike in the unperturbed PXP model, the structure of these states and their energies can be written down analytically. This generally allows to perform a (local) change of basis that completely decouples the

subspace containing the scarred states from the rest of the Hilbert space. As such, the scarred states in this model are referred to as *exact scars*, as opposed to the ones in the unperturbed PXP model where such constructions hold only approximately.

One clear limitation of $\delta\hat{\mathbf{H}}$ (and so of $\delta\hat{H}$) is that it is non-Hermitian. Furthermore, $\delta\hat{H}$ will not be translation invariant, either, in the spin-1/2 formulation. One can still enforce these properties by adding the Hermitian conjugate and the translation by one (spin-1/2) site, but the resulting model will not have exact scars. Nonetheless, we can expect it to show relatively good scarring and an enhanced algebra when compared to the unperturbed PXP model. In fact, in the spin-1/2 language this perturbation $\delta\hat{H}_{\text{inv}}$ is exactly proportional to the PXPP perturbation in Eq. (2.32). Thus the origin of this perturbation is explained using the spin-1 picture, where it counteracts the effects of the terms perturbing the free paramagnet.

Beyond finding perturbations, the spin-1 approach also makes some properties of the scarred states in the unperturbed PXP model more evident. Indeed, the scarred eigenstates are still relatively well approximated by projecting the eigenstates of $\hat{\mathbf{H}}_{\text{FX}}$ with total spin $N/2$. As $\hat{\mathbf{H}}_{\text{FX}}$ is a free paramagnet, its eigenstates will be eigenstates of angular momentum, also called Dicke states, which have logarithmic entanglement entropy. This naturally explains why the entanglement entropy of the PXP scarred eigenstates was found to also obey a similar type of scaling. In the unconstrained spin-1 model, one can also see that the Néel state is the ground state of the free paramagnet along the Z direction. As such, it has maximum total spin and only has overlap on the eigenstates of $\hat{\mathbf{H}}_{\text{FX}}$ with the same characteristic, which once projected will end up being the scarred eigenstates. As a result we see these states have maximum overlap with the Néel state. Finally, we can write down the spin-1/2 operators corresponding to the projection of the su(2) algebra of the spin-1 free model into the constrained space. These operators, denoted as $\hat{S}^{\alpha}$, are defined as

$$\hat{S}^{\alpha} \otimes \hat{0}_{\perp} = \hat{\mathbf{P}}\mathbf{S}^{\alpha}\hat{\mathbf{P}}. \tag{2.43}$$

With the definitions in Eq. (2.30), these are equal to

$$\hat{S}^{x} = \frac{1}{\sqrt{2}}\hat{H}_{\text{PXP}}, \quad \hat{S}^{y} = \frac{1}{\sqrt{2}}\hat{H}_{\text{PYP}}, \quad \hat{S}^{z} = \frac{1}{2}\sum_{j=1}^{N}(-1)^{j}\hat{\sigma}_{j}^{z}, \tag{2.44}$$

in the spin-1/2 language. We note that a similar algebra was first used in Ref. [73]. In that work, the algebraic structure was used to create a raising operator in the X basis and the scarred states were then approximated by acting with this operator on the ground state. As the eigenstates of $\sum_{b\in\Lambda_B}\hat{S}_{b}^{x}$ have energy spacing one and $\hat{\mathbf{H}}_{\text{FX}}$ is equal to $\sqrt{2}$ times this operator, we would expect the scarred eigenstates of PXP to be spaced in energy by $\sqrt{2}$. This approximation can be refined by computing the first order perturbation in energy due to $\hat{\mathbf{H}}_1$, which predicts an energy spacing of $13\sqrt{2}/14 = 1.31$ in the middle of the spectrum, very close to the 1.34 found numerically [68]. Overall, the spin-1 derivation of Ref. [68] provides an explanation for the appearance of non-thermal eigenstates in the PXP model. It also highlights the origin of the approximate su(2) algebra and how some specific perturbations can enhance it.

2.4.4 Beyond the original PXP model

Due to its intriguing properties, many variations of the PXP model have been studied since the original experiment on Rydberg atoms. This comprises studying the effect of perturbations [54, 70, 74] as well as disorder [75], and extensions to higher dimensions [64, 68, 76–79] and higher spin [59]. Interestingly, is has also been shown that the PXP exactly maps to a quantum link model (QLM) corresponding to a regularisation of the lattice Schwinger model of electrodynamics in 1+1D [80]. This provides another way to generalise the PXP model to values of spin beyond 1/2, with scarring still being present in all of them accessible to numerical simulations [81, 82]. Beyond static Hamiltonians, the impact of adding a periodic drive was also studied [78, 83–87], showing that it can improve the scarred dynamics. In parallel to these findings, scarred dynamics was also found in a flurry of other models, unrelated to PXP. We discuss these models and the underlying scarring mechanisms in the next section.

2.5 Mechanisms of weak ergodicity breaking

While the term QMBS was first put forward in Ref. [50], the quest to identify and construct isolated non-thermalising eigenstates in quantum systems has a much longer history. Most notably, such states were theoretically established in the Affleck-Kennedy-Lieb-Tasaki (AKLT) model in Ref. [88] back in 1989. Since then, there has been a flurry of models in which various aspects of QMBS physics have been witnessed, see the reviews [89–92]. In this section, we will go over the most important of these mechanisms. We will focus on the case of exact scars, in which there exists a dynamically disconnected subspace with a relatively simple structure, where all scarred eigenstates are located, as illustrated in Fig. 2.10**a**. In this section, we will mention three important mechanisms how such a subspace can arise in non-integrable many-body systems, which are summarised in Fig. 2.10**b-d**.

Before discussing in detail the QMBS mechanisms, we need to introduce the broader concept of Krylov restricted thermalisation [34]. As the name indicates, Krylov restricted thermalisation means that equilibration dos not happen at the level of the full Hilbert space but is limited to a single Krylov subspace. For any pure state $|\psi\rangle$, the Krylov subspace $\mathcal{K}$ is spanned by the states $|\psi\rangle$, $\hat{H}|\psi\rangle$, $\hat{H}^2|\psi\rangle$, $\hat{H}^3|\psi\rangle$, etc. In general, this procedure provides a subspace closed under the action of $\hat{H}$ only after the full Hilbert space is explored, i.e., once the state $\hat{H}^{\mathcal{D}-1}|\psi\rangle$ is reached, with $\mathcal{D}$ the Hilbert space dimension. However, for certain models and certain initial states, it can happen that $\hat{H}^n|\psi\rangle = 0$ or that $\hat{H}^n$ is not linearly independent from the previous states. In both cases, the Krylov subspace has dimension n and is closed under the action of $\hat{H}$. As a consequence, if a quench is performed from $|\psi\rangle$, the time-evolved wavefunction $e^{-i\hat{H}t}|\psi\rangle$ will always be in $\mathcal{K}$ spanned by $\{|\psi\rangle, \hat{H}|\psi_k\rangle, \ldots, \hat{H}^{n-1}|\psi\rangle\}$, which has dimension n. Due to $\mathcal{K}$ being separated from the rest of states, the properties of the eigenstates in this subspace can be drastically different, and thus create ergodicity

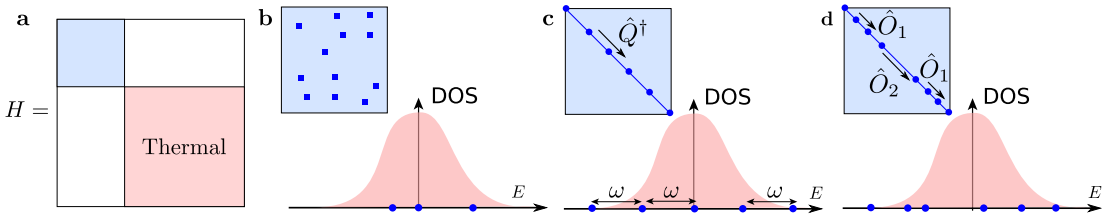

Figure 2.10: Schematic illustration of the Hamiltonian matrix structure for the main mechanisms to engineer QMBSs. **a** The Hamiltonian matrix is split between the ergodic subspace containing the vast majority of states (red) and the scarred subspace (blue), which can be generated using various mechanisms summarised in **b-d**. **b** For projector embedding, the Hamiltonian in the scarred subspace can have any structure specified by $\hat{H}_0$. **c** In the case of a restricted spectrum generating algebra, the scarred eigenstates are equidistant in energy and can be generated iteratively by the raising operator $\hat{Q}^\dagger$. **d** For rainbow scarring, the scarred eigenstates are generated by acting on the rainbow state with the generators of the half-system symmetries $\hat{O}_k$. The spacing in energy is dictated by the interplay of $\hat{O}_k$ and the interaction Hamiltonian $\hat{H}_{\text{int}}$.

breaking. We emphasise that we only consider the non-trivial Krylov subspaces that are *not* created by any global property of the Hamiltonian such as symmetries.

One example of Krylov restricted thermalisation occurs in so-called "fractonic" models, in which the conjunction of a global dipole conservation law and a purely local dynamical terms creates many frozen sectors [32–35]. This creates an exponential number of Krylov subspaces, i.e., much larger than the number of invariant subspaces for the dipole symmetry alone. This phenomenon is named "Hilbert space fragmentation" [91] and it also leads to a form of ergodicity breaking. However, within that framework one needs to distinguish two different cases. In the classification or Ref. [35], the fragmentation is called *strong* if the fraction of the Hilbert space each Krylov subspace takes goes to zero in the thermodynamic limit. In that case, we observe strong ergodicity breaking as all states will thermalise in a small portion of the Hilbert space. In contrast, fragmentation is considered *weak* when the fraction of the Hilbert space occupied by the largest Krylov subspace goes to 1 in the thermodynamic limit. As a consequence, eigenstates in this sector will dictate the microcanonical values of all observables and we expect agreement with the ETH. However, the vanishing fraction of eigenstates located in other sectors may not obey the ETH, leading to weak ergodicity breaking.

Exact QMBS is similar in principle to weak Hilbert space fragmentation, with the caveat that there is a sub-exponential number of Krylov subspace. In most models, there is in fact a single large thermal subspace and a small (vanishing in the thermodynamic limit) scarred subspace. We will now review the main mechanisms to create such Krylov subspaces.

2.5.1 Projector embedding

Shiraishi and Mori [93] introduced a general method to "embed" desired non-thermal eigenstates into a spectrum of a chaotic many-body Hamiltonian. As the name indic-

ates, this method relies on a set of local projectors $\hat{P}_j$ to protect a set of eigenstates from the action of the local operators $\hat{h}_j$, both centred around site j. Let us consider the global Hamiltonian

$$\hat{H} = \hat{H}_0 + \sum_j \hat{P}_j \hat{h}_j \hat{P}_j, \tag{2.45}$$

with $\hat{H}_0$ such that $[\hat{H}_0, \hat{P}_j] = 0$ for all j. Then if there exists a set of states $|\psi_k\rangle$ that obey $\hat{P}_j |\psi_k\rangle = 0 \ \forall \ j, k$, this set must be closed under the application of $\hat{H}$. Indeed, $|\phi_k\rangle = \hat{H} |\psi_k\rangle = \hat{H}_0 |\psi_k\rangle$ must also be annihilated by all $\hat{P}_j$ since $\hat{P}_j |\phi_k\rangle = \hat{P}_j \hat{H}_0 |\psi_k\rangle = \hat{H}_0 \hat{P}_j |\psi_k\rangle = 0$. As such, the set of all $|\psi_k\rangle$ forms its own Krylov subspace. As the $|\psi_k\rangle$ are the only states not affected by the $\hat{h}_j$, they will be non-thermal with respect to the vast majority of eigenstates. However, no additional structure is imposed on these states and their properties depend on the particular details of $\hat{P}_j$ and $\hat{H}_0$, as illustrated in Fig. 2.10**b**. Notably, the scarred construction still holds if $\hat{H}_0 = 0$. In that case, all $|\psi_k\rangle$ states are degenerate at zero energy.

We note that despite the apparent similarity between Eq. (2.45) and the PXP Hamiltonian, the scarred eigenstates in that model are not trivially due to this construction with the projector on the Rydberg ground states acting as the Shiraishi-Mori projectors. Nonetheless, a few isolated exact scars have been found in the PXP model using a similar construction [72]. Projector embedding has been used to realise scars in lattice systems with super-symmetry [94], using compact localised states [95], in a kagome lattice [96], or in topologically ordered models [97] and their deformations [98]. Generalisation of the Shiraishi-Mori construction have also been devised using the "broken unitary" picture [99] and for dual unitary circuits [100].

2.5.2 Restricted spectrum generating algebra

A system governed by Hamiltonian $\hat{H}$ is said to possess a spectrum generating algebra (SGA) – also called a dynamical symmetry – whenever there exists an operator $\hat{Q}^\dagger$ such that $[\hat{H}, \hat{Q}^\dagger] = \omega \hat{Q}^\dagger$. This means that if $|E\rangle$ is an eigenstate with energy $|E\rangle$, then $\hat{Q}^\dagger |E\rangle$ must be an eigenstate with energy $E + \omega$. This is a well-known property of models such as the Fermi-Hubbard model, where it is called η pairing symmetry [101].

More interestingly, it is also possible to have the SGA only in a reduced part of the Hilbert space. Indeed, let us suppose there exists a subspace W closed under the action of $\hat{H}$ such that the dynamical symmetry is absent at the level of the entire Hilbert space, $[\hat{H}, \hat{Q}^\dagger] \neq \omega \hat{Q}^\dagger$, but holds upon restriction to W:

$$[\hat{H}, \hat{Q}^\dagger] W = \omega \hat{Q}^\dagger W. \tag{2.46}$$

Then the Hamiltonian must admit the following exact eigenstates $|\mathcal{S}_n\rangle$ and corresponding eigenvalues E_n,

$$|\mathcal{S}_n\rangle = (\hat{Q}^\dagger)^n |\mathcal{S}_0\rangle \ , \quad E_n = E_0 + n\omega \ , \tag{2.47}$$

where $|\mathcal{S}_0\rangle$ is an eigenstate of the Hamiltonian $\hat{H}$ with eigenvalue E_0, as shown in Ref. [102]. In other words, $\hat{Q}^\dagger$ is a spectrum generating algebra of the Hamiltonian

limited to the subspace W, which we call a restricted spectrum generating algebra (RSGA).

Note that Eq. (2.47) implies equal energy spacing amongst the scarred eigenstates, as illustrated in Fig. 2.10**c**. Importantly, any state that has overlap only on these scarred eigenstates will show perfect wave-function revivals. The RSGA picture means that scarred eigenstates can be understood from a quasi-particle perspective [90]. Indeed, taking $|\mathcal{S}_0\rangle$ as the vacuum, the operator $\hat{Q}^\dagger$ then creates a quasi-particle. The scarred state $|\mathcal{S}_n\rangle$ can then be thought of as a condensate of n of these quasi-particles. The fact that they are non-interacting is manifested in the energy of these states only depending on the number of such quasi-particles.

One of the general frameworks that makes use of RSGA is the "tunnels to towers" construction [103], although other group theoretic approaches have also been devised [104, 105]. The tunnels-to-towers construction starts with a Hamiltonian $\hat{H}_{\text{sym}}$ which contains multiplets of degenerate eigenstates. In the common case of an su(2) algebra, this would be a term proportional to the total spin, while $\hat{Q}^\dagger$ could be a global raising operator for the magnetisation along a given axis. In that case, $Q^\dagger$ leaves the total spin unchanged which leads to $[\hat{H}_{\text{sym}}, \hat{Q}^\dagger] = 0$. One then adds an additional term $\hat{H}_{\text{SG}}$ that breaks the degeneracy between states in the same multiplet. In the su(2) picture, this term is typically proportional to the total magnetisation along the same axis as $\hat{Q}$, leading to the SGA structure $[\hat{H}_{\text{SG}}, \hat{Q}^\dagger] = \omega \hat{Q}^\dagger$. Finally, in order to turn the SGA into an RSGA, a third term $\hat{H}_A$ is added that annihilates only a single set of multiplets and makes the system non-integrable. This means that $\hat{Q}^\dagger$ only acts as raising operator in the subspace corresponding to that multiplet. This last step is similar to the Fermi-Hubbard model in Ref. [106, 107], where additional term couplings were added to the Hamiltonian to turn the η pairing from an SGA to a RSGA.

It is important to note that the tunnels-to-towers construction is not orthogonal to the projector embedding case. Notably, one can see that $\hat{H}_{\text{sym}} + \hat{H}_{\text{SG}}$ fills the role of $\hat{H}_0$, while $\hat{H}_A$ and $\sum_j \hat{P}_j \hat{h}_j \hat{P}_j$ have the same purpose. In fact, in the su(2) case, it is straightforward to show an example where the two construction coincide. Indeed, let us consider that the multiplet we want to preserve is the one with maximum total spin, and assume that the effective spin on each site is a spin-1/2. In that case, neighbouring effective spin pairs must all combine to have maximum spin 1. So it is easy to create an operator $\hat{H}_A$ using the Shiraishi-Mori construction where $\hat{P}$ is a projector on the maximum effective spin configurations on two sites. Such a projector will then commute with the global total spin and global magnetisation, meaning that $\hat{H}_0 \equiv \hat{H}_{\text{sym}} + \hat{H}_{\text{SG}}$ commutes with all $\hat{P}_j$. In fact, this is exactly what happens in the XY spin-1 magnet, where an effective spin-1/2 corresponding to the states $|m = +1\rangle$ and $|m = -1\rangle$ is used on each site [108]. The PXP model also resembles this construction. When formulated in the spin-1 language and when the perturbation $\delta\hat{\mathbf{H}}$ is used, $\hat{\mathbf{H}}_{\text{FX}}$ acts as $\hat{H}_0 \equiv \hat{H}_{\text{sym}} + \hat{H}_{\text{SG}}$ while $\hat{\mathbf{H}}_1 + \delta\hat{\mathbf{H}}$ acts as $\hat{H}_A$, locally projecting out pairs of states with total spin-2 to annihilate only eigenstates of $\hat{\mathbf{H}}_{\text{FX}}$ with maximum total spin. The main differences here is the presence of the additional projection steps that gets rid of $\hat{\mathbf{H}}_2$ and has a non-trivial effect on the eigenstates of $\hat{\mathbf{H}}_{\text{FX}}$. Nonetheless, we see a

close resemblance to the tunnels-to-towers and Shiraishi-Mori constructions, explaining the emergence of an approximate RSGA.

However, we stress that the tunnels-to-towers formalism is not simply a specific case of projector embedding. For example, the spin-1 AKLT chain features an RSGA [109] but it has been shown that it cannot be recast using projectors that are local in the spin-1 Hilbert space, despite the Hamiltonian being purely local [102] in that space. The only way to recover locality of projectors is to first fractionalise each spin-1 into two spin-1/2, and then only build local projectors into this expanded Hilbert space [110]. This procedure bears resemblance to the PXP case, showing that fractionalisation can play an import role in QMBS phenomena [110]. Other QMBSs stemming from an RSGA have been devised in a spin-1/2 model with emergent kinetic constraints [111], in a model with the dynamical Onsager algebra [112] and in a three-coloured model on a kagome lattice [113], amongst others.

2.5.3 Rainbow scars

The final mechanism we choose to discuss is a way to engineer scarring in models that can be decomposed into two identical subsystems. This so-called "rainbow scars" construction [114, 115] is based on having two subsystems, labelled "1" and "2". These subsystems have L sites with each site having p levels. Let us denote their Hilbert spaces by $\mathcal{H}_1$ and $\mathcal{H}_2$, and the Hilbert space dimension $\mathcal{D}_1 = \mathcal{D}_2 = p^L$. The construction requires that the subsystems' Hamiltonians obey the relation

$$\hat{H}_2 = -\hat{\mathcal{M}}\hat{H}_1^{\star}\hat{\mathcal{M}}^{\dagger}, \tag{2.48}$$

where $\hat{\mathcal{M}}$ is a unitary transformation mapping between the subsystems 1 and 2. This implies that the eigenvalues of $\hat{H}_1$ and $\hat{H}_2$ are identical but with an opposite sign. Notably, we can see that the eigenstates $|E_{1,j}\rangle$ in subsystem 1 and $|E_{2,j}\rangle$ in subsystem 2 have opposite energies are are related by $|E_{2,j}\rangle = \hat{\mathcal{M}}\,|E_{1,j}^{\star}\rangle$.

One consequence of the previous construction is that $|E_{1,j}\rangle \otimes |E_{2,j}\rangle$ will be an eigenstate of the composite system with energy exactly 0 for all j. Such states form an orthonormal basis of a zero-energy subspace of dimension $\mathcal{D}_1$, which always contains the state

$$|\mathbf{I}\rangle = \frac{1}{\sqrt{\mathcal{D}_1}}\sum_{j=1}^{\mathcal{D}_1}|E_{1,j}\rangle \otimes |E_{2,j}\rangle\,. \tag{2.49}$$

This state is special as it can be recast into a simpler form that is independent of the microscopic details of $\hat{H}_1$. To do that, we first rewrite it as

$$|\mathbf{I}\rangle = \frac{1}{\sqrt{\mathcal{D}_1}}\sum_{j=1}^{\mathcal{D}_1}|E_{1,j}\rangle \otimes \hat{\mathcal{M}}\,|E_{1,j}^{\star}\rangle = \frac{1}{\sqrt{\mathcal{D}_1}}\sum_{j=1}^{\mathcal{D}_1}\sum_{|\vec{\tau}\rangle,|\vec{\sigma}\rangle\in\mathcal{H}_1}(|\vec{\sigma}\rangle\langle\vec{\sigma}|E_{1,j}\rangle) \otimes \hat{\mathcal{M}}\left(|\vec{\tau}\rangle\langle\vec{\tau}|E_{1,j}^{\star}\rangle\right) \tag{2.50}$$

where σ_j denotes the state of site j, and $\vec{\sigma}$ denotes a configuration of multiple sites in the computational basis. In the second equation, we introduced two resolutions of the

identity as sums of projectors $|\vec{\sigma}\rangle\langle\vec{\sigma}|$ (and same for $\vec{\tau}$) on all configurations in subsystem 1. We can manipulate this further to show

$$|\mathbf{I}\rangle = \frac{1}{\sqrt{\mathcal{D}_1}} \sum_{|\vec{\tau}\rangle,|\vec{\sigma}\rangle\in\mathcal{H}_1} |\vec{\sigma}\rangle \otimes \hat{\mathcal{M}}\,|\vec{\tau}\rangle \left(\sum_{j=1}^{\mathcal{D}_1} \langle\vec{\sigma}|E_{1,j}\rangle\langle\vec{\tau}|E_{1,j}^{\star}\rangle\right) = \frac{1}{\sqrt{\mathcal{D}_1}} \sum_{|\vec{\sigma}\rangle\in\mathcal{H}_1} |\vec{\sigma}\rangle \otimes \hat{\mathcal{M}}\,|\vec{\sigma}\rangle\,, \tag{2.51}$$

The term in parentheses simply reduces to $\langle\vec{\sigma}|\vec{\tau}\rangle$ as the $|E_{1,j}\rangle$ form an orthonormal basis of $\mathcal{H}_1$. Importantly, the final expression for $|\mathbf{I}\rangle$ only depends on $\hat{\mathcal{M}}$.

If an additional condition is met, then we can recast $|\mathbf{I}\rangle$ in a more local form, which gets rid of the sum over all possible configurations in subsystem 1. This requires the operator $\hat{\mathcal{M}}$ to be composed of a mapping operator $\hat{\mathcal{R}}$ and another operator $\hat{\mathcal{O}}$ as $\hat{\mathcal{M}} = \hat{\mathcal{O}}\hat{\mathcal{R}}$, where $\hat{\mathcal{R}}$ maps site j (located in subsystem 1) to site $\bar{j}$ located in subsystem 2, thus creating pairs of sites across subsystems. $\hat{\mathcal{O}}$ must be a tensor product of single-site operator acting in subsystem 2 as $\hat{\mathcal{O}} = \bigotimes_j \hat{o}_j$. The state $|\mathbf{I}\rangle$ can then finally be written as

$$|\mathbf{I}\rangle = \frac{1}{\sqrt{\mathcal{D}_1}} \sum_{|\vec{\sigma}\rangle\in\mathcal{H}_1} |\vec{\sigma}\rangle\otimes\hat{\mathcal{M}}\,|\vec{\sigma}\rangle = \frac{1}{\sqrt{\mathcal{D}_1}} \sum_{|\vec{\sigma}\rangle\in\mathcal{H}_1} |\vec{\sigma}\rangle\otimes\hat{\mathcal{O}}\left(\hat{\mathcal{R}}\,|\vec{\sigma}\rangle\right) = \bigotimes_{j=1}^{L} \frac{1}{\sqrt{p}} \sum_{\sigma_j} |\sigma_j\rangle\otimes(\hat{o}_{\bar{j}}\,|\sigma_{\bar{j}}\rangle). \tag{2.52}$$

To get the final expression, we use the fact that the sum on all possible configurations in $\mathcal{H}_1$ can be rewritten as a tensor product of the sum of all states on the individual sites. This decomposition is also possible for $\hat{\mathcal{M}}\,|\vec{\sigma}\rangle$ as $\hat{\mathcal{R}}$ maps any site j to another site $\bar{j}$ in subsystem 2 and as $\hat{\mathcal{O}}$ is a tensor product of local operators $\hat{o}_{\bar{j}}$.

The state $|\mathbf{I}\rangle$ is called the rainbow state and is simply a tensor product of Bell pairs. For example, in the case where each subsystem is composed of spin-1/2 and $\hat{\mathcal{O}}$ is the identity, we end up with

$$|\mathbf{I}\rangle = \bigotimes_{j=1}^{L} \frac{1}{\sqrt{2}} \left(|\uparrow\rangle_j\,|\uparrow\rangle_{\bar{j}} + |\downarrow\rangle_j\,|\downarrow\rangle_{\bar{j}}\right). \tag{2.53}$$

Importantly, in this state there is maximum entanglement within the Bell pairs but no entanglement between them. This means that the bipartite entanglement entropy of this state will heavily depend on the chosen cut. If the cut separates subsystems 1 and 2, then it separates all Bell pairs and the entanglement entropy of $|\mathbf{I}\rangle$ is *maximal* and scales as the volume of the system. We can also have the opposite case where no Bell pairs are separated and the entanglement entropy is identically 0. Any behaviour between these can also be observed, with area-law or sub-area-law scaling possible.

Due to the relatively simple structure of $|\mathbf{I}\rangle$, it is straightforward to add a term $\hat{H}_{\text{int}}$ that connects subsystems 1 and 2 and has $|\mathbf{I}\rangle$ as eigenstate. For example, for the state in Eq. (2.53) any XY-type term between states in the same Bell pair will do. The dynamics of full system is then

$$\hat{H}_{\text{full}} = \hat{H}_{\text{int}} + \hat{H}_1 \otimes \hat{\mathbf{1}}_2 + \hat{\mathbf{1}}_1 \otimes \hat{H}_2, \tag{2.54}$$

with $|\mathbf{I}\rangle$ as one of its eigenstates. It is important to note that $|\mathbf{I}\rangle$ is an eigenstate of the full Hamiltonian *independent* of the microscopic details of $\hat{H}_1$. Its structure only depends on $\hat{\mathcal{O}}$ and its energy on $\hat{H}_{\text{int}}$. As such, the rainbow state will generically be very different from other eigenstates that depend heavily on the details of $\hat{H}_1$.

We note that this mechanism is not limited to embedding a single scarred eigenstate. Indeed, if there is an operator $\hat{O}_1$ that only acts on subsystem 1 and commutes with $\hat{H}_1$ then acting with $\hat{O}_1 \otimes \hat{\mathbf{1}}_2$ on $|\mathbf{I}\rangle$ leads to another eigenstate of $\hat{H}_1 \otimes \hat{\mathbf{1}}_2 + \hat{\mathbf{1}}_2 \otimes \hat{H}_2$. Indeed, it is straightforward to check that $\hat{O}_1 |E_{1,j}\rangle$ is also an eigenstates of $\hat{H}_1$ with the same energy as $\hat{H}_1 \hat{O}_1 |E_{1,j}\rangle = \hat{O}_1 \hat{H}_1 |E_{1,j}\rangle = E_{1,j} \hat{O}_1 |E_{1,j}\rangle$. It can thus be used instead of $\hat{O}_1 |E_{1,j}\rangle$ in Eq. (2.49), and if it is taken out of the sum in subsequent manipulations, we simply end up with $\left(\hat{O}_1 \otimes \hat{\mathbf{1}}_2\right) |\mathbf{I}\rangle$. Therefore, if this state is also an eigenstate of $\hat{H}_{\text{int}}$, it will be an eigenstate of the full Hamiltonian. If there are multiple symmetries $\hat{O}_k$ of $\hat{H}_1$, it also possible to combine them to create additional scarred states as $\hat{O}_1 \hat{O}_2 |\mathbf{I}\rangle$ as shown in Fig. 2.10**d**. Note that if there are multiple states generated this way, the scarred eigenstates might not be exactly equal to them. Indeed, these states are not guaranteed to be orthogonal. What is important is that they are all degenerate eigenstates of $\hat{H}_1 \otimes \hat{\mathbf{1}}_2 + \hat{\mathbf{1}}_1 \otimes \hat{H}_2$ with energy zero. Thus, they span a degenerate subspace, from which we can construct eigenstates of $\hat{H}_{\text{int}}$ that will automatically be eigenstates of the full system.

This addition of new scarred states can also be achieved with higher powers of a single operator. Notably, if $\hat{H}_1$ has a U(1) symmetry with n different values, we can have $n+1$ scarred eigenstates using $\hat{O}_1^k \hat{H}_1$ with $k = 0$ to n. As $\hat{O}_1^k \hat{H}_1$ generates the k-th states from state $k-1$, it will then act as a raising (or effective $\hat{J}^x$) operator. We can then chose a suitable $\hat{H}_{\text{int}}$ that acts as an effective $\hat{J}^z$ operator such that the (orthogonalised) states are equally spaced in energy, giving a tower of scarred eigenstates obeying the spectrum generating-algebra construction [114]. This precise case occurs in the spin-1 XY magnet [108, 115]. However, to be made apparent, it requires splitting the spin-1 into two spin-1/2 that will constitute the two subsystems. Some η-pairing tower of states in the spinful Fermi-Hubbard model [106, 107] can also be explained in that way, with the up and down spin species acting as the two subsystems [115]. Finally, we note that it is also possible to engineer other algebraic structures. To do this, one needs to chose $\hat{H}_1$ with a compatible symmetry and the possibility to engineer an $\hat{H}_{\text{int}}$ that acts as the required operator within the effective algebra [114].

2.5.4 Other constructions

As we already mentioned while discussing the individual cases, the three mechanisms of QMBS reviewed in this chapter are far from orthogonal to each other. In some cases, like the XY magnet [108], we can explain the appearance of scarring through *all* of them. These constructions are mostly useful as a way to engineer Hamiltonian systems featuring QMBSs. Other such mechanisms have been proposed, relying on proximity to Floquet evolution [116] or making use of matrix product states [117]. We note that recently, a new framework based on commutant algebras has been proposed to unify

the different construction above along with conventional symmetries and Hilbert space fragmentation [118–121]. Beyond these exact constructions, approximate scars have also been devised in other non-integrable lattice models [122], models of correlated fermions and bosons [123–125], and periodically driven systems [126–129]. Finally, there has been a recent interest in "inverted scarring" [130–132]. In this case, special eigenstates are instead embedded in a many-body localised system.

2.6 Summary

In this chapter, we have reviewed the key concepts of ergodicity and thermalisation in quantum systems that are explained by the ETH. We have also discussed how these notions relate to quantum chaos, in particular through the similarities between the eigenstates of physical Hamiltonians and those of random matrices, providing a way to diagnose if a given quantum system will thermalise or not. Moreover, we have surveyed some known violations of the ETH. We have introduced the concept of strong ETH violation, where all eigenstates deviate from the thermal prediction, as exemplified by integrable and MBL systems. By contrast, most of our attention was focused on weak ETH violation, where only a handful of eigenstates in the spectrum disagree with the ETH. We have first illustrated this with an example of single-particle quantum scars, arguing that similar physics occurs in a many-body system of Rydberg atoms, described by the PXP model. Finally, we have discussed a few complementary mechanisms that give rise to QMBSs in other physical systems.

Despite the plethora of theoretical models that host QMBSs, experimental realisations remain limited. Apart from Rydberg atom experiments, only a handful of other analogue quantum simulators have shown scarring-like behaviour. Exact helix states in XXZ spin models [133] have been observed in ultracold atoms, although only in 1D where the model is integrable [134]. These states only become true QMBSs in higher dimension or upon the addition of perturbations that make the model chaotic [134, 135], which has not been experimentally achieved yet. Signatures of ergodicity breaking resembling QMBS have also been measured in a 1D dipolar gas [136]. More recently, there have also been simulations of quantum many-body scarring in digital quantum systems. This include the reproduction of quenches of the original Rydberg atoms [137] as well the preparation of scarred eigenstates in the spin-1/2 scarred system [138]. Finally, using nitrogen-vacancy centres, quenches in the XY spin-1 magnet have also been simulated [139]. However, these results are limited to relatively short times and small sizes due to the restrictions of the current generation of devices.

In conclusion, the most important realisations of QMBS to date remain the ones in Rydberg atom arrays, both in 1D [43] and 2D [78]. These are the only results in large enough systems that go beyond the capabilities of classical simulation while at the same time providing clear revivals and state transfer of the wave-function in otherwise chaotic systems. This limited availability on other quantum platforms is currently a hindrance to the more widespread study of QMBSs. In this thesis, we will tackle this problem by proposing experimental implementations of QMBSs in quantum platforms

such as ultracold atoms in optical lattices (Chapters 4 and 5) and superconducting qubits (Chapter 6). We will also show results from quantum simulators for each of these platforms, demonstrating the feasibility of our proposals.

Beyond simply witnessing their presence in a quantum system, QMBSs were used in Rydberg atoms to prepare specific entangled states [140]. This hints to a potential practical use of this phenomenon: protecting a quantum trajectory from the scrambling action of chaotic quantum dynamics. This includes preserving the memory of the initial state or using QMBSs for state transfer. Beyond these simple orbits, quantum trajectory steering techniques based on QMBSs have also been devised [141, 142]. In Chapter 6, we will develop a way to tune the structure of QMBSs, allowing enhanced control on which states avoid thermalisation and the ability to change it dynamically. Similarly, due to the long coherence times associated with QMBSs, it has also been proposed that they could lead to better metrological accuracy [143]. In Chapter 3, we will show that certain classes of QMBSs have additional properties that indeed make them valuable for entanglement-enhanced quantum metrology.

Chapter 3

Algebraic structure of many-body scars and implications for transport and metrology

In the previous chapter, we have introduced various mechanisms known to give rise to QMBSs. In this chapter, we focus on the RSGA construction and explore two of its physical consequences. First, we show that when the relevant algebra is su(2), the QMBS eigenstates acquire additional desirable properties, regardless of the microscopic details of the system. In particular, we will show they possess extensive *multipartite* entanglement, making them a valuable resource for quantum metrology. Using the PXP model as an example, we demonstrate that multipartite entanglement can be experimentally accessed even when the su(2) algebra structure is only approximate. As a second consequence of RSGA, we demonstrate that it leads to anomalous behaviour in the energy transport of the PXP model. This will be attributed to the fact that this model possesses *multiple* su(2) representations, all stemming from the model's proximity to a free spin-1 paramagnet. These multiple representations conspire to produce observable dynamical signatures even at infinite temperature, e.g., oscillations in energy autocorrelation function when starting from a maximally mixed initial state. Finally, we show that even after these oscillations have dampened, an enigmatic regime of superdiffusion sets in, which is remarkably long-lived and robust to certain perturbations.

3.1 Multipartite entanglement of eigenstates

Thus far, we have repeatedly made use of von Neumann bipartite entanglement entropy to elucidate the difference of scarred eigenstates from thermal states. However, this is not the only measure of entanglement, and in particular it does not quantify

useful entanglement. Indeed, while classical states have no entanglement and are not a good resource from a quantum information (QI) point of view, thermal states that feature maximal volume-law entanglement scaling are also of little use. In comparison, the Greenberger-Horne-Zeilinger (GHZ) state is heavily used in QI despite having a constant (area-law) entanglement entropy of ln(2). In order to better characterise the potential usefulness of scarred states, we now turn to multipartite entanglement, which describes how many particles in a given system are entangled together.

3.1.1 Multipartite entanglement and quantum Fisher information

A quantum state state $|\psi\rangle$ is said to be k-producible granted it can be written as [144]

$$|\psi\rangle = |\phi_1\rangle \otimes |\phi_2\rangle \otimes \cdots \otimes |\phi_n\rangle \,, \tag{3.1}$$

where the $|\phi_j\rangle$ all contain k or fewer particles. This means that there are no groups of more than k particles entangled together. From this, we can say that a state contains *genuine* k-partite entanglement if it is k-producible but not $(k-1)$-producible, meaning that it contains at least a block of k particles entangled together. These definitions can be straightforwardly extended to mixed states via convex combinations [144].

Clearly, inspecting every possible bipartition to check which ones are non-entangled is not practical. In order to determine multipartite entanglement, one can use the quantum Fisher information (QFI) denoted by $\mathcal{F}_Q$ [145–147]. QFI has key mathematical properties such as convexity, additivity and monotonicity [146, 148–150]. It is also fundamental in quantum metrology, as it is the main factor determining the achievable accuracy in parameter estimation.

Let us consider the situation where we want to know the value of a parameter λ that enters some quantum phenomenon. For that, we let it act on a quantum state $\hat{\rho}$, giving us a new state $\hat{\rho}_\lambda$ that now directly depends on λ. By measuring $\hat{\rho}_\lambda$ we can then estimate the true value of this parameter. However, our estimator has some uncertainty characterised by the variance $(\Delta\lambda)^2$. The lower limit that this variance can take is given by the quantum Cramér-Rao bound

$$(\Delta\lambda)^2 \geq \frac{1}{M\mathcal{F}_Q(\hat{\rho}_\lambda)}, \tag{3.2}$$

where M is the number of independent measurements made during the measurement protocol [148, 150]. If $\hat{\rho}_\lambda$ is generated by an Hermitian operator $\hat{O}$ such that $\hat{\rho}_\lambda = e^{i\lambda\hat{O}}\hat{\rho}e^{-i\lambda\hat{O}}$, then $\mathcal{F}_Q$ admits an exact expression. For a general mixed state $\hat{\rho} = \sum_n p_n|n\rangle\langle n|$, it is [148]

$$\mathcal{F}_Q(\hat{O},\hat{\rho}) = 2\sum_{n,m}\frac{(p_n - p_m)^2}{p_n + p_m}|\langle n|\hat{O}|m\rangle|^2. \tag{3.3}$$

This quantity is upper bounded by $4\mathrm{Tr}\left[\hat{\rho}\,\hat{O}^2\right] - 4\mathrm{Tr}\left[\hat{\rho}\,\hat{O}\right]^2$, with the inequality saturated only if $\hat{\rho}$ is a pure state. In that case, the density matrix is simply $\hat{\rho} = |\psi\rangle\langle\psi|$ and the

QFI is

$$\mathcal{F}_Q(\hat{O}, |\psi\rangle) = 4\,\langle \Delta \hat{O}^2 \rangle = 4\,\langle \psi | \hat{O}^2 | \psi \rangle - 4\,\langle \psi | \hat{O} | \psi \rangle^2 . \tag{3.4}$$

Finally, there is a direct relation between the QFI and multipartite entanglement [151–153]. Let us consider a system with N particles and a global operator $\hat{O} = \frac{1}{2}\sum_{i=1}^{N} \hat{o}_i$ which is an extensive sum of operators $\hat{o}_i$ with local support and with eigenvalues λ such that $\lambda_{\max} - \lambda_{\min} = 2$, e.g. Pauli matrices. If the QFI density satisfies the inequality

$$f_Q \equiv \frac{\mathcal{F}_Q(\hat{O}, \hat{\rho})}{N} > m \ , \tag{3.5}$$

then at least $(m+1)$ parties in the system are entangled (with $1 \leq m \leq N-1$ a divisor of N). This means that the system has genuine $(m+1)$-partite entanglement. In particular, if $N - 1 \leq f_Q(\hat{O}) \leq N$, then the state is genuinely N-partite entangled.

Now that we have defined QFI and multipartite entanglement, we move on to computing the expected values for both chaotic and scarred eigenstates. We will show that there is a stark contrast between the two when QMBSs stem form an su(2) RSGA, as derived with our collaborators in Ref. [1].

3.1.2 QFI for chaotic eigenstates

Computing the QFI for generic eigenstates might seem an impossible task without the knowledge of microscopic details of the system. However, in this section we show that this can be done by relying on their similarity to thermal states. In general, different operators $\hat{O}$ lead to different bounds on QFI and there is no systematic method (without some knowledge about the physical system [154, 155]) to choose the optimal one. Here, we restrict ourselves to one-dimensional systems and collective operators $\hat{O} = \frac{1}{2}\sum_{i=1}^{N} \hat{o}_i$, which are typically explored in cold-atoms experiments and in interferometric schemes [150]. For the eigenstates $|E_n\rangle$, the QFI with respect to such collective operators $\mathcal{F}_Q(\hat{O}, |E_n\rangle) = 4\langle E_n | \Delta \hat{O}^2 | E_n \rangle$ can be expressed in terms of the connected correlation functions $G_{i,j}(E_n) \equiv \langle E_n | \hat{o}_i \hat{o}_j | E_n \rangle - \langle E_n | \hat{o}_i | E_n \rangle \langle E_n | \hat{o}_j | E_n \rangle$. If we further assume *translational invariance*, then $G_{i,j} = G_{|i-j|}$ and the QFI density (3.5) reads

$$f_Q(\hat{O}, |E_n\rangle) = G_0(E_n) + 2\sum_{r=1}^{N-1} G_r(E_n) \ . \tag{3.6}$$

Note that $G_0(E_n) = \mathcal{O}(1)$ is always an intensive quantity[1], hence the scaling of f_Q depends on the behaviour of $G_r(E_n)$ as a function of distance r. Generic chaotic eigenstates of a locally-interacting many-body Hamiltonian far from criticality are well-known to obey ETH [13, 156]. In this case, the connected correlation functions scale as

$$G_r(E_n) \sim c_r e^{-r/\xi} \ , \quad r \gg \xi \ , \tag{3.7}$$

where $|c_r| = \mathcal{O}(1)$ is an intensive constant that depends on the operators, and ξ is the correlation length at energy E_n. This is a consequence of the clustering property

[1] For instance, $G(E_n) = 1$ for spin operators and eigenstates in the middle of the spectrum.

of connected correlation functions of local observables, which has been demonstrated for canonical thermal states [157]. Appealing to ETH [158], the same clustering property holds for eigenstates of local Hamiltonians up to sub-extensive corrections [159]. Notable exceptions include global conserved quantities, e.g., $\hat{B} = \sum_i \hat{b}_i$, which obeys $[\hat{H}, \hat{B}] = 0$. In this case the variance of the conserved operator is zero in each eigenstate, $\langle \hat{B}^2 \rangle_c = 0$, imposing a sum rule that leads to $\langle \hat{b}_i \hat{b}_{i+r} \rangle \sim -\frac{1}{2(N-1)}$, see e.g. Ref. [28].

A few remarks are in order. The scaling in Eq.(3.7), despite being unambiguous classically, might look counterintuitive with respect to common wisdom about quantum chaotic eigenstates. Namely, the latter are well known to be highly entangled quantum states, characterised by a volume law scaling of the entanglement entropy [160–162]. In other words, they can not be represented as matrix product states (MPS) of finite bond dimension. This might seem to contradict Eq.(3.7), which states the absence of long-range correlations between local operators. First of all, the connected correlation functions $G_r(E_n)$ of local (small) operators encode only the *local* information of the two-point reduced density matrix (on sites i and $i + r$). Hence, their scaling makes no predictions on the non-local structure encoded in the entanglement entropy of the — usually large — region A. Such entanglement entropy S_A is defined as the von Neumann entropy of the reduced density matrix $\hat{\rho}_A$ and, to study its scaling with the system size, one typically lets the region A scale with the volume of the system. Therefore, to falsify the volume law scaling, one would need exponential decay of correlations of non-local (large) operators with support over $A \propto \text{Vol}$. This statement is much stronger than Eq. (3.7) and it is usually wrong (interestingly, this occurs for many-body-localised eigenstates [31]). A final comment concerns the MPS representation of the eigenstates. While one could always describe the two-point reduced density matrix (on sites i and $i+r$) as an MPS of finite bond dimension, the MPS representation of the full eigenstate constitutes a *global* description and, for what argued above, the site in the middle of the system should carry the non-local correlations for size $N/2$.

The previous comments highlight in what sense chaotic ETH eigenstates are different from thermal density matrices $\hat{\rho}_{\text{Gibbs}}$: they have the same correlations as local operators, but when it comes to non-local ones they can be very different. Indeed, the mutual information of $\hat{\rho}_{\text{Gibbs}}$ is area law and this state can be written efficiently as a matrix product operator (MPO). On the other hand, chaotic eigenstates are more complicated, hosting volume law entanglement and non-local correlations.

Now that we have argued that correlations in chaotic eigenstates obey Eq. (3.7), this equation can be plugged in Eq. (3.6). Summing over r, we obtain for $N \gg 1$

$$f_Q(\hat{O}, |E_n\rangle) \lesssim G_0(E_n) + \frac{2c}{e^{1/\xi} - 1} + \mathcal{O}(e^{-N}) \ , \tag{3.8}$$

where we have used $|c_r| \leq c = \mathcal{O}(1)$. This equation shows that generically the QFI density of chaotic eigenstates, away from criticality, is an intensive quantity that can be evaluated explicitly from the knowledge of a thermal correlation length. Furthermore, whenever the correlation length ξ is large (but finite), one has

$$f_Q(\hat{O}, |E_n\rangle) \simeq 2\xi \quad \text{for} \quad \xi \gg 1 \ . \tag{3.9}$$

Thus, the QFI is also large and finite. By comparing this expression with the relation to multipartite entanglement (3.5), we find that the size of the biggest entangled block scales as twice the correlation length. This finding is fully consistent with known results for critical pure or thermal states, where the QFI for the order parameter diverges universally [154, 163–167].

3.1.3 QFI for scarred eigenstates

We now contrast the scaling of the QFI for thermal eigenstates (3.8) to the one for a class of *exact* scars. More precisely, we focus on QMBS eigenstates that stem from an RSGA, as introduced in Chapter 2. Additionally, we require here that the raising operator $Q^\dagger$ is a collective operator $\hat{Q}^\dagger = \sum_{i=1}^{N} \hat{o}_i$ with $\hat{o}_i$ an operator with local support. For convenience and additional clarity when considering the su(2) case, let us define

$$\hat{J}^+ \equiv \frac{\hat{Q}^\dagger}{2} \ , \quad \hat{J}^- \equiv \frac{\hat{Q}}{2} \ , \quad \hat{J}^z \equiv \frac{\hat{H}}{\omega} \ . \tag{3.10}$$

The commutation relations between $\hat{J}^z$ and $\hat{J}^\pm$ (in the scarred subspace W) are already known from Eq. (2.46). However, there is the some freedom in the properties of $[\hat{J}^+, \hat{J}^-]W$. These will prove to be important, as $\langle \mathcal{S}_n | \hat{J}^+ \hat{J}^- | \mathcal{S}_n \rangle / N^2$ acts as probe for off-diagonal long-range order (ODLRO) [168], which would be signalled by values of this quantity scaling as $\mathcal{O}(1)$. If, for instance, one has $([\hat{J}^+, \hat{J}^-] - 1)W = 0$ – the standard algebra of the harmonic oscillator – then $\hat{J}^\pm$ act like creation and annihilation operators, while $\hat{J}^+\hat{J}^-$ acts as a number operator. It then follows

$$\frac{\langle \mathcal{S}_n | \hat{J}^+ \hat{J}^- | \mathcal{S}_n \rangle}{N^2} = \frac{1}{N}\frac{n}{N} \ , \tag{3.11}$$

and there is no long-range order. Suppose, instead, that the operators $\hat{J}$ obey the usual su(2) commutation relations

$$[\hat{J}^+, \hat{J}^-] =_w 2\hat{J}^z, \tag{3.12}$$

where we use $=_w$ to denote that the equality only holds in the subspace W. Then Eq. (3.10) is simply the Cartan-Weyl basis and we can define the effective spin operators $\hat{J}^x = \left(\hat{J}^+ + \hat{J}^-\right)/2$ and $\hat{J}^y = \left(\hat{J}^+ - \hat{J}^-\right)/(2i)$ as well as a the total spin

$$\begin{aligned} \hat{\mathbf{J}}^2 &= (\hat{J}^x)^2 + (\hat{J}^y)^2 + (\hat{J}^z)^2 = (\hat{J}^z)^2 + \frac{1}{2}\left(\hat{J}^+\hat{J}^- + \hat{J}^-\hat{J}^+\right) \\ &=_w \hat{J}^z\hat{(}J^z + 1) + \hat{J}^-\hat{J}^+ =_w \hat{J}^z(\hat{J}^z - 1) + \hat{J}^+\hat{J}^- \ . \end{aligned} \tag{3.13}$$

Since $[\hat{\mathbf{J}}^2, J^{z,\pm}] =_w 0$, the scarred states $|\mathcal{S}_n\rangle$ are characterised by a fixed eigenvalue of $\hat{\mathbf{J}}^2$ that can be determined directly from the ground state as

$$\hat{\mathbf{J}}^2 |\mathcal{S}_0\rangle = \left[\hat{J}^z(\hat{J}^z - 1) + \hat{J}^+\hat{J}^-\right] |\mathcal{S}_0\rangle = \frac{E_0}{\omega}\left(\frac{E_0}{\omega} - 1\right) |\mathcal{S}_0\rangle \ , \tag{3.14}$$

where we have used $J^- |\mathcal{S}_0\rangle = 0$ and the definition of $\hat{J}^z$ in Eq. (3.10). This is equivalent to a total spin $S = -E_0/\omega$. Note that this quantity is always positive as the Hamiltonian in W is proportional to the total magnetisation along the Z axis, which has a ground state with $E_0 < 0$. While Eq. (2.46) leaves the possibility that an additional term proportional to the identity is also included in the Hamiltonian, it would then not directly satisfy Eq. (3.12). Nonetheless, in such a case our results would still apply. Due to the part of the Hamiltonian acting as μ times the identity in W, the total spin would then be $S = -(E_0 - \mu)/\omega$.

For simplicity, let us only consider the case $\mu = 0$, for which we can compute

$$\begin{aligned} \langle \mathcal{S}_n | \hat{J}^+ \hat{J}^- | \mathcal{S}_n \rangle &= \langle \mathcal{S}_n | \hat{\mathbf{J}}^2 - \hat{J}^z(\hat{J}^z - 1) | \mathcal{S}_n \rangle \\ &= \frac{E_0}{\omega}\left(\frac{E_0}{\omega} - 1\right) - \frac{E_n}{\omega}\left(\frac{E_n}{\omega} - 1\right) \\ &= -2\frac{E_0}{\omega} n - n^2 + n \ . \end{aligned} \tag{3.15}$$

If we now use the extensivity of the ground state energy $E_0 = -\epsilon_0 N$ and divide everything by N^2, we directly obtain

$$\frac{\langle \mathcal{S}_n | \hat{J}^+ \hat{J}^- | \mathcal{S}_n \rangle}{N^2} = \frac{2\epsilon_0}{\omega}\frac{n}{N} - \left(\frac{n}{N}\right)^2 + \frac{n}{N^2} \ , \tag{3.16}$$

As $n = 0$ to N, the first two terms are $\mathcal{O}(1)$ while the last one is only $\mathcal{O}(1/N)$. Note that Eq. (3.15) gives back exactly Eq. (8) of Ref. [108] with $\omega = 2h$ and $\epsilon_0 = h$.

Hence, we have shown that exact scars with finite energy density ($n/N = \mathcal{O}(1)$) possess long-range order [168]. As such, for the local operators $\hat{o}_i$ appearing in $\hat{Q}^\dagger$, the connected correlation functions are finite in the thermodynamic limit i.e.

$$G_r(E_n) \sim \text{const} \ , \quad r \to \infty \ , \quad N \to \infty \ . \tag{3.17}$$

This property was used in Ref. [73] to interpret scarred eigenstates as finite-energy-density condensates of weakly interacting π-magnons that possess long-range order in both space and time. Our key result is that, through Eq. (3.6), the presence of long-range order implies genuine multipartite entanglement of this class of QMBSs. In fact, the QFI density with respect to the operator $\hat{J}^x$ can be directly computed. We first decompose $\hat{J}^x$ into $\hat{J}^+$ and $\hat{J}^-$ to get

$$\begin{aligned} f_Q(\hat{J}^x, |\mathcal{S}_n\rangle) &= \frac{4}{N}\langle \mathcal{S}_n | \left(\frac{\hat{J}^+ + \hat{J}^-}{2}\right)\left(\frac{\hat{J}^+ + \hat{J}^-}{2}\right) | \mathcal{S}_n \rangle - \frac{4}{N}\left(\langle \mathcal{S}_n | \hat{J}^x | \mathcal{S}_n \rangle\right)^2 \\ &= \frac{\langle \mathcal{S}_n | \hat{J}^+ \hat{J}^- + \hat{J}^- \hat{J}^+ | \mathcal{S}_n \rangle}{N} \\ &= 2\frac{\langle \mathcal{S}_n | \hat{J}^+ \hat{J}^- | \mathcal{S}_n \rangle}{N} - 2\frac{\langle \mathcal{S}_n | \hat{J}^z | \mathcal{S}_n \rangle}{N}, \end{aligned} \tag{3.18}$$

where we used $\langle \mathcal{S}_n | \hat{J}^x | \mathcal{S}_n \rangle = \langle \mathcal{S}_n | (\hat{J}^\pm)^2 | \mathcal{S}_n \rangle = 0$ to go from the first to the second line and the definition of $\hat{J}^z$ in Eq. (3.12) to go between the second and third line. Finally,

looking at the last line, we can use Eq. (3.16) to obtain the analytical expression for the first term while the second is equal to $-\epsilon_0 N/\omega + n$ by construction. This leads to the final expression

$$f_Q(\hat{J}^x, |\mathcal{S}_n\rangle) = 2\left(\frac{2\epsilon_0}{\omega} - \frac{n}{N}\right) n + \frac{2\epsilon_0}{\omega} \ , \tag{3.19}$$

Therefore, exact scars with finite energy density $n \sim N$ possess super-extensive QFI $F_Q \sim N^2$ and they are genuinely multipartite entangled. This is an important result, as it is highly non-trivial to engineer super-extensive scaling of quantum Fisher information for many-body states [149]. We note that results can be obtained for $\hat{J}^y$ and for linear combinations of $\hat{J}^x$ and $\hat{J}^y$.

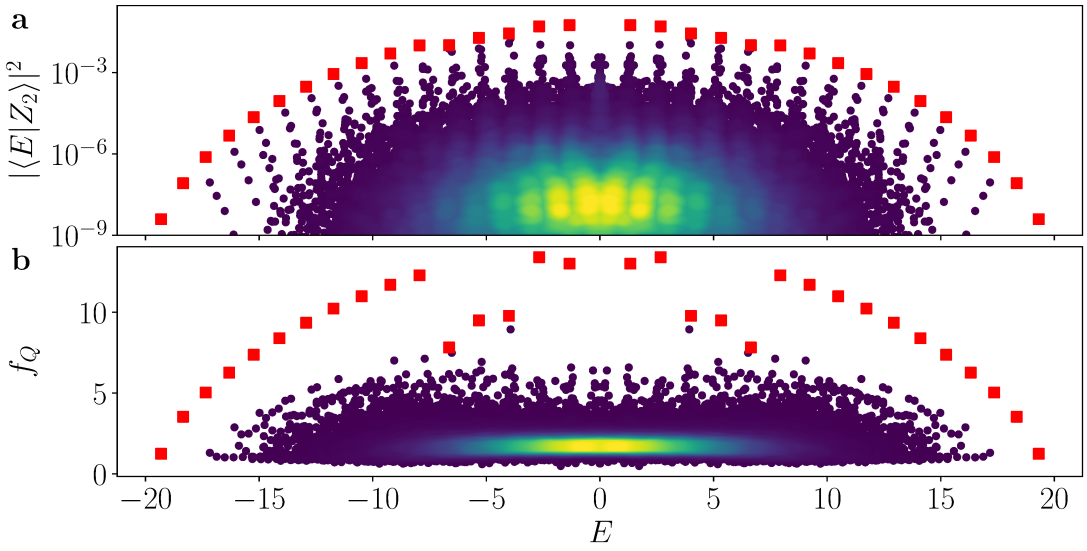

Figure 3.1: **a** Overlap between exact PXP eigenstates and the Néel state. Red squares indicate the QMBS eigenstates. **b** The QFI density of the PXP eigenstates in the $k = 0, p = 1$ and $k = \pi, p = -1$ sectors. The red squares denote the same QMBS eigenstates as in **a**. In both plots, the dips in the middle of the spectrum are due to hybridisation of QMBS eigenstates with thermal states. The colour code indicates the density of points and all data is for the PXP model in Eq. (2.20) with N=32 spins.

3.2 Multipartite entanglement in the PXP model

In the PXP model (introduced in Chapter 2), the algebraic structure of scarred states is only approximate, hence Eq. (2.46) is not exactly obeyed. Nonetheless, we can numerically probe the QFI density using the staggered magnetisation

$$\hat{M}_S = \frac{1}{2}\sum_j (-1)^j \hat{\sigma}_j^z, \tag{3.20}$$

which is exactly equal to $\hat{S}^z$ as obtained from the total magnetisation along the Z axis in the parent spin-1 model, see Eq. 2.44. This operator is a natural choice because it is experimentally accessible and it is proportional to the total spin $\hat{J}^x$ operator in the language of the RSGA, while QMBSs are eigenstates of the corresponding $\hat{J}^z$ operator.

For simplicity, we will set $\Omega = 1$ in the rest of this chapter. The numerical results for the QFI density of eigenstates are then shown on Fig. 3.1. As for exact scars, the scarred eigenstates in the PXP model have largest QFI among all eigenstates. However, as the scarred PXP subspace is weakly connected to the rest of the Hilbert space, in larger systems the QMBS eigenstates begin to hybridise with thermal eigenstates [54], which is manifested as a reduction in QFI and the overlap with the Néel state. Signatures of this in the middle of the spectrum can be observed in Fig. 3.1. Hybridisation can thus prevent the QFI of the individual scarred eigenstates to scale super-extensively beyond a certain size, see Fig. 3.2. The same figure also shows that, for thermal eigenstates, f_Q does not show a clear dependence on N, as predicted in Eq. (3.8). While hybridisation will likely prevent any single QMBS eigenstate from

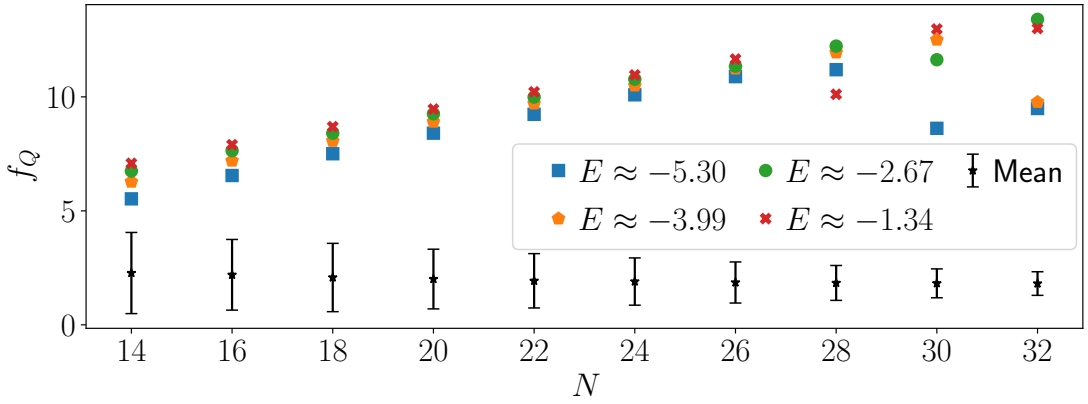

Figure 3.2: Finite size scaling of QFI density for several QMBS eigenstates of the PXP model with energies E near the middle of the spectrum, contrasted against the mean value over all eigenstates. The scaling is extensive until N=28, where hybridisation between the scarred eigenstates and thermal eigenstates with a similar energy starts to lower f_Q.

having a super-extensive QFI, $F_Q \propto N^2$, in the asymptotic limit, such exact eigenstates cannot realistically be prepared in Rydberg atom experiments, as they lack protection from any global symmetry. Instead, we propose that extensive QFI in this model can be leveraged in practice by dynamically evolving the system to moderate times, i.e., times longer than the initial relaxation scale $\sim 1/\Omega$, where Ω is the Rabi frequency for the model in Eq. (2.20). In Fig. 3.3 we computed the evolution of QFI density when the PXP model is quenched from various initial states, contrasting the behaviour of $|\mathbb{Z}_2\rangle$ with thermalising initial states, such as the polarised state, $|\circ\circ\circ\cdots\rangle$, and other random product states.

The dynamics from the $|\mathbb{Z}_2\rangle$ state in Fig. 3.3 clearly stands out from other thermalising initial states. Following the initial spreading, f_Q undergoes a fast growth in the

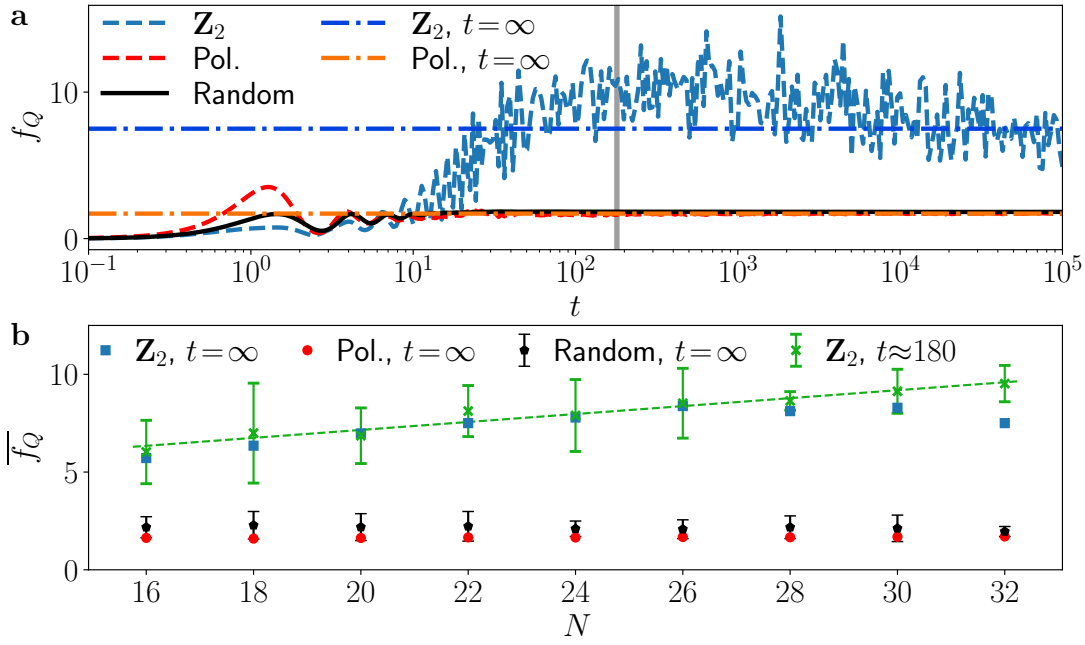

Figure 3.3: **a** Time evolution of QFI density following quenches from various initial states for $N = 32$. The horizontal lines show the infinite-time QFI density averages for the Néel state and the polarised state. **b** Long-time QFI density averages for various initial states as a function of system size. The green crosses correspond to the average over the time window indicated in grey in **a**. Its width is longer than the revival period of the Néel state in order to average over these higher-frequency oscillations. The window is centred around $t = 180$, because at this time the maximum has been reached for all system sizes investigated but the drop at even later times has not started yet. The dashed green line is a linear fit $0.20N + 3.06$ to this data. In both plots the data for random states is an average over 20 samples and the error bars correspond to the standard deviation.

$|\mathbb{Z}_2\rangle$ case, reaching a broad maximum at intermediate times, $O(10^2)$. For all system sizes investigated (including the ones where eigenstate hybridisation is observed), the value of this maximum is *extensive* in system size. At much later times, however, f_Q starts to drop, as expected from the eigenstate plot in Fig. 3.1. The non-extensivity of the late-time value of f_Q can be independently confirmed by computing the infinite-time average using the diagonal ensemble with corrections for higher moments (see App. A). We attribute this behaviour as stemming from the very small energy difference between the scarred eigenstate and the thermal state it hybridises with. This spacing only becomes apparent at very late time, and before that the two states essentially have the same phase. As such, the fact that the anomalous properties become "spread" between these two states has no effect.

3.2.1 Effect of perturbations

Beyond quenches, we can also try to improve the QFI of eigenstates themselves by using the quasi-local PXPZ perturbation in Eq. (2.34). This further separates the top band of scarred states from the rest and makes the approximate su(2) algebra almost exact in the scarred subspace. As a consequence, the QFI of the scarred states is essentially equal to the analytical formula in Eq. (3.19). While this perturbation

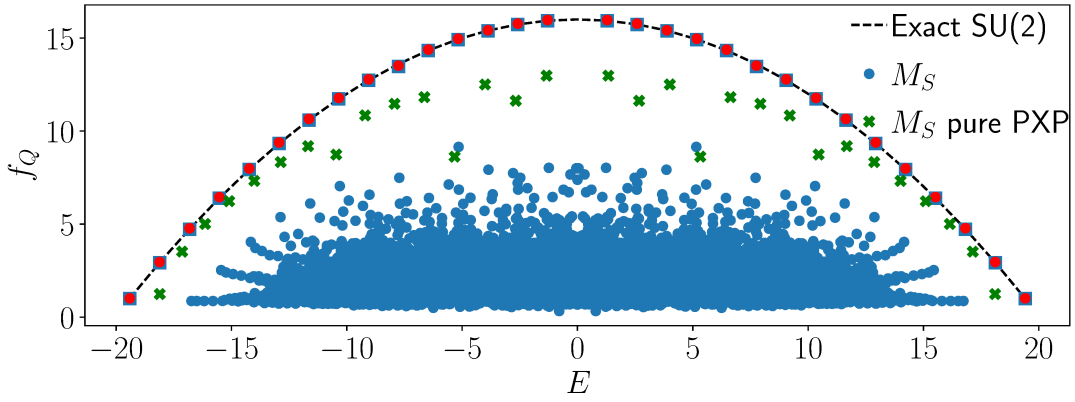

Figure 3.4: QFI density of the PXP eigenstates with and without perturbation probed with staggered magnetisation M_S for $N = 30$. The scarred states (identified by their high-overlap with the Néel state) are highlighted in red. The QFI density of the scarred eigenstates of the perturbed PXP model shows good agreement with the expectations based on the exact su(2) algebra. In the perturbed case, no hybridisation is visible, unlike in the pure PXP model. This is a consequence of the algebra being almost closed, and thus providing a much stronger separation between the scarred states and the thermal bulk.

restores the extensive QFI density of scarred states for the system sizes we can reach numerically, this is a quasi-local perturbation that is extremely complicated to engineer in a quantum device.

To try and overcome this last issue, we can turn towards more experimentally friendly perturbations. Among these, a prime candidate is the staggered magnetisation itself. Indeed, as it is part of the approximate su(2) algebra, one can wonder about its impact on both the dynamics and the eigenstates. More precisely we study the effect of χ in the Hamiltonian

$$\hat{H}_{\text{Stag}} = \hat{H}_{\text{PXP}} + 2\chi\hat{M}_S = \sum_{j=1}^{N} \hat{P}_{j-1}\hat{\sigma}_j^x\hat{P}_{j+1} + \chi\sum_{j=1}^{N}(-1)^j\hat{\sigma}_j^z. \tag{3.21}$$

Looking at the PXP su(2) algebra in Eq. (2.44), it is straightforward to see that the first term corresponds to the total X operator of the algebra, while the second term corresponds to the total Z operator, and so the Hamiltonian can be rewritten as $\sqrt{2}\hat{S}^x + 2\chi\hat{S}^z$. Due to this, the dynamics of the model in Eq. (3.21) can be understood in a simple spin-precession picture for all χ, similar to what was discussed in Chapter 2

for the case $\chi = 0$. We illustrate this with the help of the Bloch sphere in Fig. 3.5**a**. The Néel state is at the South Pole, along the Z axis. For $\chi = 0$, the precession axis is the X axis, lying in the equatorial plane. As χ is increased, the precession axis is tilted out of plane and moved closer to the Z axis. Hence, the antipodal point on the trajectory is no longer the anti-Néel state (at the North Pole), but another state placed on the opposite side of the precession axis. As χ is further increased, this opposite point gets closer and closer to the Néel state. In the limit $\chi \to \infty$, the precession axis becomes the Z axis and the Néel state an exact eigenstate of the system. As a consequence, we would naively expect better revivals as χ increases. However, detailed analysis (see Appendix B) shows that the improvement of revivals is non-monotonic in χ, with local maxima at $\chi = 0$, $\chi = \pm 1/\sqrt{8}$ and $\chi \to \pm\infty$. Importantly, the maximum at $\chi = \pm 1/\sqrt{8}$ leads to better revivals than $\chi = 0$.

In practical terms, using staggered magnetisation with $\chi = \pm 1/\sqrt{8}$ provides a relatively simple way to enhance dynamical signatures of scarring compared to the other perturbations with similar effect that were discussed in Chapter 2. Nonetheless, it also has limitations. Indeed, the staggered magnetisation does not make the algebra as closed as do PXPP and PXPZ perturbations, as it main effect is a more equal spacing between QMBS states. The fact that the Hamiltonian is now $\sqrt{2}\hat{S}^x + 2\chi\hat{S}^z$ instead of just $\sqrt{2}\hat{S}^x$ also means that the staggered magnetisation (equal to $\hat{S}^z$) will no longer be orthogonal to it. As such, the variance of the scarred eigenstates with respect to it will no longer be maximal. This can be seen in Fig. 3.5**b**, where it is clear that the QFI of eigenstates is higher in the unperturbed PXP model than for $\chi = 1/\sqrt{8}$ when probed with the staggered magnetisation. While this is in general not a problem and one could simply use $\hat{S}^y$ instead, this operator is equal to staggered PYP in the PXP model. So this is no longer a sum of single-site operators. The projectors $\hat{P}$ also mean that the extremal value of this operator are not $\pm N/2$ like for $\hat{M}_S$ but will be smaller, leading to a significantly reduced value of the maximum variance. The main message is that, while it provides a clear advantage for the lifetime and amplitude of oscillations after a quench, the staggered magnetisation does not lead to a clear improvement for metrology.

So overall, we find that there is no experimentally realisable perturbation that allows to restore the extensive QFI density for eigenstates. Beyond this, preparing high-energy eigenstate is generally a very difficult task as well, as the energy gap to the neighbouring states decreases exponentially with system size. On the other hand, the Néel state is straightforward to prepare thanks to its simple structure. As such, we view performing quenches from that state until intermediate times as the most promising way to obtain states with extensive QFI density in the PXP model.

3.3 Multiple su(2) representations and spectral properties of the PXP model

In the previous sections, we have discussed the consequences of RSGA on the structure of the eigenstates. We have also studied the PXP case, where this algebra is only

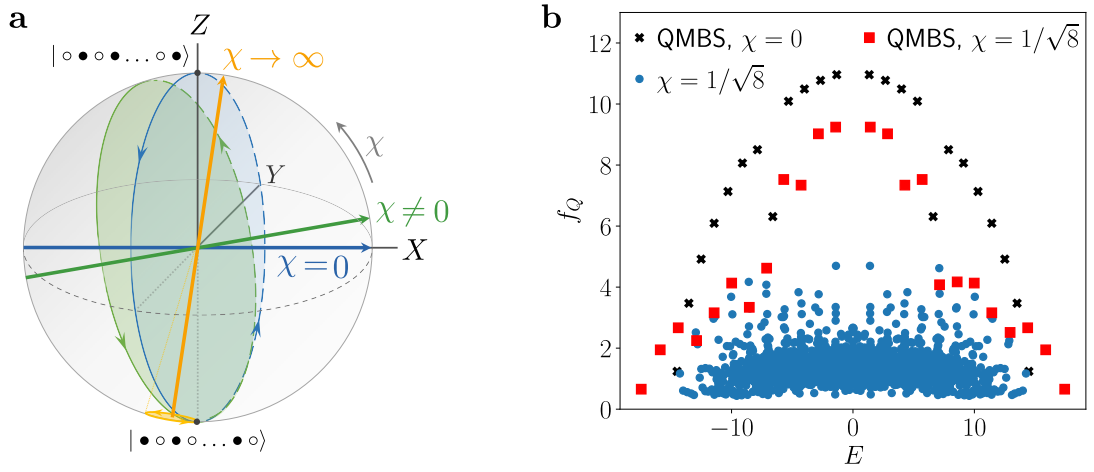

Figure 3.5: **a** Schematic picture of the effect of staggered magnetisation on the dynamics after a quench form the Néel state. As χ is increased, the precession axis is tilted towards the Z axis. The X, Y and Z labels refer to the the approximate su(2) algebra, which matches with the spin-1 description. **b** QFI density of the PXP eigenstates with $\chi = 1/\sqrt{8}$ and in the pure PXP model ($\chi = 0$) probed with staggered magnetisation M_S for $N = 24$. The scarred states (identified by their high-overlap with the Néel state) are highlighted in red. The scarred eigenstates of the perturbed PXP model show a smaller value of QFI that in the unperturbed one. This is mainly explained by the staggered magnetisation not being orthogonal to the Hamiltonian anymore.

approximate. As we reviewed in Chapter 2, the algebraic structure in the PXP model can be linked to a parent spin-1 model, where the Hamiltonian is simply the free paramagnet $\hat{\mathbf{H}}_{\mathrm{FX}}$ plus some perturbations $\hat{\mathbf{H}}_1$ and $\hat{\mathbf{H}}_2$. The scarred states can then be understood as the eigenstates of this paramagnet (projected into the constrained space) with the largest total spin. However, it is natural to ask what is the fate of the other eigenstates of $\hat{\mathbf{H}}_{\mathrm{FX}}$. Do they get completely scrambled by $\hat{\mathbf{H}}_1$ and $\hat{\mathbf{H}}_2$, or can we still find traces of them in the PXP model?

In order to answer this question, it is important to recall why the scarred states are left relatively untouched by these two perturbations. In Ref. [68], it was found that the effect of $\hat{\mathbf{H}}_1$ could be counterbalanced by adding a small term $\delta\hat{\mathbf{H}}$, but only for neighbouring spin-1 pairs forming a spin-2 quintuplet. The only eigenstates for which this is true for all pairs are the one with maximal total spin, i.e $|\vec{S}| = N/2$. Hence the effect of $\hat{\mathbf{H}}_1$ on them is relatively small. However the proportion of these spin-2 pairs (in contrast to spin 0 or spin 1) is still close to 1 for all large spin representations $|\vec{S}| = N/2 - d$, $d \ll N/2$ for sufficiently many sites. So while the perturbation cannot preserve them from the effect of $\hat{\mathbf{H}}_1$, we can still expect them to have an imprint in the PXP model. In this section, we will explore this and the effects these multiple su(2) representations have on the dynamics.

As discussed in Chapter 2, the Néel state can be obtained as the projection of the eigenstates of the spin-1 $\mathbf{S}^z$ operator with total spin $|\vec{S}| = N/2$ and magnetisation $m_z = -N/2$. As such, it has overlap with states with $|\vec{S}| = N/2$ and $m_x = -N/2$

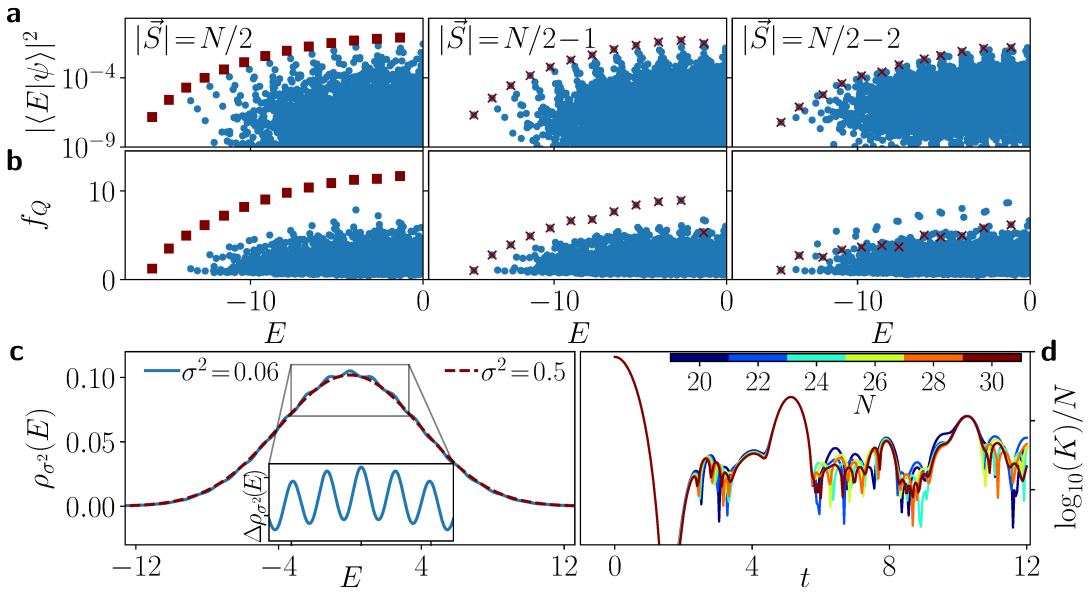

Figure 3.6: Signatures of multiple su(2) representations in the PXP model. **a** Overlap between eigenstates of the global spin-1 S^z operator with $m_z = -|\vec{S}|$ and the PXP eigenstates. Each panel corresponds to a different momentum sector. The red squares indicate the primary QMBS eigenstates with high overlap on the Néel state. **b** QFI density of PXP eigenstates. The red crosses in **a** and **b** highlight the same eigenstates, which are the ones with the highest overlap in **a**. **c** Oscillations in the smoothened density of states for $N = 26$ sites, with the inset showing the difference between different sDOS (see text). **d** Spectral form factor for various system sizes.

to $N/2$. So in order to probe if there are eigenstates of the PXP model which are approximately projection of states with $|\vec{S}| = N/2 - d$ and $m_x = -N/2 + d$ to $N/2 - d$, we can probe overlap with a projected eigenstate of $\mathbf{S}^z$ with $|\vec{S}| = -m_z = N/2 - d$, which will fulfil the role of the Néel state for these representations. Anomalously high overlap with this state would then indicate the presence of additional su(2) structures in the PXP model. Let us denote the projected state with $|\vec{S}| = -m_z = N/2 - d$ by $|s_z = N/2 - d\rangle$. The $d = 1$ state is the superposition of all single-spin flips with momentum k,

$$|s_z{=}N/2{-}1\rangle_k \propto \sum_{j=1}^{N/2} e^{ikj}\sigma^-_{2j-1}|\mathbb{Z}_2\rangle. \tag{3.22}$$

The anomalous overlap of these states with some eigenstates was already noted in [80], but the connection with multiple su(2) representations was not established. For any $k \neq 0$ we obtain a state with similar properties that is the lowest weight state of its own approximate su(2) representation. Initial states with $d \geq 2$ have more complicated forms due to the non-trivial effect of the projection to the constrained Hilbert space. On Fig. 3.6**a**, we show the overlap of the states $|s_z = N/2{-}d\rangle_k$ with the eigenstates of the

PXP model with $d = 0$ to 2. In order to make sure that the middle and right panels have no overlap with the usual scarred eigenstates, all three panels are for different momenta sectors. As such, this clearly indicates the presence of other anomalous eigenstates in the model. We note that on this figure, for $d = 0$ and $d = 1$ there are $N/2 - d$ visible towers of states implying a total of $N+1-2d$ in the full spectrum. This is the expected number for total spin $N/2 - d$. However, this is not the case for $d = 2$. We attribute this to the relatively strong mixing between the representations as d increases. This mixing is also the reason why we see towers of states instead of a clean top band. It explains why, even for $d = 0$, we generally see additional structure below the top band of states.

Fig. 3.6**b** shows f_Q using staggered magnetisation for the PXP eigenstates with the same momentum as the projected state. We generally see a higher f_Q for state displaying high-overlap with our projected states. However, in the rightmost panel the states with maximal QFI density are not those with maximal overlap on $|s_z{=}N/2{-}2\rangle_k$. Further inspection reveal that these eigenstates instead display large overlap on the state $|s_z{=}N/2{-}1\rangle_k$, which is the highest total spin present in that momentum sector. This illustrates well that the su(2) representations get progressively worse as the total spin decreases. For f_Q this effect is further amplified as this quantity scales with total spin even for an exact algebra.

This deterioration with $|\vec{S}|$ makes it unclear if these multiple su(2) representations leave imprints on the system beyond quenches from specific states. To show that the bulk spectral properties of the PXP model are indeed affected, we consider a smoothened density of states (sDOS) and spectral form factor (SFF) [19]. The sDOS is defined as

$$\rho_{\sigma^2}(E) = (1/\mathcal{D}) \sum_n \exp\Big(-(E - E_n)^2/2\sigma^2\Big)/\sqrt{2\pi\sigma^2}, \tag{3.23}$$

where E_n are eigenenergies, $\mathcal{D}$ is the reduced Hilbert space dimension, and σ sets the smoothing interval. Fig. 3.6**c** shows that the sDOS has tiny oscillations in the middle of the spectrum. These oscillations can be made more prominent by subtracting the sDOS at low and high variances, $\Delta\rho = \rho_{\sigma^2=0.06} - \rho_{\sigma^2=0.5}$, plotted in the inset. The energy difference between the peaks in sDOS roughly coincides with the oscillation period in the SFF, defined as

$$K(t) = \sum_{n,m} e^{-i(E_n - E_m)t}, \tag{3.24}$$

and plotted in Fig. 3.6**d** for a range of system sizes. Although the SFF, in general, is not a self-averaging quantity, the peaks appear converged in system size, and thus they are expected to persist in the thermodynamic limit.

These other su(2) representations can also be stabilised by the PXPZ perturbation in Eq. (2.33) with the same strength $\lambda = 0.051$. This is reflected in the presence of clearer peaks in the sDOS and by more prominent oscillations in the SFF. More importantly, it can lead to fidelity close to 1 for initial states $|s_z = N/2{-}d\rangle_k$ linked to $k, d \neq 0$. In Fig. 3.7, we show the fidelity at the first QMBS revival for $d = 0$ and $d = 1$ for various system sizes. For the Néel state ($d = 0$), the fidelity is always close to

1 but decreases slowly as N gets larger due to the Hilbert space size increasing. This is the usual behaviour in systems with non-exact QMBSs. However for $d = 1$, where the initial state is given in Eq. (3.22) with $k = -4\pi/N$, the revivals actually get *better* with an increase in system size, at least in the range of N probed. Based on the data, it is likely that for larger system sizes the case $d = 1$ will have very close fidelity and period to the $d = 0$ case. We can understand this behaviour by remembering that in the dimerised model the perturbation stabilises neighbouring spin-1 pairs forming spin-2 quintuplets. In the case with maximal total spin ($d = 0$), all pairs form such quintuplet regardless of system size. While this is not the case for $d = 1$, the total deviation from quintuplets is constant while the number of pairs increases with system size. As a consequence, each pair gets closer and closer to a quintuplet as system size increases. This explains the increase in fidelity that we observe.

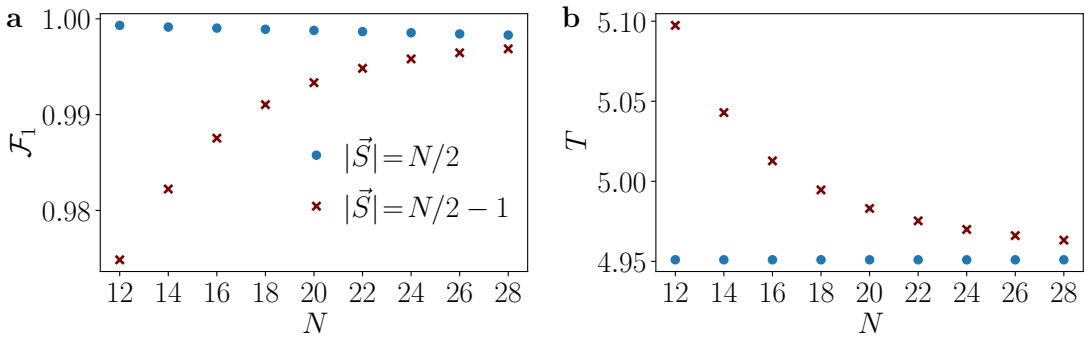

Figure 3.7: **a** Fidelity and **b** period of revivals for two eigenstates of S^z projected into the PXP Hilbert space and evolved with PXP and the PXPZ perturbation. For $|\vec{S}| = N/2 - 1$ the revivals get better as system size is increased, and should theoretically match up with those of $|\vec{S}| = N/2$ in the thermodynamic limit.

3.4 Superdiffusive energy transport in the PXP model

While the SFF and DOS are fine probes of special features in the spectrum, they are not directly accessible in experiment. We now turn towards observables to show that the multiple su(2) representations also impact their behaviour. In particular, we focus on correlation functions of the type $\langle \hat{O}(t=0)\hat{Q}(t)\rangle = \mathrm{Tr}\left[\hat{O}(t=0)\hat{Q}(t)\right]$. The absence of any explicit density matrix $\hat{\rho}$ means that $\hat{\rho} \propto \mathbf{1}$, and so the trace corresponds to the expectation value at infinite temperature. The prime candidates for demonstrating non-thermal behaviour are the ones of the approximate su(2) algebra in Eq. 2.44. Indeed, in the parent Hamiltonian the operators $\hat{\mathbf{S}}^x$, $\hat{\mathbf{S}}^y$ and $\hat{\mathbf{S}}^z$ obey the usual su(2) commutation relations. If sufficiently many su(2) representations survive in the PXP model, we expect the projection of these operators to at least approximately obey the same commutation relations as well. In that case, we should see

$$\langle \hat{S}^y(t)\hat{S}^y(0)\rangle \approx \langle \hat{S}^z(t)\hat{S}^z(0)\rangle \approx \cos(\omega t), \tag{3.25}$$

provided that the operators are normalised such that $\langle \hat{O}(0)\hat{O}(0)\rangle = 1$ As the operator $\left(\hat{\mathbf{S}}^y\right)^2 + \left(\hat{\mathbf{S}}^z\right)^2 = \vec{\mathbf{S}}^2 - \left(\hat{\mathbf{S}}^x\right)^2$ commutes with $\hat{\mathbf{S}}^x$, one can also probe if the operator $\hat{S}^2_{y,z} = \left(\hat{S}^y\right)^2 + \left(\hat{S}^z\right)^2$ gives rise to $\langle \hat{S}^2_{y,z}(t)\hat{S}^2_{y,z}(0)\rangle \approx 1$ as expected for a constant of motion. Fig. 3.8 shows that all these relations are sufficiently well obeyed at short times in a finite system with 20 sites.

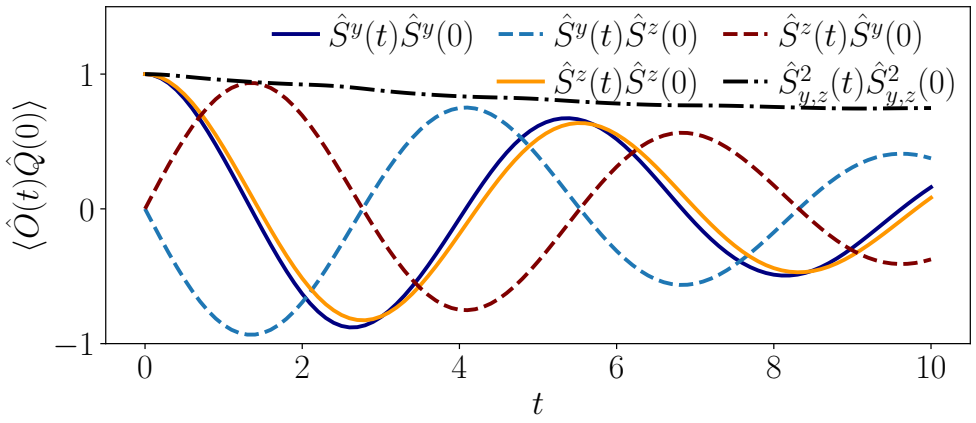

Figure 3.8: Time evolution of the various global spin operators projected to the constrained space. In particular, $\langle \hat{S}^2_{y,z}(t)\hat{S}^2_{y,z}(0)\rangle$ remains close to 1, indicating an approximate conservation law. All operators are normalised to satisfy $\langle \hat{O}(0)\hat{O}(0)\rangle = 1$.

We now turn towards quantum transport as a probe that is agnostic to the exact form of the approximate algebra. Importantly, transport is also a universal behaviour, with generic chaotic models typically exhibiting diffusive transport of conserved quantities such as spin [169–175], charge [169, 172] or energy [170, 172, 176–178]. On the other hand, disorder can give rise to slower than diffusive (subdiffusive) dynamics or even localisation [27, 171, 179–183].

For the PXP model, as only energy is conserved we study its transport using the energy-energy correlation function. Intuitively, this setup tracks the spreading of a small energy "hump" created at the central site of the chain, atop of the infinite temperature density matrix. We probe energy transport via the connected energy correlation function

$$\langle \hat{h}_0(0)\hat{h}_\ell(t)\rangle_c \;=\; \langle \hat{h}_0(0)\hat{h}_\ell(t)\rangle - \langle \hat{h}_0(0)\rangle\langle h_\ell(t)\rangle, \tag{3.26}$$

where $\hat{h}_\ell(0) = \hat{P}_{\ell-1}\hat{\sigma}^x_\ell\hat{P}_{\ell+1}$ is the energy density operator at site ℓ, and $h_\ell(t) = e^{i\hat{H}_{\rm PXP}t}h_\ell(0)e^{-i\hat{H}_{\rm PXP}t}$. As before, we set $\mu = 0$ and restrict our study to the reduced Hilbert space containing no neighbouring excitations. This is a crucial difference with respect to the earlier studies of particle transport in constrained models, e.g., in Refs. [184, 185]. In particular, in Ref. [184] a magnetisation-conserving variant of the PXP model was studied *without* restricting to a single sector of the Hilbert space. Due

to the large number of disconnected sectors and frozen local configurations, this model displayed localisation, with the initial energy hump never spreading homogeneously into the whole system. More generally, Refs. [184, 185] have found that kinetic constrains lead to subdiffusive transport.

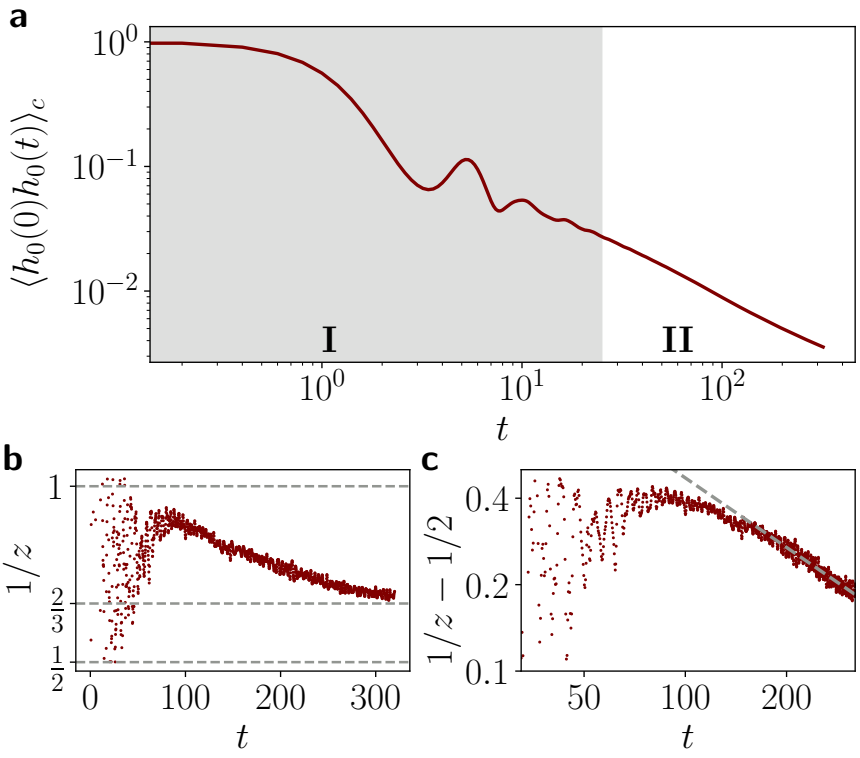

Figure 3.9: **a** The connected energy autocorrelation function in the PXP model has a short-time oscillatory regime (I) followed by power-law decay (II). **b** The inverse instantaneous dynamical exponent extracted from the correlation function approaches the ballistic value of one at $t \sim 100$, followed by slow decay at later times that appears to saturate to a superdiffusive value $1/z \approx 2/3$. **c** Double-logarithmic plot of the data in **b** shows that power-law convergence to diffusion $1/z = 1/2$ is also consistent with the data. Dashed line corresponds to $\propto t^{-0.8}$ dependence. The data is for a chain with $N = 1024$ sites and bond dimension of $d_{\mathrm{Max}} = 512$.

Accessing energy transport in the thermodynamic limit requires the evaluation of the connected correlation function (3.26) in large systems at late times. To access the required system sizes and times, we use a state-of-the-art massively parallel implementation of the TEBD algorithm [61, 186] based on the ITensor library [187], performed with our collaborators at IST Austria in Ref. [2]. This allows us to simulate operator dynamics in the PXP model up to times exceeding $t \gtrsim 300$, requiring $N = 1024$ lattice sites to avoid the operator-spread reaching the boundary of the system.

Fig. 3.9**a** highlights two distinct regimes in the decay of the connected energy autocorrelation function for the PXP model. At short times, marked by the shaded area,

we observe oscillatory behaviour. This is due to due to the multiple su(2) representations discussed above and the period of the oscillations matches with the ones in the SFF and the energy spacing in the DOS. As expected, at long times the oscillations disappear and the correlation function settles to a power-law like decay. This decay is conveniently probed via the instantaneous dynamical exponent

$$z^{-1}(t) = -\frac{\mathrm{d}\ln\langle\hat{h}_0(0)\hat{h}_0(t)\rangle_c}{\mathrm{d}\ln t}, \tag{3.27}$$

that gives the running exponent of the power-law decay. For diffusion we expect $1/z = 1/2$, while any larger value implies superdiffusive behaviour. Fig. 3.9**b** shows that $1/z$ first approaches the ballistic value of 1 before relaxing slowly to a smaller value. Despite the decrease of $1/z$, its value remains superdiffusive ($1/z > 1/2$) even at extremely long times $t \approx 300$, at which the correlation function has spread approximately 300 sites from the centre.

This superdiffusive behaviour is very surprising. Indeed, in contrast to (sub)diffusion, faster-than-diffusive transport typically rests on the existence of special structures. In one dimension, integrable models [26] can support ballistic transport since their macroscopic number of conserved quantities may prevent currents from decaying. Furthermore, intermediate behaviour between diffusion and ballistic transport can arise in integrable models with certain symmetries, where superdiffusive Kardar-Parisi-Zhang (KPZ) dynamics has been observed [173, 175, 188–198] with an exponent of $1/z = 2/3$. Importantly, all examples of faster-than-diffusive dynamics in short range models rely on integrability. The same, naturally, does not hold for long-range models where superdiffusion has also been observed and explained by classical arguments using Lévy flights [199, 200].

As the PXP model is neither integrable nor long-range, the appearance of superdiffusion with an exponent close to the KPZ one is unexpected. Nevertheless, plotting the data for $1/z$ on a log-log scale in Fig. 3.9**c**, one cannot rule out power-law relaxation of z to diffusion at times that are inaccessible to our numerics. We note that even if diffusion is recovered at long-times, the fact that such timescales are observed is anomalous in itself.

3.4.1 Stability of superdiffusion to perturbations

Possible origins of this superdiffusion could be the proximity of the PXP model to an integrable Hamiltonian (as discussed in Chapter 2) and the presence of multiple su(2) representations. In order to test this, we can use the PXPZ perturbation that can enhance both depending on the strength. To further probe the relevance of multiple su(2) representations, we deform the model with the local PXPZ perturbation,as defined in Eq. (2.33). We chose it over Eq. (2.34) to avoid introducing any long-range coupling and for its much simpler implementation with TEBD. Previously, it was shown that $\lambda \approx 0.05$ stabilises the highest-spin su(2) representation [67]. Our results indicate that they also lead to stronger signs of multiple su(2) representations in the sDOS and SFF. It was also seen that $\lambda \approx 0.024$ leads to level statistics close to integrability [70].

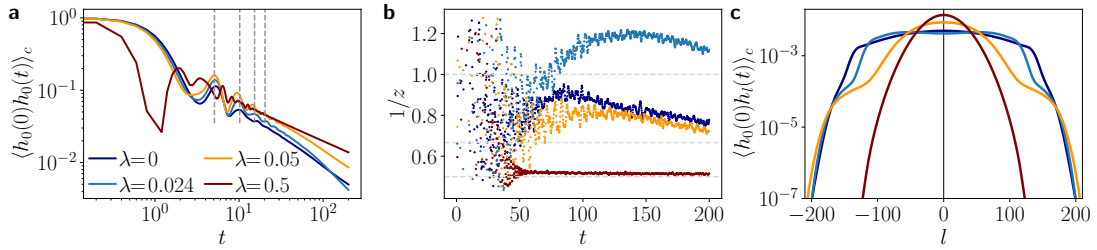

Figure 3.10: **a** Connected energy auto-correlation function for several strengths λ of the PXPZ deformation. Early time oscillations approximately peak at times $t \in \{5.1, 10.2, 15.3, 20.4\}$ (dashed lines) for the su(2)-enhancing perturbation $\lambda = 0.05$. **b** Long time decay is fastest for $\lambda = 0.024$, as manifested by the inverse dynamical exponent approaching the value of one from above. In contrast, large $\lambda = 0.5$ results in a rapid onset of diffusive dynamics. **c** Spatial dependence of the connected energy correlation function at $t = 200$ in the PXP model with the PXPZ deformation. In the vicinity of $\lambda \approx 0.026$, the profile becomes visibly flat. The data is for $N = 768$ and bond dimensions $d_{\text{Max}} = 384$ [panels **a**, **b**] and $d_{\text{Max}} = 256$ in **c**.

Fig. 3.10**a** illustrates its effect on the energy autocorrelation function and the dynamical exponent. We observe that the deformation strength $\lambda = 0.05$ gives the strongest enhancement of oscillations in the early time regime, further confirming that oscillations are caused by multiple su(2) representations. However, the long-time value of $1/z$ for $\lambda = 0$ and 0.05 behave nearly identically. In contrast, the value $\lambda = 0.024$ only weakly enhances the oscillations but yields a much faster decay of the correlation function at late times. The extracted $1/z$ exponent in Fig. 3.10**b** overshoots the ballistic value $z = 1$ and converges to it from above, consistent with a proximate integrable point. Finally, a large deformation $\lambda = 0.5$ leads to fast saturation of $1/z \approx 0.5$ corresponding to conventional diffusion.

In the vicinity of an integrable point, superdiffusion can appear as a crossover between nearly-ballistic behaviour at short times and diffusion at late times [172, 201, 202] (see also the review [203]). The intuition is that transport should at first behave as in a corresponding integrable model until the system starts to feel the effect of the integrability-breaking perturbation, which leads to slow quasiparticle decay processes. To corroborate this picture of ballistic transport followed by slow decay, we computed the spatial profiles of the correlation function in the PXP model with the PXPZ deformation in Fig. 3.10**c**. As seen in this figure, the profile exhibits a nearly flat dependence on position. This is similar to what is seen in the same model at the integrable hard-square point [2].

The proximity of an integrable point naturally explains the observed long timescales in the dynamics of the PXP model. In order to avoid slow convergence towards the thermodynamic limit, we must consider stronger deformations of the model. While a large PXPZ deformation restores diffusion in Fig. 3.10, such a perturbation is not readily available in experiments. Instead, we focus on the detuning/chemical potential μ introduced in Eq. (2.20) in Chapter 2. As a reminder, this term counts the number of Rydberg excitations in the constrained Hilbert space. We note this term cannot be

expressed using the generators of the approximate su(2) structure in Eq. 2.44. As such, it destroys the peaks in the sDOS already for small values of μ and it has been shown to make the dynamics from the $|\mathbb{Z}_2\rangle$ state ergodic [204].

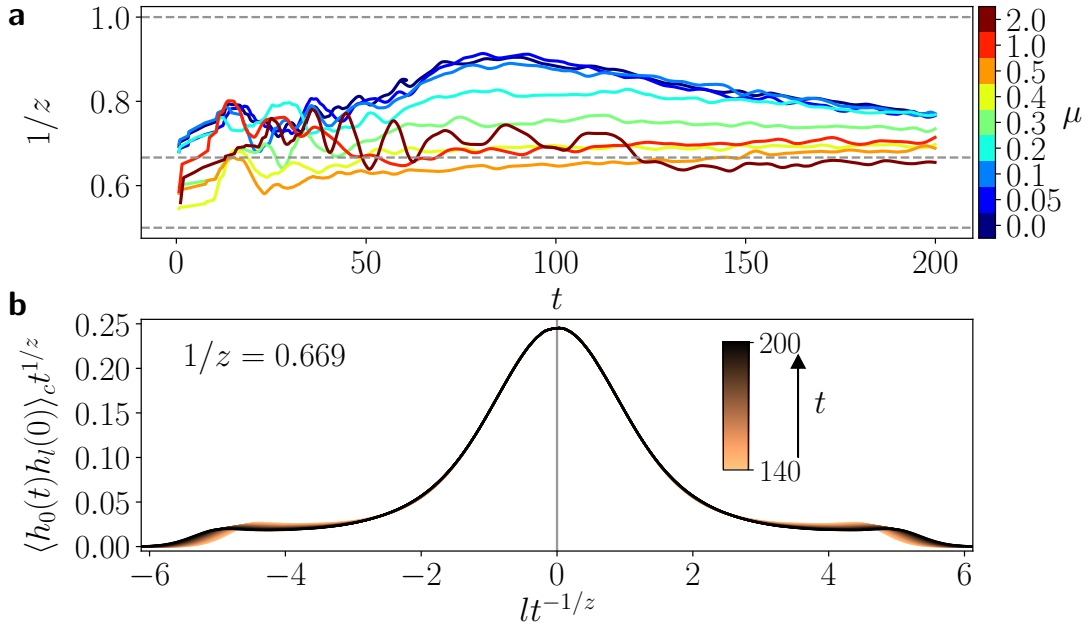

Figure 3.11: Stable superdiffusive energy transport for a large detuning in the PXP model. **a** Sufficiently large deformations $\mu \geq 0.4$ lead to a clear superdiffusive exponent $z \approx 1.5$. **b** Single-parameter scaling of the spatial profiles of the connected correlation function for $\mu = 0.5$ shows a collapse for $1/z \approx 0.669$ (average value of $1/z$ in the interval $t \in [100, 200]$). The ballistically propagating peaks at large $|x|$ are expected to disappear as $t \to \infty$. The data is for $N = 1024$ sites with bond dimensions $d_{\text{Max}} = 384$ for $\mu = 2$ and $d_{\text{Max}} = 256$ for $\mu \leq 1$. For clarity purposes, data in panel **a** has been smoothed using a Gaussian filter.

Fig. 3.11**a** shows the instantaneous dynamical exponent for a range of deformation parameters $\mu \in [0, 2]$. For weak deformations $\mu \leq 0.2$, the exponent varies slowly, similar to the PXP model in Fig. 3.9**b**. However, the effect of a nearby integrable point diminishes once the deformation is sufficiently strong. Surprisingly, for large deformations $\mu \geq 0.4$, we observe clear superdiffusive transport with a well-converged dynamical exponent $z \approx 1.5$. The robust superdiffusion, observed over a broad range of μ, suggests that even the PXP model itself may have $z \approx 1.5$, although much longer times may be needed to observe the convergence of the exponent to this value. We note that other perturbations lead to superdiffusion for small strengths λ, but for $\lambda > 1.5$ diffusion is generally recovered. We do not show these results here, but they can be found in Ref. [2].

The transport exponent $z = 3/2$ is one of the hallmarks of the KPZ universality class, which has recently been observed in integrable quantum systems with certain symmetries [175, 188, 189, 191, 193]. To further test if H_{PXP} with $\mu \neq 0$ belongs to

the same universality class, we analyse the spatial profile of the correlation function in Fig. 3.11**b**. The profiles of correlation function at different times show a clear collapse with a single scaling parameter that matches the average value of $1/z$ in the interval $t \in [100, 200]$. However, the presence of ballistic peaks visible at the edges of numerically computed profiles in Fig. 3.11**b** prohibits us from reliably discriminating between the theoretically expected KPZ or Gaussian scaling functions.

Finally, we note that this anomalous transport is not a generic consequence of projecting a free paramagnet onto a reduced Hilbert space. If instead the range-2 Rydberg blockade is used – the constraint now excludes both nearest-neighbour as well as next-nearest-neighbour up spins – diffusion is quickly recovered, as we discuss in Ref. [2].

3.4.2 Origin of superdiffusion

Overall, our observations challenge the current understanding of chaotic quantum models, which are expected to exhibit diffusive (or slower) transport dynamics. In particular, our findings suggests that certain classes of constrained models, when studied in the reduced Hilbert space, may provide stable examples of superdiffusive transport. At present, the explanation for the robust superdiffusive transport observed here is missing, highlighting the need for the development of a theoretical description of transport in systems with constraints. Indeed, while proximity to integrability seemed like the obvious candidate, strong deformations with the chemical potential were shown to move the PXP model away from an integrable point but still gave rise to a broad regime of superdiffusive energy transport. The observed transport exponent, $z \approx 3/2$, is tantalisingly close to the value corresponding to KPZ universality class. Nevertheless, it remains unclear why the PXP model would belong to this class, given the existing examples of KPZ dynamics in integrable spin chains with SU(2) or higher symmetry. Furthermore, it is known that higher order corrections can lead to a transient KPZ-like exponent [176]. However, with perturbations such as detuning, the observed superdiffusion remains stable up to long times of ~ 200 in natural units $1/\Omega$, casting doubt on the relevance of higher-order corrections. Moreover, it is not clear why the chemical potential would particularly enhance such corrections.

One potential explanation for superdiffusion in chaotic models could stem from nonlinear fluctuating hydrodynamics [205], provided additional conserved charges exist within the reduced Hilbert space. Indeed, KPZ transport has been shown to arise in a broad class of low-dimensional classical models with particle, momentum and energy conservation [206]. Our brute-force numerical search did not yield a clear signature of additional conservation laws in the PXP model, hence it remains unclear whether its transport fits the framework of Refs. [205, 206]. Another potential explanation for the unusual transport could be related to the semiclassical aspects of the PXP dynamics when the latter is projected onto the variational manifold of matrix product states [59]. The study of quantum dynamics with translationally-invariant initial conditions in Ref. [64] revealed the existence of large Kolmogorov-Arnold-Moser (KAM) tori in the classical phase space resulting from the variational projection. Provided

these tori survive in the absence of translation invariance, they may play a role in energy transport. Finally, the current capabilities of Rydberg quantum simulators [207] may allow to probe our predictions experimentally and to gain further insights into the energy transport, in particular in higher dimensions.

The link between scarring and superdiffusion also remains to be understood. On the one hand, as we explained above, the chemical potential μ destroys the su(2) structure responsible for scarring from the $|\mathbb{Z}_2\rangle$ state, while at the same time this does not appear to affect the late-time dynamical exponent, suggesting the two phenomena to be unrelated.

3.5 Summary

We have shown that QMBS eigenstates stemming from su(2) RSGA have QFI scaling quadratically with system size. This means that these states have extensive multipartite entanglement and so they constitute a valuable resource for quantum metrology. A recent work expands on these results to propose an actual implementation protocol [208]. Using the PXP model as an example, we have demonstrated numerically that scarred eigenstates also have similar properties when the RSGA is only approximate. However, in that case, the quadratic scaling breaks down in large systems due to the hybridisation with thermal eigenstates. Nonetheless, we can still obtain states with large QFI by quenching from a simple product state that is easy to prepare in experiment. At intermediate times, the QFI of the time-evolved state displays the desired quadratic scaling.

In the same PXP model, we have demonstrated that there exists multiple approximate su(2) representations beyond the maximal total spin representation studied in the previous literature. The origin of these algebraic structures is traced back to the parent spin-1 model introduced in Ref. [68] and reviewed in Chapter 2. As their total spin decreases, the number of representations increases but their quality (i.e., how close to exact they are) gets worse. This makes it hard to quantify the impact of lower-spin representations on the observable properties of the PXP model. Nonetheless, we can see that they leave clear spectral signatures in the form of peaks in the DOS and oscillations in the SFF, even at *infinite* temperature. Beyond this, they also impact energy transport by inducing oscillations at short times.

Surprisingly, beyond these initial oscillations, the PXP model also shows superdiffusive transport when restricting to the largest connected component of its Hilbert space. The long-time behaviour is shown to be affected by a nearby integrable point, confirming that the PXPZ deformation gives rise to nearly ballistic transport, as suggested by the level statistics indicators [70]. However, while deforming the PXP model with a chemical potential removes the remnants of integrability, instead of restoring diffusion it leads to a stable superdiffusive regime with a dynamical exponent $z \approx 3/2$. The exact origin of this superdiffusive behaviour is still unknown, and further work on the topic is needed.

Chapter 4

Realising many-body scars in Bose-Hubbard quantum simulators

In the previous chapter, we have shown that, under certain conditions, QMBSs can be useful for quantum metrology. One obvious limitation to their practical usage in that context is a small number of experimental realisations [43, 78, 136, 139]. In particular, the only large-scale example of QMBSs stemming from an (approximate) RSGA is in Rydberg atoms, in the form of the PXP model and its generalisations to higher dimensions [43, 78]. Therefore, engineering QMBSs in other experimental platforms is paramount. Moreover, as the previous chapter has demonstrated, many properties of the PXP model remain poorly understood, such as its energy transport behaviour. Thus, implementing this model in new experimental setups with different measurement capabilities could shed new light on these intriguing properties.

In this chapter, we realise the PXP model on a large-scale quantum simulator made of ultracold bosonic atoms in a tilted optical lattice, designed and operated by our experimental collaborators at Universities of Hefei and Heidelberg [4]. We first explain the mapping between the models and contrast our implementation to the Rydberg atom arrays. We then benchmark our experimental setup by performing quenches from the Néel state, showing that local fidelity and entanglement entropy can be extracted using interference between identical copies of the system. One of the notable new findings of our experiment is that scarred dynamics is not limited to the Néel initial state but can also be observed in the polarised initial state in the presence of chemical potential. This result is surprising as the polarised state has previously served as a reference for ergodic dynamics in the PXP model. We derive a semi-classical description of quantum dynamics after a quench from the polarised state, and relate it to an approximate su(2) algebra. Finally, we demonstrate that periodic driving can enhance the scarring behaviour from both the polarised and Néel initial states.

4.1 The tilted Bose-Hubbard model

We begin by describing our experimental setup, before showing its effective Hamiltonian and how it maps to the PXP model. Our experiment consists of a ^{87}Rb Bose-Einstein condensate, which is compressed in the z-direction and loaded into a single layer of a pancake-shaped trap. We then perform superfluid to Mott insulator phase transition with optical lattices in the $x-y$ plane. In both x and y directions, we have a superlattice that is formed by super-imposing the "short" lattice, with $a_s = 383.5$ nm spacing, and the "long" lattice, with $a_l = 767$ nm spacing [209, 210], each can be individually controlled. We realise independent 1D Bose-Hubbard models in the y-direction by ramping up the short lattice depth in the x-direction over $40E_r$, with $E_r{=}h^2/8ma_s^2$ the short-lattice recoil energy, where h is the Planck constant and m is the ^{87}Rb atomic mass.

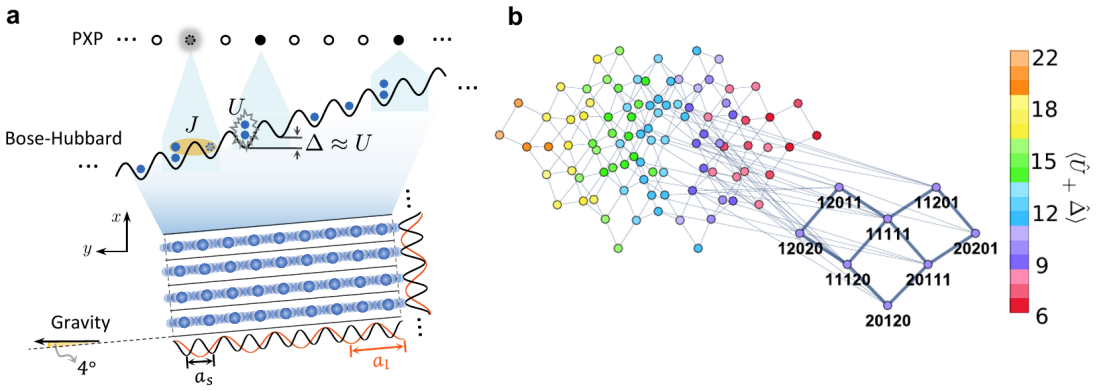

Figure 4.1: Realising the PXP model in a Bose-Hubbard quantum simulator. **a** A schematic of the optical lattice. Deep lattice potential in the x-direction forms isolated chains in the y-direction, where the linear tilting potential is applied. Spin-dependent superlattices consisting of two standing waves in each direction can be individually controlled for state preparation and measurement. At the resonance $U{\approx}\Delta{\gg}J$, the dominant hopping process is $11 \leftrightarrow 20$. The PXP excitations, $\bullet$, live on the bonds between the lattice sites. The doublon configuration 20 in the Bose-Hubbard model maps to an excitation in the PXP model, while all other configurations are mapped to an empty site, $\circ$. For example, the given state $|\ldots\circ\bullet\circ\bullet\circ\circ\circ\bullet\ldots\rangle$ maps to the Fock state $|\ldots 120201120\ldots\rangle$. **b** Emergence of the PXP subspace in the Bose-Hubbard model at the resonance $U{\approx}\Delta{\gg}J$. Dots represent Fock states of the tilted Bose-Hubbard model with 5 bosons on 5 sites (restricting to at most three bosons on any site). Lines denote the allowed hopping processes. The colour scale shows the sum of interaction and tilt energies $\langle\hat{U}+\hat{\Delta}\rangle$ for each Fock state, and this value is conserved by resonant processes. The PXP dynamical subspace and its Fock states are explicitly labelled.

The short lattice in the y-direction makes an approximate 4° angle with gravity, which results in a static linear tilt per site of $\Delta_g{=}816$ Hz, see Fig. 4.1**a**. An external magnetic field gradient Δ_B may be added to create a tunable linear tilting potential

$\Delta{=}\Delta_g{+}\Delta_\mathrm{B}$. The effective Hamiltonian describing each 1D array of the atoms is then

$$\hat{H} = -J\sum_{i=1}^{L-1}\left(\hat{b}_i^\dagger\hat{b}_{i+1} + \hat{b}_{i+1}^\dagger\hat{b}_i\right) + \hat{U} + \hat{\Delta}, \tag{4.1}$$

where J is the hopping amplitude and $\hat{b}$, $\hat{b}^\dagger$ are the standard Bose annihilation and creation operators. The interaction energy is $\hat{U} = (U/2)\sum_{i=1}^{L}\hat{n}_i\,(\hat{n}_i - 1)$ and the tilt potential is $\hat{\Delta} = \Delta\sum_{i=1}^{L}(i-1)\hat{n}_i$, with $\hat{n}_i$ the number operator $\hat{n}_i = \hat{b}_i^\dagger\hat{b}_i$. L denotes the number of sites in the chain with open boundary conditions and we restrict to the total filling equal to 1, i.e., with the same number of bosons as lattice sites.

4.1.1 Mapping the PXP model onto the tilted Bose-Hubbard model

In order to realise the PXP model in the Bose-Hubbard quantum simulator, we tune the parameters to the resonant regime $U{\approx}\Delta{\gg}J$ [211, 212], which has been studied extensively in the context of quantum Ising chains [213–215]. In that limit, the energy spectrum of the Hamiltonian in Eq. (4.1) splits into bands with essentially constant expectation value of the diagonal terms, $\langle\hat{U}{+}\hat{\Delta}\rangle \approx$ const, and the Hilbert space becomes fragmented. Performing a Schrieffer-Wolff transformation [47] at this resonance, we find that the first-order effective Hamiltonian is equal to

$$\hat{H}_\mathrm{eff} = -J\sum_{i=1}^{L-1}\left(\hat{b}_i^\dagger\hat{b}_{i+1}\delta_{\hat{n}_i,1}\delta_{\hat{n}_{i+1},1} + \hat{b}_{i+1}^\dagger\hat{b}_i\delta_{\hat{n}_i,2}\delta_{\hat{n}_{i+1},0}\right) + \hat{U} + \hat{\Delta}. \tag{4.2}$$

This operator only allows the hopping $11 \leftrightarrow 20$, as it is the only resonant process that conserves $\langle\hat{U} + \hat{\Delta}\rangle$. Indeed, moving a particle to the left decreases the energy by Δ while creating a doublon increases it by U, leading to no net energy difference when $U = \Delta$. We note that due to this limited number of resonant processes, $\hat{H}_\mathrm{eff}$ splits the Hilbert into disconnected sectors beyond the conservation of $\langle\hat{U} + \hat{\Delta}\rangle$.

We focus on the connected component of the Hilbert space containing the Mott state $|111\ldots111\rangle$. In that sector, the Hamiltonian (4.2) is equivalent to the PXP Hamiltonian [45, 46], as we show now (see also Ref. [211] for the original derivation of the mapping in the context of Ising phase transitions and a recent review [212]). As mentioned before, the only allowed dynamical process is $11 \leftrightarrow 20$. Let us now think of each bond between overlapping pairs of sites as a spin-1/2. We can then say that setting this pair to 20 is flipping the corresponding spin up, while otherwise it is down. But if one pair is 20, the neighbouring pair to the left must be 12 or 02 as it shares one site. It is thus dynamically frozen and cannot be flipped up. The same is true for the pair to the right which must be 01 or 02. It is straightforward to see that this is exactly the PXP constraint for the spin-1/2 living on the bonds. The mapping to the usual notation is simple, with 20 being equivalent to $\bullet$, while all other possible configurations (11, 12, 02 and 01) map to $\circ$. Note that as we use open boundary conditions, there is one less PXP spin that bosonic site. We identify the unit-filling state $|111\ldots11\rangle$ with the PXP polarised state, $|0\rangle$. The exact mapping to the Néel state depends on the

parity of L, as for even L it becomes $|20\ldots2020\rangle$ while for odd L it is $|20\ldots20201\rangle$. The same is true for the anti-Néel state which is respectively $|02\ldots0202\rangle$ or $|102\ldots0202\rangle$. Fig. 4.1**b** illustrates the profound change in the connectivity of the Fock space near the resonance $U{\approx}\Delta{\gg}J$, with an emergent dynamical subspace isomorphic to the PXP model in the sector containing the Mott state.

We now derive the effective Hamiltonian in the PXP formulation. To do that, we need to account for the diagonal terms $\hat{U}$ and $\hat{\Delta}$. Exactly at the $U=\Delta$ resonance, their sum is simply equal to $\Delta L(L-1)/2$ for all states in the sector. But what happens if we are not exactly at the resonance? As long as $U,\Delta \gg |U-\Delta|$, the Schrieffer-Wolff transformation still holds. Nonetheless, we now need to account for the fact that the diagonal terms are not equal for all states in the sector. Let us denote the detuning between them by U_0, such that $U=\Delta+U_0$. The polarised state (or Mott insulator state) still has energy $\Delta L(L-1)/2$, but now every process that creates a doublon by moving a boson to the left loses energy Δ and gains energy U. So each doublon leads to an increase of energy of U_0 on top of the constant energy $E_0=\Delta L(L-1)/2$. As the latter is an additive constant, we can get rid of it when restricting to the sector of interest. This allows to write the effective Hamiltonian in the sector of interest in both the bosonic and spin languages as

$$\hat{H}_{\text{eff}}{=}{-}J\sum_{i=1}^{L-1}\left(\underbrace{\hat{b}_i^\dagger\hat{b}_{i+1}\delta_{\hat{n}_i,1}\delta_{\hat{n}_{i+1},1}}_{\sqrt{2}\hat{P}_{j-1}\hat{\sigma}_j^+\hat{P}_{j+1}}+\underbrace{\hat{b}_{i+1}^\dagger\hat{b}_i\delta_{\hat{n}_i,2}\delta_{\hat{n}_{i+1},0}}_{\sqrt{2}\hat{P}_{j-1}\hat{\sigma}_j^-\hat{P}_{j+1}}\right)+\frac{U_0}{2}\sum_{i=1}^{L}\underbrace{\hat{n}_i\left(\hat{n}_i-1\right)}_{\hat{n}_j=1-\hat{P}_j}. \tag{4.3}$$

In this equation, the index i labels the bosonic sites, while j labels the bonds between sites. The Kronecker delta functions have been expressed in terms of projectors, $\hat{P}_j=|\circ_j\rangle\langle\circ_j|$, and the bosonic hopping terms correspond to the spin raising and lowering operators, $\hat{\sigma}_j^{\pm}$, on the bond j. Moving a particle to a neighbouring site on the left corresponds to creating an excitation, moving to the right to annihilating, while the delta functions act as constraints. Due to this equivalence between creating a doubly-occupied site and an excitation, the detuning term counting the former can be turned into a chemical potential term counting the latter.

Finally, the effective Hamiltonian is equivalent to the PXP Hamiltonian in Eq. (2.20) as

$$\hat{H}_{\text{PXP}}=\hat{X}_1\hat{P}_2+\hat{P}_{N-1}\hat{X}_N+\Omega\sum_{j=2}^{N-1}\hat{P}_{j-1}\hat{X}_j\hat{P}_{j+1}+\mu_0\sum_{j=1}^{N}\hat{n}_j, \tag{4.4}$$

with $\Omega=-\sqrt{2}J$, $\mu_0=U_0=U-\Delta$, and $N=L-1$. The number operator $\hat{n}_j$ is 1 if there is an excitation and 0 otherwise. As the last bosonic sites can never be doubly-occupied using the resonant process, the U_0 term acting on it has been dropped. This shows that it is straightforward to engineer the PXP chemical potential in the Bose-Hubbard model use a simple detuning between U and Δ. This will make it possible to create a time-dependent chemical potential by modulating U. It is important to note that as $\Omega=-\sqrt{2}J$, it must hold that $U_0/J=-\sqrt{2}\mu/\Omega$. While the minus sign is

not important for dynamics from the Néel or polarised state, the factor of $\sqrt{2}$ must be accounted for when converting parameters between the two models.

Using numerics we can verify the mapping between the ideal PXP dynamics and the Bose-Hubbard model. We use exact diagonalisation techniques to obtain the full energy spectrum of both the PXP and Bose-Hubbard Hamiltonian with $L \lesssim 12$, which allows us to directly access the system's eigenstate properties. Unless specified otherwise, we restrict the occupancy of any site to be at maximum 3 bosons, as our results are found to be insensitive to allowing more than 3 bosons on any site. In analogy with the PXP model, the system initialised in the state $2020\ldots201$ is expected to oscillate between this state and the state $12020\ldots20$. This is not only the case for the effective model (4.3) which is exactly equivalent to PXP, but also for the full tilted Bose-Hubbard model (4.1) at the $U = \Delta$ resonance, as can be observed in Fig. 4.2. This figure also shows the evolution of the bipartite von Neumann entanglement entropy $S_{\mathrm{vN}}(t)$. The system is initially prepared in the state $2020\ldots201$ or the completely homogeneous state $111\ldots111$. As in the PXP model, the entanglement entropy for the $2020\ldots201$ state exhibits slow and approximately linear growth in time. In contrast, the entanglement entropy for the state $111\ldots111$ rapidly saturates, implying that the system quickly thermalises.

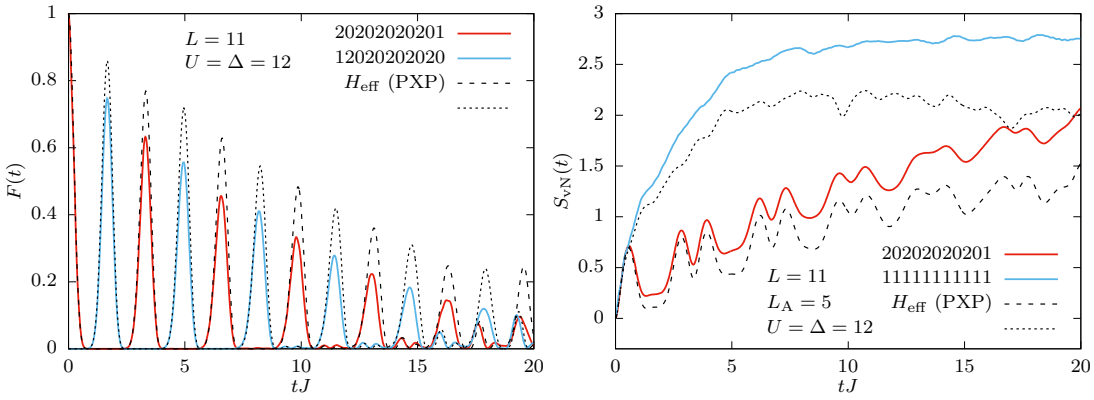

Figure 4.2: Comparison between the full Bose-Hubbard model at the resonance and the PXP model. Left: Evolution of quantum fidelity starting from the state $|\psi_0\rangle = |2020\ldots201\rangle$ (red) and the amplitude of state transfer with the state $|\psi\rangle = |12020\ldots2020\rangle$ (blue). Right: Evolution of the bipartite entanglement entropy for the initial states $|2020\ldots201\rangle$ (red) and $|111\ldots111\rangle$ (blue). The dashed and dotted black lines correspond to the effective model from Eq. (4.3). System size $L = 11$, subsystem $L_{\mathrm{A}} = 5$, filling factor $\nu = 1$.

4.1.2 Higher-order terms in the mapping

The implementation of the PXP model is only exact at $U = \Delta \to \infty$. For any finite values of these two parameters, there will be additional contributions. These correspond to the higher-order terms in the Schrieffer-Wolff transformation and can be computed in the same way. We find that the next leading terms are at order 2. To simplify the

notation we write these terms as sums of range-3 operators, where $|111\rangle\langle 120|_j$ denotes the operator changing sites $j-1$, j and $j+1$ from 120 to 111 while leaving all other sites unaffected. First, we can identify the matrix elements that take the system out of the PXP sector. This happens by an appearance of sites with 3 bosons via the operator

$$\hat{H}^{(2)}_{\text{Out}} = \frac{\sqrt{3}J^2}{U}\sum_{j=2}^{L-1}\Big(|300\rangle\langle 201|_j + |201\rangle\langle 300|_j + 2\,|300\rangle\langle 120|_j + 2\,|120\rangle\langle 300|_j\Big). \quad (4.5)$$

The off-diagonal matrix elements connecting states within the PXP sector are given by:

$$\hat{H}^{(2)}_{\text{OD}} = \frac{2J^2}{U}\sum_{j=2}^{L-1}\Big(|120\rangle\langle 201|_j + |201\rangle\langle 120|_j\Big). \quad (4.6)$$

There are also additional off-diagonal matrix elements connecting states various states outside of the PXP sector, but as they do not directly influence the dynamics out of it we do not describe them here. Finally, the diagonal operator in this sector is given by

$$\begin{aligned}\hat{H}^{(2)}_{\text{Diag}} = &\frac{J^2}{U}\sum_{j=2}^{L-1}\Big(4\,|120\rangle\langle 120|_j - |111\rangle\langle 111|_j + |020\rangle\langle 020|_j - |112\rangle\langle 112|_j\Big)\\ &+\frac{J^2}{U}\Big(|01\rangle\langle 01|_{L-1} - |11\rangle\langle 11|_1 - |12\rangle\langle 12|_1\Big),\end{aligned} \quad (4.7)$$

where the two-site operator $|11\rangle\langle 12|_j$ acts on sites j and $j+1$.

In order to see how these second-order terms change the effective model we can rewrite Eqs. (4.6)-(4.7) for the PXP model with $N = L-1$ sites. We then obtain

$$\begin{aligned}\hat{H}^{(2),\text{PXP}}_{\text{OD}} = &\frac{2J^2}{U}\sum_{j=1}^{N-2}\Big(\hat{P}_{j-1}\hat{\sigma}^+_j\hat{\sigma}^-_{j+1}\hat{P}_{j+2} + \hat{P}_{j-1}\hat{\sigma}^-_j\hat{\sigma}^+_{j+1}\hat{P}_{j+2}\Big)\\ &+\frac{2J^2}{U}\Big(\hat{\sigma}^+_1\hat{\sigma}^-_2\hat{P}_3 + \hat{\sigma}^-_1\hat{\sigma}^+_2\hat{P}_3\Big) + \frac{2J^2}{U}\Big(\hat{P}_{N-3}\hat{\sigma}^+_{N-1}\hat{\sigma}^-_N + \hat{P}_{N-2}\hat{\sigma}^-_{N-1}\hat{\sigma}^+_N\Big)\end{aligned} \quad (4.8)$$

and

$$\begin{aligned}\hat{H}^{(2),\text{PXP}}_{\text{Diag}} = &\frac{J^2}{U}\sum_{j=1}^{N-2}(4\hat{P}_{j-1}\hat{P}_j\hat{n}_{j+1}\hat{P}_{j+2} - \hat{P}_{j-1}\hat{P}_j\hat{P}_{j+1}\hat{P}_{j+2}\\ &+\hat{n}_{j-1}\hat{P}_j\hat{n}_{j+1}\hat{P}_{j+2} - \hat{P}_{j-1}\hat{P}_j\hat{P}_{j+1}\hat{n}_{j+2})\\ &+\frac{J^2}{U}(4\hat{P}_0\hat{n}_1\hat{P}_2 - \hat{P}_0\hat{P}_1\hat{P}_2 - \hat{P}_0\hat{P}_1\hat{n}_2 + 4\hat{P}_{N-2}\hat{P}_{N-1}\hat{n}_N - \hat{P}_{N-2}\hat{P}_{N-1}\hat{P}_N\\ &+\hat{n}_{N-2}\hat{P}_{N-1}\hat{n}_N) + \frac{J^2}{U}\Big(\hat{n}_{N-1}\hat{P}_N - \hat{P}_0\hat{P}_1 - \hat{P}_0\hat{n}_1\Big),\end{aligned} \quad (4.9)$$

respectively. We notice that the off-diagonal correction has the form of a constrained XY term.

Now that we have a more complete list of subleading perturbations, a few things need to be highlighted. First, all terms are local, with a maximum range of 4 sites. This means that there is no process where hopping to the left on one side of the chain is compensated by hopping to the right on the other. Thus there will not be any effective long-range process that could significantly impact the dynamics even at small strength. Second, all terms have a prefactor J^2/U. While this is expected from perturbation theory, it is important to contrast that with the Rydberg case in Eq. 2.16. In the latter, higher-order terms are also suppressed with a term proportional to Ω^2/V_1. However, there is an undesirable diagonal term at first order $\hat{n}_j\hat{n}_{j+2}$ which is equal to $V_2 = V_1/64$, and so it *increases* with V_1. Thus there is always a trade-off between this next-nearest-neighbour interaction and the Schrieffer-Wolff terms at higher orders. In other words, one cannot make the blockade more perfect without increasing longer-range correlations. This is not the case in the Bose-Hubbard model, where increasing $U = \Delta$ suppresses *all* terms which are not part of the PXP model. Thus our implementation has an advantage over the Rydberg experiment in that regard.

4.2 Observation of $\mathbb{Z}_2$ quantum many-body scars

Equipped with the mapping between Bose-Hubbard and PXP models, we are now in position to benchmark our quantum simulator against the known results for the $|\mathbb{Z}_2\rangle$ initial state. To prepare the initial state, we first employ an entropy-redistribution cooling method [209] with the superlattice in the y-direction to prepare a $\overline{n}$=2 Mott insulator in the left (odd) sites, while removing all atoms on the right (even) sites via site-dependent addressing [210]. This gives us the desired initial state $|\psi_0\rangle = |\mathbb{Z}_2\rangle = |2020\ldots\rangle$. In the region of interest, we have prepared 50 copies of the initial state $|\psi_0\rangle$ isolated by the short lattice along the x-direction. Each copy extends over 50 short lattice sites along the y-direction.

Following the state preparation, we quench the system out of equilibrium by abruptly dropping the y-lattice depth to $11.6E_r$, which corresponds to switching J from 0 to 51(1) Hz. This is done while simultaneously adjusting the lattice depth in the x and z-directions accordingly, such that the interaction strength matches the linear tilt with $U{=}\Delta{=}\Delta_g{\approx}16J$. After evolution time t, we freeze the dynamics by ramping up the y-lattice depth rapidly, and read out the atomic density on the left ($\langle\hat{n}_{\text{Left}}\rangle$) and right ($\langle\hat{n}_{\text{Right}}\rangle$) sites of the double-wells formed by the y-superlattice successively [210, 216]. This provides access to density imbalance, $\langle\hat{M}_z\rangle = (\langle\hat{n}_{\text{Left}}\rangle - \langle\hat{n}_{\text{Right}}\rangle)/(\langle\hat{n}_{\text{Left}}\rangle + \langle\hat{n}_{\text{Right}}\rangle)$, an observable corresponding to the staggered magnetisation in the PXP model, see Fig. 4.3**a**. Another observable is the density of excitations in the PXP model, which is measured by projecting out the even atomic number occupancy on each site, then reading out the average odd particle density $\langle\hat{P}_{\hat{n}\in\text{odd}}\rangle_{(1)}$ [216]. Due to highly suppressed multi-boson occupancy, we have $\langle\hat{P}_{|\bullet\rangle}\rangle = \langle\hat{n}_{\text{doublon}}\rangle_{(1)} \approx (1 - \langle\hat{P}_{\hat{n}\in\text{odd}}\rangle_{(1)})/2$.

Away from the resonance, the dynamics is ergodic and the staggered magnetisation present in the initial $|\mathbb{Z}_2\rangle$ state quickly decays with time, see Fig. 4.3**b**. In contrast, by

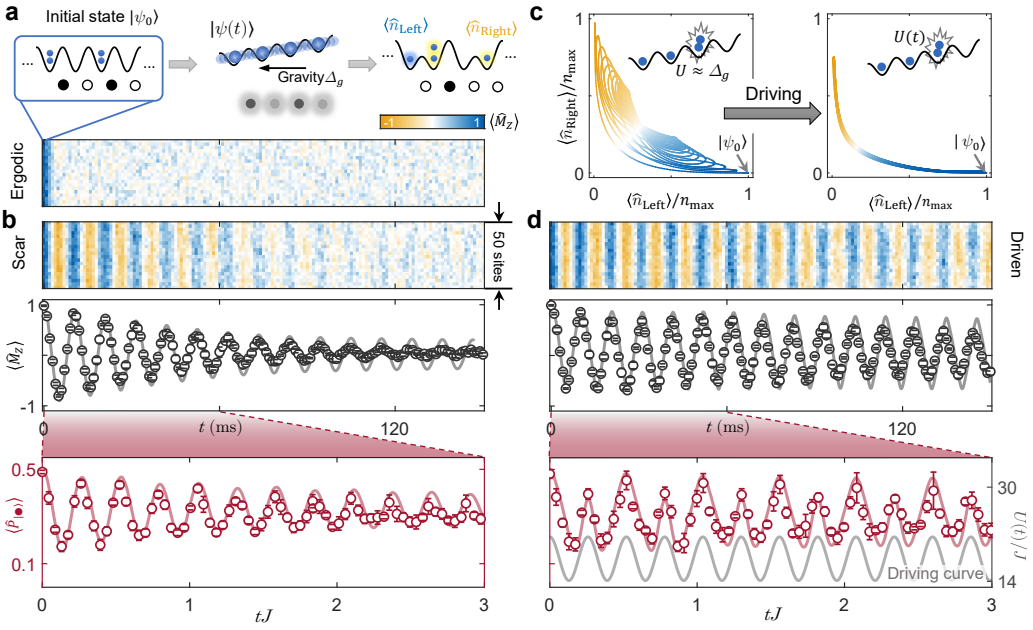

Figure 4.3: Observation of $\mathbb{Z}_2$ quantum many-body scars in a Bose-Hubbard quantum simulator. **a** Starting from the state $|\psi_0\rangle = |\ldots 2020 \ldots\rangle$ – the analogue of $|\mathbb{Z}_2\rangle$ state in the PXP model – we utilise gravity to provide linear tilt $\Delta{=}\Delta_g$. We characterise quench dynamics by measuring density imbalance and the number of doublons, corresponding to staggered magnetisation $\langle \hat{M}_z\rangle$ and density of excitations $\langle \hat{P}_{|\bullet\rangle}\rangle$ in the PXP model. In the detuned regime $\Delta - U \approx -2J$, the dynamics is ergodic and the system has no memory of the initial state at late times. **b**: Tuning to $U{\approx}\Delta$, we observe persistent oscillations in both $\langle \hat{M}_z\rangle$ and $\langle \hat{P}_{|\bullet\rangle}\rangle$. This memory of the initial state is a signature of weak ergodicity breaking due to quantum many-body scars. **c**, **d**: Periodic modulation of the interaction $U(t) = \Delta + U_0 + U_m \cos(\omega t)$ with $U_0{=}1.85J$, $U_m{=}3.71J$, $\omega{=}3.85J \times 2\pi$ leads to an enhancement of scarring. Panel **c** shows the numerically computed trajectory in the sublattice occupation plane for the PXP model with $N = 24$ sites, with and without driving. The sublattice occupancies $\langle \hat{n}_{\rm Left}\rangle$, $\langle \hat{n}_{\rm Right}\rangle$ are normalised to interval the [0,1]. The driving is seen to strongly suppress the spreading of the trajectory. **d**: Experimental measurements on the driven Bose-Hubbard model show robust scarred oscillations at all accessible times. In both the static and driven case, experimental data for $\langle \hat{M}_z\rangle$ and $\langle \hat{P}_{|\bullet\rangle}\rangle$ are in excellent agreement with TEBD numerical simulations shown by gray and red solid lines. Gray line in the lowest panel shows the modulation $U(t)$.

tuning to the vicinity of the resonance, $\Delta{=}U$, we observe distinct signatures of scarring: the system approximately undergoes persistent oscillations between the Néel and anti-Néel states, as can be seen in the staggered magnetisation profile and the density of excitations in Fig. 4.3**b**. The density of excitations does not distinguish between the Néel and anti-Néel states, hence there is a trivial factor of 2 difference between the oscillation frequencies of $\langle \hat{P}_{|\bullet\rangle}\rangle$ and $\langle \hat{M}_z\rangle$.

The scarred oscillations in Fig. 4.3**b** are visibly damped with a decay time $\tau = 49.6{\pm}0.8$ ms. Nevertheless, as shown in Ref. [78], by periodically driving the system it is possible to 'refocus' the spreading of the many-body wave-function in the Hilbert space

and thereby enhance the scarring effect, as we demonstrate numerically in Fig. 4.3**c** and experimentally in Fig. 4.3**d**. Our driving protocol is based on modulating the laser intensity of the z-lattice, which translates into periodic modulation of the interaction energy, $U(t) = \Delta + U_0 + U_m \cos(\omega t)$, while Δ is kept fixed. This results in a modulation of the detuning in the chain, acting as the analogue of the chemical potential in the PXP model.

Numerical simulations of the PXP model with the driven chemical potential, using the TEBD method [186] as implemented in TenPy package [217], are shown in Fig. 4.3**c**. These results demonstrate the dynamical stabilisation of the Hilbert space trajectory. We visualise the trajectory by plotting the average sublattice occupations, $\langle \hat{n}_{\text{Left}} \rangle$ and $\langle \hat{n}_{\text{Right}} \rangle$, normalised to the interval [0,1]. The $|\mathbb{Z}_2\rangle$ and $|\mathbb{Z}_2'\rangle$ states are located at the coordinates (1,0) and (0,1), which are the lower right and upper left corners of this diagram, respectively. The polarised state $|0\rangle$ is at the origin (0,0). In the undriven case [left panel of Fig. 4.3**c**], the trajectory at first oscillates between $|\mathbb{Z}_2\rangle$ and $|\mathbb{Z}_2'\rangle$ states, while passing through a region with a lower number of excitations. However, as the time passes, the trajectory drifts, exploring progressively larger parts of the Hilbert space. By contrast, when the driving is turned on [right panel of Fig. 4.3**c**], the trajectory approximately repeats the first revival period of the undriven case, even at late times. Thus, the driving stabilised the scarred revivals without significantly altering their period.

Experimental measurements on the driven Bose-Hubbard model in Fig. 4.3**d** find a strong enhancement of the amplitude of the oscillations in staggered magnetisation with the decay time τ increasing to 208 ± 10 ms, while the period remains nearly the same as in the static case. Optimal driving parameters were determined numerically using a combination of simulated annealing and brute force search.

We note that the experimental measurement of $\langle \hat{M}_z \rangle$ damps slightly faster than the theoretical prediction, shown by a line in Fig. 4.3**b**, at late times (t>60 ms). We attribute this to an inherent residual inhomogeneity across the lattice, which results in dephasing between different parts of the system, as well as possible decoherence induced by scattering of the lattice lasers. To avoid the effect of these undesired dephasing or decoherence effects, in the following we limit our investigation up to 60 ms.

4.3 Unravelling the details of scarred dynamics via quantum interference

Now that we have benchmarked our platform by reproducing observable dynamics after a quench from the Néel state, we can move on to measuring more challenging but informative quantities. Fidelity and entanglement entropy are key for characterising scarring behaviour. They provide a window to the evolution of the system's wavefunction and the spreading of quantum correlations. For a system trapped in a scarred subspace, thermalisation is inhibited and the system exhibits suppressed entropy growth and periodic fidelity revivals.

Measuring fidelity and entanglement entropy usually requires brute-force state tomo-

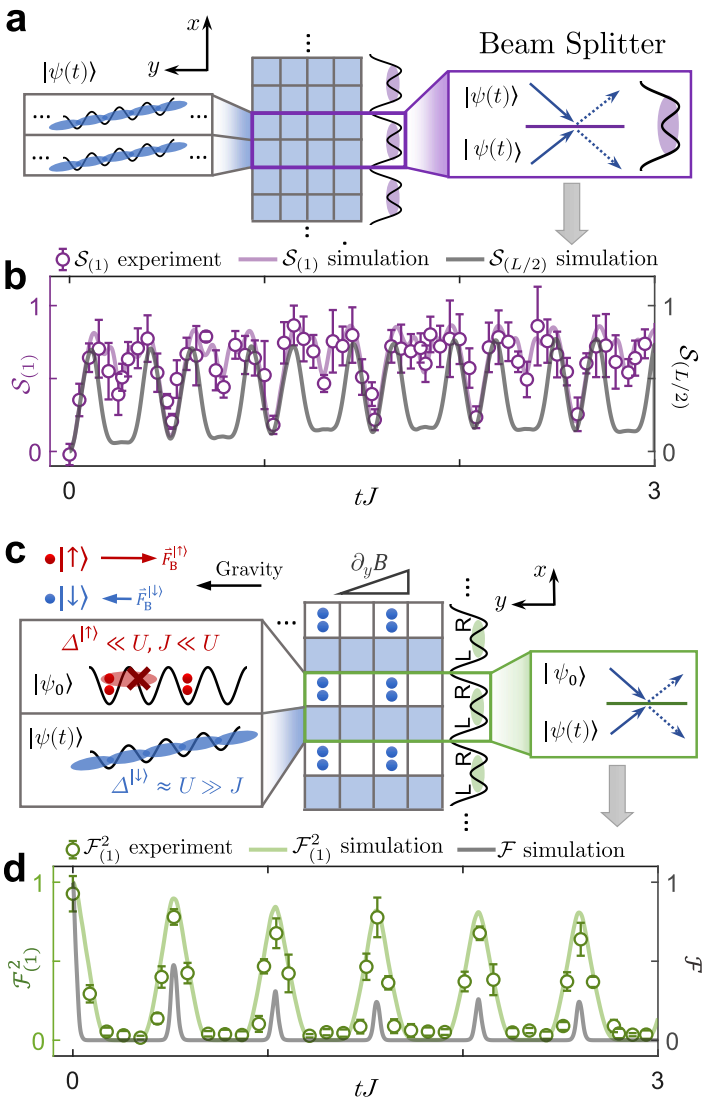

Figure 4.4: Probing many-body scarred dynamics via quantum interference. **a** After evolution time t, we freeze the dynamics in the y-direction, then by interfering two identical copies in the double wells along the x-direction, we obtain the second order Rényi entropy. **b** The entropy for a single site, $S_{(1)}$, shows robust oscillations with the same frequency as in Fig. 4.3**b**, indicating a lack of thermalisation. The single-site entropy is a good approximation to the half-chain entropy, $S_{(L/2)}$, evaluated numerically using TEBD (grey line). **c** In the x-superlattice, we flip all atoms on right sites to the state $|\uparrow\rangle$ (red), while keeping atoms on left sites $|\downarrow\rangle$ (blue). Then we apply a magnetic field gradient in the y-direction, creating state-dependent linear tilting with $\Delta_{\mathrm{B}}^{|\uparrow\rangle} = -2\Delta_{\mathrm{B}}^{|\downarrow\rangle}$. The magnetic force almost cancels out gravitational force for $|\uparrow\rangle$ atoms, thus breaking the resonance condition. Fine tuning of the interaction strength makes $|\downarrow\rangle$ atoms undergo scarred dynamics to $|\psi(t)\rangle$, while keeping $|\uparrow\rangle$ frozen in the initial state $|\psi_0\rangle$. Finally, we flip $|\uparrow\rangle$ atoms back to $|\downarrow\rangle$ and interfere many-body states $|\psi_0\rangle$ and $|\psi(t)\rangle$ in the x-superlattice to read out the average fidelity. **d** The square fidelity of single-site subsystems $\mathcal{F}^2_{(1)}$ displays pronounced revivals, indicating periodic returns close to the initial state. The global fidelity $\mathcal{F}$, obtained numerically using TEBD, is shown by the grey line.

graphy, but for our 50-site Bose-Hubbard system with a Hilbert space dimension exceeding 10^{28}, this approach is generally impossible. However, the superlattice in the x-direction allows us to probe these observables by interfering identical copies in the double wells, analogous to the 50 : 50 beam splitter (BS) interference employed in photonics experiments [218]; see Fig. 4.4**a**. This is done by freezing the dynamics along the chains in the y-direction after evolution time t, then we interfere copies of $|\psi(t)\rangle$ in the double wells formed by the x-superlattice. After the interference, a parity projection helps read out the average odd particle density $\langle \hat{P}^{\mathrm{BS}}_{\hat{n}\in\mathrm{odd}}\rangle_{(1)}$, which gives us access to the second-order Rényi entropy [219]. We measure the entropy of single-site subsystems $S_{(1)} = -\ln(\mathrm{Tr}_{(1)}\,[\hat{\rho}(t)^2]) = -\ln(1-2\langle \hat{P}^{\mathrm{BS}}_{\hat{n}\in\mathrm{odd}}\rangle_{(1)})$, where $\hat{\rho}(t) = |\psi(t)\rangle\langle\psi(t)|$ is the density matrix. Entanglement entropy $S_{(1)}$, shown in Fig. 4.4**b**, grows much more slowly than expected in a thermalising system. The growth is accompanied by oscillations with the same frequency as $\langle \hat{P}_{|\bullet\rangle}\rangle$ in Fig. 4.3**b**, implying that the system returns to the neighbourhood of product states $|\mathbb{Z}_2\rangle$ and $|\mathbb{Z}_2'\rangle$. Furthermore, the entropy growth becomes almost fully suppressed by periodic driving, indicating that the scarred subspace disconnects from the thermalising bulk of the spectrum. Numerical TEBD simulations confirm that this lack of thermalisation at the single-site level provides a good approximation for the behaviour of larger subsystems, as demonstrated by the half-chain bipartite entropy $S_{(L/2)}$ plotted in Fig. 4.4**b**. This shows that scarring traps the system in a vanishingly small corner of an exponentially large Hilbert space.

Furthermore, we demonstrate a protocol for probing unequal-time correlators without brute-force tomography. Before initiating the evolution, we first transfer atoms on the right sites of the double wells in the x-superlattice to the hyperfine internal state $|\uparrow\rangle = |F{=}2, m_F{=}-2\rangle$ while leaving the atoms on the left sites in the state $|\downarrow\rangle = |F{=}1, m_F{=}-1\rangle$. By applying the magnetic field gradient, we generate a state-dependent linear tilt with $\Delta_{\mathrm{B}}^{|\uparrow\rangle} = -2\Delta_{\mathrm{B}}^{|\downarrow\rangle}$, see Fig. 4.4**c**. We fine-tune the gradient strength such that the total linear potential $\Delta^{|\uparrow\rangle} = \Delta_g^{|\uparrow\rangle} - |\Delta_{\mathrm{B}}^{|\uparrow\rangle}| \ll U$ would avoid resonant processes while suppressing the direct tunnelling. This means that the $|\uparrow\rangle$ atoms on the right sites are effectively "frozen" in the initial state $|\psi_0\rangle$, while evolving the chains along the left sites to $|\psi(t)\rangle$. After the evolution, we transfer $|\uparrow\rangle$ atoms back to $|\downarrow\rangle$, such that all atoms are identical bosons again. We then interfere these copies of $|\psi_0\rangle$ and $|\psi(t)\rangle$ in the x-superlattice, and thus read out the single-site fidelity with $\mathcal{F}_{(1)} = \mathrm{Tr}_{(1)}\,[\hat{\rho}_0\hat{\rho}(t)] = 1 - 2\langle \hat{P}^{\mathrm{BS}}_{\hat{n}\in\mathrm{odd}}\rangle_{(1)}$.

A few remarks are in order. First, as our system does not have single-site addressing, we will measure the average single-site fidelity and single-site entropy over all sites. In Appendix C we provide a rigorous proof that the single-site fidelity is an upper bound for the many-body fidelity $\mathcal{F} = |\langle\psi_0|\psi(t)\rangle|^2$ and show the different quantities for the same quench. We also discuss the use of the square average single-site fidelity $\mathcal{F}^2_{(1)}$. While it can fail to act as an upper bound for the many-body fidelity in some cases, we find through our numerical simulation that this virtually never happens and that this quantity gives a much closer approximation of it. We will thus use it as a proxy of $\mathcal{F}(t)$. In Fig. 4.4**d**, we observe that $\mathcal{F}^2_{(1)}$ displays persistent revivals at the frequency of $\langle \hat{M}_z\rangle$, revealing the system's periodic return to the vicinity of its initial state. The behaviour

of $\mathcal{F}^2_{(1)}$ and $\mathcal{F}(t)$ (computed numerically) in that figure is qualitatively identical.

4.4 Emergence of detuned scarring in the polarised state

Up to this point, we have provided extensive benchmarks of our quantum simulator against the previously known case of $\mathbb{Z}_2$ quantum many-body scars [43] and shown how we can measure fidelity and entanglement entropy after quenches. In this section we demonstrate that our quantum simulator also hosts distinct scarring regimes for initial states other than $|\mathbb{Z}_2\rangle$, which are enabled by detuning and can be further stabilised by a periodic drive. We highlight this finding by observation of scarring behaviour in the polarised state $|0\rangle$, previously not associated with scars.

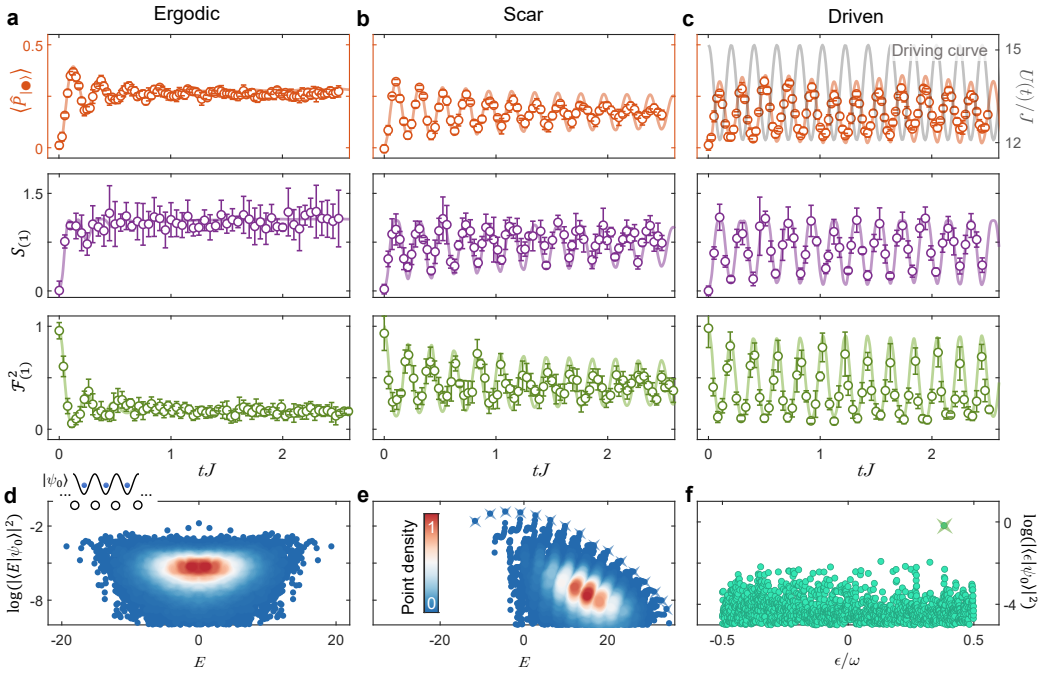

Figure 4.5: **a**: Fast thermalisation from the unit-filling Mott insulator state in the Bose–Hubbard chain at $U{=}\Delta$ resonance. **b**: Emergence of scarred dynamics in the presence of static detuning. **c**: Dynamical stabilisation of scarred dynamics in the presence of both detuning and periodic driving. Panels **a**, **b**, **c** are experimental measurements of the density of excitations, second Rényi entropy and squared fidelity for a single site. Static detuning is $U_0{=}-2.38J$ and the modulation parameters are $U_m{=}1.54J$, $\omega{=}4.9J{\times}2\pi$. Lines are the results of TEBD simulations. **d**, **e**, **f**: Exact diagonalisation results for the PXP model. **d**,**e** show overlaps of all eigenstates with the polarised state in the PXP chain on a ring with $N{=}32$ sites. The value of static detuning in **e** matches that used in **b**. **f** shows the spectrum of the Floquet unitary for the PXP chain with $N{=}24$ sites and driving parameters corresponding to **c**.

We first prepare the unit-filling state $|1111\ldots\rangle$ by transferring $|2,0\rangle$ to $|1,1\rangle$ states in the superlattice [209], which maps to the polarised state in the PXP model. In

the absence of detuning or periodic drive, we observe fast relaxation: the density of excitations, single-site entropy, and fidelity all rapidly relax, with no visible oscillations beyond the timescale $\sim 1/J$, see Fig. 4.5**a**. Interestingly, when we bias the system by a static detuning, $U_0 = -2.38J$ (corresponding to $\mu_0 = 2.38/\sqrt{2} = 1.68$ in the PXP model), we observe the emergence of oscillations in all three observables, accompanied by a slight decay, see Fig. 4.5**b**. Finally, if we also periodically modulate the interaction with amplitude $U_m = 1.54J$ and frequency $\omega = 4.9J \times 2\pi$, we find a dramatic enhancement of scarring, Fig. 4.5**c**. In particular, both entropy and fidelity now show pronounced oscillations, signalling robust scar-induced coherence at all experimentally-accessible times.

The intuitive picture behind our observations is summarised as follows. In the absence of detuning or periodic drive, the system initialised in the polarised state undergoes chaotic dynamics and rapidly explores the entire Hilbert space. By biasing the system via static detuning, thermalisation can be suppressed over moderate timescales. Finally, by periodically driving the system it is possible to 'refocus' the spreading of the many-body wave-function in the Hilbert space and thereby enhance the scarring effect, similar to the findings of Ref. [78] for the $|\mathbb{Z}_2\rangle$ state.

Fig. 4.5**d**, **e** show the results of exact diagonalisations of the PXP model in Eq. (2.20) in the presence of static detuning μ_0, which is proportional to the Bose-Hubbard detuning parameter U_0. Fig. 4.5**a** plots the overlap of all energy eigenstates $|E\rangle$ of the pure PXP model ($\mu_0 = 0$) with the polarised state $|\psi_0\rangle = |0\rangle$. As expected, we do not see any hallmarks of scars, such as ergodicity-violating eigenstates with anomalously enhanced projection on $|0\rangle$. On the other hand, when we add the static chemical potential $\mu_0 = 1.68\Omega$, corresponding to the detuning value in Fig. 4.5**b**, a band of scarred eigenstates with anomalously large overlap with $|0\rangle$ emerges; see Fig. 4.5**e**. The band of scarred eigenstates pans the entire energy spectrum, but their support on $|0\rangle$ is biased towards the ground state due to the breaking of particle-hole symmetry by detuning. Finally, similar to the $|\mathbb{Z}_2\rangle$ case, scarring from the $|0\rangle$ state can be further enhanced by periodic modulation of the PXP chemical potential, $\mu(t) = \mu_0 + \mu_m \cos(\omega t)$. By evaluating the corresponding Floquet operator, we find that a single Floquet mode develops a very large overlap with the $|0\rangle$ state, as shown on Fig. 4.5**f**. The existence of a single Floquet mode, whose mixing with other modes is strongly suppressed, gives rise to robust oscillations in the dynamics well beyond the experimentally accessible timescales.

A few comments are in order. We note that exact diagonalisation confirms that the PXP model remains chaotic for the value of detuning used in Fig. 4.5**e**, and this detuning is not large enough to trivially fragment the entire spectrum into disconnected sectors with the given numbers of excitations. Moreover, we confirmed that the scarred eigenstates in Fig. 4.5**e** are distinct from the ones associated with the $|\mathbb{Z}_2\rangle$ state. The Hilbert space trajectory of $|0\rangle$ is also very different from that of the $|\mathbb{Z}_2\rangle$ state. In the latter case, there is approximate state transfer between two product states that correspond to the highest- and lowest-weight states of some approximate su(2) spectrum-generating algebra. This is distinct from the $|0\rangle$ state, where the tra-

jectory after half the period passes through the highest entropy state along the orbit. In the rest of this chapter, we focus on understanding scarring from the polarised state.

4.5 Mechanism of scarring in the polarised state

While our experimental results have shown conclusive evidence of ergodicity breaking at moderate times from the polarised state, we now develop theoretical understanding of the non-ergodic long-time behaviour. First, we compare the difference between the predictions of the diagonal and canonical ensembles for an observable such as the average number of excitations, see Fig. 4.6. These two ensembles are expected to give the same result if the ETH holds [11] and all eigenstates at a similar energy density yield the same expectation value for local observables. This diagnostic correctly identifies that scarring from the Néel state is the strongest at $\mu_0 = 0$ as shown on Fig. 4.6**a**. Meanwhile, for the polarised state, Fig. 4.6**b** shows that the discrepancy between the two ensembles is the strongest around $\mu_0 \approx 1.68\Omega$, where we observe strong scarring. For μ_0/Ω close to 0, the polarised state thermalises quickly towards the thermal value expected for an infinite-temperature states. For very large μ_0/Ω, we enter a trivial regime where the polarised state is close to the ground state and only a few eigenstates at low energies are relevant for the dynamics. Hence, in this regime, quenching from the polarised state is similar to quenching from a thermal state at a very low temperature and the agreement between the two ensembles is again very good. However, in this regime, only a very small part of the many-body Hilbert space is explored by the dynamics. This is not the case in the scarred regime that we investigate experimentally, and this can be demonstrated by studying the relevant classical limit, as shown in the next section. Finally, Fig. 4.6**c** conclusively shows that the Néel and polarised states are highly atypical at $\mu_0/\Omega = 0$ and $\mu_0/\Omega = 1.68$ respectively when compared to other initial states. As the diagonal and canonical ensembles both relate to infinite-time, this shows that ergodicity-breaking is not limited to oscillations at short time.

4.5.1 Semi-classical limit

In Chapter 2, we have discussed the semi-classical limit that gave a good approximation to the dynamics from the Néel state. Here, we extend the same approach to the polarised state. Instead of the parameterisation in Eq. (2.27) given in Ref. [59], we use the one from Ref. [64] where the MPS matrices describing the state of each site are

$$A^{\bullet}(\theta_j, \phi_j) = \begin{pmatrix} 0 & ie^{-i\phi_j} \\ 0 & 0 \end{pmatrix}, \quad A^{\circ}(\theta_j, \phi_j) = \begin{pmatrix} \cos(\theta_j) & 0 \\ \sin(\theta_j) & 0. \end{pmatrix} \tag{4.10}$$

We recall that the full wave-function is obtained from these matrices using Eq. (2.28). While this parameterisation has a few minor differences from the one in Eq. (2.27) (e.g., normalisation, the θ_j angles being different by a factor of 2, etc.), it encodes the same type of product state where each site is characterised by θ and ϕ, which is then projected into the constrained PXP space. As we now consider the polarised state

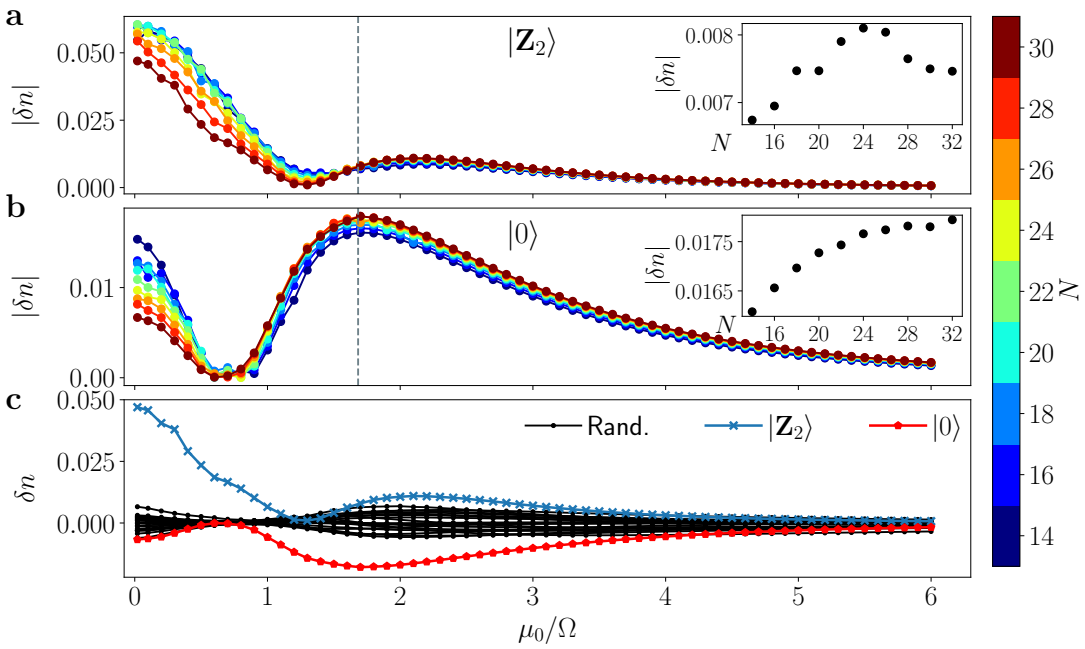

Figure 4.6: Difference between the expectation values of the diagonal and canonical ensembles for the average number of excitations in the PXP model. **a** Discrepancy after a quench from the Néel state. As expected, the difference is maximised at $\mu_0 = 0$ for this state. The inset shows the scaling of $|\delta n|$ at $\mu_0/\Omega \approx 1.68$. **b**: Discrepancy after a quench from the polarised, for which the difference is maximised at $\mu_0 \approx 1.68$. The inset shows the scaling of $|\delta n|$ at this point, displaying an increase of the difference with system size. **c**: Values of δn for $N = 30$ for various initial states. The Néel and polarised states show much larger discrepancies between the ensembles than all other states.

which is homogeneous in space, we will set all $\theta_j = \theta$ identical and the same for all $\phi_j = \phi$. This means that our Ansatz essentially describes a single large-spin coherent state. The derivation of the equations of motion and instantaneous leakage out of the manifold can be found in Appendix D for an infinite system. The equations of motion are given by

$$\dot{\theta} = -\Omega \cos(\theta)\cos(\phi)\left[1+\sin^2(\theta)\right], \tag{4.11}$$

$$\dot{\phi} = \mu_0 + \Omega\frac{\sin(\phi)}{\sin(\theta)}\left[1-4\sin^2(\theta)-\sin^4(\theta)\right]. \tag{4.12}$$

Moreover, this simple Ansatz also allows to determine analytically the important quantities such as the excitation density

$$\frac{1}{N}\sum_j \langle \hat{n}_j \rangle = \frac{\sin^2(\theta)}{1+\sin^2(\theta)}, \tag{4.13}$$

and the energy density

$$E(\theta,\phi)/N = \frac{\sin(\theta)}{1+\sin^2(\theta)}\left(\mu_0\sin(\theta) + 2\Omega\cos^2(\theta)\sin(\phi)\right). \tag{4.14}$$

Using these results, we can get a better understanding of the trajectory in the manifold. In particular, we can get the maximum angle θ reached for a given value of μ_0/Ω. From Eq. (4.11), we see that the turning point in the derivative of θ along the trajectory is governed by $\cos(\phi)$. A sign flip therefore must occur when $\phi = \pm\pi/2$. Energy is exactly conserved along a TDVP trajectory, and for the polarised state we have that $E(0,0) = 0$. Setting $\phi_{\max} = \pi/2$ in Eq. (4.14) and setting it to zero then allows us to determine the $\theta_{\max}$ coordinate of the turning point:

$$\sin(\theta_{\max}) = \left(|\mu_0/\Omega| - \sqrt{(\mu_0/\Omega)^2+16}\right)/4. \tag{4.15}$$

We can compare these analytical predictions against exact quantum dynamics. While we were not able to find an analytical solution for the equations of motions, they can be integrated numerically. This comparison is shown in Fig. 4.7 and the agreement with exact diagonalisation results gets increasingly better with μ_0/Ω. We note that at $\mu_0 = 1.68\Omega$ the TDVP numerics already gives a good prediction for short times, correctly capturing the oscillation period and amplitude.

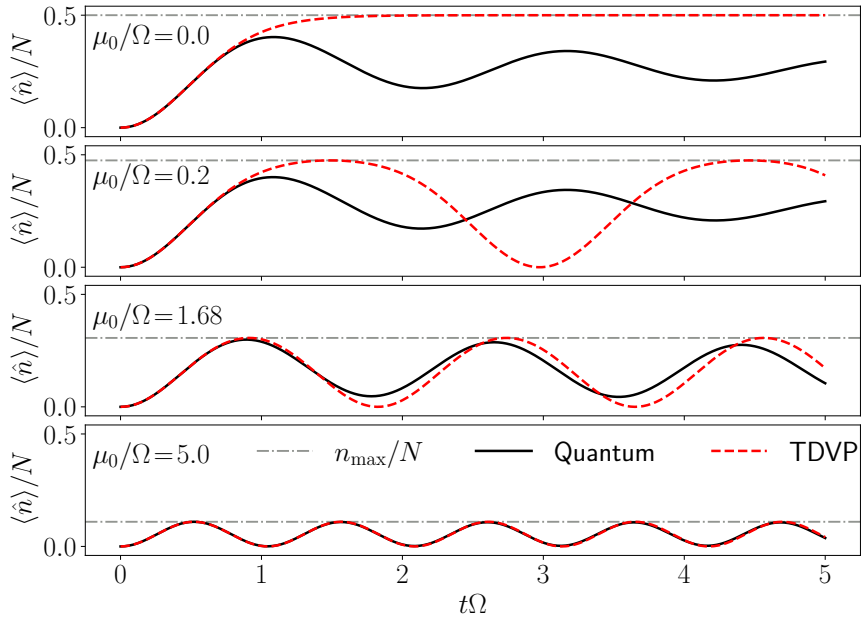

Figure 4.7: Comparison between the exact quantum results for $N = 32$ and the semi-classical prediction for an infinite system for the density of excitation after a quench from the polarised state. The two agree better as μ_0/Ω increases. The horizontal dashed line corresponds to the analytical value for the maximum excitation density for a given μ_0/Ω value.

Finally, as the TDVP approach is variational, it is important to quantify its accuracy in capturing the quantum dynamics. This can be characterised by "quantum leakage" – the instantaneous norm of a component of the state vector that lies outside the TDVP manifold – which was introduced in Eq. (2.26). We find that the analytical expression for the intensive leakage is

$$\gamma^2 = \Omega^2 \frac{\sin^6(\theta)}{1+\sin^2(\theta)}, \tag{4.16}$$

see Appendix D for the full derivation. The leakage is higher as θ is increased, corresponding to a larger density of excitations. This can be intuitively understood, as in this regime the PXP constraint has a strong effect and the spin-coherent state Ansatz does not faithfully capture the dynamics. On the other hand, for large values of μ_0/Ω, the leakage is low but θ is confined to values near zero, thus the trajectory does not explore much of the Hilbert space. This corresponds to the trivial case where the dynamics is confined to very low densities of excitations, rendering the constraint unimportant. Finally, in the intermediate regime of μ_0/Ω where we observe the scarring, the TDVP dynamics is able to "avoid" the high-leakage area, as seen in Fig. 4.8**a**, while at the same time θ is not pinned to zero and the dynamics explores a sizeable part of the Hilbert space.

As the TDVP results are computed for an infinite system, they also allow us to make prediction about the quantum dynamics in that limit. Indeed, from the instantaneous leakage rate γ one can compute $\Gamma_T = \left[\int_{t=0}^{T} \gamma(t)dt\right]^2$ by doing the integral over a periodic orbit with period T. Γ_T then provides an upper bound [64] on the quantum fidelity density after one period $f_T = -\ln(|\langle\psi(T)|\psi(0)\rangle|^2)/N$, and thus a lower bound on the fidelity itself. Essentially, Γ_T gives the fidelity density in the worst possible case where every part of the wave-function that leaves the manifold never returns into it. We also compute f_T in the thermodynamic limit through finite-size scaling of the exact dynamics. Both Γ_T and f_T can be seen in Fig. 4.8**b**. For the value of $\mu_0/\Omega = 1.68$ investigated experimentally, we find $f_T \approx 0.0268$ and $\Gamma_T = 0.0327$, an order of magnitude closer to zero than the value of $-\ln\left(\frac{1}{\mathcal{D}}\right)/N = \ln\left(\frac{1+\sqrt{5}}{2}\right) = 0.481$, expected for a thermalising state [1]. This indicates that ergodicity breaking will be present in the thermodynamic limit for this value of μ_0/Ω.

4.5.2 Algebraic picture

As the Ansatz used in the previous section is a single large-spin coherent state, it hints at the presence of an approximate su(2) algebra in the polarised state, similar to he Néel state discussed in Chapter 2. We propose that the parent model in the former case is simply the unconstrained spin-1/2 paramagnet along the X direction. Once

[1] While our state is restricted to the symmetry sector with zero momentum and +1 eigenvalue under spatial reflection, the size of this sector grows asymptotically as $\phi^N/(2N)$. So $-\ln\left(\frac{1}{\mathcal{D}}\right)/N$ is the same up to a $\ln(N)/N$ correction that will go to zero in the thermodynamic limit.

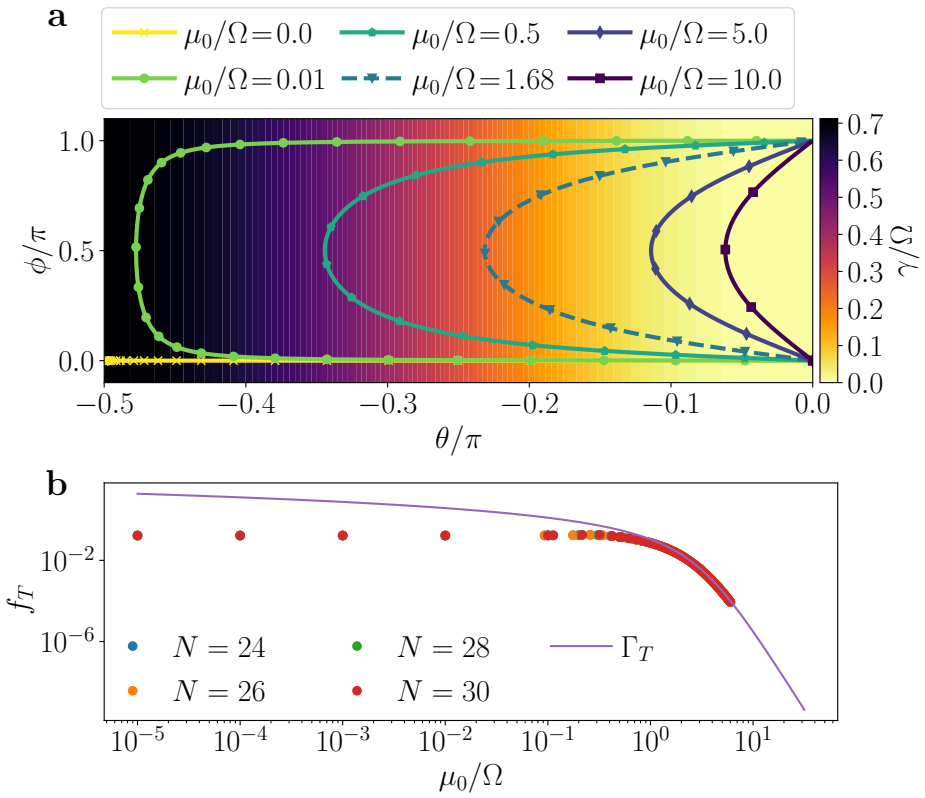

Figure 4.8: **a**: Trajectory in the TDVP manifold for different values of μ_0/Ω. Colour scale denotes quantum leakage γ, which serves as a bound on the accuracy of the TDVP approximation. The markers are spaced in time by $\Delta t = 0.15/\Omega$. For the optimal value $\mu_0 = 1.68\Omega$ also used in experiment, the trajectory avoids the high-leakage region and approximates well the quantum dynamics, while it is not limited to a small corner of the many-body Hilbert space. **b** Fidelity density after one period computed using exact dynamics and its upper bound Γ_T computed using the TDVP framework. A smaller value indicates better revivals.

projected into the constrained space, the generator of the algebra are equal to

$$\hat{S}^x = \frac{1}{2}\hat{H}_{\mathrm{PXP}}, \quad \hat{S}^y = \frac{1}{2}\sum_{j=1}^{N}\hat{P}_{j-1}\hat{\sigma}_j^y\hat{P}_{j+1}, \quad \hat{S}^z = \frac{1}{2}\sum_{j=1}^{N}\hat{\sigma}_j^z = -\frac{N}{2} + \sum_{j=1}^{N}\hat{n}_j. \tag{4.17}$$

Unlike in the Néel state case, it is clear that this projected algebra is poor, as can be checked from the commutation relation. However, the quality of the algebra actually depends on the density of excitations. Indeed, in the dilute limit where $\langle\hat{n}\rangle \ll N$, the excitations essentially do not see each other and, consequently, the projectors $\hat{P}$ in the $\hat{S}^x$ and $\hat{S}^y$ operators effectively act as the identity. Thus we recover the usual su(2) commutation relations and the dynamics can be well described as the precession of a big spin. As the density of excitation gets larger, this is no longer the case and the algebra drifts further and further from being exact. As this happens, the wave-function

can no longer be described as a large spin and the TDVP description breaks down. The effect of the detuning μ_0/Ω can be easily understood in that context. As it is equivalent to the global $\hat{S}^z$ operator (up to an irrelevant constant factor), changing μ_0/Ω is akin to tilting the axis of precession of the spin. This is the same effect that the staggered magnetisation had in the Néel state case, as was showcased in Fig. 3.5 **a**. This changes the trajectory on the Bloch sphere and brings the antipodal point closer to the initial state. In the Néel case, the algebra is good in the entire Bloch sphere and revivals can be witnessed for all values of the staggered magnetisation (see Appendix B). For the polarised state, the algebra is only good in the lower portion of the sphere. As such, the axis needs to be sufficiently tilted in order for the trajectory to avoid the upper part, corresponding to a high density of excitation. This is shown schematically on Fig. 4.9.

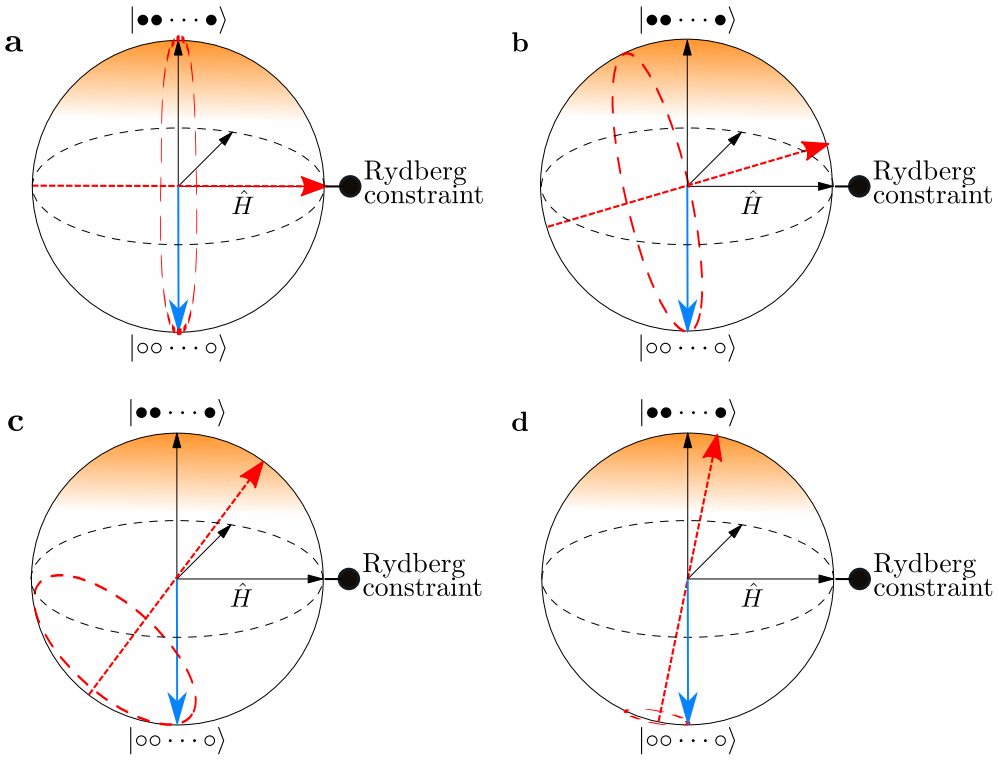

Figure 4.9: Representation of scarring from the polarised state as precession on a Bloch sphere with additional effects from the Rydberg constraint. Panels **a** to **d** represent the trajectory for increasing values of μ_0/Ω, corresponding to an increasingly tilted precession axis. The orange colour scale indicates the areas of the sphere where the spin coherent state approximation breaks down, which is essentially equivalent to the leakage in Fig. 4.8**a**. Panels **a** and **b** lead to thermalisation due to this. Panels **c** correspond to the scarred regime while panel **d** is the trivial regime where only low-energy physics occur.

4.6 Summary

We performed a quantum simulation of the paradigmatic PXP model of many-body scarring using a tilted Bose-Hubbard optical lattice. We demonstrated the existence of persistent quantum revivals from the $|\mathbb{Z}_2\rangle$ initial state and their dynamical stabilisation, opening up a new route for the investigation of scarring beyond Rydberg atom arrays. By harnessing the effect of detuning and periodic driving, we observed a distinct scarring regime associated with the polarised initial state. As the latter state is spatially homogeneous, its preparation does not require a superlattice, which makes further investigations of scarring phenomena accessible to a large class of ultracold atom experiments. The versatility of such platforms allows to directly probe the link between many-body scarring and other forms of ergodicity breaking phenomena, such as Hilbert space fragmentation and disorder-free localisation, as the latter can be conveniently studied in our setup by varying the tilt.

Our methods for probing unequal-time correlators allow for state-of-the-art monitoring of non-equilibrium dynamics and its applications in quantum technology. Notably, this protocol can be used to probe the global fidelity, as well as the unequal-time correlations between arbitrary quantum states, e.g., $|\langle\psi(t_1)|\psi(t_2)\rangle|^2$, with the help of single-atom resolution quantum gas microscopes [219, 220]. This would empower detailed experimental studies of exotic quantum phenomena such as dynamical quantum phase transitions [221]. Moreover, the observation of long-lived quantum coherence due to scarring and its controllable enhancement via periodic modulation, lays the foundation for applications such as quantum memories and quantum sensing [143]. The dynamical manipulation of a many-body system employed in this work can be directly used to prepare states with extensive multipartite entanglement [1] discussed in Chapter 3, thus lending itself to novel protocols for phase estimation and quantum metrology.

Finally, our discovery of scarring in the $|0\rangle$ state highlights the ubiquity of su(2) algebraic structures in the PXP model. Indeed, we have shown that scarring from that state can be captured by a semi-classical Ansatz corresponding to the precession of a single large spin. We have also proposed that the origin of this is an unconstrained paramagnet which leaves a strong imprint in the PXP model for sufficiently low density of excitations. By adding a strong enough detuning, the system can be kept in this regime, where remnants of the algebraic structure of the unconstrained paramagnet are relatively well preserved.

Chapter 5

Graph-theoretic approach to quantum many-body scarring in tilted Fermi-Hubbard chains

In the previous chapter, we have emphasised the need for engineering QMBS on different experimental platforms, and we have demonstrated that the emblematic PXP model itself can be simulated using a Bose-Hubbard simulator with a tilted potential. A natural question, in particular in view of solid-state material realisations, is whether this construction can be generalised to systems described by a Fermi-Hubbard model. We will now show that we can use the same mechanism – linear tilt potential – to create a constrained effective model in the Fermi-Hubbard chain. However, in contrast to the Bose-Hubbard case in Chapter 4, the effective Hamiltonian will turn out *not* to be equivalent to the PXP or any other previously-known QMBS model. Nevertheless, we will show that the new model exhibits familiar QMBS phenomenology, including revivals from simple product states. We will explain the mechanism of scarring from a graph-theoretical point of view by visualising the Hamiltonian as an adjacency graph, where each computational basis state represents a graph vertex. The origin of scarring is traced back to a subset of this graph which is isomorphic to an integrable system, whilst being weakly coupled to the rest of the Hilbert space. The graph picture will also allow us to directly identify the reviving initial states, as they are the only vertices belonging to the integrable subgraph which have no edges connecting them to the remainder of the graph representing thermal states.

The model studied in this chapter is motivated by a recent experiment [222], which demonstrated the existence of Hilbert space fragmentation in a tilted Fermi-Hubbard optical lattice. The study of QMBSs in that system would allow to investigate its interplay with both fragmentation as well as Stark many-body localisation [223–225], which can similarly be induced by a strong tilt.

5.1 The tilted Fermi-Hubbard model

The 1D Fermi-Hubbard model is given by the Hamiltonian

$$\hat{H} = \sum_{j,\, s=\uparrow,\downarrow} -J\hat{c}^{\dagger}_{j,s}\hat{c}_{j+1,s} + \text{h.c.} + \Delta j\hat{n}_{j,s} + U\sum_{j}\hat{n}_{j,\uparrow}\hat{n}_{j,\downarrow}, \tag{5.1}$$

where $\hat{c}^{\dagger}_{j,s}$ denotes the usual electron creation operator on site j with spin projection s, $\hat{n}_{j,s} \equiv \hat{c}^{\dagger}_{j,s}\hat{c}_{j,s}$ is the density operator, J and U are the hopping and on-site interaction terms, respectively. Tilt of the optical lattice is parameterised by Δ, which can be experimentally implemented via an electric field gradient and we assume it to be spin-independent [222]. Note that tilting has the structure of a dipole term, $\sim j\hat{n}_j$. Below we impose open boundary conditions on the model in Eq. (5.1), and restrict to the electron filling factor $\nu = 1$, i.e., with $N/2$ fermions with spin $\uparrow$ and $N/2$ fermions with spin $\downarrow$ on a chain of N sites (assumed to be even). We also set $J = 1$ for simplicity. We label the Fock states using $\uparrow$ to denote a fermion with spin up and $\downarrow$ with spin down, while 0 stands for an empty site and $\updownarrow$ denotes a doublon.

As in the previous chapter, we focus on the regime $\Delta \approx U \gg J$. In this case the sum of the dipole moment and the number of doublons is effectively conserved. The dominant contribution to the Hamiltonian (using a Schrieffer-Wolff transformation at first order [47]) is then given by

$$\hat{H}_{\text{eff}} = -J\sum_{j,s}\hat{c}^{\dagger}_{j,s}\hat{c}_{j+1,s}\hat{n}_{j,\bar{s}}(1-\hat{n}_{j+1,\bar{s}}) + \text{h.c.} + (U-\Delta)\sum_{j}\hat{n}_{j,\uparrow}\hat{n}_{j,\downarrow}, \tag{5.2}$$

where j is summed over all lattice sites while s is summed over the spin values $\downarrow$ and $\uparrow$, and $\bar{s}$ denotes opposite spin from s. As in the bosonic case, in this effective Hamiltonian hopping to the left (which decreases the total dipole moment by 1) is only allowed if it increases the number of doublons by the same amount, which is enforced by the projectors. While this might seem identical to the Bose-Hubbard case, the exclusion principle affecting fermions and their spin result in a completely different model. Indeed, creating a doublon is only possible with fermions of opposite spins. Thus, configurations like $|\uparrow\uparrow\rangle$ and $|\downarrow\downarrow\rangle$ are dynamically frozen. Meanwhile, $|\updownarrow\, 0\rangle$ is connected to both $|\uparrow\downarrow\rangle$ and $|\downarrow\uparrow\rangle$. This means that each link between fermions can no longer be mapped to a spin-1/2 and we need to keep track of the fermion spins.

In order to simplify the computations, we perform a Jordan-Wigner transformation to express the Hamiltonian in terms of Pauli spin operators $\hat{\sigma}^z$, $\hat{\sigma}^{\pm} = (\hat{\sigma}_x \pm i\hat{\sigma}_y)/2$. As we have two species $\uparrow$, $\downarrow$ of fermions, each species therefore gets mapped to a corresponding Jordan-Wigner spin $\hat{\sigma}^{\alpha}_{\uparrow}$, $\hat{\sigma}^{\alpha}_{\downarrow}$. In order to minimise the confusion between the spin of the original fermions and the Jordan-Wigner spins, we will reserve the term "spin" to exclusively refer to the original fermion spin. For the Jordan-Wigner spins, we will describe the physics in term of "excitations", e.g., the action of $\hat{\sigma}^{+}_{j,\downarrow}$ is to create an excitation on site j with spin down. Furthermore, as a Jordan-Wigner convention, we will set that the spin-down fermions are located "on the right" of the up-spin ones.

For open boundary conditions the resulting Hamiltonian of the effective model is:

$$\hat{H}_{\text{eff,JW}} = -J\sum_j \hat{\sigma}^+_{j,\downarrow}\hat{\sigma}^-_{j+1,\downarrow}\hat{n}_{j,\uparrow}\left(1-\hat{P}_{j+1,\uparrow}\right) + J\sum_j \hat{\sigma}^+_{j,\uparrow}\hat{\sigma}^-_{j+1,\uparrow}\hat{n}_{j,\downarrow}\left(1-\hat{P}_{j+1,\downarrow}\right), \quad (5.3)$$

where $\hat{P}$ and $\hat{n}$ are projectors respectively on the non-excited and excited state of the Jordan-Wigner spin. The two subscript on the $\hat{\sigma}$ operators denote the site and spin of the fermion.

5.1.1 Largest connected component of the Hilbert space

The action of the Hamiltonian (5.2) within the $\nu = 1$ sector fragments the Hilbert space beyond the simple conservation of $U + \Delta$. In this work we focus on the largest connected component, which is the one containing the state with alternating $\uparrow$ and $\downarrow$ fermions. From this state, neighbouring $\downarrow$ and $\uparrow$ fermions can always be exchanged through the $\updownarrow 0$ configuration. Thus, all possible configurations of fermions with no doublons must be in the same sector. On top of this, we also have states with a $\updownarrow 0$ instead of neighbouring $\uparrow$ and $\downarrow$. Meanwhile, the other sectors all contain at least one frozen site through which $\uparrow$ and $\downarrow$ fermion cannot be exchanged. This splits the chain into multiple disconnected fragments, leading to a reduced number of states.

The dimension of the largest connected sector can be computed analytically by relying on the similarity of its structure to that of the PXP model. Indeed, while the spin of the fermions means that the mapping used in the Bose-Hubbard model is no longer correct, it still captures some of the characteristics of our effective Hamiltonian. In particular, we can start with it and then add the action of the fermionic spin on top. As for the Bose-Hubbard case treated in Chapter 4, let us put a spin-1/2 on each link between fermions. Let $N = 2M$ be the number of fermionic sites, the effective PXP model then has $2M-1$ sites. We can map any link between $|\updownarrow 0\rangle$ as an excitation while other configurations corresponding to unexcited PXP sites. This captures all possible configurations of doublons in the effective model, but now for each of these there are multiple ways to arrange the remaining fermions depending on their spin. If there are n doublons/PXP excitations, then we are left with $2(M-n)$ fermions. Half of them have spin up and the other half spin down, and they live on the $2(M-n)$ remaining sites. As such they can take exactly $\binom{2(M-n)}{M-n}$ different configurations. For the PXP model with $N-1 = 2M-1$ sites, it has been shown in Ref. [226] that the number of configurations with n excitations is

$$\mathcal{N}_{\text{PXP}}(2M-1,n) = \binom{2M-1-n}{n} + \binom{2M-1-n}{n-1} = \binom{2M-n}{n}, \quad (5.4)$$

with n taking any value between 0 and M. This leaves us with a total number of states in the effective Fermi-Hubbard model of

$$\mathcal{D}_M = \sum_{n=0}^{M}\binom{2M-n}{n}\binom{2(M-n)}{M-n}, \quad (5.5)$$

which, after some combinatorial manipulations and using a change of variable $k = M - n$, can be written as

$$\mathcal{D}_M = \sum_{k=0}^{M} \binom{M+k}{k}\binom{M}{k} = \sum_{k=0}^{M} \binom{M+k}{k}\binom{M}{k}\left(\frac{3-1}{2}\right)^k = P_M(3), \tag{5.6}$$

where $P_M(3)$ denotes the Legendre polynomial of degree M evaluated at the point $x = 3$. This also allows us to use the recursion relation for Legendre polynomials to get

$$\mathcal{D}_M = \frac{3(2M-1)\mathcal{D}_{M-1} - (M-1)\mathcal{D}_{M-2}}{M}, \tag{5.7}$$

which makes it straightforward to compute $\mathcal{D}_M$ numerically using only integers. It also allows to analytically get the asymptotic behaviour of $\mathcal{D}_M$. Let us use the Ansatz $\mathcal{D}_M = \alpha^M$. Then in the $M \to \infty$ limit, we can rewrite Eq. (5.7) as

$$\alpha^M = 6\alpha^{M-1} - \alpha^{M-2}. \tag{5.8}$$

Dividing this by α^{M-2} and solving the resulting degree-2 equation leads to $\alpha = 3+2\sqrt{2}$.

5.1.2 Symmetries of the model and level statistics

In order to verify that the effective Hamiltonian in the largest connected sector is chaotic, we first need to identify and explicitly resolve the various symmetries of the model. The full model in Eq. (5.1), has two symmetries linked to the fermionic spin. Namely the SU(2) spin symmetry and a $\mathbb{Z}_2$ symmetry related to spin-reversal [227]. The latter is given by

$$\hat{y}_1 = \prod_j e^{-i\pi\frac{1}{2}(i\hat{c}^\dagger_{j,\downarrow}\hat{c}_{j,\uparrow} - i\hat{c}^\dagger_{j,\uparrow}\hat{c}_{j,\downarrow})}. \tag{5.9}$$

After the Jordan-Wigner transformation, this symmetry cam be simply formulated using the joint action of the doublon parity operator and the spin inversion operator. The doublon parity is diagonal in the product basis and gives +1 if there is an even number of doublons and -1 otherwise. The spin inversion simply changes the excitations between up spin and down spin. The symmetry can then be expressed as

$$\hat{z}_1 = \prod_{j=1}^{N} (-1)^{\hat{n}_{j,\downarrow}\hat{n}_{j,\uparrow}} \left(\hat{\sigma}^+_{j,\uparrow}\hat{\sigma}^-_{j,\downarrow} + \hat{\sigma}^+_{j,\downarrow}\hat{\sigma}^-_{j,\uparrow} + \frac{1+\hat{\sigma}^z_{j,\uparrow}\hat{\sigma}^z_{j,\downarrow}}{2}\right). \tag{5.10}$$

This is equivalent to Eq. (5.9) up to an overall spin-rotation and some charge-dependent phase factors.

In the largest Hilbert space sector, the Hamiltonian (5.2) has an additional symmetry related to spatial inversion and particle-hole exchange. In the fermionic language, it can be written as

$$\hat{y}_2 = \prod_j (-1)^{\hat{n}_{j,\uparrow}\hat{n}_{j,\downarrow}} \hat{\mathcal{P}}\hat{\mathcal{R}}, \tag{5.11}$$

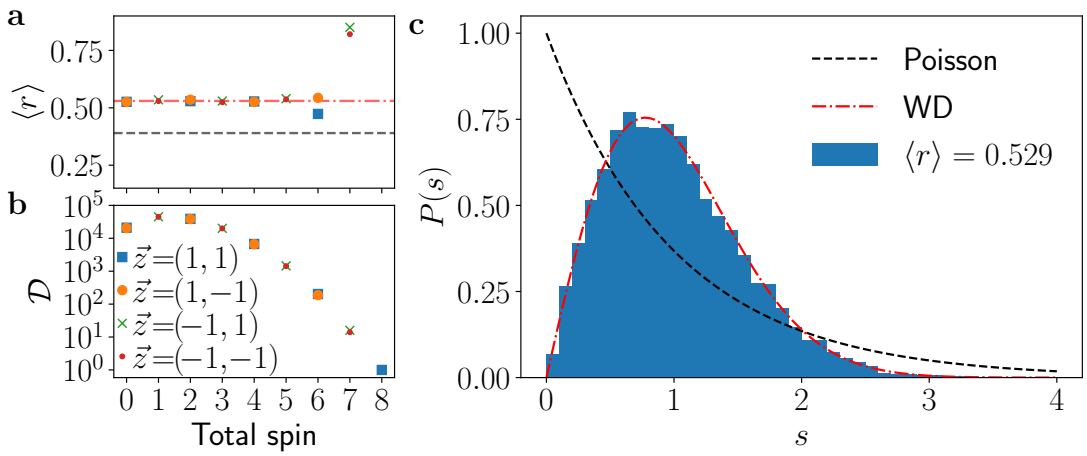

Figure 5.1: Level-spacing statistics for the effective Fermi-Hubbard model in Eq. (5.2) for $N = 16$. **a** Average r value in all sectors in the relevant Hilbert space sector. The black dotted line is at $\langle r \rangle = 0.39$ (expected value for Poisson statistics) while the red dash-dotted line is at $\langle r \rangle = 0.53$ (expected value for Wigner-Dyson statistics). **b** Number of states in each symmetry sector. Overall we find that in all sectors with at least $\mathcal{D} \approx 10^3$ states, $\langle r \rangle$ is very close to 0.53 **c** Full distribution of the energy level spacing after unfolding [19] in the sector $\vec{z} = (1, 1)$ and total spin $S = 2$. We again find good agreement with the Wigner-Dyson ensemble.

using the particle-hole operator $\hat{\mathcal{P}}$ and spatial-reflection operator $\hat{\mathcal{R}}$ defined by the adjoint actions,

$$\hat{\mathcal{P}} c^\dagger_{j,s} = c_{j,s} \hat{\mathcal{P}}, \qquad \hat{\mathcal{R}} c^\dagger_{j,s} = c^\dagger_{N-j-1,s} \hat{\mathcal{R}}. \tag{5.12}$$

The particle-hole operator also has a non-trivial action on the vacuum state

$$\hat{\mathcal{P}} |0\rangle = \prod_j c^\dagger_{j,\uparrow} c^\dagger_{j,\downarrow} |0\rangle . \tag{5.13}$$

After the Jordan-Wigner transformation, the second symmetry generator can be expressed as

$$\hat{z}_2 = \prod_{j=1}^{N/2} \prod_s \left(\hat{\sigma}^+_{j,s} \hat{\sigma}^+_{N-j-1,s} + \hat{\sigma}^-_{j,s} \hat{\sigma}^-_{N-j-1,s} + \frac{1 - \hat{\sigma}^z_{j,s} \hat{\sigma}^z_{N-j-1,s}}{2} \right). \tag{5.14}$$

The spatial inversion swaps sites j and $N-j$, while the particle-hole conjugation places an excitation in every empty site and vice-versa.

As our numerical results are obtained using the spin formulation, we will specify the symmetry sectors by $\vec{z} = (z_1, z_2) = (\pm 1, \pm 1)$, where z_1 and z_2 are the eigenvalue of the operators in Eqs. (5.10) and (5.14) respectively. After resolving these symmetries, we find the level statistics parameter $\langle r \rangle$ [24] to be close to 0.53 for all symmetry sectors with large numbers of states ($\gtrsim 10^3$). From these values which coincide with

the Wigner-Dyson statistics [19], we expect the model in Eq. (5.2) to be chaotic. In Fig. 5.1, we further probe the full distribution of level spacings after unfolding for one sector. Once again, we recover extremely good agreement with Wigner-Dyson. Of course, it will turn out that our model does not represent a completely generic chaotic system, as it contains special QMBS eigenstates in its spectrum. We next outline an intuitive approach based on graph theory that allows us to identify QMBSs in the model (5.2).

5.2 Embedded hypergrid subgraph

One of the main difficulties of identifying weak ergodicity breaking is that its effect is restricted to a small class of initial states and cannot be detected using global quantities such as the level spacing statistics. As a brute force search from all product states is numerically demanding, we propose here an approach to find the reviving states based on the graph of the model. In this graph each vertex corresponds to a basis state (usually in the Fock basis), and two vertices are connected by an edge if the Hamiltonian matrix element between their respective basis states is non-zero. We next show, by examining the adjacency graph of the model in Eq. (5.2), that we can identify a subgraph, weakly coupled to the rest of the Hilbert space, which contains the reviving initial states and leaves a strong imprint on the scarred eigenstates. This leads to a transparent manifestation of scarring in the original Fock basis, in contrast with the PXP model. In the latter case, the subspace which is weakly coupled to the rest of the Hilbert space has a much more complicated structure, leading to the wave-function spreading across the entire adjacency graph [54] before refocusing onto the Néel state.

In order to reduce the Hamiltonian to its connectivity, it is desirable for it to be purely off-diagonal, and to have all its non-zero matrix elements of equal sign and magnitude. This means that the corresponding graph can be treated as an *unweighted* graph. In the case of the tilted Fermi-Hubbard chain, the off-diagonal condition is satisfied for the effective Hamiltonian in Eq. (5.2). However, it is clear that there are both positive and negative matrix elements. We show that a simple basis transformation is enough to get rid of all minus signs in the Hamiltonian. These occur only when moving a spin down excitation. Here we propose the following convention for fixing the signs: we assign to each product a sign equal to the parity of the number of spin down excitations on the even sites. This corresponds to a change of basis using the diagonal matrix $\hat{T} = \sum_{j=1}^{N/2}(-1)^{\hat{P}_{j,\downarrow}}$. If a spin up excitation is moved, this does not change this quantity and it follows that both states connected by this move have the same sign. Whether it is +1 or -1 is irrelevant as the matrix element will get a factor equivalent to their product, which is always +1. On the other hand, if a spin down excitation is moved, this parity number will always change by 1, and the states connected by the move will have opposite signs. From this, it follows that all the matrix elements of $\hat{T}\hat{H}_{\text{eff,JW}}\hat{T}$ are equal to +1, thus we can view the model in terms of an undirected, unweighted graph. Alternatively, the same result can be obtained by choosing a different convention for the Jordan-Wigner transformation. Instead of

interleaving the fermions with a different spin-projection, one can first place all up-spin fermions and then all down-spin ones with a simple linear order for each species. This has the effect of ensuring that each of the 'hopping' terms never takes a fermion past another. Then, all these matrix elements are equal and can be brought to 1 by the choice of the coupling constant J.

In Fig. 5.2 we plot the adjacency graph of the Hamiltonian in Eq. (5.2) for a small system. We recall that each vertex corresponds to a Fock state, and two states are connected by an edge if the matrix element between them is non-zero. As the Hamiltonian (5.2) (for $U = \Delta$) has no diagonal elements and the spectrum is symmetric around zero, all product states effectively belong to the infinite temperature ensemble and thus are expected to thermalise quickly. As we will confirm numerically below, there are two important exceptions.

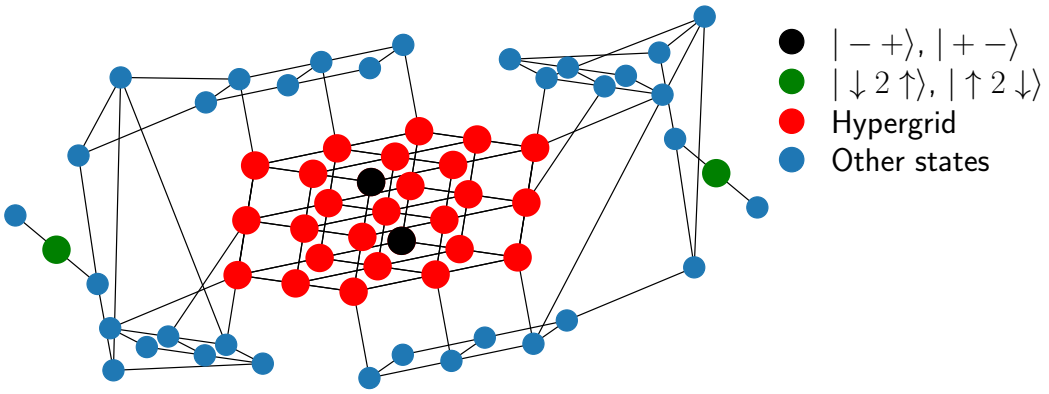

Figure 5.2: Adjacency graph of the effective model in Eq. (5.2) for $N = 6$. Red vertices denote the states belonging to the hypergrid, with the black vertices corresponding to the states $|-+\rangle$ and $|+-\rangle$ defined in the text. Green vertices are the isolated states $|\downarrow 2\uparrow\rangle$ and $|\uparrow 2\downarrow\rangle$ which live on the tails of the graph. For this graph, the hypergrid contains 27 vertices out of 63.

First, as highlighted in red colour in Fig. 5.2, there is a regular subgraph which has the form of the hypergrid – a Cartesian product of line graphs (in our case, of length 3), i.e., the hypergrid is isomorphic to an adjacency graph of a free spin-1 paramagnet. This mapping can be understood by looking at the state $|\downarrow\uparrow\downarrow\uparrow\downarrow\uparrow\ldots\rangle$. Each cell of two sites (comprising sites $2j-1$ and $2j$ with $j = 1$ to $N/2$) can take the values $- \equiv\downarrow\uparrow$, $2 \equiv\updownarrow 0$ or $+ \equiv\uparrow\downarrow$, leading to a three level system. Note that the configuration $0 \updownarrow$ is omitted, as doublons can only be formed by hopping to the left. On the other hand, hopping between two neighbouring cell will break this mapping and take the system out of the hypergrid subgraph. Inside the hypergrid, we identify two states for which the cell alternates between $-$ and $+$. These are the state $|-+\rangle \equiv |-+-+\ldots\rangle = |\downarrow\uparrow\uparrow\downarrow\downarrow\uparrow\uparrow\downarrow\ldots\rangle$ and its spin-inverted partner, $|+-\rangle = |+-+-\ldots\rangle \equiv |\uparrow\downarrow\downarrow\uparrow\uparrow\downarrow\downarrow\uparrow\ldots\rangle$. The states $|-+\rangle$ and $|+-\rangle$ for $N = 6$ are shown in black colour in Fig. 5.2. These two states are the only corners of the hypergrid (state with only $+$ and $-$ cells) with no edges going out of it. As we show below, both of these states shows persistent oscillations in quench dynamics,

undergoing robust state transfer to their spin-inverted counterpart. While other corners of the hypergrid also show revivals, they are much smaller in amplitude and decay faster due to the leakage out of this substructure. The second example of a reviving state is $|\downarrow 2\uparrow\rangle \equiv |\downarrow\downarrow\ldots\downarrow\updownarrow 0\uparrow\uparrow\ldots\uparrow\rangle$ (and its spin-reversed partner $|\uparrow 2\downarrow\rangle$), which is situated on a tail-like structure of length 3 (independent of system size) with minimal connectivity to the rest of the Hilbert space (green points in Fig 5.2). Similar tail-like structures occur in constrained spin models such as the quantum East model [228].

5.3 Scarred dynamics

Having identified candidate states for quantum revivals in the hypergrid picture, we now scrutinise their quench dynamics using large-scale exact diagonalisation simulations of the effective model in Eq. (5.2). Making use of various symmetries present in the model, we have been able to exactly simulate dynamics for up to $N = 22$ fermions. For convenience, the simulations were performed in the spin representation of the model.

Fig. 5.3**a** shows the time dependence of the entanglement entropy $S_{\text{ent}}(t)$ when the system is quenched from various initial product states, such as $|{-}{+}\rangle$, $|\downarrow 2\uparrow\rangle$ and a few randomly-chosen product states. S_{ent} is defined as the von Neumann entropy of the reduced density matrix for one half of the chain. In all cases, entropy grows linearly in time, consistent with thermalisation of the system. However, the coefficient of linear growth is visibly different for $|{-}{+}\rangle$ and $|\downarrow 2\uparrow\rangle$ states, and it is smaller than that of random states, indicating non-ergodic dynamics. The long-time value of the entropy is also different for the $|{-}{+}\rangle$ state, hinting that the wave-function is still not completely spread into the whole Hilbert space. The hallmark of many-body scars are the oscillations superposed on top of the linear growth, as seen in the scarred dynamics in the PXP model [50]. Rapid growth of entropy at short times is a consequence of the bipartition being located in the middle of an two-site effective cell.

Entropy oscillations mirror those of the wave-function return probability $\mathcal{F}(t)$ in Fig. 5.3**b**. For the isolated state $|\downarrow 2\uparrow\rangle$, only a single revival is clearly visible as the return probability decays rapidly once the wave-function leaks out of the tail of the graph. The revival time can be accurately estimated by assuming the tail is completely disconnected, leading to the period $\pi/\sqrt{2}$. In contrast, the state $|{-}{+}\rangle$ displays several revivals with the sizeable weight of the wave-function $\sim 40\%$ returning to its initial value. The fidelity density at the first revival, $\frac{1}{N}\ln(\mathcal{F})$, shown in the inset, converges as $1/N$ to a value of -0.058. In contrast, the inverse Hilbert space dimension, $\mathcal{D}^{-1}$, expected for a random state leads to a fidelity density of -0.855 – an order of magnitude higher. The scarred dynamics in this case can be visualised as the state bouncing within the hypergrid between $|{-}{+}\rangle$ and its partner $|{+}{-}\rangle$, illustrated by the dotted line in Fig. 5.3**b**. From the hypergrid analysis, we expect the revival period to be $\sqrt{2}\pi$, coming from the 2π period of free precession and the spin-1 matrix elements $\sqrt{2}$. This prediction closely matches the revival period observed in Fig. 5.3**b**.

The importance of the hypergrid for scarred dynamics is illustrated in Fig. 5.3**c** which plots the probability to remain in the hypergrid, $P_{\text{HG}}(t) = \langle\psi_0|e^{i\hat{H}t}\hat{P}_{\text{HG}}e^{-i\hat{H}t}|\psi_0\rangle$,

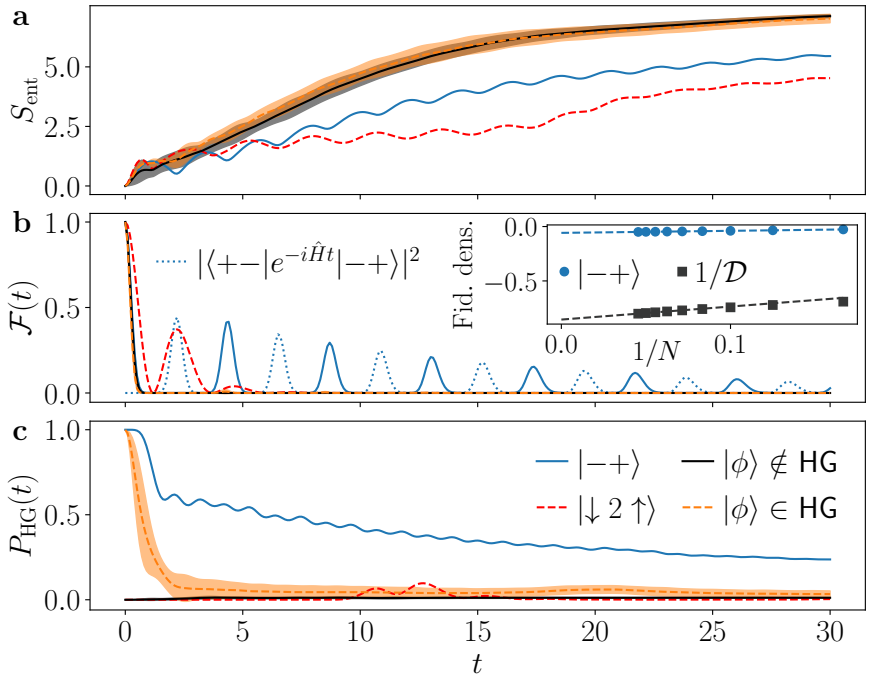

Figure 5.3: Dynamics in the effective model (5.2) for $N = 18$ for $|-+\rangle$, $|\downarrow 2\uparrow\rangle$ and randomly chosen initial states. **a** Entanglement entropy S_{ent} for an equal bipartition of the system. Entropy grows linearly in time for all states, consistent with thermalising dynamics, but for the special initial states it shows QMBS oscillations. $|\phi\rangle \notin$ HG and $|\phi\rangle \in$ HG denote the average over 10 random product states outside or within the hypergrid, respectively, and the shading represents standard deviation. **b** Fidelity dynamics for the same initial states as in **a**. Inset shows the finite-size scaling of the fidelity density $\frac{1}{N}\ln|\langle\psi_0|e^{-i\hat{H}t}|\psi_0\rangle|^2$ at the first revival for $|-+\rangle$ state, demonstrating a value much higher than $\frac{1}{N}\ln(1/\mathcal{D})$ (with $\mathcal{D}$ the dimension of the Hilbert space derived in Section 5.1.1), expected for a random state. Blue dotted line shows the amplitude of state transfer between $|-+\rangle$ and $|+-\rangle$ states. **c** Probability to remain within the hypergrid over time is much higher for $|-+\rangle$ than other states.

where $\hat{P}_{\text{HG}}$ is the projector onto the subspace spanned by product states belonging to the hypergrid. For the initial state $|-+\rangle$, we observe that the wave-function remains concentrated inside the hypergrid, even at late times. This is in stark contrast with the PXP model [54], where the wave-function spreads across the entire graph by the time it undergoes the first revival. Finally, for this initial state after a long time P_{HG} converges to a non-zero value which is higher than expected from the relative size of the hypergrid in the Hilbert space, hinting that the subgraph has additional structure that prevents states from leaking out. This is important, because in the thermodynamic limit the hypergrid occupies a vanishing fraction of the Hilbert space. Indeed, as the hypergrid has dimension $3^{N/2}$ while the Hilbert has dimension $(3+\sqrt{8})^{N/2}$, the fraction of states in the former decreases exponentially with N. The fact that this higher-than-expected value is only witnessed for $|-+\rangle$ state and not for other random states *within* the

hypergrid confirms that this state occupies a special position within this substructure.

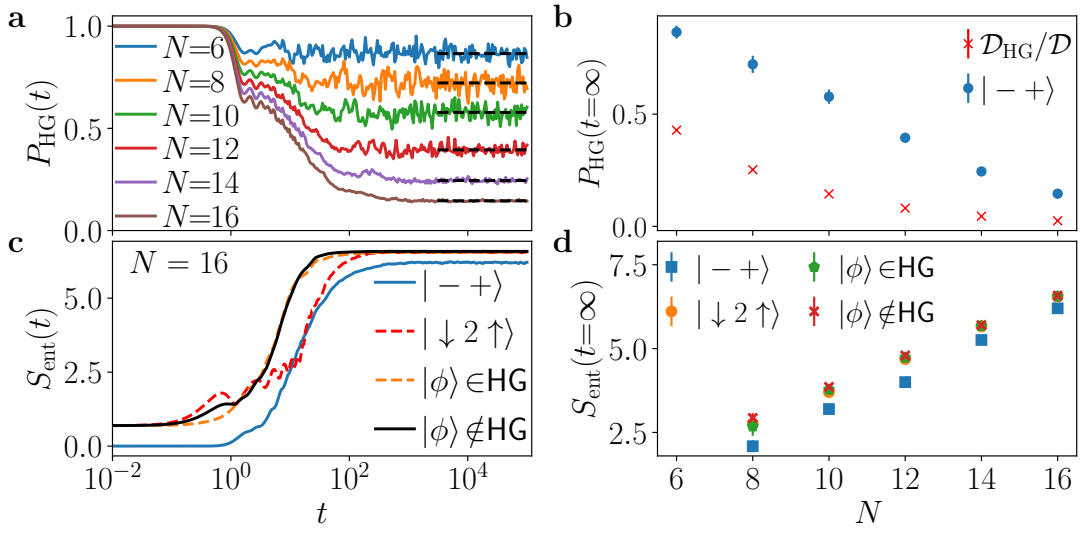

Figure 5.4: Signatures of the non-trivial embedding of the hypergrid in the effective tilted Fermi-Hubbard model. **a** Expectation value of the projector on the hypergrid states over time for various system sizes with the initial state $|-+\rangle$. The dotted black lines show the average of this projector at long times. Panel **b** shows these long-time value compared to the expected value from the relative size of the hypergrid for various system sizes. **c** Entanglement entropy as a function of time for different initial states and system size $N = 16$. $|\phi\rangle \notin$ HG and $|\phi\rangle \in$ HG denote the average over 10 random product states, respectively outside of and within the hypergrid, that have been projected into the symmetry sectors in which the $|-+\rangle$ state has support. This was done to remove the influence of these symmetries in the entanglement entropy. The shaded area corresponds to the standard deviation. Panel **d** shows the long-time value for different initial states as a function of system size. For the system sizes investigated, all states except $|-+\rangle$ converge towards the same entropy value.

In Fig. 5.4, we perform similar quench dynamics but now for much longer times and for a range of system sizes. The same kind of behaviour of P_{HG} as in Fig. 5.3 is observed. This is also true for the long-time value of the entanglement entropy. For a large enough system, most states saturate to the same entropy but for $|-+\rangle$ this saturation value is lower, showing that the wave-function is not entirely spread into the entire Hilbert space. This lower saturation entropy is *not* visible for generic states, even the ones picked from within the hypergrid. This is consistent with our picture of the wave-function being partially trapped in the hypergrid when the system starts out in $|-+\rangle$ state. These long-time results show that our previous results are not merely a prethermal regime. While the scaling with system size does not allow us to make decisive prediction on the fate of scarring in the thermodynamic limit, it at least hints that we can expect similar infinite-time results for several tens of atoms.

5.4 Eigenstate properties

Properties of eigenstates of the model (5.2) are summarised in Fig. 5.5. The projection of eigenstates onto the $|{-}{+}\rangle$ state, shown in panel **a**, displays prominent tower structures reminiscent of other scarred models. The existence of towers implies that eigenstates tend to concentrate around certain energies in the spectrum, causing an ETH violation. The separation between the towers is approximately $\Delta E \approx \sqrt{2}$, as expected from the embedded hypergrid. Note that the eigenstates have been classified according to the conserved total value of spin S; in contrast, the $|{-}{+}\rangle$ state is not an eigenstate of $\mathbf{S}^2$. One can show that for this state, $\langle \mathbf{S}^2 \rangle = N/2$, thus $|{-}{+}\rangle$ is predominantly supported by $S = 1$ and $S = 2$ eigenstates for $N = 16$ used in Fig. 5.5 . The $S = 1$ eigenstates are indicated by red points in that figure.

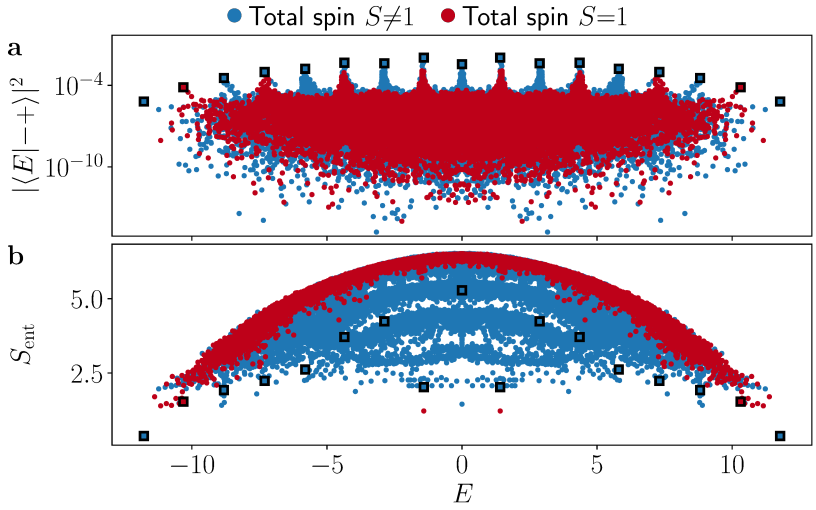

Figure 5.5: Eigenstate properties of the effective model (5.2) for $N = 16$. **a** Overlap of eigenstates with the $|{-}{+}\rangle$ state as a function of their energy E. **b** Entanglement entropy S_{ent} of the eigenstates. Red dots correspond to eigenstates with total spin $S = 1$, while the blue ones ones mark all other spin values. The squares indicate the eigenstates sitting at the top of each tower of states. These towers have an energy separation of approximately $\sqrt{2}$, as expected for the spin-1 hypergrid.

Similar ETH violation can be seen in the entanglement properties of eigenstates, shown in Fig. 5.5**b**, showing that eigenstates of similar energy have very different amounts of entanglement. This broad entanglement distribution, however, can mostly be attributed to the eigenstates belonging to different spin sectors S, giving rise to multiple bands that do not fully overlap at the system size shown in Fig. 5.5**b**. The distribution of entropy in $S = 1$ sector [red points in Fig. 5.5**b**] is relatively narrow apart from two "outliers" shown at energy $E \approx \pm\sqrt{2}$. These two outliers have high-overlap with $|{-}{+}\rangle$ and sit at the top of their respective towers of states when restricting to the sector $S = 1$. The states at the top of each tower are indicated by squares, but

unlike the PXP model [54] these states are not well separated from other states in the same tower.

In a fully ergodic system, one expects the support of an eigenstate on a subset of states to be approximately equal to the ratio of the number of states belonging to this subset and the total dimension of the Hilbert space. Performing this computation for the effective model and choosing the hypergrid subgraph as the subset shows anomalous concentration of some eigenstates – see Fig. 5.6. As the overlap with the $|-+\rangle$ state forms a lower bound to the support on the hypergrid, we find the same kind of towers of states, located at the same energies, in this plot. However, where the maximum overlap with $|-+\rangle$ was approximately 0.011 for $N = 16$, the maximum support on the hypergrid is instead close to 0.76 for the same size. This confirms that the hypergrid subgraph still leaves a large imprint on the eigenstates, even when it only comprises less than 2.5% of the Hilbert space for $N = 16$. This means that there are special eigenstates that are concentrated within the hypergrid, and especially onto the $|-+\rangle$ state. As a consequence, the $|-+\rangle$ state has a large overlap within these states, leading to a permanent concentration of its time-evolved wave-function within the hypergrid. This explains the quench results shown previously.

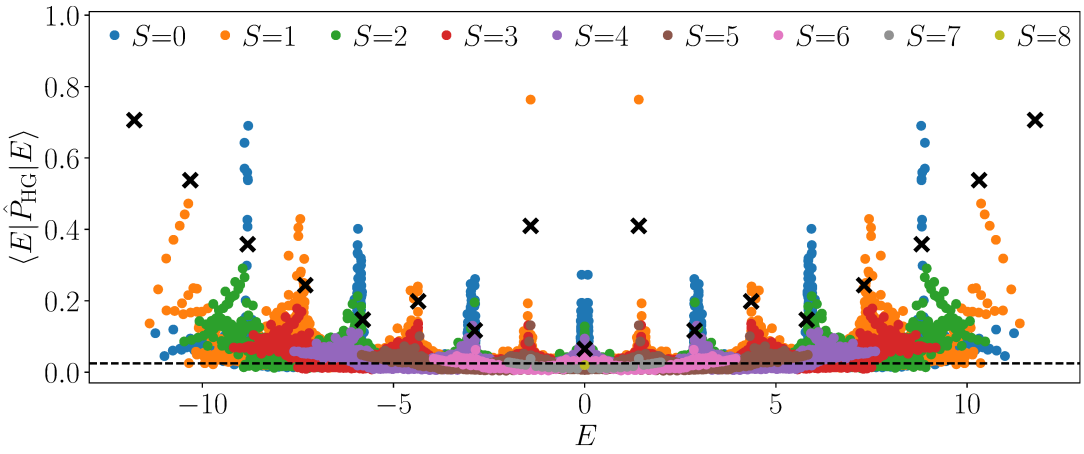

Figure 5.6: Expectation value of the projector onto the hypergrid for the eigenstates at $N = 16$. The colours indicate the value of total spin for each eigenstate and the dashed line is the average value of P_{HG} for the system. Crosses are the states with highest overlap on the $|-+\rangle$ state around their energy, irrespective of spin.

5.5 Algebraic structure and scar-enhancing perturbation

From the graph picture, we can easily develop the su(2) algebra behind scarring. The raising operator is

$$\hat{H}^{+}_{\text{eff}} = \sqrt{2}\sum_{j=1}^{N/4}\hat{c}^{\dagger}_{4j-1,\downarrow}\hat{c}_{4j,\downarrow}\hat{n}_{4j-1,\uparrow}(1-\hat{n}_{4j,\uparrow}) + \sqrt{2}\sum_{j=1}^{N/4}\hat{c}^{\dagger}_{4j,\uparrow}\hat{c}_{4j-1,\uparrow}\hat{n}_{4j-1,\downarrow}(1-\hat{n}_{4j,\downarrow}) + \sqrt{2}\sum_{j=1}^{N/4}\hat{c}^{\dagger}_{4j+1,\uparrow}\hat{c}_{4j+2,\uparrow}\hat{n}_{4j+1,\downarrow}(1-\hat{n}_{4j+2,\downarrow}) + \sqrt{2}\sum_{j=1}^{N/4}\hat{c}^{\dagger}_{4j+2,\downarrow}\hat{c}_{4j+1,\downarrow}\hat{n}_{4j+1,\uparrow}(1-\hat{n}_{4j+2,\uparrow}), \tag{5.15}$$

from which the lowering operator can be derived as $\hat{H}^{-}_{\text{eff}}$. Finally, the Z operator is

$$\hat{H}^{z}_{\text{eff}} = \frac{1}{2}\sum_{j=1}^{N/4}[\hat{n}_{4j-1,\uparrow} - \hat{n}_{4j-1,\downarrow} + \hat{n}_{4j,\downarrow} - \hat{n}_{4j,\uparrow}] + \frac{1}{2}\sum_{j=1}^{N/4}[\hat{n}_{4j+1,\downarrow} - \hat{n}_{4j+1,\uparrow} + \hat{n}_{4j+2,\uparrow} - \hat{n}_{4j+2,\downarrow}]\,. \tag{5.16}$$

While these formulas are rather complicated, their interpretation is actually simple. Essentially, the raising operator $\hat{H}^{+}_{\text{eff}}$ acts as a spin-1 raising operator by generating the transition $|-\rangle \to |0\rangle \to |+\rangle$ on odd cells and $|+\rangle \to |0\rangle \to |-\rangle$ on even cells. Similarly, the $\hat{H}^{z}_{\text{eff}}$ operator acts as $|+\rangle\langle+|-|-\rangle\langle-|$ on odd cells and $|-\rangle\langle-|-|+\rangle\langle+|$ on even cells. This means that the $|-+\rangle$ state is the ground state of $\hat{H}^{z}$ and repeated applications of $\hat{H}^{+}_{\text{eff}}$ on it will lead to the $|+-\rangle$ state. Thus, the algebra is that of a free spin-1, with the correct sign that ensures $|-+\rangle$ and $|+-\rangle$ are the ground and, respectively, ceiling state of $\hat{H}^{z}_{\text{eff}}$.

One notable difference from the PXP model is that the operator $\hat{H}^{x}_{\text{eff}} = \left(\hat{H}^{+}_{\text{eff}} + \hat{H}^{-}_{\text{eff}}\right)/2$ is *not* proportional to the effective Hamiltonian. Indeed, $\hat{H}^{x}$ only encompasses hopping within cells, and not between them. The effective Hamiltonian is then

$$\hat{H}_{\text{eff}} = -J\sqrt{2}\hat{H}^{x}_{\text{eff}} - \hat{H}_{\text{Pert,eff}}, \tag{5.17}$$

where $\hat{H}_{\text{Pert,eff}}$ generates hopping between cells and is defined as

$$\hat{H}_{\text{Pert,eff}} = J\sum_{j=1}^{N/2-1}\sum_{s}\hat{c}^{\dagger}_{2j,s}\hat{c}_{2j+1,s}\hat{n}_{2j,\bar{s}}(1-\hat{n}_{2j+1,\bar{s}}) + \text{h.c.}. \tag{5.18}$$

As such, it is natural to use $\hat{H}_{\text{Pert,eff}}$ as a perturbation to $\hat{H}_{\text{eff}}$, and vary the corresponding perturbation strength λ to tune the scarred revivals. For $\lambda = 1$, the hopping term between the cells in the Hamiltonian and in the perturbation cancel each other. As a result, the hypergrid becomes completely isolated from the rest of the Hilbert space, resulting in perfect wave-function revival. This is confirmed in Figure 5.7. These results also show that the perturbation has a very weak effect on the period of the revivals, but only modulates their amplitude.

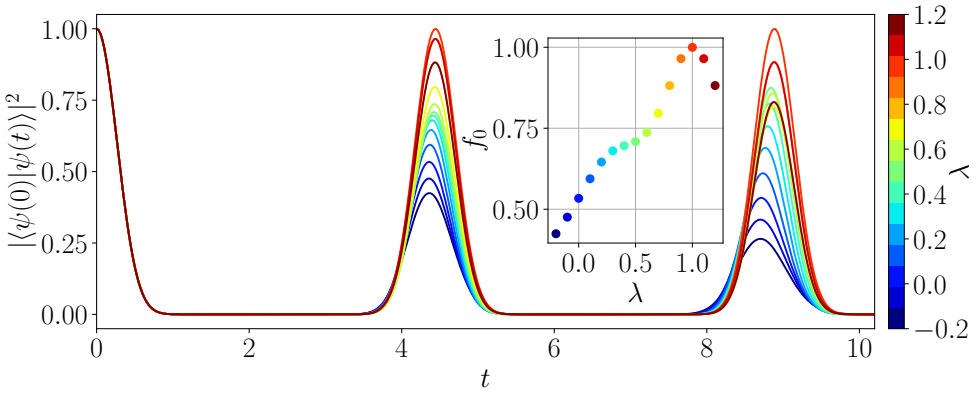

Figure 5.7: Fidelity revivals for the perturbed effective model for $N = 14$. At $\lambda = 1$ the hypergrid subgraph is completely isolated from the rest of the Hilbert space and the revivals from the $|{-}{+}\rangle$ state (and from any other of the hypergrid corners) become perfect.

5.6 Experimental implications

The effective model studied above is exact in the limit $U = \Delta \to \infty$. For experimental realisations, it is important to ascertain that the same physics persists for accessible values of U, Δ. First of all, we can analytically compute the leading order corrections to the effective model at $U = \Delta$ using the Schrieffer-Wolff transformation framework. We find that, at second order, there are both diagonal and off-diagonal terms that affect the Hilbert-space sector of interest. These can be written respectively as

$$\begin{aligned}\hat{H}^{(2)} = \frac{J^2}{\Delta}\sum_{j=1}^{N-1}\Big[&|0\updownarrow\rangle\langle 0\updownarrow| + |\uparrow\updownarrow\rangle\langle\uparrow\updownarrow| + |\downarrow\updownarrow\rangle\langle\downarrow\updownarrow| \\ &+ |0\uparrow\rangle\langle 0\uparrow| + |0\downarrow\rangle\langle 0\downarrow| - \frac{1}{2}\big(|\uparrow\downarrow\rangle\langle\uparrow\downarrow| + |\downarrow\uparrow\rangle\langle\downarrow\uparrow|\big)\Big]\end{aligned} \tag{5.19}$$

and

$$\hat{H}^{(2)}_{\mathrm{OD}} = -\frac{J^2}{\Delta}\sum_{j=1}^{N-2}|\uparrow\updownarrow 0\rangle\langle\updownarrow 0\uparrow| + |\downarrow\updownarrow 0\rangle\langle\updownarrow 0\downarrow| + \frac{J^2}{2\Delta}\sum_{j=1}^{N-1}|\uparrow\downarrow\rangle\langle\downarrow\uparrow| + \mathrm{H.c}\ . \tag{5.20}$$

In order to have a more compact notation, we described the system after the Jordan-Wigner transformation, where all plus and minus signs due to fermionic commutation relations are written explicitly. The indices of all kets and bras have been kept implicit, and we use the convention that the leftmost site is j and the subsequent ones are to its right. This means that $\langle 0\updownarrow\uparrow|$ describes sites j, $j+1$ and $j+2$. As expected, all terms are local and have a prefactor of J^2/Δ, meaning that they can be efficiently suppressed provided U and Δ can reach large enough values.

Importantly, unlike in the Bose-Hubbard case, these second-order terms do not create leakage out of the Hilbert space sector we have investigated. To show that, we

first recall what differentiates terms in this sector to disconnected terms with the same value of $\langle \hat{U} + \hat{\Delta} \rangle$. In the former, all occurrences of doubly-occupied sites must have an empty site on their right. Meanwhile, all states that violate this must be in a different sector. We can look at the different off-diagonal terms individually. Terms in Eq. (5.20) of the form $|\uparrow\updownarrow 0\rangle \langle \updownarrow 0 \uparrow|$ move a $|\updownarrow 0\rangle$ block but do not separate its components. As $|\uparrow\downarrow\rangle \langle\downarrow\uparrow|$ terms only shuffle sites with a single fermion, they also cannot destroy $|\updownarrow 0\rangle$ blocks. So the Hilbert space sector we investigate is still disconnected at second order. In other sectors, additional terms are present such as $|0 \updownarrow\uparrow\rangle \langle\uparrow 0 \updownarrow|$. However, they act as identically zero in the sector of interest and so we do not describe them in detail.

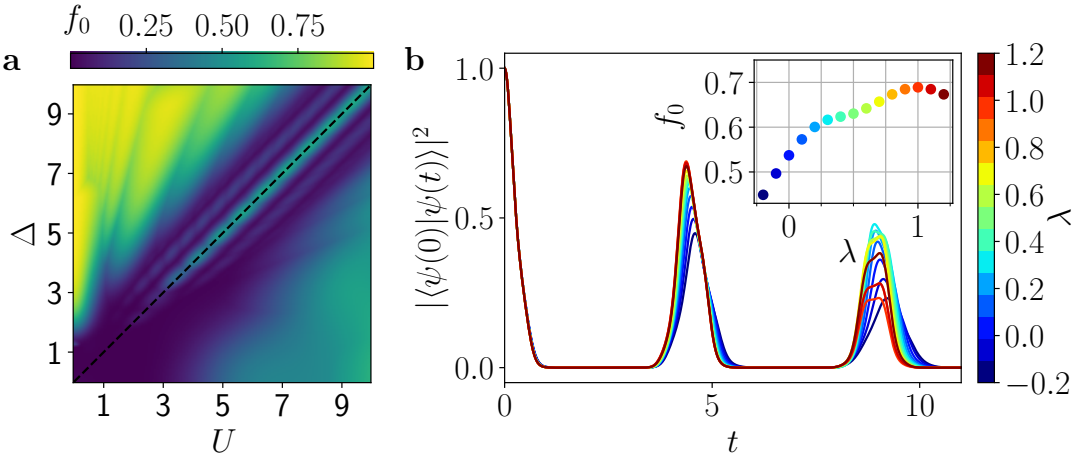

Figure 5.8: Signatures of scarring in fidelity after quenches from the $|{-}{+}\rangle$ state in the full Fermi-Hubbard model for $N = 12$. **a** Maximum revival fidelity in the full model between $t = 1$ and $t = 10$ for a wide range of U and Δ values. The revivals show an increasingly better fidelity on the $U = \Delta$ diagonal as the value of these parameters get larger. The high fidelity in the top left corner corresponds to the high-tilt regime investigated in [222], where a large number of states show revivals due to Hilbert space fragmentation linked to the conservation of the dipole moment. We emphasise that in this regime the large fidelity is not due to scarring but to Hilbert space fragmentation. **b** Fidelity after a quench for different perturbation strengths λ and $U = \Delta = 5$. As for the effective model $\lambda = 1$ gives the best revivals for the this state.

In our analysis of the effective model, we looked at the fidelity of wave-function revivals; here we show that they are also visible in the full model for a relatively broad range of parameters U and Δ, see Fig. 5.8 **a**. As the origin of scarring in the full model should still be the presence of the hypergrid, the perturbation in Eq. (5.18) can also be used. In that case it takes the form

$$\hat{H}_{\text{Pert}} = J \sum_{j=1}^{N/2-1} \sum_{s} \hat{c}^{\dagger}_{2j,s} \hat{c}_{2j+1,s} + \text{h.c.} \tag{5.21}$$

As shown in Fig. 5.8 **b**, the optimal value of λ for the first peak of the fidelity revivals is also at $\lambda = 1$, but the revivals are no longer perfect (the first peak reaches $\sim 70\%$).

Furthermore, unlike in the effective model, looking at the second revival peak gives an optimal value of lambda closer to 0.3. This is likely caused by interactions between the perturbation and the high-order terms in the Schrieffer-Wolff transformation. The fact that this perturbation still significantly improves the revivals in the full model strongly suggests that the oscillatory dynamics is still due to the imprint of the hypergrid in this case.

Finally, as fidelity is generally not accessible in experiment, we now show that scarring can also be detected using local measurements. We demonstrate this in Fig. 5.9 for the full model in Eq. (5.1) focusing on the regime $U, \Delta < 10$. Panel **a** shows the dynamics of imbalance on the even/odd sublattices, $\mathcal{I} = (N_o - N_e)/(N_o + N_e)$, where $N_{e/o}$ is the total number of fermions on the even or odd sites. This observable was chosen as it was used in Ref. [222] to witness Hilbert space fragmentation. The imbalance is bounded between -1 and 1. We see robust oscillations in $\mathcal{I}$ with the frequency matching half the wave-function revival frequency in Fig. 5.3**b**. The amplitude of the imbalance revival remains close to the infinite-limit value for $U = \Delta \gtrsim 6$.

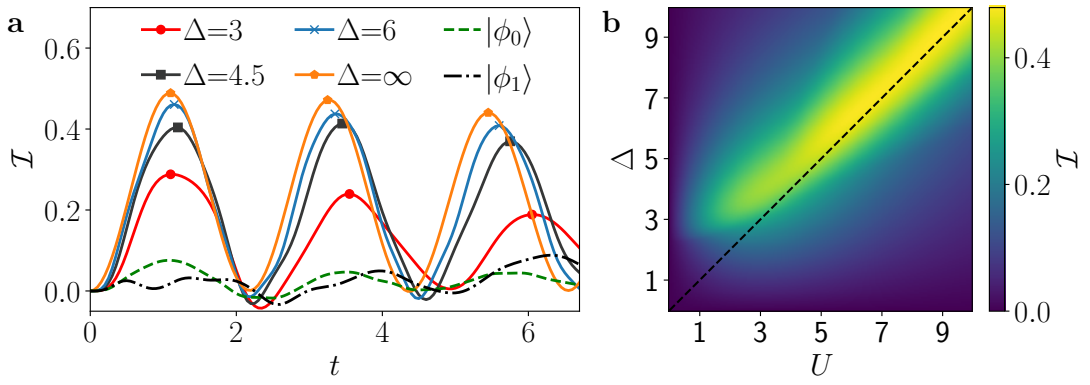

Figure 5.9: **a** Occupation imbalance in the full model in Eq. (5.1) with N=12 for various values of U=Δ for the initial state $|{-}{+}\rangle$, and for U=Δ=6 for the initial states $|\phi_0\rangle = |\uparrow\downarrow\uparrow\downarrow\cdots\uparrow\downarrow\rangle$ (within the hypergrid) and $|\phi_1\rangle = |\downarrow\updownarrow 0\uparrow\updownarrow 0\updownarrow 0\downarrow\updownarrow 0\uparrow\rangle$ (outside of it). **b** $U-\Delta$ phase diagram showing the scarring regime near the diagonal (dashed line). The colour scale represents the value of the first peak of the imbalance for N=12.

5.7 Scarring at half-filling in the large-tilt limit

Up to this point we have exclusively focused on the $U = \Delta$ resonance. We will now show that other regimes can lead to similar constrained models which display scarring. In particular, we will investigate the high-tilt regime $\Delta \gg U, J$ that was investigated experimentally in Ref. [222]. In that limit, the dipole term is effectively conserved and one can similarly write down an effective Hamiltonian. However, unlike in the $U = \Delta$ case, here the leading term appears only at third order. The corresponding effective

Hamiltonian was derived in Ref. [222] and can be written as, up to constant terms,

$$\hat{H}_{\text{eff}}^{\text{dip}} = J^{(3)}\hat{T}_3 + U\Big(1 - \frac{4J^2}{\Delta^2}\Big)\sum_i \hat{n}_{j,\uparrow}\hat{n}_{j,\downarrow} + 2J^{(3)}\hat{T}_{XY} + 2J^{(3)}\sum_{j,s}\hat{n}_{j,s}\hat{n}_{j+1,\bar{s}}, \tag{5.22}$$

where

$$J^{(3)} = \frac{J^2U}{\Delta^2}, \quad \hat{T}_3 = \sum_{i,s}\hat{c}_{i,s}\hat{c}^\dagger_{i+1,s}\hat{c}^\dagger_{i+1,\bar{s}}\hat{c}_{i+2,\bar{s}} + \text{H.c.}, \quad \hat{T}_{XY} = \sum_{i,s}\hat{c}^\dagger_{i,\bar{s}}\hat{c}_{i+1,\bar{s}}\hat{c}^\dagger_{i+1,s}\hat{c}_{i,s}. \tag{5.23}$$

The $\hat{T}_3$ term acts as a "squeezing" operator that creates transitions of the form $|\downarrow 0 \uparrow\rangle \leftrightarrow |0 \updownarrow 0\rangle$. The other dynamical term, $\hat{T}_{XY}$, engineers an XY-type interaction that exchanges fermions of opposite spin between neighbouring sites. Finally, the two potential terms count respectively the number of doubly-occupied sites and the number of neighbouring sites occupied by fermions of different spin.

Due to the rather peculiar form of the dynamical terms, the Hilbert space shows further fragmentation than predicted purely by the conserved quantities (expectation value of the tilt and filling factor). We will now focus on a particular sector characterised by a filling of fraction of $\nu = 1/2$ (with $N/4$ fermions with spin down and $N/4$ with spin up). This sector contains the charge-density wave (CDW) state $|\uparrow 0 \downarrow 0 \uparrow 0 \downarrow 0 \uparrow \cdots 0\rangle$, with fermions of alternating spin on every other site. The effective Hamiltonian projected to the sector of this state can be further simplified by noticing that some terms exactly vanish. The $\hat{T}_3$ operator only allows to squeeze two fermions with opposite spin to create a doublon between them. As all fermions are originally separated by an empty site it is impossible for this operator to reach a state with neighbouring fermions: they will always be either on the same site or with an empty site between them. Hence, the operator $\hat{T}_{XY}$ and the potential terms $\hat{n}_{j,s}\hat{n}_{j+1,\bar{s}}$ are always zero. As the doublon-counting term is diagonal, the only term that allows for hopping between product states is $\hat{T}_3$. By studying the effect of this operator in a 4-site cell we will show that it leads to the same constrained Hilbert space structure as the sector studied at filling $\nu = 1$ in the $U = \Delta$ limit.

For $\nu = 1$ with two sites we have the possible states $|\uparrow\downarrow\rangle \leftrightarrow |\updownarrow 0\rangle \leftrightarrow |\downarrow\uparrow\rangle$ forming a three level system. For $\nu = 1/2$, the operator $\hat{T}_3$ also only allows 3 states but now for four sites as $|\uparrow 0 \downarrow 0\rangle \leftrightarrow |0 \updownarrow 00\rangle \leftrightarrow |\downarrow 0 \uparrow 0\rangle$. In both cases, in each "cell" there are two fermions with opposite spin, and there can only be interactions between cells if fermions of different spin are at the boundaries. As all actions of the Hamiltonian can be understood in terms of these cells, it ensues that both models have *exactly* the same off-diagonal matrix elements if $N_{\nu=1/2} = 2N_{\nu=1}$. The $|-+\rangle$ state we investigate at filling 1 can be directly mapped to the half-filling case by inserting empty sites between every fermion. This is illustrated on Fig. 5.10, which shows equivalent configurations between the two different filling levels and how their respective dynamical operator engineer identical moves.

As a consequence, we can also expect to see scarring in the $\Delta \gg U, J$ and $\nu = 1/2$ regime. One main difference is the presence of an additional diagonal term counting

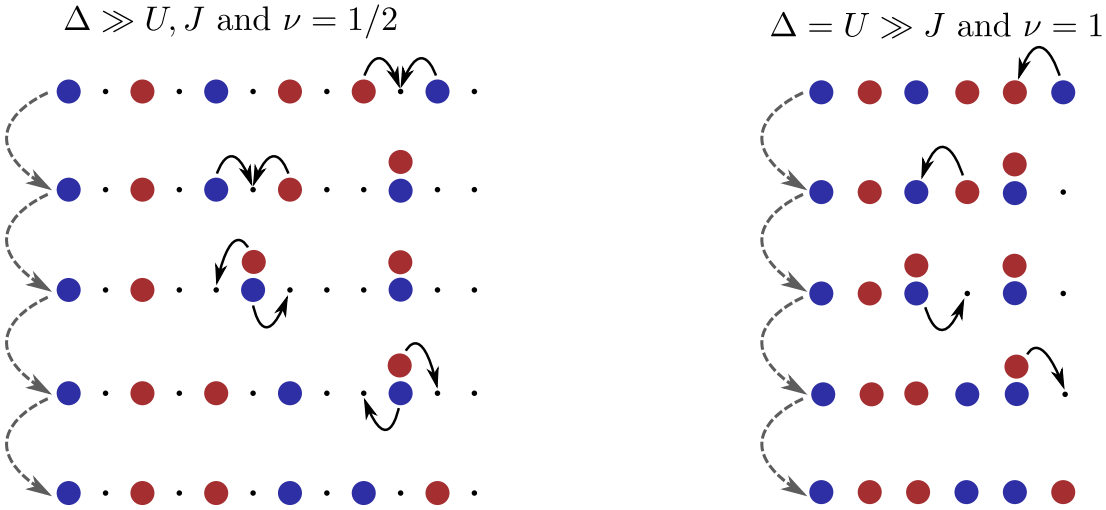

Figure 5.10: Mapping between the $\nu = 1/2$ and $\nu = 1$ sectors of the tilted Fermi-Hubbard model with $N = 12$ and $N = 6$ respectively. Blue and red circles denote fermions with down and up spin respectively, while black dots denote empty lattice sites. A sequence of states that can be induced by the effective Hamiltonian of each model is displayed. In all cases, we see that the order of the fermions is identical.

the number of doublons in that case. To better grasp the consequences of this potential term, it is useful to rewrite the effective Hamiltonian in Eq. (5.22) without the redundant terms (i.e the one that are identically zero in this sector) and with the $J^{(3)}$ prefactor in front. This leads to the compact expression

$$\hat{H}_{\mathrm{CDW}} = J^{(3)}\hat{T}_3 + U\Big(1 - \frac{4J^2}{\Delta^2}\Big)\sum_i \hat{n}_{j,\uparrow}\hat{n}_{j,\downarrow} = J^{(3)}\left[\hat{T}_3 + \Big(\frac{\Delta^2}{J^2} - 4\Big)\sum_i \hat{n}_{j,\uparrow}\hat{n}_{j,\downarrow}\right]. \quad (5.24)$$

As the Hamiltonian in Eq. (5.22) is only valid for $\Delta \gg U, J$, this is also the case for the one in Eq. (5.24). However, it is easy to see that as Δ/J increases, the potential term will dominate the dynamics. Thus, there is no way to obtain the Hamiltonian $\hat{T}_3$ on its own. Set Δ too low and the higher order terms in the Schrieffer-Wolff transformation will not be negligible, set it too high and the potential term will dominate the dynamics. Thus, we conclude that the conditions $\Delta \gg U, J$ and $\nu = 1/2$ will generally lead to worse scarring compared to $\nu = 1$ case we focused on. However, $\nu = 1/2$ may have a practical advantage in that it requires only one large parameter instead of two. Most importantly, this analysis clearly illustrates there are many possibilities for engineering very complex kinetically-constrained models by playing with electron spin, filling factor and parameter regimes of the Fermi-Hubbard model.

5.8 Summary

In this chapter, we have proposed an experimental realisation of QMBSs in the regime $U = \Delta$ of the tilted Fermi-Hubbard model. We have identified product states $|{-}{+}\rangle$,

$|+-\rangle$ at filling factor $\nu = 1$ which give rise to scarred dynamics and reveal towers of ergodicity-breaking many-body eigenstates. To understand the origin of QMBSs in this model, we have developed a new approach inspired by the graph structure of the Hamiltonian matrix, which highlighted the presence of an integrable subgraph isomorphic to that of a free spin-1 paramagnet. This integrable subsystem provides a new type of scarring mechanism that extends beyond the PXP model. Furthermore, the graph picture also allowed us to devise a perturbation that improved the revivals in the quantum dynamics, both in the effective model $U = \Delta = \infty$ and in the full model, at experimentally relevant values of U and Δ. We then showed that QMBS oscillations could be directly probed using observables that are routinely measured in current experiments, such as the density imbalance. Finally, we demonstrated how an analogous subgraph-induced scarring can be observed in a different parameter regime of $\Delta \gg U, J$ at filling factor $\nu = 1/2$.

These results show that the tilted Fermi-Hubbard is a promising model for future investigations of scarring. Our theoretical predictions could be directly tested in current setups, such as the one in Ref. [222] which uses potassium-40 atoms trapped in an optical lattice. In addition, the presence of other ergodicity breaking phenomena such as Hilbert space fragmentation [222] and localisation would allow to study their interplay. Nevertheless, one potential problem is the preparation of the initial state. Indeed, unlike the PXP model (both with Rydberg atoms and in the Bose-Hubbard implementation) where the scarred initial states have period 1 and 2, the $|-+\rangle$ state has period 4, thus it cannot be prepared using two optical lattices with wavelengths λ and 2λ. Given that most setups are currently limited to this type of lattice/superlattice combinations, it makes probing scarring from the $|-+\rangle$ state more challenging than other proposals in this thesis.

We note that subsequent studies have also found relations between subgraphs and QMBSs [229, 230]. In particular, Ref. [230] found that sampling random graphs and their corresponding Hamiltonians led to the appearance of many scarred eigenstates. However, these are generally linked to tail-like structures like the $|\downarrow 2 \uparrow\rangle$ state discussed in this chapter.

5. GRAPH-THEORETIC APPROACH TO QUANTUM MANY-BODY SCARRING IN TILTED FERMI-HUBBARD CHAINS

Chapter 6

Tunable many-body scars on a superconducting quantum processor

In the previous chapter, we argued that QMBSs could be engineered using ultracold fermionic atoms trapped in optical lattices. The main idea was to employ the resonance between the tilt potential and the Fermi-Hubbard interaction, in order to create an effective model with kinetic constraints. The resulting QMBS states stem from a subgraph of the Hamiltonian adjacency graph, which has two important features: it is a highly regular graph on its own and it is weakly connected to the rest of the Hilbert space. Both features were directly enabled by the constraints of the effective model. In this chapter, we will show that a similar subgraph mechanism can be used to create QMBSs in *unconstrained* models implemented on a superconducting (SC) quantum processor. SC qubit arrays are now widely used for both digital and analogue quantum computing and show impressive capabilities [231, 232]. For quantum simulation, they have advantages over cold-atom systems such as compact integration and a high level of control [233, 234]. This granular tunability of the coupling parameters allows to emulate many models with a single device (e.g., the Heisenberg and Ising spin models [235], among others). Moreover, the readout of the SC platform enables direct measurements of important quantities beyond population-related dynamics, such as the entanglement entropy [236], out-of-time-ordered correlation [237, 238], and energy spectrum information [239].

In this chapter, we will explore QMBS phenomena on SC chips with fully tunable XY coupling between nearest-neighbour qubits, fabricated and operated by our experimental collaborators at Zhejiang University [7, 8]. We will focus on two classes of models that host QMBS states. The first type of model draws inspiration from the topological structure of the Su-Schrieffer-Heeger (SSH) model of polyacetylene [240], which features alternating strong and weak XY couplings. Similar to the previous chapter, we will utilise this structure to create a nearly decoupled subgraph with the

structure of a hypercube, that will give rise to emergent QMBS phenomena. Signatures of QMBSs will be confirmed in experiment, with circuits consisting of up to 30 qubits and a Hilbert space dimension of $\binom{30}{15} = 155,117,520$. In contrast to optical lattice experiments in Chapter 4, the capabilities of the SC platform will allow us to perform full quantum state tomography on a subset of 4 qubits. With this, we can extract the subsystem *many-body* fidelity and entanglement entropy, extending beyond the single-site observables in Chapter 4. Furthermore, going beyond 1D geometry, our second model will allow to create tunable QMBSs in a ladder geometry. This will be achieved using a different mechanism – the rainbow scar construction discussed in Chapter 2. The versatility of the rainbow construction will allow to create QMBS eigenstates that are not only robust to disorder, but that can be *tuned* by it.

6.1 Experimental device and the effective XY model

We use a SC quantum processor in a flip-chip package, see Fig. 6.1 for an illustration. The processor contains a square of 6×6 transmon qubits (Q_i), with 60 couplers (Q_c), each inserted in-between two neighbouring qubits. Each qubit (coupler) is effectively a quantum two-level system with ground state $|\circ\rangle$ and excited state $|\bullet\rangle$, whose energy separation can be dynamically tuned in the frequency range $4.3 - 4.8$ GHz ($4.9 - 6.0$ GHz). Each qubit has individual microwave (XY) and flux (Z) controls and is capacitively coupled to a readout resonator for state discrimination. Each coupler has an individual flux (Z) control and remains in the ground state during the experiment. We use high-precision synchronised analogue signals to control the qubits and couplers, with microwave pulses for qubit XY rotations and state readout, and square flux pulses for tuning the qubit and coupler frequencies. A complete experimental sequence consists of three stages: (1) state preparation where single-qubit $\boldsymbol{\pi}$ pulses are applied to half of the qubits, (2) multi-qubit interaction stage where the nearest neighbouring qubit couplings are programmed by adjusting the frequencies of the couplers, and (3) the measurement stage where all qubits are jointly read out. The mean values of the singe-qubit energy relaxation times and Ramsey dephasing times are respectively $T_1 = 53.4$ μs and $T_2^\star = 1.9$ μs, while the mean of the single-qubit randomised benchmarking fidelities is 0.993.

We first derive the effective spin-1/2 XY model describing our experimental SC processor. The full Hamiltonian of the SC system with both qubits and couplers is given by [241]

$$\begin{aligned}\hat{H}_{\text{full}} = &\sum_i (\omega_i \hat{b}_i^+ \hat{b}_i^- + \frac{\eta_i}{2} \hat{b}_i^+ \hat{b}_i^+ \hat{b}_i^- \hat{b}_i^-) + \sum_c (\omega_c \hat{b}_c^+ \hat{b}_c^- + \frac{\eta_c}{2} \hat{b}_c^+ \hat{b}_c^+ \hat{b}_c^- \hat{b}_c^-) \\ &+ \sum_{\langle i,j \rangle} g_{ij} (\hat{b}_i^- \hat{b}_j^+ + \hat{b}_j^- \hat{b}_i^+) + \sum_{\langle i,c \rangle} g_{ic} (\hat{b}_i^+ \hat{b}_c^- + \hat{b}_i^- \hat{b}_c^+),\end{aligned} \tag{6.1}$$

where ω_i (ω_c) is the frequency of the ith qubit (cth coupler), $\hat{b}_i^+$ ($\hat{b}_i^-$) is the creation (annihilation) operator of Q_i, g_{ij} (g_{ic}) is the coupling strength between Q_i and Q_j (Q_c), and the rotating wave approximation is imposed on the qubit-coupler and qubit-qubit

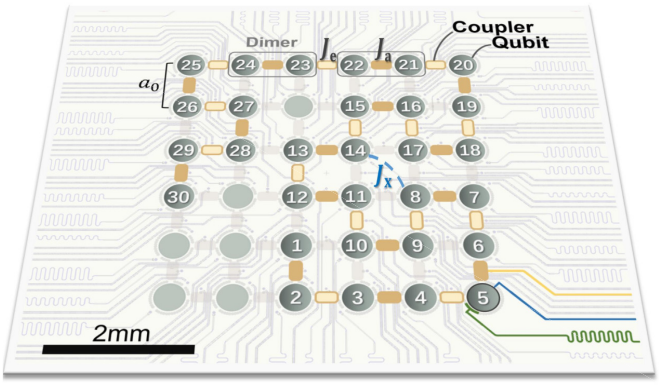

Figure 6.1: Experimental superconducting circuit of Device I with qubits and couplers in a square geometry. Light gray dashed rectangles represent dimers that constitute the chain with intra coupling J_a, inter coupling J_e, and small cross coupling J_x.

couplings. The subscripts "i, j" and "c" represent the indices of qubits and couplers, respectively. $\langle i, j\rangle$ or $\langle i, c\rangle$ stands for a nearest-neighbour qubit-qubit or qubit-coupler pair.

While each qubit can technically hold more than one photon (which are the excitations in our system), in our experiment the anharmonicity η_i is much larger than the couplings between the nearest neighbouring qubits (typically $\eta_i/g_{ij} > 50$). As a consequence, any double occupancy is strongly suppressed. The degrees of freedom can therefore be treated as spin-1/2, and we can replace the bosonic creation and annihilation operators by the Pauli operators $\hat{\sigma}^+$ and $\hat{\sigma}^-$. The full Hamiltonian (6.1) then reduces to the XY Hamiltonian:

$$\hat{H} = \sum_i \omega_i \hat{\sigma}_i^+ \hat{\sigma}_i^- + \sum_c \omega_c \hat{\sigma}_c^+ \hat{\sigma}_c^- + \sum_{\langle i,j\rangle} g_{ij}(\hat{\sigma}_i^- \hat{\sigma}_j^+ + \hat{\sigma}_j^- \hat{\sigma}_i^+) + \sum_{\langle i,c\rangle} g_{ic}(\hat{\sigma}_i^+ \hat{\sigma}_c^- + \hat{\sigma}_i^- \hat{\sigma}_c^+). \tag{6.2}$$

We apply the Schrieffer-Wolff transformation [47] $\mathcal{U} = e^{\mathcal{W}}$ to the Hamiltonian with

$$\mathcal{W} = \sum_c \sum_i \frac{g_{ic}}{\Delta_{ic}} (\hat{\sigma}_i^+ \hat{\sigma}_c^- - \hat{\sigma}_i^- \hat{\sigma}_c^+), \tag{6.3}$$

since all qubits are far detuned from the couplers with $|\Delta_{ic}| = |\omega_i - \omega_c| \gg |g_{ic}|$. The effective Hamiltonian can then be approximated as

$$\hat{H}_{\text{eff}} \approx \sum_{\langle i,j\rangle} J_{ij}(\hat{\sigma}_i^- \hat{\sigma}_j^+ + \hat{\sigma}_i^+ \hat{\sigma}_j^-) + \sum_i \Omega_i \hat{\sigma}_i^+ \hat{\sigma}_i^-, \tag{6.4}$$

where the effective coupling strength and transition frequencies are, respectively, given by

$$J_{ij} = g_{ij} + \sum_c g_{ic} g_{jc} \Big[\frac{1}{\Delta_{ic}} + \frac{1}{\Delta_{jc}}\Big] \quad \text{and} \quad \Omega_i = \omega_i + \sum_c \frac{g_{ic}^2}{\Delta_{ic}}. \tag{6.5}$$

The strength of the indirect coupling can be tuned by adjusting the coupler frequency, so the net coupling strength for J_{ij} can be dynamically tuned over a wide range, typically $J_{ij}/2\pi \in [-15, 1]$ MHz.

6.2 One-dimensional XY model

We consider the model described by Eq. (6.4) where the qubits follow a "snake"-like layout shown in Fig. 6.1. This layout allows us to accommodate a 1D chain of length L of up to 30 qubits on the given device. The qubits $2i-1$ and $2i$ (with $i=1$ to $L/2$) are grouped into dimers, with the intra-dimer coupling $J_{i,i+1}=J_a$, $i\in$ odd, set to be slightly stronger than the inter-dimer coupling $J_{i,i+1}=J_e$, $i\in$ even. This pattern of couplings along the chain reproduces the structure of the SSH model [240], with the Hamiltonian

$$\hat{H}=J_a\sum_{j=1}^{L/2}(\hat{\sigma}^-_{2j-1}\hat{\sigma}^+_{2j}+\hat{\sigma}^+_{2j-1}\hat{\sigma}^-_{2j})+J_e\sum_{j=1}^{L/2-1}(\hat{\sigma}^-_{2j}\hat{\sigma}^+_{2j+1}+\hat{\sigma}^+_{2j}\hat{\sigma}^-_{2j+1}). \tag{6.6}$$

We consider an even number of sites, such that the Hamiltonian is invariant under spatial reflection that takes site i to site $L+1-i$. Eq. (6.6) also conserves the number of excitations, and we will restrict our study to half-filling, meaning that there are $L/2$ excitations. In that case, as all couplings are of XY type, the model is also invariant under particle-hole transformation $\circ\leftrightarrow\bullet$.

The chain above only features hopping between nearest-neighbours, hence it maps to a fermionic model with only quadratic terms. As such, the model Eq. (6.6) is integrable and it can be expressed in terms of free fermions. Nonetheless, recent studies of the quench dynamics from certain initial states, such as the fully polarised and Néel states [242, 243], have shown that the integrability of the model generally does not imply persistent revivals. Below we will show that it is possible to identify, based on the graph structure of the Hamiltonian, other initial states that *do* exhibit quantum revivals, even after we make the system interacting and break integrability. Indeed, on top of the nearest-neighbour couplings J_a and J_e, there is also non-negligible hopping between qubits placed diagonally from each other in Fig. 6.1. These couplings are also of XY type and are essentially random in strength in a range $J_x/2\pi\in[0.3,1.2]$ MHz. This breaks integrability and spatial reflection in the physical device.

6.2.1 Embedded hypercubic subgraph and signatures of scarring

Beyond the free-fermionic limit, there is another limit in which the SSH chain turns into a non-interacting model. In the limit of $J_a\gg J_e$, each dimer only weakly interacts with its neighbours. The dynamics is dominated by intra-dimer hopping, i.e., transitions between $|\mathrm{d}_+\rangle=|\bullet\circ\rangle$ and $|\mathrm{d}_-\rangle=|\circ\bullet\rangle$. If we start in a state with a single photon in each dimer, we will have very low connectivity to any state with dimers containing zero or two photons. The relevant part of the Hilbert space is the span of all states with a single photon per dimer. Each dimer then acts as a two-level system ($|\mathrm{d}_+\rangle$ and $|\mathrm{d}_-\rangle$), and the Hamiltonian is isomorphic to that of a free spin-1/2 paramagnet, i.e $\hat{H}_{\text{free}}=\sum_j\hat{\sigma}^x_j$. Such a Hamiltonian is known to lead to perfect state transfer and revivals from many initial states. But this effect is not "many-body", as the dimers do not interact with each other. Another useful property of this Hamiltonian is the

structure of its adjacency graph. As in the previous chapter, let us use one vertex for each Fock basis state and draw an edge between two of them if there is a non-zero matrix element between them in the Hamiltonian. For the non-interacting Hamiltonian in the $J_a \gg J_e$ limit, this adjacency graph takes the form of a hypercube of dimension $N = L/2$, as each dimer can have two states and there are $L/2$ of them.

When we move away from the limit $J_a \gg J_e$, the assumption that the dimers are non-interacting is no longer valid and we have to consider the entire Hilbert space. The adjacency graph of the full Hamiltonian acquires a non-trivial structure, but it still contains the hypercube as a subgraph. Note that as we have coupling with strength J_a and J_e, the graph is now weighted. The hypercube has many edges connecting it to the rest of the Hilbert space (all with weight J_e), which has a negative effect on the revivals from most states inside the hypercube. Typically, we find the dynamics becomes ergodic, with the wave-function spreading into the entire Hilbert space. However, not all states with one photon per dimer have the same leakage out of the hypercube. Two states that are very anomalous in this respect are the states

$$|\Pi\rangle = |\mathrm{d}_+\mathrm{d}_-\mathrm{d}_+\mathrm{d}_-\cdots\rangle, \quad \text{and} \quad |\Pi'\rangle = |\mathrm{d}_-\mathrm{d}_+\mathrm{d}_-\mathrm{d}_+\cdots\rangle. \tag{6.7}$$

These states are located at opposite corners of the hypercube and have the unique property of only having intra-dimer couplings. This can be seen by explicitly writing out the action of the Hamiltonian on pairs of dimers

$$\hat{H}|\mathrm{d}_+\mathrm{d}_-\rangle = \hat{H}|\bullet\circ\circ\bullet\rangle = J_a\left(|\circ\bullet\circ\bullet\rangle + |\bullet\circ\bullet\circ\rangle\right) = J_a\left(|\mathrm{d}_-\mathrm{d}_-\rangle + |\mathrm{d}_+\mathrm{d}_+\rangle\right), \tag{6.8}$$

$$\hat{H}|\mathrm{d}_-\mathrm{d}_+\rangle = J_a\left(|\mathrm{d}_-\mathrm{d}_-\rangle + |\mathrm{d}_+\mathrm{d}_+\rangle\right). \tag{6.9}$$

In both cases, the dimers always have a single photon. This property strongly reduces the leakage out of the hypercube and allows the revivals from these two state to persist outside of the trivial regime $J_a \gg J_e$. We note that, in contrast to the model investigated in the previous chapter, the existence of states with no leakage outside the hypercube is not due to strong kinetic constraints. It can instead be understood simply from the locality of the hopping and the geometry of the lattice. As such, the same kind of subgraph persists in other lattice geometries, e.g., the comb geometry [7].

To quantify the impact of the hypercube on the dynamics, note that the sum of the hypercubic-thermal couplings (inter dimer and cross couplings) gives the decay rate Γ of the hypercube to the thermal parts. The summation of intra hypercubic couplings Δ is given by the number of hypercubic edges, $\Delta = N2^{N-1}J_a$. Their ratio Δ/Γ converges to a finite value for different values of J_a/J_e, see Fig. 6.2 **a**, which shows that the hypercube is *not* trivially disconnected from the rest of the Hilbert space. At the same time, while other parts of the Hilbert space are frustrated by the irregular J_x couplings, no two states within the hypercube are linked by them. Thus these couplings lead to increased leakage out of the hypercube, but do not disturb the dynamics within it. Indeed, as the J_x connect sites with a distance of at least two in the chain, they cannot be intra-dimer. As a consequence, if we start from a state in the hypercube and act with a J_x coupling, it will take a photon from one dimer to another dimer. Hence, we

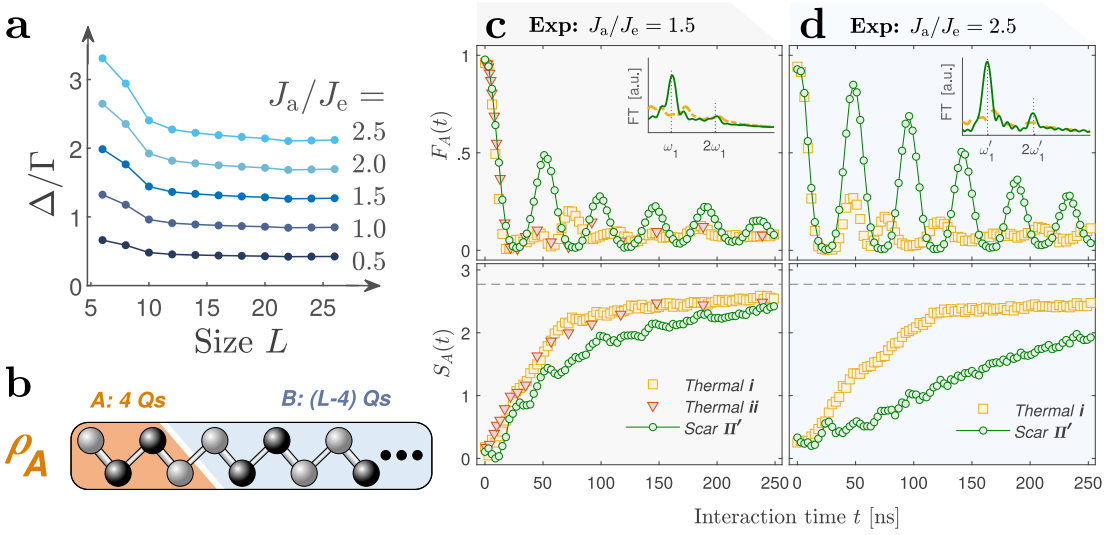

Figure 6.2: **a** Ratio Δ/Γ as a function of the system size L evaluated numerically for different ratios of J_a/J_e and the experimentally measured values of J_x. **b** Schematic of the bipartition of the system. Tomography is performed on the first four qubits forming subsystem A. **c** Quantum state tomography for the four-qubit fidelity $F_A(t)$ and entanglement entropy $S_A(t)$ in a 30-qubit chain for thermalising initial states, $|\circ\bullet\circ\bullet\ldots\circ\bullet\bullet\circ\rangle$ (labelled as "i") and $|\circ\bullet\circ\circ\bullet\ldots\bullet\circ\circ\bullet\bullet\circ\bullet\bullet\circ\rangle$ ("ii") and the QMBS state Π' (green). The couplings are $J_a/2\pi = 1.5J_e/2\pi \simeq -9$ MHz. The inset shows the Fourier transform of the four-qubit fidelity with the peak at $\omega_1/2\pi \approx 21$ MHz. The dashed grey line in the bottom panel represents the maximal thermal entropy for the subsystem, equal to $4\ln(2)$. **d**: Same as **c**, but for different couplings $J_a/2\pi = 2.5J_e/2\pi \simeq -10$ MHz from Device II and $\omega_1'/2\pi \approx 22$ MHz.

will no longer be in the hypercube, which is characterised by all dimers having a single photon.

After these theoretical considerations, in Fig. 6.2**c-d** we present the experimental observations of QMBS states in our SC processor. With the high-precision control and readouts, we were able to perform tomography measurements to directly obtain elements of the reduced density matrix of subsystem A, $\hat{\rho}_A$, which determine the fidelity dynamics of the subsystem $F_A(t)$ and the bipartite entanglement entropy $S_A(t)$. The fidelity and entanglement entropy of a subsystem are respectively defined as $F_A(t) = \mathrm{Tr}\left[\hat{\rho}_A(0)\hat{\rho}_A(t)\right]$ and $S_\mathrm{A}(t) = -\mathrm{Tr}\left[\hat{\rho}_A(t)\log\hat{\rho}_A(t)\right]$. The complexity of such measurements grows rapidly with the size of the subsystem A and below we consider A to be four qubits, as schematically illustrated in Fig. 6.2**b**. We emphasise that although we consider a relatively small subsystem here, the four-qubit fidelity F_A mirrors the behaviour of the full fidelity. The data points in Fig. 6.2**c** give, for a 30-qubit chain, the time evolution of the four-qubit fidelity for the collective state $|\Pi'\rangle$ and two typical thermalising states. The fidelity of the QMBS state exhibits revivals with the period of about 50 ns and the peak value of the first revival can be as high as 0.5, while no such revivals occur for the thermalising states.

In the bottom panel of Fig. 6.2**c** we measure the time evolution of the entanglement

entropy $S_A(t)$ for the same states as in the upper panel. Compared to the thermalising states, scarred dynamics leads to a slightly slower growth of entanglement entropy, superposed with oscillations whose frequency is twice that of fidelity revivals. This double frequency is due to the fact that the system oscillates between the $|\Pi'\rangle$ and $|\Pi\rangle$ states. Thus, entropy is locally minimised or maximised (depending on the choice of subsystem) when the system is near either of these states, while the fidelity only measures the return to its initial state $|\Pi'\rangle$. In our experiment, both scarred and thermalising states ultimately approach the Page entropy $4\ln(2)$ of the 4-qubit subsystem.

We note that scarring, and in particular the difference in *rate* of entanglement entropy growth between the scarred vs. thermalising initial states, can be improved by increasing the coupling ratio J_a/J_e to 2.5, as experimentally demonstrated by Fig. 6.2**d**. This ratio controls the coupling of the hypercube to the rest of the Hilbert space, as we emphasised above. For the data in Fig. 6.2**d**, we have used a second superconducting chip (Device II) with a similar design as the first. Indeed, some couplings in Device I could not be tuned to large enough frequencies to engineer the ratio $J_a/J_e = 2.5$ on 30 qubits. The geometry and design of both devices are identical, with device II showing longer single-qubit energy relaxation time $T_1 = 101.0\ \mu$s.

6.2.2 Integrability-breaking perturbations

In order to show that $|\Pi\rangle$, $|\Pi'\rangle$ are *bona fide* QMBS states, it is crucial to demonstrate that revivals from $|\Pi\rangle$, $|\Pi'\rangle$ states are not trivially due to the integrability of the SSH chain in Eq. (6.6). Thermalisation in our setup is naturally induced by the irregular cross couplings J_x with strengths $J_x(i,j)/2\pi \in [0.3, 1.2]$. The exact values of these couplings have been measured in Device I and are given in Fig. 6.3. Due to their

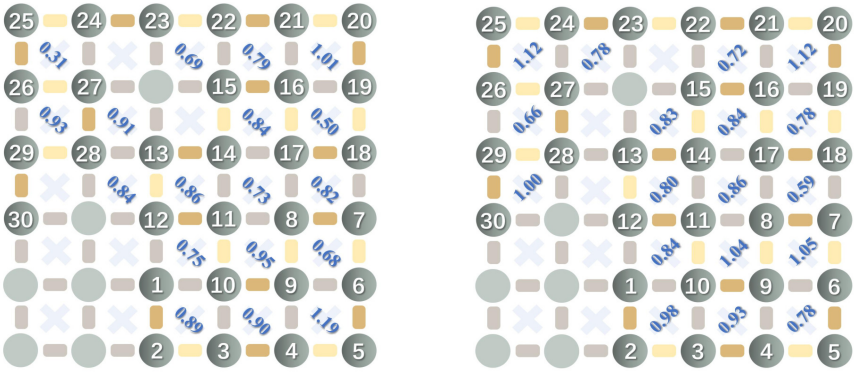

Figure 6.3: The dominant cross coupling values $J_x/2\pi$ in MHz from experimental measurements.

random nature, it is clear that they break any spatial symmetry of the circuit as well as making it non-integrable. Indeed, due to their long-range nature (they connect sites with labels j and k with $|j-k| > 1$) they cannot be mapped to quadratic fermionic

operators due the Jordan-Wigner string of $\hat{\sigma}^z$ that should be present between the two sites. As such the system is expected to thermalise.

To confirm thermalisation, we numerically compute the average energy level-spacing ratio $\langle r \rangle$ for various system sizes and strengths of the J_x couplings. For a chaotic system, we expect $\langle r \rangle \approx 0.53$. For an integrable system, the usual value given is $\langle r \rangle \approx 0.39$. However this assumes that all energies are independent, which is usually not the case in non-interacting models. Indeed, as the many-body spectrum is composed of combinations of the single-body spectra, its structure can actually favour degeneracies. This leads to an average level-spacing ratio lower than 0.39. As we are only interested in distinguishing the integrable and non-integrable regimes and not in the precise structure in the integrable case, we will treat all values of $\langle r \rangle$ smaller than 0.38 as equal to 0.38. Using this convention, the results for $\langle r \rangle$ are shown in Fig. 6.4 and confirm our expectation: as the mean J_x gets larger, we see a rapid transition from integrability to chaos. At the same time, large J_a/J_e ratio brings us closer to integrability because the system becomes essentially a set of non-interacting dimers. As the system size gets larger, it becomes more sensitive to perturbations, requiring a larger J_a/J_e ratio and smaller J_x to be close to integrability. Already at $L = 16$, we see that the regime used in the experiment is deep in the chaotic phase with $\langle r \rangle \approx 0.53$. This means that at $L = 30$ there should be no effect due to proximity to integrability.

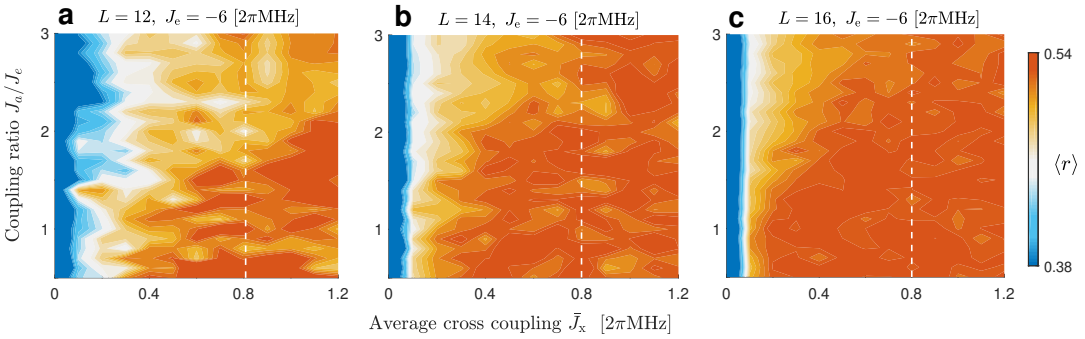

Figure 6.4: Average energy level spacing parameter $\langle r \rangle$ as a function of the coupling ratio J_a/J_e and average cross coupling $\bar{J}_x$ for system sizes **a** 12, **b** 14 and **c** 16 qubits. For clarity the values of $\langle r \rangle$ are limited to the range $[0.38, 0.54]$, meaning that any value below 0.38 is set to 0.38 and any value above 0.54 is set to 0.54. $J_e/2\pi$ is fixed at -6 MHz. The white dashed lines denote the average value of J_x in our experiments.

As conclusive evidence that revivals we see are not linked to the integrability of the SSH chain, we devise a regular perturbation that *enhances* revivals while breaking integrability. For that we turn on the next-next-nearest-neighbour couplings $J_{\text{nn}} = J_{i,i+3}$, such that the following Hamiltonian is added to the SSH chain:

$$\hat{H}_{\text{nn}} = J_{\text{nn}} \sum_{j=1}^{L-3} \left(\hat{\sigma}_j^+ \hat{\sigma}_{j+3}^- + \hat{\sigma}_{j+3}^+ \hat{\sigma}_j^- \right), \tag{6.10}$$

Note that this perturbation is translation-invariant (i.e., there is no disorder) and pre-

serves the reflection symmetry as well as the particle-hole symmetry. Fig. 6.5**a** shows that for $J_a/J_e = 1.5$, scarring is present for a relatively broad range of values of J_{nn}, and that it is most prominent not at $J_{\mathrm{nn}} = 0$ but at $J_{\mathrm{nn}}/J_e \approx -0.21$. Meanwhile, Fig. 6.5**b** shows that a small J_{nn} is enough to break integrability. As for the J_x coupling, the J_{nn} terms induce long-range hopping and so cannot be mapped to quadratic fermionic operators. Thus the perturbed model no longer maps to free fermions and is not integrable. The values of $\langle r \rangle$ smaller than 0.39 that can be seen on Fig. 6.5 **b** at $J_{\mathrm{nn}} = 0$ are due to the system being non-interacting at that point, as discussed in the previous paragraph.

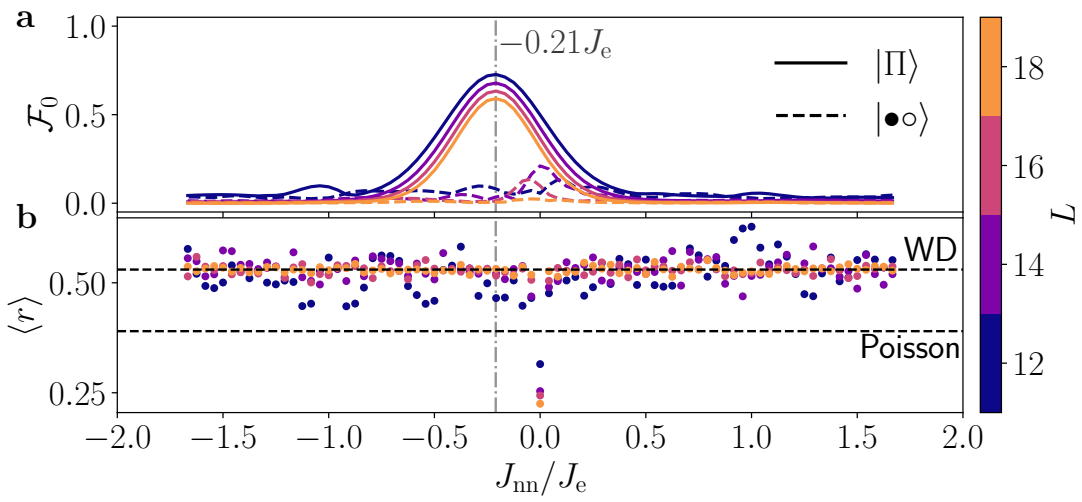

Figure 6.5: SSH chain with $\hat{H}_{\mathrm{nn}}$ perturbation and no cross coupling J_x. The parameters used are $J_a/2\pi = -9$ MHz and $J_e/2\pi = -6$ MHz. **a**, Fidelity at the first revival peak $F(t_1)$ for the $|\Pi\rangle$ and $|\bullet\circ\rangle = |\bullet\circ\ldots\bullet\circ\rangle$ states for different systems sizes L and perturbation strengths in units of J_e. **b**, Average level-spacing ratio for the same data in the sector with eigenvalues $+1$ for both spatial reflection particle-hole exchange. The vertical dash-dotted line indicates the optimal points for revivals from the $|\Pi\rangle$ state, while the horizontal dashed lines indicate the expected value of $\langle r \rangle$ for Poisson and Wigner-Dyson distributions.

While it is easy to see how the J_{nn} perturbation breaks integrability, at first glance it is unclear why it should improve the revivals. Indeed, it induces hopping between different dimers, and as such creates additional leakage out of the hypercube. In particular, it induces leakage out of the initial states $|\Pi\rangle$ and $|\Pi'\rangle$. However, if we look at other states during the dynamics we will see that it can cancel the leakage induced by J_e. Let us consider an example with $L = 4$. If we start from the $|\Pi\rangle$ state and only consider the wave-function within the hypercube, after a quarter of a period the wave-function should be approximately $(|\bullet\circ\rangle + i\,|\circ\bullet\rangle)(|\bullet\circ\rangle - i\,|\circ\bullet\rangle)/2$ up to an overall phase. Acting on this state with inter-dimer hopping (which acts between sites 2 and 3) gives $J_e(|\bullet\bullet\circ\circ\rangle + |\circ\circ\bullet\bullet\rangle)/2$. Meanwhile, acting with the J_{nn} perturbation (which acts between sites 1 and 4) will give the same term $J_{\mathrm{nn}}(|\bullet\bullet\circ\circ\rangle + |\circ\circ\bullet\bullet\rangle)/2$ but with a

different prefactor. It is then clear that setting $J_{\mathrm{nn}} = -1$ will exactly cancel the leakage from this state. So the optimal value of J_{nn} is a trade-off between the additional leakage from certain configurations and the enhanced leakage from other ones. While we were not able to analytically derive the value of $-0.21J_e$ found numerically, it is coherent with this picture of leakage that predicts an optimal J_{nn} between $-J_e$ and 0. It also explains why fidelity decays monotonically for J_{nn}/J_e positive, as this increases leakage from all configurations.

6.2.3 Population dynamics

Now that we have shown that the revivals are caused by genuine many-body scarring, we provide additional experimental data on qubit population dynamics. Such measurements are more time-saving than tomography, and this allows us to further probe thermalisation of the entire many-body system by randomly choosing many initial product states. The evolution of the occupation probability for individual qubits in a 30-qubit chain is shown in Figs. 6.6**a** and 6.6**b**, which contrasts the evolution of a scarred initial states with a typical thermalising state. The former exhibits remarkable oscillations which are absent in the latter.

In order to define a global marker of thermalisation, we turn towards the generalised population imbalance

$$I(t) = \frac{1}{L}\sum_{i}^{L}\langle\hat{\sigma}_i^z(0)\rangle\langle\hat{\sigma}_i^z(t)\rangle. \tag{6.11}$$

For any Fock state, this observable acts as an indicator of the memory of the initial state. Indeed, $I(t)$ will be exactly one only for the initial Fock state and should thermalise to a value of 0 as photons should be on any site with equal probability. For the scarred initial states, $I(t)$ is expected to display the same type of oscillation as the many-body fidelity, while for a thermalising state it should quickly decrease towards 0. The imbalance dynamics $I(t)$ is plotted in Figs. 6.6**c** and 6.6**d**, which reveals more clearly the differences between two initial states. In general, for the thermalising state, after about 30ns the population is nearly half photon in each qubit, meaning there is no imbalance.

The distinct features of QMBS states can be further highlighted through the overlap between the product states and the eigenstates $|\langle\alpha|E_n\rangle|^2$. For scarred initial states, we expect to see towers of states with approximate equal spacing. Meanwhile, for thermalising initial state this overlap should homogeneous among all eigenstates. While this quantity is not accessible in experiment, we can probe it indirectly by looking at the Fourier spectrum of the imbalance. This is shown in Figs. 6.6**e** and 6.6**f** for the $|\Pi\rangle$ state and thermalising states respectively. For the former, there is very sharp peak in the squared Fourier amplitude $g_\alpha(\omega)$ at $\omega_1/2\pi \approx 20$ MHz indicating that the towers of states have approximately that spacing. In the case $J_e = 0$, we would expect the peak to be at $2J_a/2\pi \approx 18.6$ MHz, so we see that the presence of the rest of the Hilbert space has an influence on the energy spacing. For a thermalising state, we see no clear peak in the Fourier amplitude, as expected form the lack of periodic behaviour

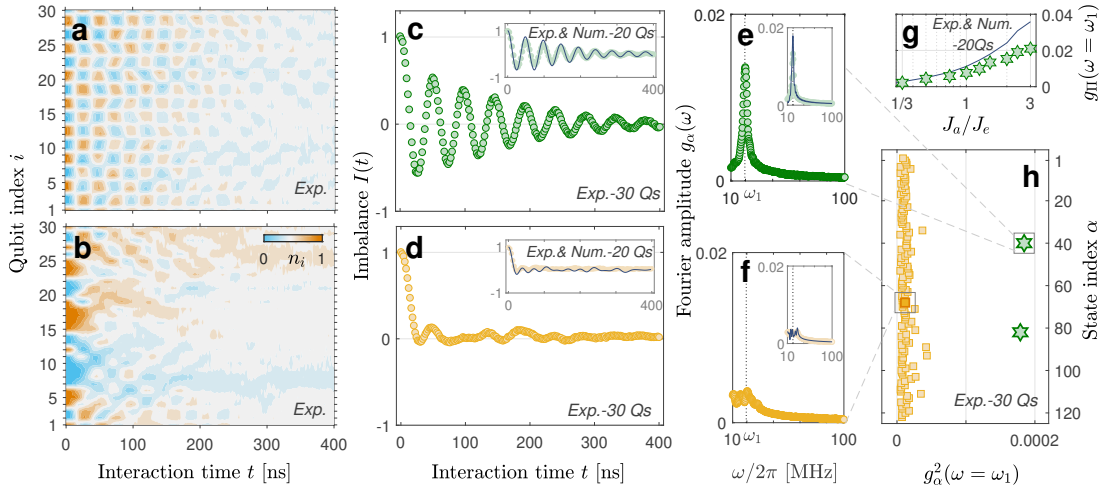

Figure 6.6: Qubit population dynamics observed in experiment on Device I. **a**-**b**, Contour diagrams of the experimental qubit population as a function of the interaction time for a scarred state and a rapidly thermalising state, respectively. **c**-**d**, Generalised imbalance $I(t)$ extracted from plots **a** and **b** as a function of the interaction time. Insets: imbalance dynamics from experiments (circles) and numerical simulations (solid curves) in a 20-qubit chain. **e**-**f** Fourier transform amplitude of the imbalance in **c**-**d**, which characterises the squared overlap between the initial states and the energy eigenstates. The time window for the fast Fourier transform is extended to 4 μs with zero padding. **g** Fourier peak as a function of the coupling ratio J_a/J_e in a chain of $L = 20$ from experimental measurements (green hexagrams) and numerical simulations (solid curve). **h** The squared Fourier amplitude $g^2_\alpha(\omega = \omega_1)$ of $|\alpha\rangle$ for 120 randomly chosen initial product states, including two QMBS states (green hexagrams) that clearly stand out from the rest of thermalising product states (yellow squares). The simulation parameter values in panels **c**-**f** are $J_a/2\pi = -9.3$ MHz, $J_e/2\pi = -6.1$ MHz and $J_x/2\pi \in [0.3, 1.2]$ MHz.

of the imbalance. We also test 120 random initial product states and find that their squared Fourier amplitudes $g^2_\alpha(\omega = \omega_1)$ are unambiguously distinct from those of the $|\Pi\rangle$ state, as shown in Fig. 6.6**h**. Note that, for the cases in Figs. 6.6**a**-**f**, full numerical diagonalisation of the system is not possible due to the large Hilbert space. To validate the experimental data numerically, it is necessary to use a smaller system size, say $L = 20$, whose results are shown in the insets in Figs. 6.6 **c**-**f**, where the agreement between numerical and experimental results is excellent.

The advantage of our experimental system – the tunable effective couplings between two nearest-neighbour qubits – allows us to systematically probe the stability of QMBS states as the ratio of intra- and inter-dimer couplings J_a/J_e is varied. As shown in Fig. 6.6**g**, both the numerical and experimental results indicate that QMBS states emerge consistently in the regime of $J_a/J_e \gtrsim 1$. Also, even for a chain with uniform nearest-neighbouring couplings (J_a/J_e=1), the value of $g_\Pi(\omega_1) \approx 0.008$ is significant compared to the average value of thermal states around 0.0035 in Fig. 6.6**h**. This implies that scarring is not trivially induced by the unbalance between intra-dimer and inter-dimer couplings since this value difference ~ 0.0045 is significantly above the

measurement standard deviations. In the regime of large coupling ($J_{a,e}/2\pi > 12$ MHz), the effective Hamiltonian describing our system [see Eq. (6.4)] is no longer accurate due to the population leakage to couplers.

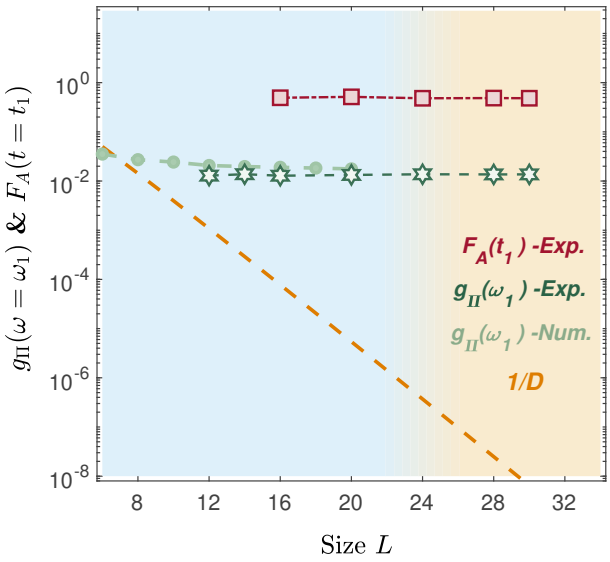

Figure 6.7: Scaling behaviour of the first revival peak $F_A(t_1 \approx 52\text{ns})$ of the subsystem A, Fourier amplitude $g_\Pi(\omega_1)$, and the inverse Hilbert space dimension $1/D$ versus the system size for $J_a/2\pi \simeq -9$ MHz and $J_e/2\pi \simeq -6$ MHz. The light blue area denotes the regime where classical simulations using exact diagonalisation is feasible.

To verify the persistence of the QMBS states for different system sizes, we perform experimental measurements of chains of sizes $L = 12$ to 30. Time evolution of the imbalance, entanglement entropy, and the four-qubit fidelity were found to behave consistently for different system sizes, thereby establishing the robustness of scarring in collective states $|\Pi\rangle$ and $|\Pi'\rangle$. The relatively small variations between the imbalance and entanglement entropy for different system sizes are due to the difference in the cross couplings and the couplers. The Fourier amplitude $g_\Pi(\omega_1)$ and the four-qubit fidelity $F_A(t_1)$ at the first revival plateaus for $L > 16$, as shown in Fig. 6.7, whereas the inverse of the Hilbert space dimension characterising the scaling of a random state shows an expected rapid exponential decrease with the system size. The plateaued behaviour in the scaling suggests that QMBS states persist in the regime of large system size approaching the thermodynamic limit.

On fig. 6.7, we also show that our experimental results go beyond system sizes where exact diagonalisation is currently possible. While this numerical method is not the only one available for this problem, we argue that alternative options are not ideal for studying QMBS in large systems. Methods based on Krylov subspace and matrix-product states can clearly access the dynamics from the Π and Π' states beyond 24 qubits. However, to show scarring requires studying the dynamics from a large number

of initial states. In contrast to exact diagonalisation, these two methods require an independent computation for each initial state. Furthermore, for MPS methods, it would also be costly to simulate the dynamics of thermalising states as their entanglement entropy quickly grows. This would limit the simulation to a relatively short time, as the bond dimension of the matrix-product states (and consequently, the computational resources needed) required to faithfully capture the dynamics would rapidly become large. Due to this, we believe that producing data like what is presented in Fig. 6.6**h** is best suited to a quantum simulator.

6.3 XY model on a ladder with tunable couplings

In the previous section, we have used part of the tunability of the couplings in our SC chip to engineer the SSH chain in 1D. However, this could also be done in a cold atom quantum simulator by using a superlattice. In the remainder of this chapter, we fully utilise the capabilities of our SC setup. To do that, we go beyond the 1D chain geometry and study a 2D ladder. We also use the tuning of each individual coupling to realise quenched disorder. Despite this increased complexity, we will be able to create QMBSs as well. More importantly, the scarred states themselves can be *deterministically* tuned by the disorder. In order to achieve that, we no longer rely on generating a weakly-coupled subgraph, but take inspiration from the rainbow scar construction [114, 115], reviewed in Chapter 2. We will show that our model hosts several distinct families of QMBS states and entanglement structures. While the first family is a direct realisation of the rainbow construction, the second family emerges from a hitherto unexplored mechanism: it is obtained by acting on the first family with the Hamiltonian of a *single* subsystem. By making the couplings spatially inhomogeneous, we can then turn these states into *disordered* QMBS states whose *exact* wave functions and entanglement structure can still be written down in analytic form. Unlike their energies, the structure of these exact eigenstates can be explicitly modulated via the disorder profile, allowing to tune their properties. We experimentally observe the two types of entanglement via their distinct ergodicity-breaking signatures in quantum dynamics at late times.

We consider a system which contains $N = 2M$ qubits arranged in a ladder configuration, with two horizontal chains containing M qubits each. Similar to the previous experiment in this chapter, we make use of a flip-chip SC quantum processor, now hosting 2×20 frequency-tunable transmon qubits in a ladder configuration, depicted in Fig. 6.8. The properties of the sample and the Hamiltonian governing it are similar to the devices used in Sec. 6.1. One notable difference is that the XY couplings between a pair of nearest-neighbour transmon qubits can be tuned in the range $[-8, 8]$ MHz and $[-8, -2]$ MHz for the parallel and vertical couplings, respectively. This means that couplings can now be tuned to large positive *and* negative values, which will be essential to the appearance of rainbow QMBSs, as we will discuss below. The mean values of the singe-qubit energy relaxation times and Ramsey dephasing times are respectively $T_1 = 26.6$ μs and $T_2^\star = 1.34$ μs, while the mean of the single-qubit randomised benchmarking fidelities is 0.993. The anharmonicity is equal to $\eta/2\pi \approx -175$ MHz. Finally,

the estimated values of the J_x cross-couplings are in the range $J_x/2\pi \in [0.10, 0.45]$ MHz. We note that, unlike in the 1D case, the model we study is chaotic even if the J_x couplings are set to zero.

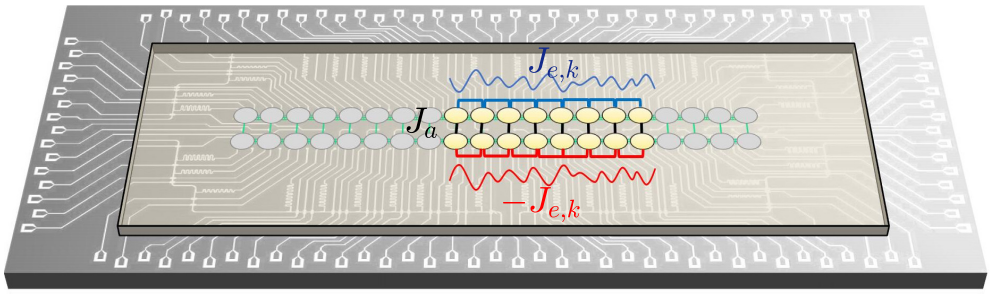

Figure 6.8: Micrograph of the superconducting quantum processor in a ladder configuration. The tunable couplings, J_a and J_e, between nearest-neighbour qubits, belonging to the same or opposite rows, are indicated. Blue and red curves illustrate the disordered coupling strengths $\pm J_{e,k}$, carrying opposite signs in the two rows.

The qubits belonging to the top row are described by $\hat{\mathbf{u}}^\alpha$ Pauli matrices (with $\alpha = x, y, z$), while $\hat{\mathbf{d}}^\alpha$ are Pauli matrices acting on the bottom-row qubits. The Hamiltonian can be written as

$$\hat{H} = \hat{H}_{\mathbf{u}} \otimes \mathbf{1} + \mathbf{1} \otimes \hat{H}_{\mathbf{d}} + \hat{H}_{\text{int}}, \tag{6.12}$$

where the top/bottom row and inter-row Hamiltonians, respectively, are given by

$$\begin{aligned} \hat{H}_{\sigma=\mathbf{u},\mathbf{d}} &= \sum_{k=1}^{M-1} \pm\frac{J_{e,k}}{2}\left(\hat{\sigma}_k^x\hat{\sigma}_{k+1}^x+\hat{\sigma}_k^y\hat{\sigma}_{k+1}^y\right) + \sum_{k=1}^{M}\omega_k\hat{\sigma}_k^z, \\ \hat{H}_{\text{int}} &= \sum_{k=1}^{M}\frac{J_a}{2}\left(\hat{\mathbf{u}}_k^x\hat{\mathbf{d}}_k^x+\hat{\mathbf{u}}_k^y\hat{\mathbf{d}}_k^y\right). \end{aligned} \tag{6.13}$$

Here, the intra-layer coupling amplitude $J_{e,k}$ and the frequency ω_k can be site-dependent, allowing for the possibility of disorder, as sketched in Fig. 6.8. We assume the inter-row couplings J_a to be uniform.

The exact nature of the couplings is chosen in order to satisfy the rainbow scars construction. As discussed in Chapter 2, this construction relies on splitting the system into two subsystems that have opposite spectra. Here, subsystem 1 is the top row of the ladder while subsystem 2 is the bottom row. The transformation relating their Hamiltonians is

$$\mathcal{M} = \left(\prod_{k=1}^{M}\hat{\mathbf{d}}_k^x\right)\hat{\mathcal{P}}_{\mathbf{d}\leftrightarrow\mathbf{u}}, \tag{6.14}$$

where $\hat{\mathcal{P}}_{\mathbf{d}\leftrightarrow\mathbf{u}}$ is the operator exchanging the top and bottom row and the term between parentheses is a particle-hole exchange. The $\hat{\mathbf{d}}_k^x$ operators will not affect the XY terms, but they will change the sign of the $\hat{\mathbf{d}}_k^z$. This is why we require the $J_{e,k}$ to be of opposite signs but the ω_k to be of identical sign between the two chains. Before discussing QMBS

states in detail, we will first show that the model we study is chaotic and identify its symmetries.

6.3.1 Symmetries of the model and level statistics

The model in Eq. (6.12) possesses a U(1) symmetry corresponding to the conservation of total magnetisation along the z-direction and, unless specified otherwise, we will restrict to its largest sector with zero magnetisation (or half-filling). Interestingly, the exchange rules of the Hamiltonian give rise to an additional, more subtle, symmetry. To formulate this symmetry, we will first express the Hamiltonian in a basis of non-overlapping dimers. This will also be convenient when discussing the structure of QMBS states. For each rung of the ladder, we can use a basis formed of doublons, holons, triplets and singlets defined respectively as

$$|\mathbf{D}\rangle := \left|\begin{smallmatrix}\bullet\\\bullet\end{smallmatrix}\right\rangle,\ |\mathbf{H}\rangle := \left|\begin{smallmatrix}\circ\\\circ\end{smallmatrix}\right\rangle,\ |\mathbf{T}\rangle := \frac{1}{\sqrt{2}}\left(\left|\begin{smallmatrix}\circ\\\bullet\end{smallmatrix}\right\rangle + \left|\begin{smallmatrix}\bullet\\\circ\end{smallmatrix}\right\rangle\right),\ |\mathbf{S}\rangle := \frac{1}{\sqrt{2}}\left(\left|\begin{smallmatrix}\circ\\\bullet\end{smallmatrix}\right\rangle - \left|\begin{smallmatrix}\bullet\\\circ\end{smallmatrix}\right\rangle\right). \tag{6.15}$$

While at first glance this new basis is not useful since the action of the Hamiltonian in it is non-trivial, it will greatly simplify the description of QMBS states and symmetries of the model.

In order to write down the Hamiltonian in the dimer basis, it will be more convenient to split it as

$$\hat{H} = \sum_{k=1}^{M-1} \hat{h}^{\parallel}_{k,k+1} + \sum_{k=1}^{M} \hat{h}^{\perp}_{k} \tag{6.16}$$

with

$$\begin{aligned} \hat{h}^{\parallel}_{k,k+1} =& \frac{J_{e,k}}{2}\left(\hat{\mathbf{u}}^x_k\hat{\mathbf{u}}^x_{k+1}+\hat{\mathbf{u}}^y_k\hat{\mathbf{u}}^y_{k+1}-\hat{\mathbf{d}}^x_k\hat{\mathbf{d}}^x_{k+1}-\hat{\mathbf{d}}^y_k\hat{\mathbf{d}}^y_{k+1}\right), \\ \hat{h}^{\perp}_{k} =& \frac{J_a}{2}\left(\hat{\mathbf{u}}^x_k\hat{\mathbf{d}}^x_k + \hat{\mathbf{u}}^y_k\hat{\mathbf{d}}^y_k\right) + \omega_k\left(\hat{\mathbf{u}}^z_k + \hat{\mathbf{d}}^z_k\right). \end{aligned} \tag{6.17}$$

We recall that $\hat{\mathbf{u}}^\alpha$ and $\hat{\mathbf{d}}^\alpha$ are Pauli matrices acting on the top and bottom rows, respectively. Terms in $\hat{h}^{\perp}_k$ act perpendicular to the ladder and so act on a single dimer, while terms in $\hat{h}^{\parallel}_{k,k+1}$ act parallel to the ladder, and act on two dimers.

Let us start by analysing the action of $\hat{h}^{\perp}_k$. It is straightforward to see that every state in the dimer basis is an eigenstate of $\hat{h}^{\perp}_k$ with

$$\begin{aligned} \hat{h}^{\perp}_k|\mathbf{H}\rangle &= -2\omega_k|\mathbf{H}\rangle, & \hat{h}^{\perp}_k|\mathbf{D}\rangle &= 2\omega_k|\mathbf{D}\rangle, \\ \hat{h}^{\perp}_k|\mathbf{T}\rangle &= \ \ J_a|\mathbf{T}\rangle, & \hat{h}^{\perp}_k|\mathbf{S}\rangle &= -J_a|\mathbf{S}\rangle. \end{aligned} \tag{6.18}$$

The action of $\hat{h}^{\parallel}_{k,k+1}$ is more complicated and requires looking at two neighbouring dimers. The first thing one can notice is that $\hat{h}^{\parallel}_{k,k+1}|\sigma\sigma\rangle = 0$ for any $\sigma = \mathbf{H}, \mathbf{D}, \mathbf{T}, \mathbf{S}$.

The non-zero terms are then

$$\begin{aligned}
\hat{h}^{\parallel}_{k,k+1}\,|\mathbf{TS}\rangle &= J_e(|\mathbf{HD}\rangle - |\mathbf{DH}\rangle), & \hat{h}^{\parallel}_{k,k+1}\,|\mathbf{HD}\rangle &= J_e(|\mathbf{TS}\rangle - |\mathbf{ST}\rangle),\\
\hat{h}^{\parallel}_{k,k+1}\,|\mathbf{TH}\rangle &= -J_e\,|\mathbf{HS}\rangle\,, & \hat{h}^{\parallel}_{k,k+1}\,|\mathbf{TD}\rangle &= J_e\,|\mathbf{DS}\rangle\,,\\
\hat{h}^{\parallel}_{k,k+1}\,|\mathbf{SH}\rangle &= -J_e\,|\mathbf{HT}\rangle\,, & \hat{h}^{\parallel}_{k,k+1}\,|\mathbf{SD}\rangle &= J_e\,|\mathbf{DT}\rangle\,.
\end{aligned} \tag{6.19}$$

The missing combinations can be obtained by flipping the two sites under consideration on the right- and left-hand sides. Importantly, this leads to the following combinations of states being annihilated by $\hat{h}^{\parallel}_{k,k+1}$:

$$\hat{h}^{\parallel}_{k,k+1}\,(|\mathbf{TS}\rangle + |\mathbf{ST}\rangle) = 0, \qquad \hat{h}^{\parallel}_{k,k+1}\,(|\mathbf{HD}\rangle + |\mathbf{DH}\rangle) = 0. \tag{6.20}$$

Fig. 6.9**a** summarises the action of $\hat{h}^{\parallel}$ on neighbouring dimers.

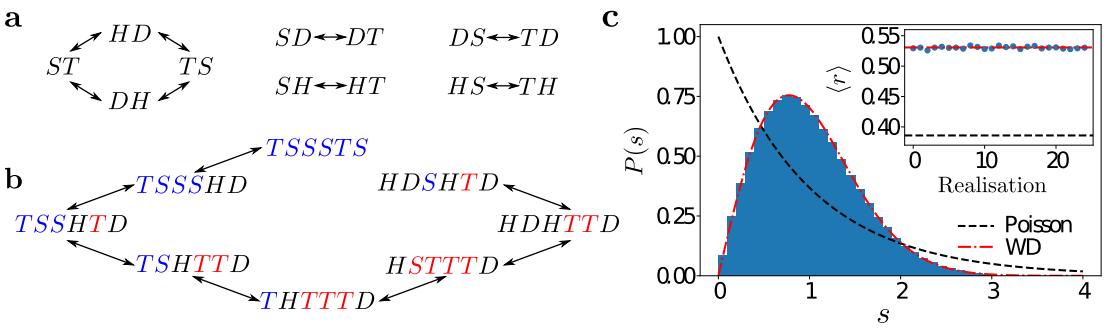

Figure 6.9: Properties of the model (6.12) on the SC ladder. **a** Schematic of the Hamiltonian action on neighbouring dimers. **b** Example of a sequence of states obtained using only allowed processes. The colour of the singlet and triplet states indicates if they have been "exchanged" an even (blue) or odd (red) number of times. This exactly corresponds to the parity of the sum of the number of holons and doublons to their left. If one gets $+1$ for all blue triplets and red singlets, and -1 for all blue singles and red triplets, then for all states in the sequence the sum is the same and gives $Q{=}-2$, illustrating the conservation of this charge. **c** Distribution of energy level spacings $s \equiv E_{n+1} - E_n$ for the model in Eq. (6.12) with $N{=}20$ sites. Data is for half filling and $Q{=}0$, with 25 disorder realisations. The level statistics displays excellent agreement with the Wigner-Dyson ensemble. The inset shows the average consecutive spacing ratio $\langle r\rangle$ for each realisation, which is very close to the expected value of 0.53 for a chaotic system. Data is for $J_a{=}3$ and $J_{e,k} \in [2, 2.5]$, $\omega_k \in [0.5, 1.5]$ drawn from a uniform distribution.

Now that we have established the action of the Hamiltonian in the dimer basis, we can discuss the additional U(1) symmetry. Consider a simple configuration like **TSSSTS**. The Hamiltonian rules dictate that we can only exchange **TS** or **ST** into **HD** or **DH**. Through this, we can exchange any neighbouring **TS** into **ST** and so reach any configuration with the same number of singlets and triplets as in the initial state. Therefore, a natural guess for the conserved quantity would be the difference between the total number of triplets and the number of singlets. This can be expressed as the operator $\sum_k(\hat{T}_k - \hat{S}_k)$, where $\hat{T}_k$ and $\hat{S}_k$ are projectors on the triplet and singlet

configurations of dimer k. This works perfectly until we start having configurations with neighbouring dimers like **SH**. In that case, we can turn it into **HT** and thus change $\sum_k(\hat{T}_k - \hat{S}_k)$. However, for that to happen it means that we first created **HD** and that the dimer that was switched between **S** and **T** must be surrounded by **H** and **D**. Effectively, the Hamiltonian creates domains inside which all **T** and **S** are "exchanged". Thus, we can keep track of how many times such exchanges have occurred for a given dimer by counting the number of doublons or holons to its left. Fig. 6.9**b** shows an example of this process. We can write the conserved quantity in a compact way in the dimer basis as

$$\hat{Q} = \sum_{k=1}^{M} \left(\hat{T}_k - \hat{S}_k\right) \prod_{l=1}^{k-1} (-1)^{\hat{H}_l + \hat{D}_l}, \tag{6.21}$$

where $\hat{T}_k$, $\hat{S}_k$, $\hat{D}_k$ and $\hat{H}_k$ are projectors on the respective dimer state at the given site k. This operator has $M+1$ sectors with eigenvalues $Q = -M,\ -M+2,\ -M+4 \ldots M-2,\ M$.

While we focus on the half-filling sector, we briefly note that $\hat{Q}$ is a symmetry at any filling. The interplay of $\hat{Q}$ and filling leads to a large number of disconnected sectors. Some of them are of small dimension and similar to the ones studied in Ref. [244]. Nonetheless, for large sectors we find good agreement with random matrix predictions, as shown on Fig. 6.9 **c**. All individual disorder realisations show $\langle r \rangle$ close to 0.53. Their average also does, and displays a very close agreement with the Wigner-Dyson distribution.

Finally, beyond the symmetry $\hat{Q}$, at half-filling the Hamiltonian *anti-commutes* with

$$\hat{C} = \hat{\mathcal{P}}_{\mathbf{d}\leftrightarrow\mathbf{u}} \prod_{k=1}^{M} \hat{\mathbf{u}}_k^x \hat{\mathbf{d}}_k^x \hat{\mathbf{d}}_k^z \tag{6.22}$$

where $\hat{\mathcal{P}}_{\mathbf{d}\leftrightarrow\mathbf{u}}$ is an operator exchanging the top and bottom rows. $\hat{C}$ is related to a particle-hole transformation along with a swap between the top and bottom row and an additional phase. In the dimer picture, $\hat{C}$ simply switches **T** and **S** as well as **D** and **H**, with a (-1) phase for every **D** present. Note that, as we are at half filling, there are always the same number of **D** and **H**, so $\hat{C} = \hat{C}^\dagger$ and $\hat{C}^2 = \mathbf{1}$. As it also anti-commutes with $\hat{Q}$, $\hat{C}$ exchanges the sectors with $Q = q$ and $Q = -q$. For M-even, we have a sector with $q = 0$; in that sector the spectrum is symmetric around E=0 because of $\hat{C}$, however, this is not the case in other sectors.

6.3.2 Two families of rainbow scars

We are now in position to identify rainbow QMBS states in the model (6.12). As the Hamiltonians of the upper and lower chains have opposite spectra and are related by the transformation $\mathcal{M}$ in Eq. (6.14), the following rainbow state is a zero eigenstate of their sum:

$$|\mathbf{I}\rangle \equiv |E_M\rangle = \bigotimes_{j=1}^{M} \frac{1}{\sqrt{2}} \left(\left| \begin{smallmatrix} \bullet \\ \circ \end{smallmatrix} \right\rangle + \left| \begin{smallmatrix} \circ \\ \bullet \end{smallmatrix} \right\rangle \right) \equiv |\mathbf{TTT} \ldots \mathbf{TT}\rangle \,. \tag{6.23}$$

The fact that the state of each atom in the lower chain is always opposite to that of its counterpart on the upper chain is directly caused by the presence of $\hat{\mathbf{d}}^x$ in $\mathcal{M}$. The form of this state reveals the structure of Bell pairs formed between the two rungs of the ladder. Importantly, upon addition of $\hat{H}_{\text{int}}$, the rainbow state $|I\rangle$ remains an exact eigenstate with energy MJ_a, thus becoming a rainbow scar of the full model. However, the rainbow construction is not limited to a single state. Two different families of scars can be built from it using operators that commute with the half-system Hamiltonian $\hat{H}_{\mathbf{u}}$, as we show next.

First family of scars

To construct the first family of QMBS states, we use the operator $\hat{Z} = \sum_{k=1}^{M} \hat{\mathbf{u}}_k^z$, which clearly commutes with $\hat{H}_{\mathbf{u}}$ as the latter conserves z-magnetisation. The powers of $\hat{Z}$ are linearly independent up to $\hat{Z}^M$, thus we can apply $\hat{Z}$ up to M times. The $\hat{Z}$ operator simply converts triplets into singlets and vice versa. The resulting states $|M-n, n\rangle$ will be symmetric superpositions of all states with a fixed number n of triplets and $M-n$ singlets. The QMBS states of the first family are precisely these states, up to normalisation:

$$|E_n\rangle = \binom{M}{n}^{-1/2} |M-n, n\rangle \propto \hat{P}^Q_{2n-M} \hat{Z} \, |E_{n+1}\rangle \,, \tag{6.24}$$

where n ranges between 0 and $M-1$ and $|E_M\rangle \equiv |\mathbf{I}\rangle$. The second equality illustrates that we can build $|E_n\rangle$ recursively from $|E_{n+1}\rangle$ by making use of the projector $\hat{P}^Q_q$ on the sector of $\hat{Q}$ with an eigenvalue q. The projector $\hat{P}^Q_q$ is introduced for convenience as it simplifies the recursion, since acting with $\hat{Z}$ on $|E_n\rangle$ creates a superposition of $|E_{n-1}\rangle$ and $|E_{n+1}\rangle$. As every singlet (triplet) gives eigenvalue $-J_a$ ($+J_a$) under $\hat{H}_{\text{int}}$, it is easy to verify that the state $|E_n\rangle$ is an eigenstate of $\hat{H}$ with energy $E_n = J_a(2n-M)$.

We note that the underlying structure of this first family of scarred states $|E_n\rangle$ is the RSGA [102], introduced in Chapter 2. This is seen by noting that its states can be built by the raising operator $\hat{S}^+ = \sum_{k=1}^{M} |T_k\rangle \langle S_k|$. If we define $\hat{S}^- = \left(\hat{S}^+\right)^\dagger$ we get that $\hat{S}^+ + \hat{S}^- \propto \hat{Z}$. So this algebraic structure is directly linked to the rainbow scar construction. We can then equivalently express the first type of scar states as

$$|E_n\rangle = \frac{1}{\mathcal{N}} (\hat{S}^+)^n \, |E_0\rangle = \frac{1}{\mathcal{N}} (\hat{S}^+)^n \, |\mathbf{SS}\ldots\mathbf{S}\rangle \,, \tag{6.25}$$

where $\mathcal{N}$ is a normalisation constant. We recognise that these scarred eigenstates are built in a similar way to previously known examples, e.g., in the spin-1 XY model [108]. In Appendix. F we compute their entanglement entropy for the bipartition perpendicular to the ladder, and we find that the eigenstate at zero energy has $S_{1,\perp} = 0.5 + 0.5\ln(\pi M/8)$, in the limit $M \to \infty$. From our discussion in Chapter 3, we note that the su(2) algebraic structure of these states implies they have extensive multipartite entanglement [1, 208].

Second family of scars

While symmetry generators come to mind when we look for operators $\hat{O}$ that commute with $\hat{H}_{\mathbf{u}}$, we can build a different family of QMBS states by using $\hat{H}_{\mathbf{u}}$ *itself* as the generator. The second scar family can be built recursively from the first family that way. Specifically, the second type of scar states are given by raising from $|E_{n-1}\rangle$ according to

$$|E'_n\rangle \propto \hat{P}^Q_{M-2n}\left[\hat{H}_{\mathbf{u}} - \left(\sum_k \frac{\omega_k}{M}\right)\hat{Z}\right]|E_{n-1}\rangle\,, \tag{6.26}$$

or, equivalently, by lowering from $|E_{n+1}\rangle$ as

$$|E'_n\rangle \propto \hat{P}^Q_{M-2n}\left[\hat{H}_{\mathbf{u}} - \left(\sum_k \frac{\omega_k}{M}\right)\hat{Z}\right]|E_{n+1}\rangle\,, \tag{6.27}$$

with $n = 1, 2, \ldots, M-1$. The second term in the square bracket automatically orthogonalises the states $|E'_n\rangle$ with respect to the first family of scars. The projectors $\hat{P}^Q_q$ once again isolate $|E'_{n-1}\rangle$ from $|E'_{n+1}\rangle$. In order to write the states $|E'_n\rangle$ in a more explicit form, let us define ensembles of sites $\Lambda = \{1, 2, \ldots M\}$, $\Lambda_k = \{k, k+1\}$ and $\bar{\Lambda}_k = \Lambda \setminus \Lambda_k$. With this, we can express $|E'_n\rangle$ as

$$|E'_n\rangle = \sum_{k=1}^{M-1} \frac{J_{e,k}}{2\mathcal{N}_n}\left(|\mathbf{HD}\rangle_{\Lambda_k} + |\mathbf{DH}\rangle_{\Lambda_k}\right)\otimes|M-n-1, n-1\rangle_{\bar{\Lambda}_k} + \frac{1}{\mathcal{N}_n}\left(\sum_{k=1}^{M}\hat{T}_k\overline{\omega}_k\right)|M-n, n\rangle_{\Lambda}\,, \tag{6.28}$$

with $n = 1, 2, \ldots, M-1$, $\overline{\omega}_j = \omega_j - \frac{1}{M}\sum_{k=1}^{M}\omega_k$, and $|a, b\rangle_A$ the symmetric superposition of all states with a singlets and b triplets on sites in the ensemble A. More details about the construction of these states and the proof that they are eigenstates of the model is given in Appendix E, where we also derive the normalisation factors $\mathcal{N}_n$. As the holons and doublons are annihilated by $\hat{H}_{\text{int}}$, only the triplet and singlets will give a non-zero energy contribution. And since the state $|E'_n\rangle$ has $M-n-1$ singlets and $n-1$ triplets, the second family of QMBS states have energies $E'_n = J_a(2n-M)$, which are identical to those of the first family $|E_n\rangle$.

To the best of our knowledge, there is no su(2) algebraic construction for the second family of scarred states $|E'_n\rangle$, despite their equal energy spacing. Indeed, the latter are generated by acting with an operator on $|E_{n-1}\rangle$ or $|E_{n+1}\rangle$, and not on $|E'_{n-1}\rangle$ or $|E'_{n+1}\rangle$. Moreover, the second type of scarred eigenstates depend sensitively on the parameters $J_{e,k}$ and ω_k of the model. Therefore, the entanglement of these states is not fixed, like in the first family of scars, as we discuss in detail in Appendix F. For a cut perpendicular to the ladder, the second type of scarred states generally possess entanglement entropy that scales logarithmically with subsystem size. While we were unable to formally rule out the possibility of volume-law entanglement scaling, our analytical and numerical results strongly suggest that, in the large M limit, the second type of scarred state with zero energy has entanglement entropy $S_{\perp,2}$ that obeys $S_{\perp,1} < S_{\perp,2} < S_{\perp,1} + \ln(4)$. This suggests it should always be possible to find a low-entangled state which has overlap only on the scarred stats of the second family, regardless of the values of parameters.

Comparison between the two families of scars

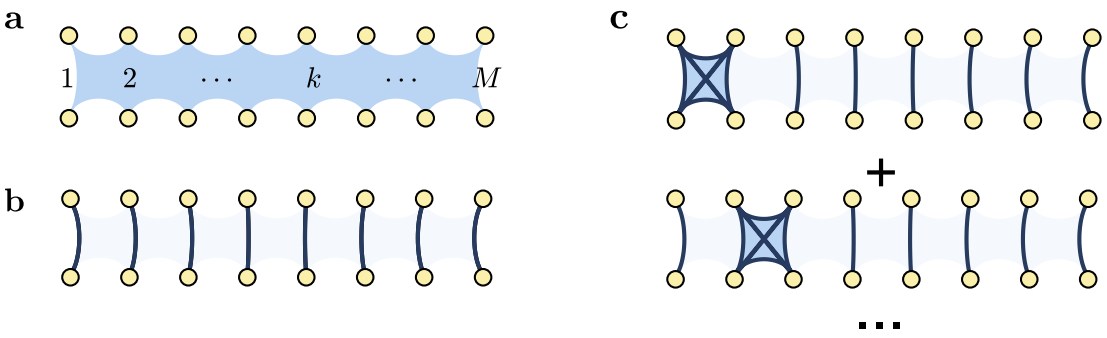

Figure 6.10: Schematic representation of entanglement structure for **a** a thermalising state, **b** the first family, and **c** second family of scars, respectively. The shaded blue region in **a** indicates large entanglement between all qubits in the thermalising case. In **b** and **c**, dark curves depict the Bell pair entanglement of neighbouring qubits, with dimers locally forming $|\mathbf{T}\rangle$ or $|\mathbf{S}\rangle$ states. The tetramer configurations denote doublon-holon entanglement $(|\mathbf{DH}\rangle + |\mathbf{HD}\rangle)/\sqrt{2}$, characteristic of the second scar family.

It is instructive to contrast the two families of scars. Their structure is shown schematically in Fig. 6.10. While both families occur at the same, regularly spaced energies throughout the spectrum, the total number of states in the second family is smaller by two than in the first family. Furthermore, there are stark differences in entanglement structures. The states belonging to the second family explicitly depend on disorder through their dependence on $J_{e,k}$ and ω_k, unlike the first family. The states in the first family contain only singlets or triplets, with no doublons or holons, Fig. 6.10**b**. By contrast, the second family has overlap with states involving a symmetric superposition on a single doublon-holon pair $|\ldots\mathbf{DH}\ldots\rangle + |\ldots\mathbf{HD}\ldots\rangle$ with weight $J_{e,k}/2$ on top of a background of $M-n-1$ singlets and $n-1$ triplets, Fig. 6.10**c**. They also have overlap with all states with $M-n$ singlets and n triplets, with prefactors depending on the ω_k and on the location of the triplets. The dependence of $|E'_n\rangle$ states on ω_k and $J_{e,k}$ allows to tune their properties, such as entanglement entropy or overlap with special initial states.

The properties of both families of scars can be contrasted with those of thermal eigenstates. This is particularly clear when looking at the entanglement entropy S_A, where A denotes the subsystem of interest. The rainbow entanglement manifests as a striking difference in entropy depending on the type of bipartition that defines the subsystem A, and we will consider two types illustrated in Fig. 6.11**a**. For the parallel cut between the two rows of the ladder, i.e., when A comprises qubits $\{u_1, u_2, \ldots, u_M\}$, the entanglement is large, as the bipartition cuts through an extensive number of Bell pairs. By contrast, for the bipartition perpendicular to the ladder, i.e., when $A = \{u_1, d_1, \ldots, u_{M/2}, d_{M/2}\} \equiv \{k = 1, 2, \cdots, M/2\}$, the entanglement is much lower. As seen in Fig. 6.11**b**-**c**, this distinction is maximal for the $|E_0\rangle$ and $|E_M\rangle$ states, which have exactly *maximal* entropy $M\ln(2)$ in the case of a parallel bipartition but zero

entanglement in the case of a perpendicular bipartition. More generally, we find that in the middle of the spectrum both types of scarred state display logarithmic entanglement growth with M for a perpendicular cut (see Appendix. F).

While the dependence of entanglement on the cut clearly shows the presence of scarred states, it is difficult to do in experiment as preparing high-energy eigenstates is an arduous task. We will thus turn towards dynamical signatures of the scarred eigenstates that can be probed on our superconducting chip. Before proceeding to that, we briefly discuss an additional property of the half-system Hamiltonian $\hat{H}_{\mathbf{u}}$. Indeed, this Hamiltonian is in 1D and only contains nearest-neighbour hopping and onsite potential. As such, it can be mapped to a free-fermionic model using a Jordan-Wigner transformation and is integrable and non-interacting. This means that this Hamiltonian technically has many conserved quantities, and one could wonder if this is what causes the presence of the second family of scars. We argue that this is not the case, as the rainbow states formed by the individual free-fermionic modes are not eigenstates of $\hat{H}_{\text{int}}$. We have also studied a similar model but with next-nearest neighbours hopping. This destroys integrability in a single chain, but the ladder still holds two families of rainbow scars generated by the same operators $\hat{Z}$ and $\hat{H}_{\mathbf{u}}$.

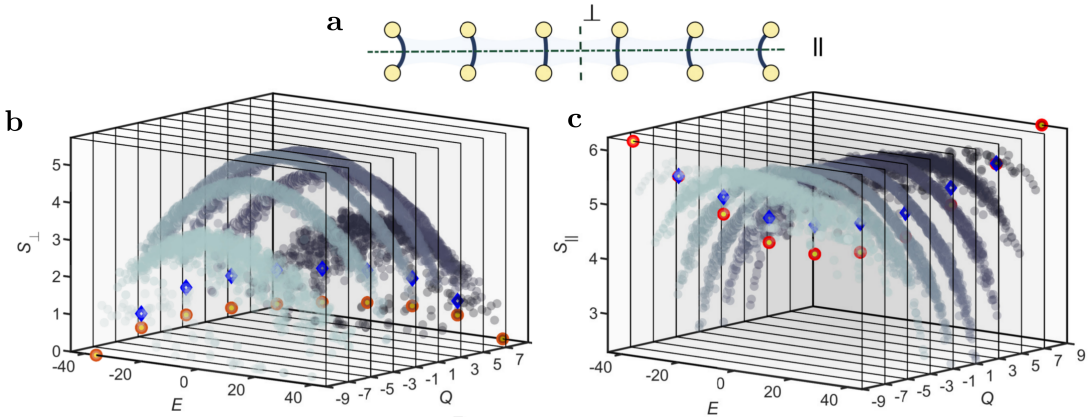

Figure 6.11: **a** Schematic of the ladder with dashed lines indicating two types of bipartitions. The parallel cut splits all entangled pairs in the rainbow state, while the perpendicular cut does not affect them. **b-c** Bipartite entropy of eigenstates in different Q-symmetry sectors for the two cuts shown in **a**. The two families of scarred states are highlighted by red circles (first family) and blue diamonds (second family). Their rainbow nature is revealed by the fact that they move between minimal and maximal entropy, depending on the cut. Coloured cross sections represent different sectors labelled by the values on the Q axis. Data is obtained by exact diagonalisation with $N = 18$ qubits, $J_a = 4$, and $J_{e,k} \in [4, 4.5]$, $\omega_k \in [0.5, 1.5]$ drawn from a uniform distribution.

6.3.3 Dynamical signatures of the two scar families

Both families of scarred states are evenly spaced in energy with spacing $2J_a$, hence they can lead to persistent revivals following the quench from a suitably chosen initial

state. Here we identify such initial states for the two scar families. To probe the first scar family, we will use the state $|\Pi\rangle$ given by:

$$|\Pi\rangle = \left|\begin{smallmatrix}\bullet & \bullet & & \bullet\\ \circ & \circ & \cdots & \circ\end{smallmatrix}\right\rangle . \tag{6.29}$$

This state must undergo perfect revivals due to the exact su(2) algebraic structure, as we now explain. From the raising operator $\hat{S}^+ = \sum_k |T_k\rangle\langle S_k|$, we can infer $\hat{S}^x \propto \hat{S}^+ + (\hat{S}^+)^\dagger$ or, equivalently,

$$\hat{S}^x \;\propto\; \sum_k \left(\left|\begin{smallmatrix}\circ\\ \bullet\end{smallmatrix}\right\rangle\left\langle\begin{smallmatrix}\circ\\ \bullet\end{smallmatrix}\right| - \left|\begin{smallmatrix}\bullet\\ \circ\end{smallmatrix}\right\rangle\left\langle\begin{smallmatrix}\bullet\\ \circ\end{smallmatrix}\right| \right)_k , \tag{6.30}$$

which we recall is proportional to the action of $\hat{Z}$ as discussed in Sec. 6.3.2. The corresponding $\hat{S}^z$ operator is given by $\hat{S}^z = \sum_k |T_k\rangle\langle T_k| - |S_k\rangle\langle S_k|$, which is easily seen to have the same action as $\hat{H}_{\text{int}}$ in this subspace. Hence, if we prepare the system in the lowest-weight state of $\hat{S}^x$, it will undergo perfect precession around an effective field in the z-direction. It is easy to see that our state $|\Pi\rangle$ in indeed the lowest weight state of Eq. (6.30). The precession that starts out in $|\Pi\rangle$ state will result in perfect state transfer to the highest-weight state $|\Pi'\rangle = |\begin{smallmatrix}\circ & \circ & & \circ\\ \bullet & \bullet & \cdots & \bullet\end{smallmatrix}\rangle$.

The existence of revivals from the $|\Pi\rangle$ initial state can be shown more explicitly by computing the overlap $|\langle\Pi|E_n\rangle|^2$ with eigenstates of the first scar family. First, it will be important to observe that we obtain a simple product state when all possible combinations of singlets and triplets are summed up:

$$\sum_{n=0}^{M} |M-n,n\rangle = \bigotimes_{k=1}^{M} (|\mathbf{T}\rangle + |\mathbf{S}\rangle) = 2^{M/2} \left|\begin{smallmatrix}\circ & & \circ\\ \bullet & \cdots & \bullet\end{smallmatrix}\right\rangle , \tag{6.31}$$

where in the second equality we made use of $|\mathbf{T}\rangle + |\mathbf{S}\rangle = \sqrt{2}\,|\begin{smallmatrix}\circ\\ \bullet\end{smallmatrix}\rangle$. Since $|E_n\rangle = \binom{M}{n}^{-1/2} |M-n,n\rangle$, it is easy to see that

$$|\Pi'\rangle = \left|\begin{smallmatrix}\circ & & \circ\\ \bullet & \cdots & \bullet\end{smallmatrix}\right\rangle = \sum_{n=0}^{M} \sqrt{\frac{\binom{M}{n}}{2^M}}\, |E_n\rangle . \tag{6.32}$$

The same procedure can be applied to the $|\Pi\rangle$ state by noting that $|\mathbf{T}\rangle - |\mathbf{S}\rangle = \sqrt{2}\,|\begin{smallmatrix}\bullet\\ \circ\end{smallmatrix}\rangle$. This means that there is now a factor of -1 for each singlet present, such that

$$|\Pi\rangle = \left|\begin{smallmatrix}\bullet & & \bullet\\ \circ & \cdots & \circ\end{smallmatrix}\right\rangle = \sum_{n=0}^{M} (-1)^{M-n} \sqrt{\frac{\binom{M}{n}}{2^M}}\, |E_n\rangle . \tag{6.33}$$

Thus, the $|\Pi\rangle$ and $|\Pi'\rangle$ states only have overlap on the first family of scarred eigenstates. As the latter are regularly spaced in energy, the dynamics initialised in $|\Pi\rangle$ or $|\Pi'\rangle$ exhibits perfect revivals.

For QMBS states belonging to the second family, the identification of the reviving initial state $|\phi_L\rangle$ is more subtle as the eigenstates now depend on disorder realisation

and there is no apparent algebraic structure. However, we can once again appeal to the fact that the sum of all singlet and triplet configurations can be written as a simple state in the Fock basis. For any n, $|E'_n\rangle$ contain terms

$$\frac{J_{e,k}}{2\mathcal{N}_n}(|\mathbf{HD}\rangle_{\Lambda_k}+|\mathbf{DH}\rangle_{\Lambda_k})\otimes|M-n-1,n-1\rangle_{\bar{\Lambda}_k}\,, \tag{6.34}$$

with $\mathcal{N}_n$ the normalisation factor given in Eq. (E.18) of the Appendix. Recall that Λ_k denotes sites k and $k+1$ and $\bar{\Lambda}_k$ denotes all sites except k and $k+1$. As a consequence, summing all $|E'_n\rangle$ with a prefactor $\mathcal{N}_n$ as $\sum_{n=1}^{M-1}\mathcal{N}_n|E'_n\rangle$ gives

$$\begin{aligned}
&\sum_{k=1}^{M}\frac{J_{e,k}}{2}(|\mathbf{HD}\rangle_{\Lambda_k}+|\mathbf{DH}\rangle_{\Lambda_k})\otimes\sum_{n=1}^{M-1}|M-n-1,n-1\rangle_{\bar{\Lambda}_k}+\left(\sum_{k=1}^{M}\overline{\omega}_k\hat{T}_k\right)\sum_{n=1}^{M-1}|M-n,n\rangle_{\Lambda}\\
=&\sum_{k=1}^{M}\frac{J_{e,k}}{2}(|\mathbf{HD}\rangle_{\Lambda_k}+|\mathbf{DH}\rangle_{\Lambda_k})\otimes 2^{\frac{M-2}{2}}|\overset{\circ}{\bullet}\cdots\overset{\circ}{\bullet}\rangle_{\bar{\Lambda}_k}+\left(\sum_{k=1}^{M}\overline{\omega}_k\hat{T}_k\right)\left(2^{M/2}|\Pi'\rangle-|E_0\rangle-|E_M\rangle\right)\\
=&2^{\frac{M-4}{2}}\sum_{k=1}^{M}J_{e,k}(|\mathbf{HD}\rangle_{\Lambda_k}+|\mathbf{DH}\rangle_{\Lambda_k})\otimes|\overset{\circ}{\bullet}\cdots\overset{\circ}{\bullet}\rangle_{\bar{\Lambda}_k}+2^{M/2}\left(\sum_{k=1}^{M}\overline{\omega}_k\hat{T}_k\right)|\Pi'\rangle\,,
\end{aligned} \tag{6.35}$$

where we recall that $\hat{T}$ is the projector on the triplet state. Between the second and third line, $|E_0\rangle$ and $|E_M\rangle$ were discarded as they are annihilated by $\sum_{k=1}^{M}\overline{\omega}_k\hat{T}_k$. This is trivial for $|E_0\rangle$ since it has no triplet, while for $|E_M\rangle$ each site is a triplet and so the overall prefactor ends up being $\sum_{k=1}^{M}\overline{\omega}_k=0$, as $\overline{\omega}_j=\omega_j-\frac{1}{M}\sum_{k=1}^{M}\omega_k$.

In order to simplify this state and to make the orthogonality with $|E_n\rangle$ obvious, we will drop the last term in Eq. (6.35) and consider the initial state

$$\begin{aligned}
|\phi'_J\rangle=&\frac{1}{\mathcal{Z}}\sum_{k=1}^{M}J_{e,k}(|\mathbf{HD}\rangle_{\Lambda_k}+|\mathbf{DH}\rangle_{\Lambda_k})\otimes\left|\overset{\circ}{\bullet}\cdots\overset{\circ}{\bullet}\right\rangle_{\bar{\Lambda}_k}=\frac{1}{\mathcal{Z}}\left(J_{e,1}\left|\begin{smallmatrix}\bullet&\circ&\circ&&\circ\\&\circ&\bullet&\cdots&\bullet\end{smallmatrix}\right\rangle+J_{e,1}\left|\begin{smallmatrix}\circ&\bullet&\circ&&\circ\\&\circ&\bullet&\cdots&\bullet\end{smallmatrix}\right\rangle\right.\\
&\left.+J_{e,2}\left|\begin{smallmatrix}\circ&\bullet&\circ&\circ&&\circ\\&\bullet&\bullet&\circ&\cdots&\bullet\end{smallmatrix}\right\rangle+J_{e_2}\left|\begin{smallmatrix}\circ&\circ&\bullet&\circ&&\circ\\&\bullet&\circ&\bullet&\cdots&\bullet\end{smallmatrix}\right\rangle+J_{e,M-1}\left|\begin{smallmatrix}\circ&&\circ&\bullet&\circ\\&\cdots&&\bullet&\circ\end{smallmatrix}\right\rangle+J_{e,M-1}\left|\begin{smallmatrix}\circ&&\circ&\circ&\bullet\\&\cdots&&\circ&\bullet\end{smallmatrix}\right\rangle\right),
\end{aligned} \tag{6.36}$$

with the normalisation factor $\mathcal{Z}=\sqrt{2\sum_{k=1}^{M-1}J_{e,k}^2}$. As the $|\phi'_J\rangle$ state only has overlap with states containing one doublon and one hole, it has zero overlap with the scarred states of the first family that have neither of those. As such, any non-trivial dynamics after a quench from this state must come from scarred states of the second family. We can compute this overlap exactly:

$$|\langle\phi'_J|E'_n\rangle|^2=\frac{\binom{M-2}{n-1}}{2^{M-2}}\frac{\sum_{k=1}^{M-1}J_{e,k}^2}{\left(\sum_{k=1}^{M-1}J_{e,k}^2+2\sum_{k=1}^{M}\overline{\omega}_k^2\right)}, \tag{6.37}$$

which leads to

$$\sum_{n=1}^{M-1}|\langle\phi'_J|E'_n\rangle|^2=\frac{\sum_{k=1}^{M-1}J_{e,k}^2}{\left(\sum_{k=1}^{M-1}J_{e,k}^2+2\sum_{k=1}^{M}\overline{\omega}_k^2\right)}. \tag{6.38}$$

It is important to notice here that it is not the ω_k that enter this equation but their counterparts $\overline{\omega}_j = \omega_j - \frac{1}{M}\sum_{k=1}^{M}\omega_k$, with the mean removed. Thus, if we draw the $J_{e,k}$ and ω_k from the same distribution $[\Delta-\delta, \Delta+\delta]$, if $\Delta \gg \delta$ then we will have that $J_{e,k}^2 \gg \overline{\omega}_k^2$ as the former is at the scale of Δ^2 but the latter at the scale of δ^2. In that case the state $|\phi'_J\rangle$ will have total overlap of order $\left(1+\frac{2M\delta^2}{(M-1)\Delta^2}\right)^{-1}$ on the QMBSs of the second family, making these states the only relevant ones.

We can also define $|\phi_J\rangle$ with the same structure as $|\phi'_J\rangle$, but with the top and bottom chain swapped. We expect that a quench from this state will lead to approximate state transfer to $|\phi'_J\rangle$ and vice versa. It obeys the same $|\langle\phi_J|E'_n\rangle|^2$ as Eq. (6.37), but with additional minus signs

$$\langle\phi_J|E'_n\rangle = (-1)^{M-1-n}\langle\phi'_J|E'_n\rangle. \tag{6.39}$$

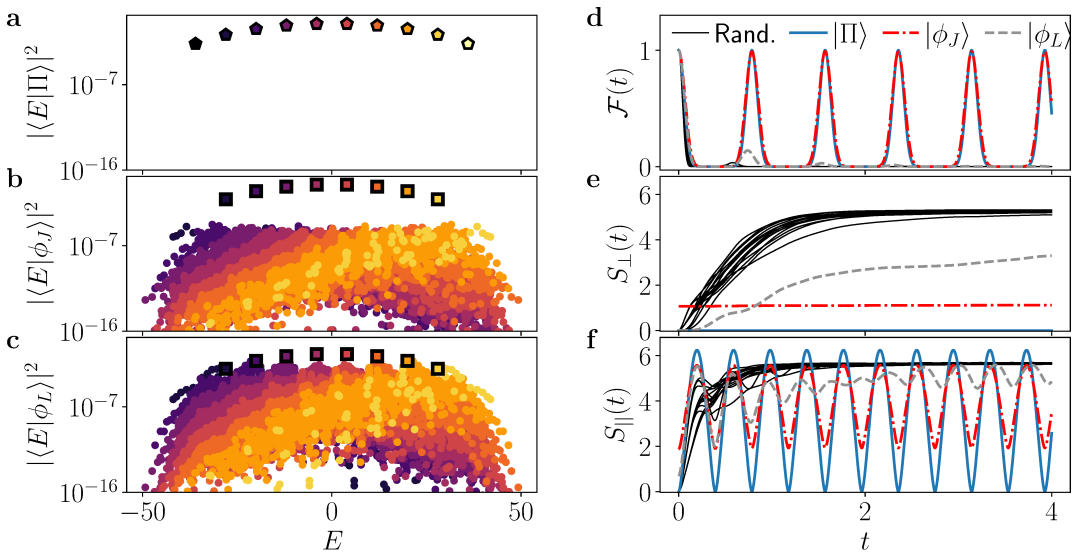

Figure 6.12: Properties of special initial states in the XY ladder. **a-c** Overlap between the $|\Pi\rangle$, $|\phi_J\rangle$ and $|\phi_L\rangle$ states and the eigenstates of the model in Eq. (6.12). Pentagrams and squares denote scarred states of the first and second family respectively, while each colour correspond to a sector of $\hat{Q}$. $|\Pi\rangle$ only has overlap on the scarred eigenstates of the first family, while $|\phi_J\rangle$ and $|\phi_L\rangle$ have no overlap on them. For both of these states the scarred states of the second family dominate. **d-f** Fidelity and bipartite entanglement entropy over time following the quench from various initial states indicated in the legend. The thin black lines are randomly chosen Fock basis states at half filling. For $|\Pi\rangle$ and $|\phi_J\rangle$ there is no visible growth of entanglement entropy, while for $|\phi_L\rangle$ the growth is strongly suppressed. For all three state the entanglement entropy heavily depends on the cut. All data is for $N = 18$, $J_a = 4$ and $J_{e,k} \in [4, 4.5]$, $\omega_k \in [0.5, 1.5]$ drawn from a uniform distribution.

Finally, for experimental implementations, it is preferable to use an initial state that requires fewest gates to prepare. Because of this, we will consider a state that is

only a superposition of two states in the Fock basis and which is defined as

$$|\phi_L\rangle = \frac{1}{\mathcal{N}}\left(|\begin{smallmatrix}\bullet & \circ & \bullet & & & \bullet \\ \bullet & \circ & \circ & \cdots & & \circ\end{smallmatrix}\rangle + |\begin{smallmatrix}\circ & \bullet & \bullet & & & \bullet \\ \circ & \bullet & \circ & \cdots & & \circ\end{smallmatrix}\rangle \right). \tag{6.40}$$

For this state, the overlap with the scarred states of the second family is

$$|\langle \phi_L | E'_n \rangle|^2 = \frac{\binom{M-2}{n-1}}{2^{M-2}} \frac{J_{e,1}^2}{\left(\sum_{k=1}^{M-1} J_{e,k}^2 + 2\sum_{k=1}^{M} \overline{\omega}_k^2\right)}. \tag{6.41}$$

To confirm our analysis above, we numerically compute the overlap of states $|\Pi\rangle$, $|\phi_J\rangle$ and $|\phi_L\rangle$ with eigenstates of the model in Eq. (6.12) in Fig. 6.12 **a-c**. All the states have predominant support on scarred eigenstates, either of the first family ($|\Pi\rangle$ state) or the second family ($|\phi_J\rangle$ and $|\phi_L\rangle$ states). We emphasise that, as scarred states of the first family have no doublons or holons, they are *exactly* orthogonal to $|\phi_J\rangle$ and $|\phi_L\rangle$. Thus, persistent revivals from the latter states provide unambiguous evidence for the second type of QMBSs. Indeed, Fig. 6.12**d-f** shows that the initial states $|\Pi\rangle$, $|\phi_J\rangle$ and $|\phi_L\rangle$ lead to revivals of the wave function and slow growth of entanglement entropy when compared to random Fock basis states – clear signatures of scarring. The rainbow nature of $|E_n\rangle$ and $|E'_n\rangle$ is also apparent in the dynamics, as the growth of entropy shows a stark difference between two different cuts, shown in Figs. 6.12 **e-f**.

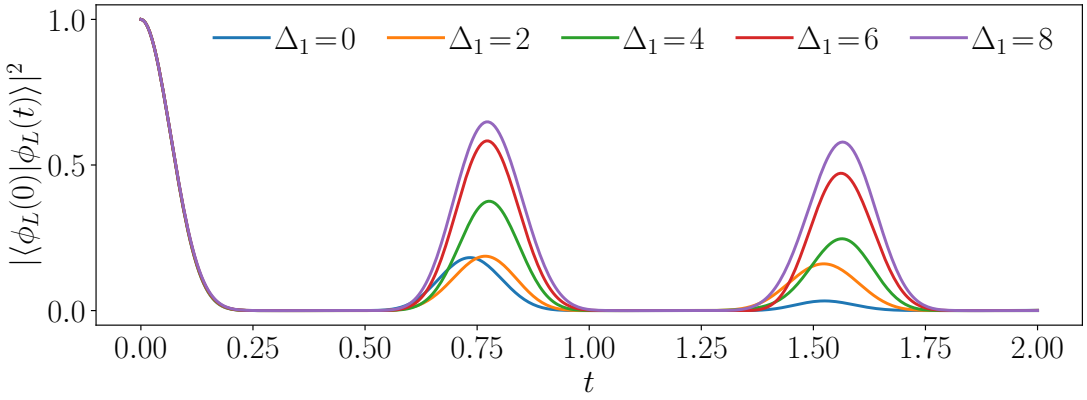

Figure 6.13: Improving the revivals by modulating the hopping strength on the first site according to $J_{e,1} = J^0_{e,1} + \Delta_1$. Monotonic increase of revival peaks can be seen as Δ_1 is increased. Data is for $N = 16$, $J_a = 4$, $J_{e,k} \in [4, 4.5]$, $\omega_k \in [0.5, 1.5]$ drawn from a uniform distribution.

While the revival fidelity from the $|\phi_L\rangle$ initial state in Fig. 6.12 is not particularly high, we can leverage the tunability of the second family of scarred states to enhance it. Indeed, from Eq. (6.41) it directly follows that the projection of $|\phi_L\rangle$ state on the set of scarred eigenstates $|E'_n\rangle$ is given by

$$\sum_{n=1}^{M-1} |\langle \phi_L | E'_n \rangle|^2 = \frac{J_{e,1}^2}{\sum_{k=1}^{M-1} J_{e,k}^2 + 2\sum_{k=1}^{M} \overline{\omega}_k^2}. \tag{6.42}$$

Thus, in the limit of $J_{e,1}\to\infty$, we recover perfect revivals. To illustrate the effect of $J_{e,1}$ on the dynamics, in Fig. 6.13 we compute the fidelity dynamics as $J_{e,1}$ is modulated by an amount $\Delta_1 \in [0, 8]$. Setting $\Delta_1 = 4$ – which amounts to approximately doubling $J_{e,1}$ – leads to a two-fold increase of the first revival peak, with the increase being even more pronounced at the second revival peak. This shows that the tunability of the initial state can be obtained with experimentally realistic values of the parameters for which the model remains chaotic.

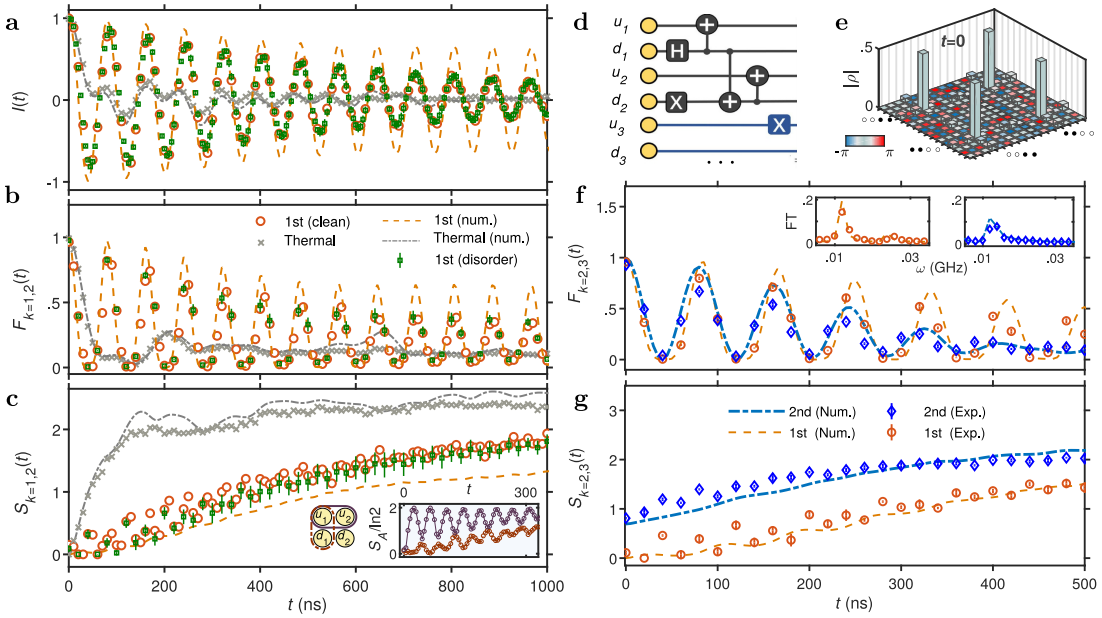

Figure 6.14: **a-c** Signature of the first family of scars in a ladder with $N = 10$ qubits. The plots show the measurements of **a** population imbalance, **b** the 4-qubit fidelity, and **c** the 4-qubit entanglement entropy, specified in the text. The inset in **c** shows the entropy of a subsystem consisting of 2 qubits, sketched on the left. Purple dots with error bars stand for the average and standard deviation over 8 disorder realisations of $J_{e,k}$, randomly selected from an interval as $J_{e,k}/2\pi \in [1, 3]$ MHz. For reference, we also show a typical thermalisation case with an initial state $|\bullet\circ\bullet\circ\bullet\circ\bullet\circ\circ\bullet\rangle$. The lines are the results of numerical simulations for the same parameters, including the additional cross couplings $J_x/2\pi \approx 0.3$ MHz and nonlinearity of qubits $\eta/2\pi \approx -175$ MHz, present in the physical device. **d-g** Signature of the second family of scar in a ladder with $N = 16$ qubits. **d** Circuit diagram for generating the entangled initial state $|\phi_L\rangle$ used to probe the dynamics of the second scar family. Symbols "+","H", and "X" stand for CNOT, Hadamard, and Pauli-X gates, respectively. **e** Absolute values of the reduced density matrix elements $\hat{\rho}_{k=1,2}$ at $t = 0$, with the colour bar denoting their phase. **f-g** Fidelity and entanglement entropy dynamics of a 4-qubit subsystem for initial states $|\Pi\rangle$ and $|\phi_L\rangle$, which overlap with the first and second family of scars, respectively. The clean couplings are set to values $J_{e,k}/2\pi = J_a/6\pi = -2$ MHz in all plots.

6.3.4 Experimental realisation of the two scar families

To observe signatures of scarring on our SC chip, we utilise an established diagnostics of QMBSs [43]: the evolution of local observable expectation values in quench dynamics of the circuit, consisting of two contiguous rows with up to 8 qubits each.

We first focus on the first family of scars and chose $|\Pi\rangle$ as our initial state. Figure 6.14**a** shows the dynamics of population imbalance, which is defined as $I(t) = (1/N)\sum_{k=1}^{M}\sum_{\sigma=\mathbf{u},\mathbf{d}}\langle\hat{\sigma}_k^z(0)\rangle\langle\hat{\sigma}_k^z(t)\rangle$. The population imbalance exhibits remarkable oscillations that persist up to time scales $\sim 1\mu$s. This is in contrast with typical thermalising states, for which the population imbalance rapidly decays to zero by $\sim$50 ns. A salient feature of the first family of scars is their insensitivity to the disorder in the Hamiltonian couplings. Thus, we expect the coherent dynamics from the $|\Pi\rangle$ state to be unchanged when inhomogeneity is introduced in $J_{e,k}$ couplings. This signature is clearly confirmed by experimental observations in Fig. 6.14**a**.

Furthermore, we utilise quantum tomography to obtain the reduced density matrix of the subsystem consisting of the 4 leftmost qubits $A = \{k = 1, 2\}$, which gives us additional information about the dynamics beyond local observables. The subsystem fidelity, $\sqrt{F_A} = \mathrm{Tr}\left[\sqrt{\sqrt{\hat{\rho}_A(t)}\hat{\rho}_A(0)\sqrt{\hat{\rho}_A(t)}}\right]$, and entanglement entropy, $S_{k=1,2}$, are shown in Figs. 6.14**b-c**. For the initial state $|\Pi\rangle$, the subsystem fidelity dynamics undergoes persistent revivals, implying that the initial information is restored many times, with a period of about 80 ns. Meanwhile, for generic initial product states, $F_{k=1,2}$ quickly decays towards a value close to the inverse of the subsystem Hilbert space dimension, as shown in Fig. 6.14**b**. The growth of entanglement entropy also shows a stark contrast between initial states. Compared to the thermal states, the $|\Pi\rangle$ state exhibits a slow linear growth with superposed oscillations. The small oscillations are in correspondence with the peaks and valleys observed in the fidelity dynamics, with roughly half the period of the latter. Furthermore, we show the entropy dynamics with different subsystems $\{u_1, u_2\}$ and $\{u_1, d_1\}$ in the inset of Fig. 6.14**c**, confirming the rainbow entanglement structure previously sketched in Fig. 6.10 **b**.

We note that, unlike in our initial numerical simulations on Fig. 6.12, Fig. 6.14 shows a weak population and fidelity decay, along with a slow growth of entanglement after a quench form the $|\Pi\rangle$ state. This is due to the presence of the J_x cross-couplings and of a less strong suppression of the third level on each site. effectively, this means that the full Hamiltonian in our superconducting chip is given by

$$\begin{aligned}
\hat{H}_{\mathrm{exp}} &= \hat{H} + \hat{H}_{\mathrm{x}} + \hat{V}, \\
\hat{H}_{\mathrm{x}}/2\pi &= J_x \sum_{k=1}^{M-1}\left(\hat{\mathbf{u}}_k^+\hat{\mathbf{d}}_{k+1}^- + \hat{\mathbf{d}}_k^+\hat{\mathbf{u}}_{k+1}^- + \mathrm{h.c.}\right), \\
\hat{V}/2\pi &= \frac{\eta}{2}\sum_{k=1}^{M}\left(\hat{\mathbf{u}}_k^+\hat{\mathbf{u}}_k^+\hat{\mathbf{u}}_k^-\hat{\mathbf{u}}_k^- + \hat{\mathbf{d}}_k^+\hat{\mathbf{d}}_k^+\hat{\mathbf{d}}_k^-\hat{\mathbf{d}}_k^-\right).
\end{aligned} \tag{6.43}$$

Here, $\hat{H}$ denotes the Hamiltonian of Eq. (6.13), which has been reformulated in terms

of bosons to allow multiple photons on a single site. The operators $\hat{\mathbf{u}}^{\pm}$ and $\hat{\mathbf{d}}^{\pm}$ are then the bosonic raising/lowering operators on the upper and lower chain respectively.

When simulating these perturbations, we will consider a maximum of 2 photons per site as triple occupations are highly suppressed. The last two terms represent the experimental imperfections due to the cross coupling J_x between the diagonal qubits and anharmonicity η of the transmon qubits [7]. Numerical simulations accounting for these additional terms, shown by lines in Fig. 6.14, confirm that these perturbations capture the main sources of decay of local observables and entanglement growth. The effect of these perturbations, however, is sufficiently weak such that clear signatures of the two families of scars can be observed.

To probe the second family of scars, we use the state $|\phi_L\rangle$. It can be prepared using the circuit schematically shown in Fig. 6.14**d**, which is composed of a few single-qubit and two-qubit gates. By utilising high-precision tomography measurements, we then obtain the reduced density matrix of the subsystems $\{k = 1, 2\}$ or $\{k = 2, 3\}$. Its value at $t = 0$ is visualised in Fig. 6.14**e**, demonstrating that the entangled state $|\phi_L\rangle$ is successfully prepared. To reveal the difference between the first and second family of scars, we focus on the subsystem $A' \equiv \{k = 2, 3\}$, whose fidelity $F_{k=2,3}(t)$ and entanglement entropy $S_{k=2,3}(t)$, are plotted in Figs. 6.14**f-g**. The choice of the subsystem is motivated by the fact that it leads to entropy $\ln(2)$ for the $|\phi_L\rangle$ initial state, while the entropy is still trivially zero for the $|\Pi\rangle$ state (up to the influence of the cross-couplings). This distinction is verified in our experiment, as shown in Fig. 6.14**d**.

6.4 Summary

We have presented the first experimental realisation of QMBS states in a solid-state SC platform. Our circuit emulates the quantum many-body systems effectively described by the hard-core Bose-Hubbard model – a model of particles freely hopping on a lattices – with local interactions. This is in contrast with previous realisations of QMBSs in ultracold atomic systems [4, 43], which relied on particles being kinetically constrained. In the 1D circuit example, scarring was engineered by utilising a regular subgraph intrinsic to the Hilbert space and taking advantage of the high level of control of our SC platform to reduce the connectivity of the subgraph to the rest of the Hilbert space. This is essentially the same mechanism that we proposed in Chapter 5 to engineer scarring in the tilted Fermi-Hubbard model. We have also provided an in-depth characterisation of QMBSs using quantum state tomography on multi-qubits subsystems. By observing the population dynamics and entanglement entropy, we distinguished the weak ergodicity breaking associated with QMBS initial states from the conventional thermalising states.

In a 2D circuit, we have used the rainbow scar method to realise two families of non-thermalising states. Our construction allows to write down exact wave functions for these states, even in the disordered case. The existence and stability of QMBSs in the presence of disorder have recently attracted much attention in theoretical studies [75, 79, 112, 245, 246]. Beyond demonstrating experimentally that scarring can survive in

the presence of disorder, our model actually allows to uniquely tailor the structure of QMBS states through the disorder realisation. To the best of our knowledge, this is the first model with such a capability. Similar to the 1D experiment, signatures of rainbow entanglement were observed on our SC device by performing quantum state tomography of a many-body state of the ladder following the quench from special initial states, confirming the expected hallmarks of QMBS behaviour.

While throughout this chapter the disorder strength was assumed to be sufficiently weak such that the system overall remains chaotic, the versatility of our setup allows direct access to *strong* ergodicity-breaking regimes, where many-body localisation was recently proposed to give rise to new types of "inverted scarring" phenomena [130–132]. More generally, our work bridges the gap between theoretical studies of QMBSs, which place the emphasis on exact constructions of scarred eigenstates [90, 91], and experimental realisations, e.g., in Rydberg atom arrays [43, 78] or optical lattices [4], in which the scarred states are not known exactly (apart from a few exceptions [72]). In contrast, our model in Eq. (6.12) hosts exact scars. While our experiment contains additional perturbations, they were shown to be sufficiently weak in our device to allow unambiguous observation of scar signatures. It would be interesting to study in detail their effects on the stability of QMBS states in larger circuits or higher-dimensional geometries that would rapidly exceed the capability of classical computers.

6. TUNABLE MANY-BODY SCARS ON A SUPERCONDUCTING QUANTUM PROCESSOR

Chapter 7

Conclusions and outlook

Unravelling how quantum systems thermalise is one of the great challenges of quantum mechanics. A major leap in understanding was the formulation of the Eigenstate Thermalisation Hypothesis (ETH) [13, 156], that relates the late-time behaviour of observables with special properties of eigenstates. However, although the ETH was put forward in the early 1990s, special cases of its violations are still being discovered, like many-body localisation (MBL) and quantum and many-body scars (QMBSs). The latter are quite special, as unlike MBL or other non-ergodic systems like integrable ones, they only weakly violate the ETH. This translates into dynamics from most initial states displaying thermalisation, with a few specific states leading to long-lived coherent oscillations. This new discovery generated some excitement as a way of protecting quantum information from scrambling, even in a chaotic system. Following the original observation of QMBSs, a plethora of theoretical realisations have been formulated. However, experimental realisations of QMBSs are still largely confined to the Rydberg atom platform in which they were first observed. This scarcity of new experimental realisations, along with difficulties of taking advantages of their special properties, means that QMBSs are currently still rarely used in quantum technology.

In this thesis, we have tackled this problem by developing new realisations of QMBSs inspired by the current generation of quantum simulators. In particular, we have targeted the popular platforms of ultracold atoms in optical lattice (with both fermions and bosons) and superconducting qubits. Through close collaboration with experimentalists working on these devices, we have conclusively demonstrated that our theoretical proposals lead to strong QMBS signatures in the lab. For example, in Chapter 4 we have realised the PXP model in a Bose-Hubbard model using ultracold bosons. Beyond making this model available to a much broader class of experimental devices, this new realisation also has advantages over its Rydberg atom version. Indeed, in both cases the PXP model is the leading order term driving the dynamics, but the additional couplings at higher orders are different. Importantly, in the Bose-Hubbard case it is

possible to suppress all unwanted terms provided the experimental device can produce high enough values of tilt and on-site interaction. Meanwhile, in the Rydberg case there is always a trade-off between a perfect blockade and next-nearest-neighbour interactions. Thus, our new implementation provides a way to create a more pristine version of the PXP model. Similarly, the models we proposed in Chapter 6 for superconducting (SC) qubit systems also offer important advantages over the other platforms, the most obvious one being the high tunability of individual couplings. Beyond that, the SC qubit processor also supports larger coupling amplitudes that directly drive the coherent dynamics. These are of the order of $\sim 10^7$ Hz in the SC platform, compared to $\sim 10^3$ Hz for Bose gases [247] (and only around 50 Hz in Chapter 4) and $\sim 10^6$ Hz for Rydberg atom [78]. This means that the SC platform can process the same quantum information in a shorter amount of time.

In order to create scarring in these different platforms, we have relied on a few different mechanisms. One common theme in our approach was using resonances to engineer effective models with kinetic constraints in otherwise unconstrained models. This provides a relatively simple way to recreate models like PXP in a multitude of systems. While kinetic constraints do not automatically imply QMBSs, through a graph-theoretic approach, we have revealed how the link between the two can emerge. While we have not included it in this thesis, we have studied this relation in more detail in a variety of models in Ref. [229]. In addition, we have used the same graph approach in an unconstrained model in Chapter. 6. We emphasise that our construction is one of the very few known ways to create non-exact scars in quantum systems and is an important addition to the various mechanisms reviewed in Chapter 2.

Beyond making scarring more widely available, we have also made several advances that make this phenomenon easier to use in quantum technology applications. This has been achieved by demonstrating conclusively that QMBSs offer an advantage for entanglement-enhanced metrology. Moreover, we have utilised the high-level of control of the SC platform to show that it is possible to tune the entanglement structure of scarred states. This opens many possibilities of dynamically controlling which states are protected from thermalisation, adding a new tool to trajectory-steering techniques based on QMBSs.

While the main focus of this work has been quantum many-body scarring in general, Chapters 3 and 4 have explored many facets of the PXP model in particular. In these chapters, we have uncovered several important – and hitherto unknown – properties of the PXP model, such as the presence of scarring from the polarised initial state, the existence of multiple approximate su(2) representations, and superdiffusion in energy transport at late times. We have shown that the polarised state dynamics can be understood from the same approximate algebraic structure as the Néel state, with the difference that the quality of the algebra depends on the number of excitations. For the multiple su(2) representations, their origin can be traced back to the spin-1 parent model from Ref. [68], however this still leaves many questions open. For example, the resilience of spin-1 eigenstates to the perturbations naturally present in the PXP model remains a puzzle. Moreover, the consequences of these multiple algebraic structures are

also largely unexplored. The oscillations that can been seen in the spectral form factor and energy transport in an infinite temperature Gibbs state imply that stronger signs of ergodicity breaking should be visible at finite temperatures. This could lead to scarring being actually resilient to finite temperatures, which would be very useful for experimental realisations. Finally, there is still much to understand regarding the anomalous transport in the PXP model. Most importantly, it remains an open question if the model is truly superdiffusive at all times, or if diffusion is eventually recovered at very late times. Furthermore, the origin of the observed superdiffusion is also unclear. While proximity to integrability provides a compelling narrative, the observed robustness of this behaviour to detuning makes it unlikely. Further study of these properties is needed, especially to understand the role of the constraints in their appearance and if they can be found in other similar models. As the results are currently only numerical, observing this anomalous energy transport in an actual quantum simulator would confirm these findings and show their robustness to experimental perturbations.

The implications of our findings for other interpretations of the PXP model should also be considered. As we have mentioned in Chapter 2, the PXP model is equivalent to a spin-1/2 regularisation of a U(1) lattice-gauge theory [80]. This provides an interesting interpretation of scarring as a "string-inversion" mechanism. It also opens a way to explore generalisations of the PXP model to higher values of spin in a way that is different from previous studies [59]. In our works [81, 82], which we did not discuss in this thesis, we have found that scarring actually survives for these higher-spin regularisations. The staggered magnetisation, which we mentioned in Chapter 3 as a mechanism for improving the revivals in the PXP model, has a particularly interesting interpretation in the lattice gauge theory language: it corresponds to the potential which induces confinement of pairs of particles and anti-particles. This implies that confinement can make scarring stronger, as we have numerically demonstrated in Ref. [3]. The interplay between scarring and confinement is currently not well understood and it is also unclear if this enhancement persists for higher spin values. As classical simulation becomes harder with increasing spin, developing a way to simulate these models on quantum hardware would likely provide an advantage already for small system sizes.

Beyond the PXP model, there are still big gaps in the overall understanding of QMBSs. Most mechanisms leading to exact scars can be unified using the commutant algebra framework [118–121], which also describes Hilbert space fragmentation and usual symmetries. However, this construction is not applicable to cases where the scarred subspace is not fully isolated from the thermal bulk. More generally, few formal results have been derived for non-exact scars, despite them forming the majority of experimentally relevant models. This means that there is no simple way of comparing different scarred models or of predicting their thermalisation timescale. The consequences of this lack of quantitative results are perhaps best illustrated in the PXP model with its multiple approximate su(2) representations. While the level statistics are that of a chaotic model with level repulsion, which suggest that most states obey the ETH and that any randomly picked product state will thermalise at infinite-time, the spectral form factor and transport properties still shows anomalous behaviour way

beyond the expected thermalisation timescale. These global non-ergodic signatures in a system that obeys the weak ETH call for markers of thermalisation that do not solely rely on infinite-time properties. Alternatively, it also questions the relation between weak and strong ETH violations. This could be explored for example in the interplay between many-body localisation and quantum scars, as made possible by our rainbow scars construction in the SC qubit device.

Finally, another major open question that was brought into focus by QMBS research is the lack of a general procedure for defining a classical limit for general many-body systems, in a way that has been achieved for single-particle scars. While such a limit has been found in the PXP model [59] and it can be generalised to other systems [142], it is a rather *ad hoc* procedure that requires prior knowledge of the scarred dynamics. Quantum field theories offer a promising way of going beyond that as they admit a well-defined classical limit and QMBSs have recently been found in these systems [248, 249]. Importantly, as some quantum field theories have direct links to microscopic quantum many-body models, this could provide a direct way to establish classical limits for the latter as well.

Appendix A

Infinite-time average of the quantum Fisher information

In this Appendix, we derive the long-time value of the quantum Fisher information from the diagonal ensemble. In particular, we focus on the case of the PXP model that we then use in Chapter 3.

As discussed in Chapter 2, if the spectrum of the Hamiltonian used for time-evolution is non-degenerate, then for an operator $\hat{O}$ the long-time average obeys the diagonal ensemble prediction as

$$\overline{\langle \hat{O} \rangle}_\infty = \lim_{T\to\infty} \frac{1}{T} \int \mathrm{d}t \, \langle \psi(t)|\hat{O}|\psi(t)\rangle = \sum_n |c_n|^2 O_{n,n}, \tag{A.1}$$

where $O_{i,j} = \langle E_i|\hat{O}|E_j\rangle$, $c_n = \langle E_n|\psi\rangle$, and $|E_j\rangle$ is the eigenstate of $\hat{H}$ with energy E_j. In the case of the PXP model we also need to consider the large number of "zero modes" [53, 54, 226] and treat them separately, leading to

$$\overline{\langle \hat{O} \rangle}_\infty = \lim_{T\to\infty} \frac{1}{T} \int \mathrm{d}t \, \langle \psi(t)|\hat{O}|\psi(t)\rangle = \sum_{\substack{n \text{ s.t.} \\ E_n \neq 0}} |c_n|^2 O_{n,n} + \sum_{\substack{n,m \text{ s.t.} \\ E_n = E_m = 0}} c_n^\star c_m O_{n,m}. \tag{A.2}$$

To simplify the notation, we introduce the diagonal ensemble density matrix $\hat{\rho}$, such that $\rho_{m,n} = c_m^\star c_n \delta(E_m - E_n)$. In that case we simply have $\overline{\langle \hat{O} \rangle}_\infty = \mathrm{Tr}\left[\hat{\rho}\hat{O}\right]$. For the PXP model this allows to compute the infinite-time average of the staggered magnetisation $\hat{M}_S$ and of its square $\hat{M}_S^2$. However in order to get the QFI we also need the infinite-time average of $\langle \hat{O} \rangle^2$. Explicitly computing this quantity leads to the more

complicated expression

$$\begin{aligned}\lim_{T\to\infty}\frac{1}{T}\int \mathrm{d}t\,\langle\hat{O}\rangle^2 &= \sum_{a,b,c,d} c_a^\star c_b c_c^\star c_d O_{a,b}O_{c,d}\lim_{T\to\infty}\frac{1}{T}\int \mathrm{d}t\,\mathrm{e}^{it(E_a-E_b+E_c-E_d)}\\ &= \sum_{a,b,c,d} c_a^\star c_b c_c^\star c_d O_{a,b}O_{c,d}\delta(E_a-E_b+E_c-E_d),\end{aligned} \tag{A.3}$$

with the Dirac delta now holding 4 energies instead of 2. Fortunately, as the number of combinations that satisfy it is relatively limited, this is still tractable numerically.

The simplest case is $E_a = E_b$, $E_c = E_d$, which can be rewritten as

$$\sum_{a,c}|c_a|^2|c_c|^2O_{a,a}O_{c,c} = \left(\sum_a |c_a|^2 O_{a,a}\right)\left(\sum_c |c_c|^2 O_{c,c}\right) = \left(\mathrm{Tr}\left[\hat{\rho}\hat{O}\right]\right)^2 = \left(\overline{\langle\hat{O}\rangle}_\infty\right)^2. \tag{A.4}$$

We note that for brevity, the first two terms are shown assuming no degeneracies in the spectrum. To include the degeneracies would require keeping the four indices a to d and adding $\delta(E_a - E_b)\delta(E_c - E_d)$, leading to a bulky expression. Nonetheless, expressing this term as $\left(\mathrm{Tr}\left[\hat{\rho}\hat{O}\right]\right)^2$ takes into account the degeneracies and that is what we will use in the final expression. The other cases will be treated in similar fashion.

Another possibility to satisfy the Dirac delta is to have $E_a = E_d$ and $E_b = E_c$. In that case we have

$$\sum_{a,b}|c_a|^2|c_b|^2O_{a,b}O_{b,a} = \sum_{a,b}\langle\psi|E_a\rangle\langle E_a|\hat{O}|E_b\rangle\langle E_b|\psi\rangle\langle\psi|E_b\rangle\langle E_b|\hat{O}|E_a\rangle\langle E_a|\psi\rangle = \mathrm{Tr}\left[\hat{\rho}\hat{O}\hat{\rho}\hat{O}\right]. \tag{A.5}$$

Finally, as in the PXP model the spectrum is symmetric around E=0, the last possibility is E_a=$-E_c$ and E_b=$-E_d$. However for $\hat{M}_S$ in the momentum sectors k=0 and k=π (where the Néel state has support) we can take advantage of the eigenstates, the operator, and the initial state being real. Indeed, as the Hamiltonian projected to one of these sectors is real and symmetric, the eigenvectors themselves can be chosen to be real. In that case $c_a = c_a^\star$ (as all initial states are real in the Fock basis) and $(\hat{M}_S)_{a,b} = (\hat{M}_S)_{b,a}$ since the matrix is symmetric (as it is both real and Hermitian). We can then rewrite

$$\sum_{a,b} c_a^\star c_b c_a^\star c_b O_{a,b}O_{a,b} = \sum_{a,b} c_a^2 c_b^2 O_{a,b}O_{b,a}\sum_{a,b}|c_a|^2|c_b|^2O_{a,b}O_{b,a} = \mathrm{Tr}\left[\hat{\rho}\hat{O}\hat{\rho}\hat{O}\right], \tag{A.6}$$

which is the same as the contribution with E_a=E_d and E_b=E_c.

Summing all these contributions together, we can compute the long-time average of the QFI in the PXP model in the sectors $k = 0$ and $k = \pi$ for a real-valued operator $\hat{O}$, and from a real initial state $|\psi\rangle$, as

$$\begin{aligned}&\lim_{T\to\infty}\frac{1}{T}\int \mathrm{d}t\, 4\left(\langle\psi(t)|\hat{O}^2|\psi(t)\rangle - \langle\psi(t)|\hat{O}|\psi(t)\rangle^2\right)\\ &= 4\,\mathrm{Tr}\left[\hat{\rho}\hat{O}^2\right] - 4\left(\mathrm{Tr}\left[\hat{\rho}\hat{O}\right]\right)^2 - 8\,\mathrm{Tr}\left[\hat{\rho}\hat{O}\hat{\rho}\hat{O}\right].\end{aligned} \tag{A.7}$$

Appendix B

Effect of staggered magnetisation on the PXP model

In this Appendix, we investigate the effect of adding staggered magnetisation to the PXP Hamiltonian. More precisely, we study the Hamiltonian

$$\hat{H}_{\text{Stag}} = \Omega \sum_{j=1}^{N} \hat{P}_{j-1}\hat{\sigma}_j^x \hat{P}_{j+1} + \chi \sum_{j=1}^{N} (-1)^j \hat{\sigma}_j^z. \tag{B.1}$$

To simplify the notation, we will keep $\Omega = 1$ and thus χ will be expressed in units of Ω. This Hamiltonian has previously been studied in Ref. [250] in the limit of $\chi \gg \Omega$. In this regime, the Hilbert space fractures and an emergent symmetry appears due to an approximate su(2) algebra. It has also been studied when driven [85]. Here we instead investigate the experimentally relevant regime where the staggered magnetisation is time independent but with strength χ of the same order as Ω.

We recall that the staggered magnetisation is equal to $2\hat{S}^z$ in the spin-1 parent Hamiltonian while the PXP itself is akin to $\sqrt{2}\hat{S}^x$, recall Eq. (2.44). Using the spin-1 representation, Eq. (B.1) can be expressed as

$$\left(\sqrt{2}\hat{\mathbf{S}}^x + \hat{\mathbf{H}}_1 + \hat{\mathbf{H}}_2\right) + 2\chi\hat{\mathbf{S}}^z = \hat{H}_{\text{Stag}} \oplus \hat{H}_\perp, \tag{B.2}$$

where the exact form of $\hat{H}_\perp$ is unimportant as it acts in the complement of the PXP subspace. Without $\hat{\mathbf{H}}_1$ and $\hat{\mathbf{H}}_2$, the Hamiltonian in Eq. (B.2) would be a free spin-1 model. There would then be perfect revivals from the Néel state ($|-0-\cdots-0-\rangle$ in the spin-1 language) with a period

$$T = \frac{2\pi}{\sqrt{4\chi^2 + 2}}. \tag{B.3}$$

This can be understood from a spin precession point of view, as discussed in Section 3.2.1 and illustrated in Fig. 3.5**a**. Without $\hat{\mathbf{H}}_1$ and $\hat{\mathbf{H}}_2$, there would be perfect

B. EFFECT OF STAGGERED MAGNETISATION ON THE PXP MODEL

revivals for all values of χ. As we know that in the actual PXP models revivals are not perfect at $\chi = 0$ and that the fidelity $\mathcal{F}(t)$ will be identically 1 for $\chi \to \infty$, we naïvely expect that the fidelity will increase monotonically as χ gets larger. However, for a large value of χ, this is no longer due to scarring but only to the dynamics being restricted to one of the edges of the spectrum. This manifests itself by a large fidelity even between the revivals. We will denote the first revival peak of the self-fidelity by $\mathcal{F}_1$, and the self-fidelity at half that time by $\mathcal{F}_{1/2}$. The signature of QMBSs therefore is $\mathcal{F}_1 \approx 1$ and $\mathcal{F}_{1/2} \approx 0$. Hence, we will use the quantity $\mathcal{F}_1 - \mathcal{F}_{1/2}$ as a probe of QMBSs, where it expected to take values close to 1. This quantity distinguishes QMBSs from the trivial situation where the initial state is close to an eigenstate, in which case $\mathcal{F}(t) \approx 1$ at all times and the fidelity difference is strongly suppressed, $\mathcal{F}_1 - \mathcal{F}_{1/2} \ll 1$.

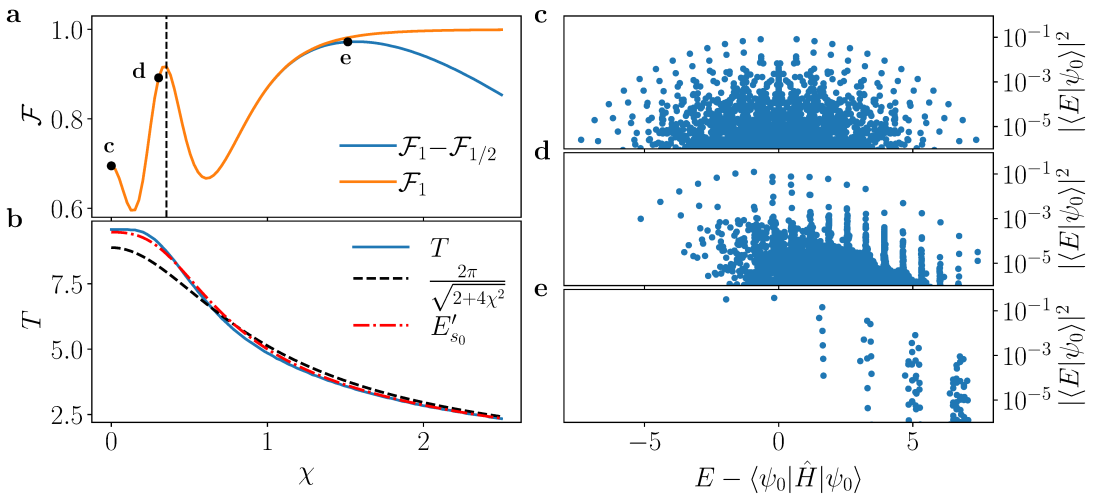

Figure B.1: Effect of staggered magnetisation on the Néel state in the PXP model with $N = 26$. **a** The first fidelity peak $\mathcal{F}_1$ is large for all values of χ, indicating the presence of revivals. However, as χ becomes large, the Néel state effectively becomes an eigenstate, leading to an increase of $\mathcal{F}_{1/2}$ and therefore a decrease of $\mathcal{F}_1 - \mathcal{F}_{1/2}$. The vertical dashed line is at $\chi = 1/\sqrt{8}$, corresponding to the prediction of perturbation theory for the maximum. **b** The revival period T is in good agreement with the prediction based on spin precession, $2\pi/\sqrt{2+4\chi^2}$. The red dashed-dotted line labelled E'_{s_0} shows the period according to perturbation theory. **c-e** The non-monotonic behaviour of $\mathcal{F}$ as a function of χ can be related to changes in the structure of the overlap between the Néel state and the energy eigenstates $|E\rangle$, here plotted for $\chi = 0$, $\chi = 0.3$ and $\chi = 1.52$. The value of χ corresponding to each plot is also indicated on panel **a**.

In Fig. B.1**a**, we plot both $\mathcal{F}_1$ and $\mathcal{F}_1 - \mathcal{F}_{1/2}$ as a function of staggered magnetisation for the PXP model with the Néel initial state. We observe interesting non-monotonic behaviour as a function of χ. Fig. B.1**b** shows the period of the revivals, and displays pretty good agreement with the prediction in Eq. B.3. The effect of χ can also be seen in the overlap between the Néel state and the corresponding PXP eigenstates, as shown in Fig. B.1**c-e**. The top band of scarred states is always visible. However, as χ is increased, the eigenstates with the highest overlap shift from the middle of the

spectrum towards its left edge, where the ground state resides.

While the precession picture, discussed in Chapter 3, gives a relatively good approximation of the revival period, it also predicts the revivals would increasingly get better as χ becomes larger. Indeed, as $\mathbf{S}^z$ starts to dominate, the relative contribution of $\hat{\mathbf{H}}_1$ and $\hat{\mathbf{H}}_2$ becomes weaker, until we reach the limit $\chi = \infty$ where the model becomes integrable. This is in stark contrast with the observed non-monotonic behaviour, in particular with the strong revival enhancement around $\chi \approx 0.342$. To explain this behaviour, we will use perturbation theory to more precisely compute the action of $\hat{\mathbf{H}}_1$ and $\hat{\mathbf{H}}_2$ on the eigenstates of $\sqrt{2}\hat{\mathbf{S}}^x + 2\chi\hat{\mathbf{S}}^z$. This approach predicts a maximum in fidelity at $\chi = 1/\sqrt{8} \approx 0.353$, close to the observed value as shown in Fig. B.1**a**. It also gives a better approximation of the revival period, see Fig. B.1**b**.

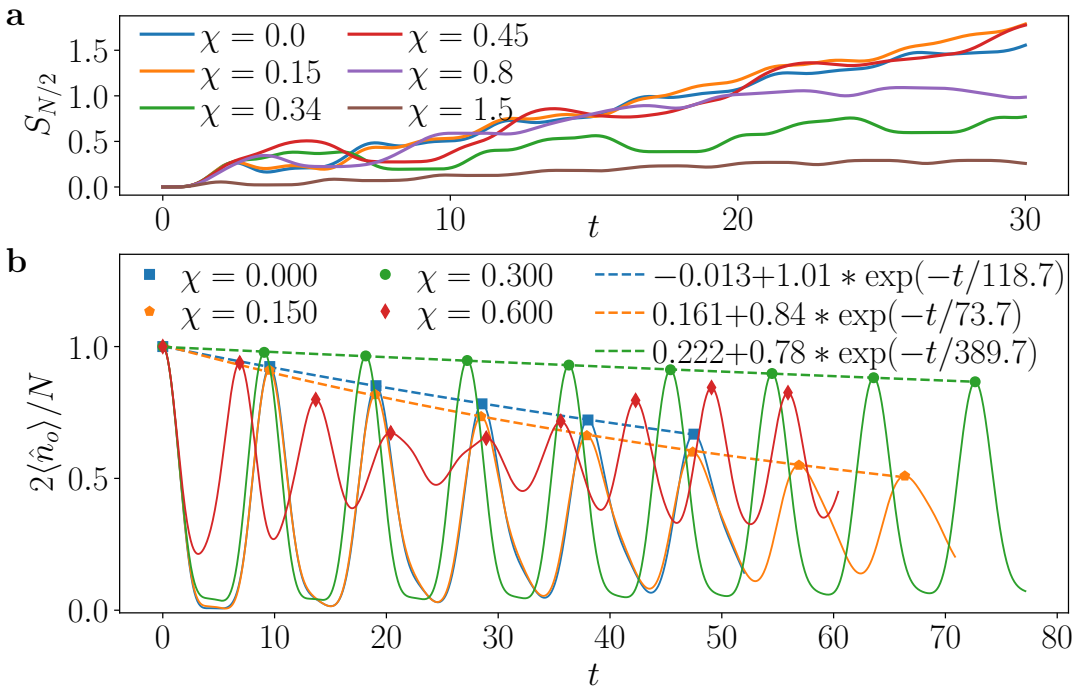

Figure B.2: **a** Bipartite von Neumann entanglement entropy after a quench from the Néel state for $N = 26$ and various values of χ. The entropy growth is strongly suppressed around $\chi = 0.34$. **b** Excitation density on odd sites for $N = 32$ and various values of χ and their exponential fit. Only times for which the expectation values are converged in system size are used. Once $\chi \geq 0.5$ oscillations are visible in the peaks and an exponential decay no longer describes their behaviour with time.

Before using the perturbative approach, let us first verify that other hallmarks of scarring are also present around $\chi \approx 0.342$. We find that the growth of entanglement entropy is highly suppressed near that point, as shown in Fig. B.2**a**. This non-monotonicity in the post-quench behaviour as a function of χ can also be witnessed in local observables, measurable in experiment. For a local observable, we choose the

B. EFFECT OF STAGGERED MAGNETISATION ON THE PXP MODEL

excitation density $\frac{2}{N}\langle \hat{n}_o \rangle$ on the odd sublattice, where $\hat{n}_o = \sum_{j \text{ odd}} \hat{n}_j$. In order to avoid finite-size effects, we consider only the times where the dynamics is converged in system size for $N = 32$. As the sublattice density oscillates in time, we first identify the local maxima and then fit its envelope. The results are shown in Fig. B.2**b** for several values of χ. Overall, we find a clear enhancement of QMBS revivals around $\chi = 0.3$ compared to other values. The decay time τ shows an approximately 3-fold increase around $\chi = 0.3$ compared to case with $\chi = 0$ (see legend). Finally, we see that for $\chi = 0.6$ the peaks themselves show an oscillatory behaviour and are no longer well approximated by a decaying exponential. We emphasise that this is not a finite-size effect but rather a sign that we enter the low-energy regime where only a handful of eigenstates participate in the dynamics. The oscillation in the maxima is then a beating frequency linked to the mismatch in the energy spacing of these eigenstates.

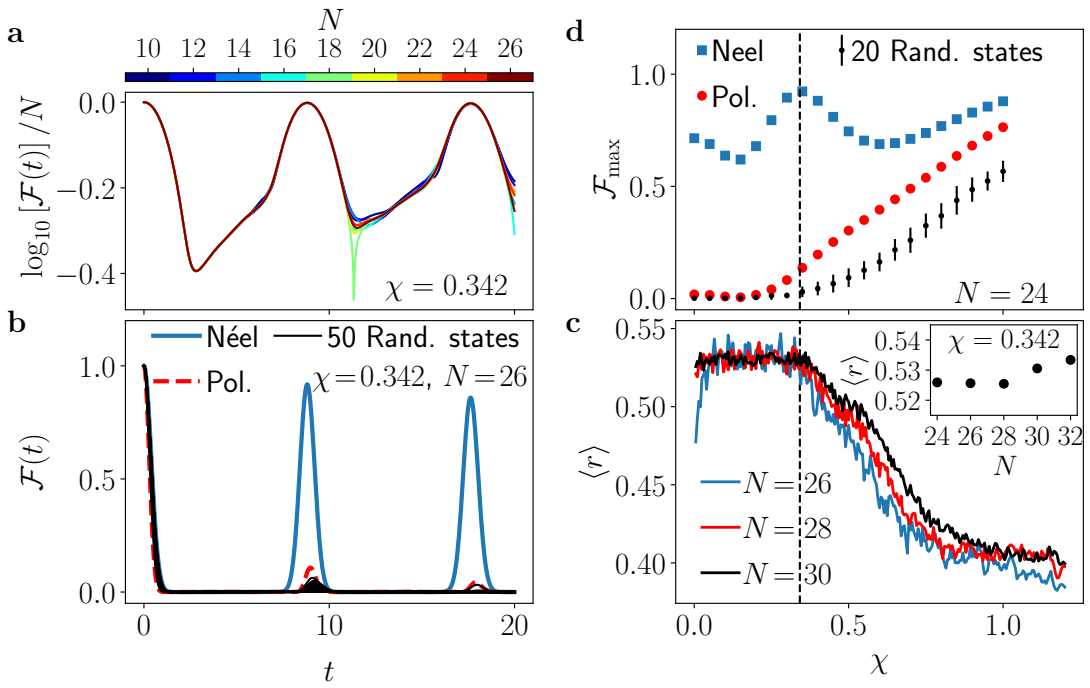

Figure B.3: Ergodicity of the PXP model with staggered magnetisation. **a** Fidelity density after a quench from the Néel state. The data is converged with system size already at small values of N. **b** Quench from various initial states at $\chi = 0.342$. **c** Maximum return fidelity after quench from various states for a wide range of values of χ. The non-monotonic behaviour is only visible for the Néel state. **d** Average level-spacing ratio for different system sizes and values of χ. At $\chi = 0.342$, $\langle r \rangle \approx 0.53$ as expected from a chaotic system. The system becomes more ergodic as the system size is increased, as shown in the inset.

Near the optimal χ, we also verify that the oscillations are stable in system size. To do that, we study the fidelity density $\log_{10}(\mathcal{F}(t))/N$, shown in Fig. B.3**a**. The agreement between different system sizes is almost perfect. We check the fidelity after

quenches from different states to assess to which extent the Néel state is atypical, as shown in Fig. B.3**b-c**. While the polarised starts showing revival with a small fidelity at $\chi = 0.342$, it is nowhere near that observed for the Néel state. Furthermore, randomly chosen states still thermalise as expected. Finally, to make sure that the system is still chaotic and is not fragmented due to χ being too large, we compute the average level spacing ratio $\langle r \rangle$ for various values of χ and system sizes. This is shown in Fig. B.3**d** and demonstrates good agreement with the Wigner-Dyson value at $\chi = 0.342$. Based on these different metrics, we can conclude that what we observe in our numerical simulation is genuine quantum many-body scarring and investigate the origin of this behaviour.

In order to understand the non-monotonic behaviour, we construct the states $|S_k\rangle$, which are the eigenstates $|\mathbf{S}_k\rangle$ of the spin-1 operator $\sqrt{2}\hat{\mathbf{S}}^x + 2\chi\hat{\mathbf{S}}^z$ (with $E_k = k\sqrt{2+4\chi^2}$) projected into the constrained PXP space, with $k = -N/2, -N/2+1, \ldots, N/2$. For simplicity, let us denote the number of sites in the spin-1 model by $N_b = N/2$. In Chapter 2, we have reviewed how these states provide a good approximation at $\chi = 0$ as found in Ref. [68]. By computing the energy variance of these approximate eigenstates, one can get a qualitative picture of how close the projected states are to the true PXP eigenstates. The lower the variance, the better the agreement and so the better we expect the spin-precession picture to hold. Formally, we define the energy variance for these states as, $\sigma^2_{E_k} \equiv \langle S_k|\hat{H}^2_{\mathrm{PXP}}|S_k\rangle - \langle S_k|\hat{H}_{\mathrm{PXP}}|S_k\rangle^2$. The variance is shown in Fig. B.4**a**, where we observe very different behaviours depending on the value of k. In

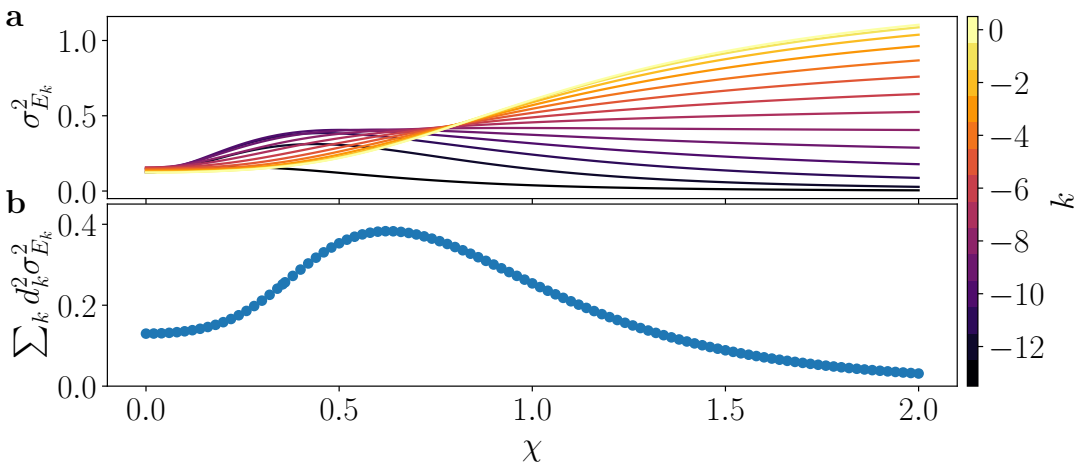

Figure B.4: Energy variance of the $|S_k\rangle$ states in the PXP model with $N = 26$. **a** Data for individual states. **b** Data weighted by the overlap with the Néel state, which accounts for their relevance in the dynamics. The non-monotonic behaviour in χ with local minima at $\chi = 0$ and $\chi \to \infty$ is clearly visible. This explains why these points are local maxima of revival fidelity.

order to pick out the relevant states, we need to understand their overlap with the Néel state. At $\chi = 0$, the Néel state can be written as a superposition of the $|\mathbf{S}_k\rangle$ states

as [68]

$$|\mathbb{Z}_2\rangle = \sum_{k=-N_b}^{N_b} d_k \, |\mathbf{S}_k\rangle \,, \quad d_k^2 = \binom{2N_b}{k+N_b}. \tag{B.4}$$

For arbitrary χ, a similar expansion holds with the weights given by

$$d_k^2 = \frac{\binom{2N_b}{k+N_b}}{4^{N_b}} \frac{(\sqrt{2}\chi - \mathrm{sgn}(k)\sqrt{1+2\chi^2})^{2|k|}}{(1+2\chi^2)^{N_b}}. \tag{B.5}$$

A simple argument as to why this is possible is that the Néel state is the highest-weight eigenstate of $\hat{\mathbf{S}}^z$ in the spin-1 picture. This implies that it also has maximal total spin, and the $|\mathbf{S}_k\rangle$ always form a basis of maximal total spin states. We can then use this to compute the average of the $\sigma^2_{E_k}$ weighted by it. This is shown in Fig. B.4**b**, where we observe a non-monotonic behaviour in χ. The local minima at $\chi = 0$ and $\chi \to \infty$ are visible, and this explain why as we go away from these points the fidelity of the revivals starts to decay. However, there is no local minimum visible around $\chi \approx 0.34$ here. To understand its appearance, a finer analysis is needed that also accounts for the energy spacing of the eigenstates.

For that we need to compute the perturbation of the energies of the $|\mathbf{S}_k\rangle$ states due to the presence of $\hat{\mathbf{H}}_1$ in the full Hamiltonian in Eq. (B.2). We can completely disregard $\hat{\mathbf{H}}_2$ as it it will not lead to an energy shift because $\hat{\mathbf{P}}\hat{\mathbf{H}}_2 = 0$ (see Section 2.4.3). Thanks to the simple structure of the $|\mathbf{S}_k\rangle$, it is possible to compute analytically the first-order correction as $\Delta E_k = \langle \mathbf{S}_k | \hat{\mathbf{H}}_1 | \mathbf{S}_k \rangle$. Our derivation follows closely the one in Appendix D of Ref. [68]. To match the notation used in that work, we will temporarily change the indexing of the $|\mathbf{S}_k\rangle$ (with $k = -N_b$ to N_b) to $|\mathbf{S}_n\rangle$ with $n = 0$ to $2N_b = N$. As the Hamiltonian of which the $|\mathbf{S}_n\rangle$ are eigenstates is the same as for $\chi = 0$ up to a rotation around $\hat{\mathbf{S}}^y$, the $|\mathbf{S}_n\rangle$ will also be identical up to a rotation. The eigenstate n will have energy $E_n = (n - N_b)\sqrt{2+4\chi^2}$. The construction from Ref. [68] is not fundamentally modified, meaning that the state $|\mathbf{S}_{N-n}\rangle$ can still be computed by applying a lowering operator on $|\mathbf{S}_N\rangle$. We can then also target a pair of spin-1 sites and decompose it in the basis of the local $\sqrt{2}\hat{\mathbf{S}}^x + 2\chi\hat{\mathbf{S}}^z$ operator with total spin equal to 2. Let us denote these local eigenstates as $|\hat{T}_2, m\rangle$, where m is the magnetisation quantum number. It is straightforward to compute $\delta e^m = -\langle \hat{T}_2, m | (|+,0\rangle + |0,-\rangle) \langle +,- | \, |\hat{T}_2, m\rangle$, and we get

$$\delta E_2 = -\delta E_{-2} = -\frac{\sqrt{2}}{8}\frac{1}{(1+2\chi^2)^{3/2}}, \quad \delta E_1 = -\delta E_{-1} = -\frac{\sqrt{2}}{2}\frac{\chi^2}{(1+2\chi^2)^{3/2}}, \quad \delta E_0 = 0. \tag{B.6}$$

The next step is to compute the coefficients c_m that describe the weight of the state $|\mathbf{S}_{N-n}\rangle$ on $|\hat{T}_2, m\rangle$. Since this computation only depends on the number of times the lowering operator has been applied, it is completely unaffected by the rotation. Hence

we get the same values as in Ref. [68]:

$$c_2 = \prod_{M=N_b-n-1}^{N_b-2} \alpha(N_b, M), \tag{B.7}$$

$$c_1 = 2n \prod_{M=N_b-n}^{N_b-2} \alpha(N_b, M), \tag{B.8}$$

$$c_0 = \sqrt{6}n(n-1) \prod_{M=N_b-n+1}^{N_b-2} \alpha(N_b, M), \tag{B.9}$$

$$c_{-1} = 2n(n-1)(n-2) \prod_{M=N_b-n+2}^{N_b-2} \alpha(N_b, M), \tag{B.10}$$

$$c_{-2} = n(n-1)(n-2)(n-3) \prod_{M=N_b-n+3}^{N_b-2} \alpha(N_b, M), \tag{B.11}$$

with $\alpha(N_b, M) = \sqrt{(N_b-1)(N_b-2)-M(M-1)}$. The overall normalisation of the state is also unaffected and is given by

$$\mathcal{N}_{N-n} = \prod_{M=N_b-n+1}^{N_b} \left[N_b(N_b+1) - M(M-1)\right]. \tag{B.12}$$

To simplify computations, we can perform an additional step that is not used in Ref. [68]. These products can be recast is a more similar way, that allows to get cancellations between their terms. Indeed, by performing the change of variable $M = N_b - K$ we get

$$\mathcal{N}_{N-n} = \prod_{K=0}^{n-1} (K+1)(2N-K). \tag{B.13}$$

Similarly, using $M = N_b - 2 - K$ we get

$$|c_2|^2 = \prod_{K=0}^{n-1} (K+1) = \prod_{K=0}^{n-1} (K+1) \prod_{K=0}^{n-1} (2N-K-4) = \prod_{K=0}^{n-1} (K+1) \prod_{K=4}^{n+3} (2N-K), \tag{B.14}$$

which leads to the simple expression

$$\frac{|c_2|^2}{\mathcal{N}_{N-n}} = \prod_{K=0}^{3} \frac{2N-K-n}{2N-K}. \tag{B.15}$$

The same kind of transformation can be done for the other c_m to get

$$\frac{|c_2|^2}{\mathcal{N}_{N-n}} = \prod_{K=0}^{3} \frac{2N-K-n}{2N-K} \tag{B.16}$$

$$\frac{|c_1|^2}{\mathcal{N}_{N-n}} = \frac{4n}{2N-3} \prod_{K=0}^{2} \frac{2N-K-n}{2N-K} \tag{B.17}$$

$$\frac{|c_0|^2}{\mathcal{N}_{N-n}} = \frac{6n(n-1)(2N-n)(2N-n-1)}{\prod_{K=0}^{3}(2N-K)} \tag{B.18}$$

$$\frac{|c_{-1}|^2}{\mathcal{N}_{N-n}} = \frac{4n(n-1)(n-2)(2N-n)}{\prod_{K=0}^{3}(2N-K)} \tag{B.19}$$

$$\frac{|c_{-2}|^2}{\mathcal{N}_{N-n}} = \prod_{K=0}^{3} \frac{n-K}{2N-K}. \tag{B.20}$$

This simplification allows to directly compute the overall energy shift of $|\mathbf{S}_{N-n}\rangle$ for any N_b, n and χ as

$$\begin{aligned}\Delta E_{N-n} = N_b \sum_{m=-2}^{2} \frac{|c_m|^2}{\mathcal{N}_{N_b-n}} \delta E_m &= \frac{(n-N_b)[1+n^2-3N_b-2nN_b+2N_b^2-8n(n-2N_b)\chi^2]}{4\sqrt{2}(1+2\chi^2)^{3/2}(N_b-1)(2N_b-1)} \\ &= (n-N_b)\frac{(1-3N_b)+(N_b-n)^2(1-8\chi^2)+N_b^2(1+8\chi^2)}{4\sqrt{2}(1+2\chi^2)^{3/2}(N_b-1)(2N_b-1)}.\end{aligned} \tag{B.21}$$

This finally allows to get

$$\Delta E_n = -(n-N_b)\frac{(1-3N_b)+(n-N_b)^2(1-8\chi^2)+N_b^2(1+8\chi^2)}{4\sqrt{2}(1+2\chi^2)^{3/2}(N_b-1)(2N_b-1)}. \tag{B.22}$$

We can perform a change of variable to recover the label k for the energies as $k = n - N_b$, where k runs between $-N_b$ and $+N_b$. The state k then has energy E_k with the correction ΔE_k given by

$$E_k = k\sqrt{2+4\chi^2} \quad \text{and} \quad \Delta E_k = -k\frac{(1-3N_b)+k^2(1-8\chi^2)+N_b^2(1+8\chi^2)}{4\sqrt{2}(1+2\chi^2)^{3/2}(N_b-1)(2N_b-1)}. \tag{B.23}$$

In general, this cannot be factorised further. However, in the special case $\chi = 1/\sqrt{8}$, we find it reduces to $-2k/(5\sqrt{10})$. This is a remarkable result: for any state $|\mathbf{S}_k\rangle$, at first order its energy will be given by

$$E_k = k\left[\sqrt{\frac{5}{2}} - \frac{2}{5\sqrt{10}}\right] = \frac{23k}{5\sqrt{10}}. \tag{B.24}$$

As a consequence, the energy spacing between two consecutive eigenstates will simply be $\frac{23}{5\sqrt{10}}$, which is independent of both k and N_b. Thus, at first order, all scarred states are exactly equidistant for any system size. This means that any superposition of these

states will have good revivals, which explains the peak in fidelity around this value of χ.

This special property of the spacing at $\chi = 1/\sqrt{8}$ is linked to a change in the behaviour of ΔE_k. Namely, for $|\chi| < 1/\sqrt{8}$, ΔE_k is larger near the middle of the spectrum, while for $|\chi| > 1/\sqrt{8}$, ΔE_k is at its largest at the edges of the spectrum. This becomes much clearer after taking the thermodynamic limit, $N_b \to \infty$. We can define $s \equiv k/N_b$, where $s \in [-1, 1]$, to get

$$\Delta E_s = -N_b s \frac{(1+8\chi^2) + s^2(1-8\chi^2)}{8\sqrt{2}(1+2\chi^2)^{3/2}} \tag{B.25}$$

Adding the nominal reference energy of $sN_b\sqrt{2+4\chi^2}$, we get

$$E_s = sN_b \frac{15 + 56\chi^2 + 64\chi^4 - s^2(1-8\chi^2)}{32(1/2+\chi^2)^{3/2}} \tag{B.26}$$

It is straightforward to see that the sign of the only term non-linear in s (which causes unequal spacing in the spectrum) switches at $\chi = 1/\sqrt{8}$. As the period of revivals is determined by the energy difference between the eigenstates, we need to compute $E_{k+1} - E_k$ which becomes the derivative $\frac{1}{N_b}\frac{\mathrm{d}E_s}{\mathrm{d}s}$, leading to

$$E'_s = \frac{1}{N_b}\frac{\mathrm{d}E_s}{\mathrm{d}s} = \frac{15 + 56\chi^2 + 64\chi^4 - 3s^2(1-8\chi^2)}{32(1/2+\chi^2)^{3/2}}. \tag{B.27}$$

Finally, in order to predict the revival frequency, we need to target the value of s which maximises the overlap with the Néel state. Eq. (B.5) gives us the overlap with $|\mathbf{S}_k\rangle$; this is not the same as $|S_k\rangle$, however the difference between the two is polynomial in N_b. As we will show later, this means we can neglect this as a subleading correction in the limit $N_b \to \infty$. In the same limit, we can use the Stirling approximation

$$\binom{2N_b}{k+N_b} \approx \frac{e^{-2N_b H(\frac{k+N_n}{2N_b})}}{\sqrt{\pi(N_b+k)(1-k/N_b)}}, \tag{B.28}$$

where $H(x) = -x\ln(x) - (1-x)\ln(1-x)$ is the Shannon entropy function. We can then rewrite the d_k^2 using $s = k/N_b$ to get

$$d_s^2 = \frac{e^{-2N_b H(\frac{1+s}{2})}}{\sqrt{\pi N_b(1-s^2)}} \frac{(\sqrt{2}\chi - \mathrm{sgn}(s)\sqrt{1+2\chi^2})^{2N_b|s|}}{(1+2\chi^2)^{N_b}}. \tag{B.29}$$

Let us first focus on the case $\chi > 0$. In that regime, $\sqrt{2}\chi - \sqrt{1+2\chi^2}$ goes to 0 as χ becomes large while $\sqrt{2}\chi + \sqrt{1+2\chi^2}$ increases with χ. This is expected as the Néel state gets closer to the ground state for larger positive χ. A consequence is that for positive χ the maximum value will always be in the range $[-1, 0]$. We can then restrict to this range and drop the signum function and absolute values. In the end, this allows us to rewrite

$$d_s^2 = \frac{e^{-N_b f(s)}}{4^{N_b}(1+2\chi^2)^{N_b}\sqrt{\pi N_b(1-s^2)}}, \tag{B.30}$$

with

$$f(s) = (1+s)\ln(1+s) + (1-s)\ln(1-s) + 2s\ln\left(\sqrt{2}\chi + \sqrt{1+2\chi^2}\right). \tag{B.31}$$

We recognise here that in the thermodynamic limit the most important term is the exponential $e^{-N_b f(s)}$ and we use a saddle point approximation. This means that the maximum of d_s^2 will simply be the minimum of $f(s)$, which yields

$$s_0 = -\frac{2\chi^2 + \sqrt{2}\sqrt{1+2\chi^2}}{1+2\chi^2+\sqrt{2}\sqrt{1+2\chi^2}}. \tag{B.32}$$

This justifies why we can neglect the difference in norm between the $|\mathbf{S}_k\rangle$ and $|S_k\rangle$: as it is polynomial in N_b and s, it will irrelevant in the thermodynamic limit and lead to the same s_0.

A quick sanity check shows that Eq. (B.32) correctly yields $s_0 = 0$ at $\chi = 0$ and $s_0 \to -1$ as $\chi \to \infty$. A similar derivation can be done for $\chi < 0$, yielding the same formula but without the minus sign in front. This allows us to estimate the frequency of oscillations for a given χ after a quench from the Néel state by plugging s_0 into Eq. (B.27) and using $T = 2\pi/E'_{s_0}$. While this derivation is done in the thermodynamic limit, Fig. B.1**b** shows that this formula leads to a good agreement with numerical data for finite systems.

To conclude, the non-monotonic behaviour observed with χ is due to two factors. On the one hand, the projected states $|S_k\rangle$ stemming from the spin-1 free paramagnet are closer to true eigenstates of the PXP model at $\chi = 0$ and $\chi \to \pm\infty$. On the other hand, the energy shift caused by $\hat{\mathbf{H}}_1$ is the most homogeneous at $\chi = 1/\sqrt{8}$, leading to almost equal energy spacing of scarred states and better revivals. This explains the local maxima in fidelity at $\chi = 0$, $\chi = \pm 1/\sqrt{8}$ and $\chi \to \pm\infty$. The case $\chi = \pm 1/\sqrt{8}$ is the most useful, as it provides a way to amplify dynamical signatures of scarring compared to $\chi = 0$ using a perturbation that is simple to implement in an experiment.

Appendix C

Single-site fidelity

In this Appendix, we discuss the relation between two measures of similarity that we use to characterise scarring in the Bose-Hubbard quantum simulator in Chapter 4. One measure is the standard quantum fidelity

$$\mathcal{F}(|\phi\rangle, |\psi\rangle) = |\langle\phi|\psi\rangle|^2, \tag{C.1}$$

i.e., the global overlap between two pure states. This measure is very convenient for numerical simulations and theoretical analysis, but hard to measure in experiment. For this reason, we also consider a different measure consisting of an average of local measurements. In a system with L sites, it is defined as

$$\mathcal{F}_{(r)}(|\phi\rangle, |\psi\rangle) \equiv \frac{1}{L+1-r} \sum_{j=1}^{L+1-r} \mathrm{Tr}\left[\hat{\rho}^{\phi}_{j,j+r-1} \hat{\rho}^{\psi}_{j,j+r-1}\right], \tag{C.2}$$

where $1 \leq r \leq L$ is the range of the measurements and

$$\hat{\rho}^{\phi}_{j,j+r-1} = \mathrm{Tr}_{\perp,j,j+r-1}\left[|\phi\rangle\langle\phi|\right] \tag{C.3}$$

is the density matrix obtained by performing the partial trace on all sites except sites j to $j-1+r$.

Both quantities, $\mathcal{F}$ and $\mathcal{F}_{(r)}$, are real and obey

$$0 \leq \mathcal{F}(|\phi\rangle, |\psi\rangle), \mathcal{F}_{(r)}(|\phi\rangle, |\psi\rangle) \leq 1, \tag{C.4}$$

and

$$\mathcal{F}_{(r)}(|\phi\rangle, |\psi\rangle) = \mathcal{F}_{(r)}(|\psi\rangle, |\phi\rangle), \quad \mathcal{F}(|\phi\rangle, |\psi\rangle) = \mathcal{F}(|\psi\rangle, |\phi\rangle). \tag{C.5}$$

It is also important to note that

$$\mathcal{F}_{(L)}(|\phi\rangle, |\psi\rangle) = \mathrm{Tr}\left[|\phi\rangle\langle\phi|\psi\rangle\langle\psi|\right] = |\langle\phi|\psi\rangle|^2 = \mathcal{F}(|\phi\rangle, |\psi\rangle).$$

While for arbitrary states $\mathcal{F}_{(r)}$ is neither an upper bound nor a lower bound of $\mathcal{F}$, it does not mean that this is never the case. We are now limiting our study to the case where the state ϕ is a product state. The consequence of that is that the reduced density matrix $\hat{\rho}^{\phi}_{j,j+r-1}$ will correspond to a pure state for any r. We can then chose a basis for each site such that $|\phi\rangle$ is a product of local basis states, and so a Fock basis state for the whole Hilbert space. Let us then denote the orthonormal states of this basis by $|\alpha\rangle$.

This allows us to rewrite the reduced density matrix as $\hat{\rho}^{\phi}_{j,j+r-1} = |\phi_{j,j+r-1}\rangle \langle\phi_{j,j+r-1}|$, where $|\phi_{j,j+r-1}\rangle$ corresponds to the state ϕ for sites j to $j+r-1$ (remember that we can only do this because $|\phi\rangle$ is a product state). This formulation implies the following simplification

$$\begin{aligned}
\mathcal{F}_{(r)}(|\phi\rangle, |\psi\rangle) =& \frac{1}{L+1-r} \sum_{j=1}^{L+1-r} \mathrm{Tr}\left[\hat{\rho}^{\phi}_{j,j+r-1}\hat{\rho}^{\psi}_{j,j+r-1}\right] \\
=& \frac{1}{L+1-r} \sum_{j=1}^{L+1-r} \mathrm{Tr}\left[|\phi_{j,j+r-1}\rangle \langle\phi_{j,j+r-1}| \, \hat{\rho}^{\psi}_{j,j+r-1}\right] \\
=& \frac{1}{L+1-r} \sum_{j=1}^{L+1-r} \sum_{|\alpha\rangle} \langle\alpha| \left(|\phi_{j,j+r-1}\rangle \langle\phi_{j,j+r-1}| \otimes \mathbf{1}\right) |\psi\rangle \langle\psi|\alpha\rangle \\
=& \frac{1}{L+1-r} \sum_{|\alpha\rangle} |\langle\alpha|\psi\rangle|^2 \sum_{j=1}^{L+1-r} \prod_{k=j}^{j+r-1} \langle\alpha_k|\phi_k\rangle \\
=& |\langle\phi|\psi\rangle|^2 + \frac{1}{L+1-r} \sum_{|\alpha\rangle\neq|\phi\rangle} |\langle\alpha|\psi\rangle|^2 \sum_{j=1}^{L+1-r} \prod_{k=j}^{j+r-1} \langle\alpha_k|\phi_k\rangle \\
\geq& |\langle\phi|\psi\rangle|^2 = \mathcal{F}(|\phi\rangle, |\psi\rangle),
\end{aligned} \tag{C.6}$$

where $\langle\alpha_k|\phi_k\rangle$ is 1 if the site k of $|\alpha\rangle$ and $|\phi\rangle$ is in the same state and 0 otherwise. This means that $|\langle\alpha|\psi\rangle|^2$ contributes to $\mathcal{F}_{(r)}(|\phi\rangle, |\psi\rangle)$ with a weight of $\frac{1}{N+1-r}$ each time r consecutive sites are in the same state in $|\alpha\rangle$ and $|\phi\rangle$. This simple rule allows us to not only derive this inequality between $\mathcal{F}$ and $\mathcal{F}_{(r)}$, but also to assess the effect of r on $\mathcal{F}_{(r)}$. Indeed, let us suppose that for a given r, a basis state $|\alpha\rangle$ has a weight of $\frac{n}{L+1-r}$, meaning that we can find n instances of r consecutive sites in the same state in $|\alpha\rangle$ and $|\phi\rangle$. Let us now consider the case with $r-1$. If $n > 0$, the minimum number of $r-1$ consecutive sites in the same state in $|\alpha\rangle$ and $|\phi\rangle$ is $n+1$. As such, $|\alpha\rangle$ has a minimum weight of $\frac{n+1}{L+2-r}$. In addition, there are a total of $L+1-r$ possibilities for the r consecutive sites, leading to the inequality $n \leq L+1-r$. This implies that $\frac{n}{L+1-r} \leq \frac{n+1}{L+2-r}$. If $n = 0$ then for $r-1$ the same state cannot contributes less, and so for any n it contributes more or the same amount. Hence we can conclude that

$$\mathcal{F}_{(1)}(|\phi\rangle, |\psi\rangle) \geq \mathcal{F}_{(2)}(|\phi\rangle, |\psi\rangle) \geq \ldots \mathcal{F}_{(L)}(|\phi\rangle, |\psi\rangle) = \mathcal{F}(|\phi\rangle, |\psi\rangle). \tag{C.7}$$

Finally, it is important to note that the inequality $\frac{n}{L+1-r} \leq \frac{n+1}{L+2-r}$ is saturated if and only if $n = L+1-r$, meaning that $|\alpha\rangle$ and $|\phi\rangle$ are the same. This is important as

$\mathcal{F}_{(r)}(|\phi\rangle, |\psi\rangle)$ is a weighted sum of all the $|\langle\alpha|\psi\rangle|^2$ with weights equal or smaller to 1. In order for $\mathcal{F}_{(r)}(|\phi\rangle, |\psi\rangle)$ to be equal to $\mathcal{F}_{(r-1)}(|\phi\rangle, |\psi\rangle)$, all weights corresponding to a non-zero $|\langle\alpha|\psi\rangle|^2$ must stay the same. But the only weights that are not increasing are either the ones that stay equal to zero or the one of $|\alpha\rangle = |\phi\rangle$ which stays equal to one. This implies that *all* inequalities of Eq. C.7 are simultaneously saturated if and only if $|\psi\rangle = |\phi\rangle$ (in which case they are all equal to one) or $\mathcal{F}_{(1)}(|\phi\rangle, |\psi\rangle) = 0$ (in that case they are all equal to 0). It is also possible for some of them to be saturated. This can only happen if all consecutive subsets of length m of $|\phi\rangle$ and $|\psi\rangle$ are orthogonal, meaning that all $\mathcal{F}_{(r)}$ are equal to 0 for all $r \geq m$.

In the experimental setup we only have access to the single-site fidelity $\mathcal{F}_{(1)}$, which already mimics the behaviour of the real fidelity $\mathcal{F}$ (see Fig. C.1). While it bounds $\mathcal{F}$ from above, that bound is fairly loose. If we instead look at its square $\mathcal{F}_{(1)}^2$, we can see that it approximates $\mathcal{F}$ much better as it takes a lower value when $\mathcal{F}$ is close to zero. While $\mathcal{F}_{(1)}^2$ is not guaranteed to be an upper bound of $\mathcal{F}$, our theoretical simulations indicate that it still effectively acts as one for the conditions we study. Our simulations also show that the single-site second Rényi entropy $S_{(1)}$ shows a very similar behaviour to the bipartite half-chain second Rényi entropy S. While it is limited in the range of values it can take, $S_{(1)}$ is clearly able to distinguish between the two regimes we are seeing in our setup: rapid entropy growth until a plateau is reached, and very slow entropy growth with oscillations on top.

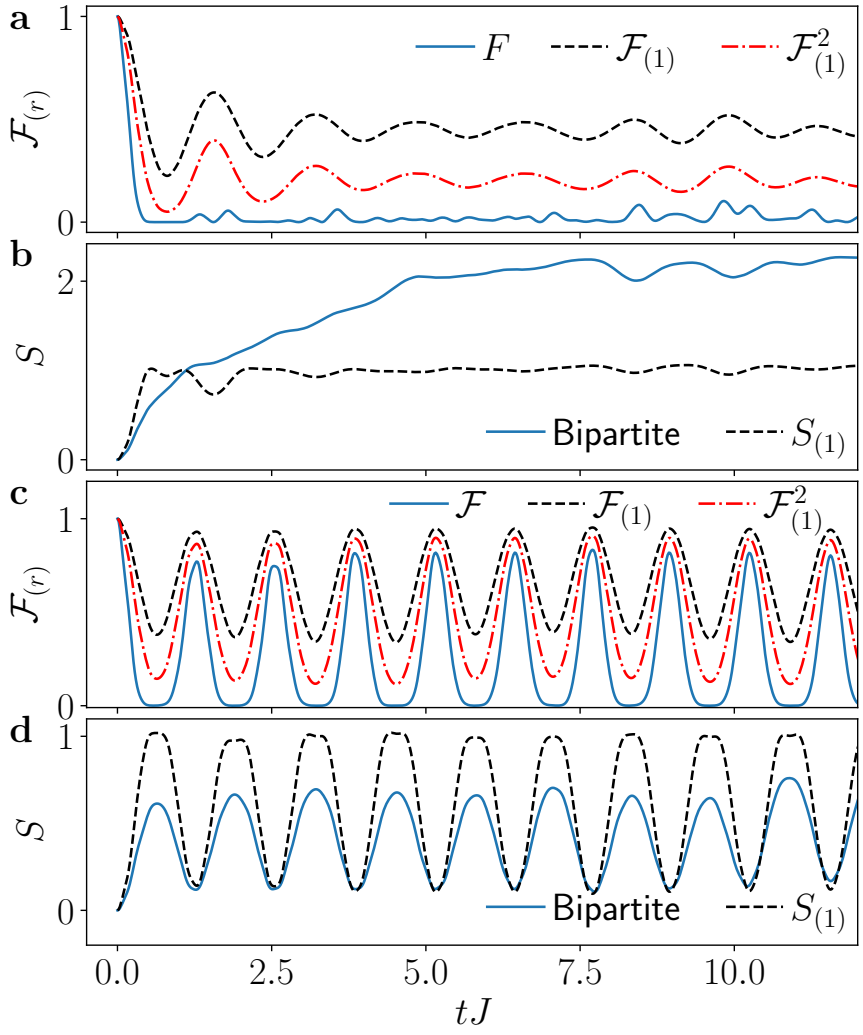

Figure C.1: Comparison between global and local quantities for the polarised state in the tilted Bose-Hubbard model introduced in Chapter 4. Panels **a-b** are without and panels **c-d** with periodic driving. Both the single-site fidelity and the single-site entropy effectively capture the behaviour of their global counterpart. In both the undriven and driven cases, the squared single-site fidelity $\mathcal{F}^2_{(1)}$ provides a better approximation of $\mathcal{F}$ than $\mathcal{F}_{(1)}$ while still acting as an upper bound. Data is for the tilted Bose-Hubbard model in Eq. (4.1), $J = 1$, $\Delta = U = 16$, $L = 11$, $L_\mathrm{A} = 5$, driving parameters $U_0 = -2.38$, $U_m = 1.54$, $\omega = 4.90$.

Appendix D

Derivation of TDVP equations of motion and quantum leakage in the PXP model

In this Appendix we first derive the TDVP equations of motion and then compute the instantaneous leakage rate for the TDVP Ansatz in Eq. (4.10) for the PXP model. These derivations follow Appendices A and C of Ref. [64].

D.1 Equations of motion

To reproduce the spatially homogeneous structure of the polarised state, all $\theta_j = \theta$ are set to be identical and the same is true for all $\phi_j = \phi$. For convenience, we split our Hamiltonian into two terms as $\hat{H}_{\mathrm{PXP}} = \hat{H}_X + \hat{H}_{\mu_0}$ and express μ_0 in units of Ω (effectively setting $\Omega = 1$). Throughout this section we will consider mixed MPS transfer matrices, denoted by

$$T_C^B = \sum_\sigma \bar{B}^\sigma \otimes C^\sigma, \tag{D.1}$$

where B and C are arbitrary MPS tensors. The MPS transfer matrix for the PXP ansatz chosen in the main text takes the form

$$T_A^A = T = \begin{pmatrix} \cos^2\theta & 0 & 0 & 1 \\ \cos\theta\sin\theta & 0 & 0 & 0 \\ \cos\theta\sin\theta & 0 & 0 & 0 \\ \sin^2\theta & 0 & 0 & 0 \end{pmatrix}. \tag{D.2}$$

D. DERIVATION OF TDVP EQUATIONS OF MOTION AND QUANTUM LEAKAGE IN THE PXP MODEL

The dominant left and right eigenvalues of the transfer matrix are equal to 1, and the corresponding eigenvectors are

$$|R) = \begin{pmatrix} 1 \\ \cos\theta \sin\theta \\ \cos\theta \sin\theta \\ \sin^2\theta \end{pmatrix}, \quad (L| = \begin{pmatrix} 1 & 0 & 0 & 1 \end{pmatrix}, \tag{D.3}$$

which obey $(L|R) = 1 + \sin^2\theta$. Using the mixed transfer matrix expression, it is straightforward to compute

$$f = -iN \frac{\left(L \left| T_A^{\partial\phi A} \right| R\right)}{(L|R)} = N \frac{2\sin^2\theta}{\cos 2\theta - 3}, \text{ with } T_A^{\partial\phi A} = \begin{pmatrix} 0 & 0 & 0 & -i \\ 0 & 0 & 0 & 0 \\ 0 & 0 & 0 & 0 \\ 0 & 0 & 0 & 0 \end{pmatrix}. \tag{D.4}$$

Next we compute the expectation value of the Hamiltonian. We first find

$$\left\langle \psi \left| \hat{H}_X \right| \psi \right\rangle = N \frac{\left(L \left| \hat{H}_X \right| R\right)}{(L|R)} = N \frac{2\cos^2\theta \sin\theta \sin\phi}{1 + \sin^2\theta}. \tag{D.5}$$

We then get

$$\langle\psi| \sum_j \hat{n}_j |\psi\rangle = N \frac{\left(L \left| \sum_j \hat{n}_j \right| R\right)}{(L|R)} = N \frac{\sin^2\theta}{1 + \sin^2\theta}, \tag{D.6}$$

leading to

$$\langle\psi|\hat{H}_{\mu_0}|\psi\rangle = N\mu_0 \frac{\sin^2\theta}{1 + \sin^2\theta}. \tag{D.7}$$

The total expectation value is given by the sum of Eqs. (D.5) and (D.7), which yields the energy density

$$E(\theta,\phi)/N = \frac{\sin\theta}{1 + \sin^2\theta} \left(\mu_0 \sin\theta + 2\cos^2\theta \sin\phi\right). \tag{D.8}$$

To get the equations of motion for θ and ϕ, we need to compute

$$\eta = \partial_\theta f = -4N \frac{\sin 2\theta}{(\cos^2\theta - 3)^2}. \tag{D.9}$$

From there the equations of motion are given by

$$\dot{\theta} = \frac{1}{\eta} \partial_\phi \langle\psi|\hat{H}|\psi\rangle, \quad \dot{\phi} = -\frac{1}{\eta} \partial_\theta \langle\psi|\hat{H}|\psi\rangle, \tag{D.10}$$

which lead to

$$\dot{\theta} = -\cos\theta \cos\phi \left(1 + \sin^2\theta\right), \tag{D.11}$$

$$\dot{\phi} = \mu_0 + \frac{\sin\phi}{\sin\theta} \left(1 - 4\sin^2\theta - \sin^4\theta\right). \tag{D.12}$$

D.2 Instantaneous leakage

The instantaneous leakage quantifies how much of the wave-function escapes from the TDVP manifold, and is given by

$$\begin{aligned}\Lambda^2(\theta,\phi) &= \||\dot{\psi}\rangle - i\hat{H}|\psi\rangle\|^2 \\ &= \left\langle \psi \left| \hat{H}^2 \right| \psi \right\rangle_c - 2\dot{\theta}\,\mathrm{Im}\left(\left\langle \partial_\theta\psi|\hat{H}|\psi\right\rangle_c\right) \\ &+ (\dot{\theta})^2\,\mathrm{Re}\left(\langle\partial_\theta\psi|\partial_\theta\psi\rangle_c\right) - 2\dot{\phi}\,\mathrm{Im}\left(\left\langle \partial_\phi\psi|\hat{H}|\psi\right\rangle_c\right) \\ &+ (\dot{\phi})^2\,\mathrm{Re}\left(\langle\partial_\phi\psi|\partial_\phi\psi\rangle_c\right) + 2\dot{\phi}\dot{\theta}\,\mathrm{Re}\left(\langle\partial_\phi\psi|\partial_\theta\psi\rangle_c\right)\end{aligned} \tag{D.13}$$

Due to the gauge choice, the leakage depends on connected correlators defined as

$$\langle\partial_\theta\psi|\partial_\theta\psi\rangle_c = \langle\partial_\theta\psi|\partial_\theta\psi\rangle - \langle\partial_\theta\psi|\psi\rangle\langle\psi|\partial_\theta\psi\rangle.$$

In order to evaluate these connected correlators, we introduce the projector on the dominant subspace, $\mathcal{P} = |R)(L|/(L|R)$, and its complement $\mathcal{Q} = \mathbf{1} - \mathcal{P}$. We also introduce $\mathcal{T}$, which is obtained by re-summing the contribution of the non-dominant subspace of T in $\sum_{q=0}^{\infty} T^q$ and is defined from $\mathcal{T}^{-1} = \mathcal{Q}(\mathbf{1} - \mathcal{Q}T\mathcal{Q})^{-1}\mathcal{Q}$. Finally, we will use the following shorthand for a 3-site local Hamiltonian term contracted with MPS tensors on every site:

$$\mathcal{H} = \mathcal{H}^{A,A,A}_{A,A,A} = \sum_{\sigma_i} \bar{A}^{\sigma_1}\bar{A}^{\sigma_2}\bar{A}^{\sigma_3} h^{\sigma_1,\sigma_2,\sigma_3}_{\sigma_4,\sigma_5,\sigma_6} A^{\sigma_4}A^{\sigma_5}A^{\sigma_6}. \tag{D.14}$$

Let us now evaluate the various terms involved in the instantaneous leakage. Taking each term one by one, we find that:

$$\langle\partial_\theta\psi|\partial_\theta\psi\rangle_c = \frac{N}{(L|R)}(L|T^{\partial_\theta A}_{\partial_\theta A} + T^{A}_{\partial_\theta A}\mathcal{T}^{-1}T^{\partial_\theta A}_{A} + T^{\partial_\theta A}_{A}\mathcal{T}^{-1}T^{A}_{\partial_\theta A} - T^{A}_{\partial_\theta A}\mathcal{P}T^{\partial_\theta A}_{A}|R), \tag{D.15}$$

which after a straightforward calculation evaluates to

$$\langle\partial_\theta\psi|\partial_\theta\psi\rangle_c = \frac{N}{1+\sin^2\theta}. \tag{D.16}$$

Turning our attention to the term $\left\langle \partial_\theta\psi|\hat{H}|\psi\right\rangle_c$, we find that this evaluates to

$$\frac{N}{(L|R)}\left(L\left|\mathcal{H}_{\partial_\theta A} + \mathcal{H}\mathcal{T}^{-1}T^{A}_{\partial_\theta A} + T^{A}_{\partial_\theta A}\mathcal{T}^{-1}\mathcal{H} - 3\mathcal{H}\mathcal{P}T^{A}_{\partial_\theta A}\right| R\right), \tag{D.17}$$

which yields

$$\left\langle \partial_\theta\psi|\hat{H}|\psi\right\rangle_c = -iN\cos\theta\cos\phi + N\frac{\cos\theta\sin\theta}{\left(1+\sin^2\theta\right)^2}\dot{\phi}. \tag{D.18}$$

As we are only interested in the imaginary part, we can discard the second term and are left with

$$\mathrm{Im}\left(\left\langle \partial_\theta\psi|\hat{H}|\psi\right\rangle_c\right) = -N\cos\theta\cos\phi = \frac{N}{1+\sin^2\theta}\dot{\theta}. \tag{D.19}$$

The expressions containing the derivatives with respect to ϕ can be calculated similarly. Starting with $\langle\partial_\phi\psi|\partial_\phi\psi\rangle_c$ which we compute as

$$\frac{N}{(L|R)}(L|T^{\partial_\phi A}_{\partial_\phi A} + T^A_{\partial_\phi A}\mathcal{T}^{-1}T^{\partial_\phi A}_A + T^{\partial_\phi A}_A\mathcal{T}^{-1}T^A_{\partial_\phi A} - T^A_{\partial_\phi A}\mathcal{P}T^{\partial_\phi A}_A|R) \tag{D.20}$$

Evaluating this term, we find

$$\langle\partial_\phi\psi|\partial_\phi\psi\rangle_c = N\frac{\cos^2\theta\sin^2\theta}{\left(1+\sin^2\theta\right)^3}. \tag{D.21}$$

The next term to compute is the cross-term

$$\langle\partial_\phi\psi|\partial_\theta\psi\rangle_c = \frac{N}{(L|R)}(L|T^{\partial_\phi A}_{\partial_\theta A} + T^A_{\partial_\theta A}\mathcal{T}^{-1}T^{\partial_\phi A}_A + T^{\partial_\phi A}\mathcal{T}^{-1}T_{\partial_\theta A} - T_{\partial_\theta A}\mathcal{P}T^{\partial_\phi A}|R). \tag{D.22}$$

The result after evaluating Eq. (D.22) is

$$\langle\partial_\phi\psi|\partial_\theta\psi\rangle_c = -iN\frac{\cos\theta\sin\theta}{\left(1+\sin^2\theta\right)^2}, \tag{D.23}$$

however, because its real part is identically zero, we get no contribution from this term. We now compute $\left\langle\partial_\phi\psi|\hat{H}|\psi\right\rangle_c$ as

$$\langle\partial_\phi\psi|\hat{H}|\psi\rangle_c = \frac{N}{(L|R)}(L|\mathcal{H}_{\partial_\phi A} + \mathcal{H}\mathcal{T}^{-1}T^A_{A\partial_\phi A} + T^A_{\partial_\phi A}\mathcal{T}^{-1}\mathcal{H} - 3\mathcal{H}\mathcal{P}T_{\partial_\phi A}|R). \tag{D.24}$$

We find this can be expressed as:

$$\left\langle\partial_\phi\psi|\hat{H}|\psi\right\rangle_c = N\cos\theta\cos\phi + iN\frac{\cos^2\theta\sin^2\theta}{\left(1+\sin^2\theta\right)^3}\dot{\phi} \tag{D.25}$$

We now move onto the terms involving the square of the Hamiltonian, $\hat{H}^2$. The connected correlator in this case is

$$\left\langle\psi\left|\hat{H}^2\right|\psi\right\rangle_c = N\frac{\left(L\left|\mathcal{H}^{(2)} + 2\mathcal{H}\mathcal{T}^{-1}\mathcal{H} - 5\mathcal{H}\mathcal{P}\mathcal{H}\right|R\right)}{(L|R)}. \tag{D.26}$$

where $\mathcal{H}^{(2)}$ is the product of two overlapping local Hamiltonian terms. As the local Hamiltonian spans three sites, the two terms will both act upon one, two, or three shared sites. Evaluating this expression, we obtain

$$\left\langle\psi\left|\hat{H}^2\right|\psi\right\rangle_c = \frac{N\sin^6\theta}{1+\sin^2\theta} + \frac{N\cos^2\theta\sin^2\theta(\dot{\phi})^2}{\left(1+\sin^2\theta\right)^3} + \frac{N(\dot{\theta})^2}{1+\sin^2\theta}. \tag{D.27}$$

Substituting each of these into the equation for the leakage, we finally arrive at:

$$\Lambda^2 = N\frac{\sin^6\theta}{1+\sin^2\theta}$$

Rescaling this by the system size yields the intensive expression for the leakage

$$\gamma^2 = \frac{\sin^6\theta}{1+\sin^2\theta}\ . \tag{D.28}$$

D. DERIVATION OF TDVP EQUATIONS OF MOTION AND QUANTUM LEAKAGE IN THE PXP MODEL

Appendix E

Structure of rainbow scars

In this Appendix we derive the exact form of the scarred states of the second family in the superconducting ladder discussed in Sec. 6.3. We then prove that both families of rainbow states are eigenstates of the Hamiltonian in Eq. (6.12).

E.1 Building scarred states of the second family

Scarred states of the second family $|E'_n\rangle$ are obtained by acting on scarred states of the first family with $\hat{H}_{\mathbf{u}} - (\sum_k \omega_k/M)\,\hat{Z}$. Let us first derive the action of this operator in the dimer basis. To this end we define

$$\hat{h}^{\parallel,\mathbf{u}}_{k,k+1} = \frac{J_{e,k}}{2}\left(\hat{\mathbf{u}}^x_k\hat{\mathbf{u}}^x_{k+1} + \hat{\mathbf{u}}^y_k\hat{\mathbf{u}}^y_{k+1}\right). \tag{E.1}$$

From there it is straightforward to see that

$$\hat{H}_{\mathbf{u}} - \left(\sum_k \frac{\omega_k}{M}\right)\hat{Z} = \sum_{k=1}^{M-1}\hat{h}^{\parallel,\mathbf{u}}_{k,k+1} + \sum_{k=1}^{M}\overline{\omega}_k\mathbf{u}^z_k, \tag{E.2}$$

where $\overline{\omega}_k = \omega_k - (\sum_i \omega_i/M)$. As we will only apply this operator to scarred states of the first family, which contain no $|\mathbf{D}\rangle$ or $|\mathbf{H}\rangle$, we can ignore any configurations containing them. The action of $\hat{h}^{\parallel,\mathbf{u}}_{k,k+1}$ and $\mathbf{u}^z_k$ on dimers is then

$$\begin{aligned}
\hat{h}^{\parallel,\mathbf{u}}_{k,k+1}|\mathbf{TT}\rangle &= \frac{1}{2}J_{e,k}(|\mathbf{HD}\rangle + |\mathbf{DH}\rangle) & \hat{h}^{\parallel,\mathbf{u}}_{k,k+1}|\mathbf{SS}\rangle &= -\frac{1}{2}J_{e,k}(|\mathbf{HD}\rangle + |\mathbf{DH}\rangle),\\
\hat{h}^{\parallel,\mathbf{u}}_{k,k+1}|\mathbf{TS}\rangle &= \frac{1}{2}J_{e,k}(|\mathbf{HD}\rangle - |\mathbf{DH}\rangle), & \hat{h}^{\parallel,\mathbf{u}}_{k,k+1}|\mathbf{ST}\rangle &= -\frac{1}{2}J_{e,k}(|\mathbf{HD}\rangle - |\mathbf{DH}\rangle),\\
\overline{\omega}_k\hat{\mathbf{u}}^z_k|\mathbf{S}\rangle &= -\overline{\omega}_k|\mathbf{T}\rangle, & \overline{\omega}_k\hat{\mathbf{u}}^z_k|\mathbf{T}\rangle &= -\overline{\omega}_k|\mathbf{S}\rangle.
\end{aligned} \tag{E.3}$$

From there, we immediately see that

$$\hat{h}^{\parallel,\mathbf{u}}_{k,k+1}(|\mathbf{TS}\rangle + |\mathbf{ST}\rangle) = 0. \tag{E.4}$$

E. STRUCTURE OF RAINBOW SCARS

To represent symmetric superpositions of triplets and singlets, we recall the notation where $|L{-}n, n\rangle$ is the (non-normalised) symmetric superposition of all configurations on L sites with $L-n$ singlets and n triplets. We also remind that the scarred states of the first family can be written directly using this notation as

$$|E_n\rangle = \frac{1}{\mathcal{N}} |M{-}n, n\rangle = \frac{1}{\mathcal{N}} \sum_{|\phi\rangle \in (M-n,n)} |\phi\rangle \,. \tag{E.5}$$

We now compute explicitly Eq. (6.26), where $|E'_n\rangle$ is obtained as by acting with $\hat{P}^Q_{M-2n}\left[\hat{H}_{\mathbf{u}} - \left(\sum_k \frac{\omega_k}{M}\right)\hat{Z}\right]$ on $|E_{n-1}\rangle$. For brevity, we will first work out what happens when we apply $\hat{h}^{\parallel,\mathbf{u}}_{1,2}$ to $|E_{n-1}\rangle$ (the same is true for any $\hat{h}^{\parallel,\mathbf{u}}_{k,k+1}$):

$$\begin{aligned}
\hat{h}^{\parallel,\mathbf{u}}_{1,2} |E_{n-1}\rangle &= \frac{\hat{h}^{\parallel,\mathbf{u}}_{1,2}}{\mathcal{N}} |M{-}n{+}1, n{-}1\rangle \\
&= \frac{\hat{h}^{\parallel,\mathbf{u}}_{1,2}}{\mathcal{N}} \Big[(|\mathbf{TS}\rangle + |\mathbf{ST}\rangle) |M{-}n, n{-}2\rangle + |\mathbf{TT}\rangle |M{-}n{+}1, n{-}3\rangle + |\mathbf{SS}\rangle |M{-}n{-}1, n{-}1\rangle \Big] \\
&= \frac{J_{e,1}}{2\mathcal{N}} (|\mathbf{HD}\rangle + |\mathbf{DH}\rangle) |M{-}n{+}1, n{-}3\rangle - \frac{J_{e,1}}{2\mathcal{N}} (|\mathbf{HD}\rangle + |\mathbf{DH}\rangle) |M{-}n{-}1, n{-}1\rangle \,,
\end{aligned} \tag{E.6}$$

where we used the condition (E.4) to cancel the contribution of the first term. Applying the projector $\hat{P}^Q_{M-2n}$ singles out one of the terms:

$$\hat{P}^Q_{M-2n} \hat{h}^{\parallel,\mathbf{u}}_{1,2} |E_{n-1}\rangle = -\frac{J_{e,1}}{2\mathcal{N}} (|\mathbf{HD}\rangle + |\mathbf{DH}\rangle) |M{-}n{-}1, n{-}1\rangle \,. \tag{E.7}$$

Next, we look at the action of $\overline{\omega}_1 \hat{\mathbf{u}}^z_1$:

$$\begin{aligned}
\overline{\omega}_1 \hat{\mathbf{u}}^z_1 |E_{n-1}\rangle &= \frac{\overline{\omega}_1 \hat{\mathbf{u}}^z_1}{\mathcal{N}} |M{-}n{+}1, n{-}1\rangle = \frac{\overline{\omega}_1 \hat{\mathbf{u}}^z_1}{\mathcal{N}} \Big[|\mathbf{T}\rangle |M{-}n{+}1, n{-}2\rangle + |\mathbf{S}\rangle |M{-}n, n{-}1\rangle \Big] \\
&= \frac{-\overline{\omega}_1}{\mathcal{N}} \Big[|\mathbf{S}\rangle |M{-}n{+}1, n{-}2\rangle + |\mathbf{T}\rangle |M{-}n, n{-}1\rangle \Big].
\end{aligned} \tag{E.8}$$

Applying the projector in this case gives

$$\hat{P}^Q_{M-2n} \overline{\omega}_1 \hat{\mathbf{u}}^z_1 |E_{n-1}\rangle = -\frac{\overline{\omega}_1}{\mathcal{N}} |\mathbf{T}\rangle |M{-}n, n{-}1\rangle \,. \tag{E.9}$$

The result is similar if we act on another site k, with a prefactor $\overline{\omega}_k$ and a triplet on that site. Ultimately, we end up with a collection of all states with $M-n$ singlets and n triplets, but each of them has a prefactor that depends on the location of the triplets. Let us introduce the operator $\hat{T}_k$ that gives 1 if this site is a triplet and 0 otherwise. We can then write

$$\hat{P}^Q_{M-2n} \sum_{k=1}^{M} \overline{\omega}_k \hat{\mathbf{u}}^z_k |E_{n-1}\rangle = -\frac{1}{\mathcal{N}} \left(\sum_{k=1}^{M} \hat{T}_k \overline{\omega}_k \right) |M{-}n, n\rangle \,. \tag{E.10}$$

To write down the scarred states of the second family, we now simply need to gather the terms from Eqs. (E.7) and (E.10). We also remove the overall minus sign and normalise the state. Let us introduce the ensembles of sites $\Lambda = \{1, 2, \dots M\}$, $\Lambda_k = \{k, k+1\}$ and $\bar{\Lambda}_k = \Lambda - \Lambda_k = \{1, 2 \dots k-1, k+2, k+3, \dots M\}$. They represent, respectively, all sites, sites k and $k+1$, and all sites except k and $k+1$. This allows us to write $|E'_n\rangle$ as

$$|E'_n\rangle = \sum_{k=1}^{M-1} \frac{J_{e,k}}{2\mathcal{N}_n} (|\mathbf{HD}\rangle_{\Lambda_k} + |\mathbf{DH}\rangle_{\Lambda_k}) \otimes |M-n-1, n-1\rangle_{\bar{\Lambda}_k} + \frac{1}{\mathcal{N}_n} \left(\sum_{k=1}^{M} \hat{T}_k \overline{\omega}_k \right) |M-n, n\rangle_{\Lambda} \,, \tag{E.11}$$

with $n = 1, 2, \dots, M-1$. As an example, let us write out the case for $M = 4$ and $n = 1$:

$$\begin{aligned} |E'_1\rangle = \frac{1}{2\mathcal{N}_1} \Big[& J_{e,1}(|\mathbf{DHSS}\rangle + |\mathbf{HDSS}\rangle) + J_{e,2}(|\mathbf{SDHS}\rangle + |\mathbf{SHDS}\rangle) \\ & + J_{e,3}(|\mathbf{SSDH}\rangle + |\mathbf{SSHD}\rangle) \Big] \\ + \frac{1}{\mathcal{N}_1} \Big[& \overline{\omega}_1 |\mathbf{TSSS}\rangle + \overline{\omega}_2 |\mathbf{STSS}\rangle + \overline{\omega}_3 |\mathbf{SSTS}\rangle + \overline{\omega}_4 |\mathbf{SSST}\rangle \Big]. \end{aligned} \tag{E.12}$$

Finally, let us show that the same result is obtained if we generate $|E'_n\rangle$ by "lowering" from $|E_{n+1}\rangle$ as discussed in Eq. (6.27). We have

$$\hat{P}^{Q}_{M-2n} \hat{h}^{\parallel,\mathbf{u}}_{1,2} |E_{n+1}\rangle = \frac{J_{e,1}}{2\mathcal{N}} (|\mathbf{HD}\rangle + |\mathbf{DH}\rangle) |M-n-1, n-1\rangle \,. \tag{E.13}$$

and

$$\hat{P}^{Q}_{M-2n} \overline{\omega}_1 \hat{\mathbf{u}}^z_1 |E_{n+1}\rangle = \frac{-\overline{\omega}_1}{\mathcal{N}} |\mathbf{S}\rangle |M-n-1, n\rangle \,. \tag{E.14}$$

From the latter equation, we can derive that

$$\hat{P}^{Q}_{M-2n} \sum_{k=1}^{M} \overline{\omega}_k \hat{\mathbf{u}}^z_k |E_{n-1}\rangle = \frac{-1}{\mathcal{N}} \left(\sum_{k=1}^{M} \hat{S}_k \overline{\omega}_k \right) |M-n, n\rangle \,, \tag{E.15}$$

where $\hat{S}_k$ gives 1 if this site is a triplet and 0 otherwise. Now we can notice that $|M-n, n\rangle$ is composed entirely of triplets and singlets. Consequently, $(\hat{T}_k + \hat{S}_k) = \mathbf{1}_k$ when acting on that state. Moreover, we know that the $\overline{\omega}$ must sum to 0 by construction. This allows us to state that

$$\sum_{k=1}^{M} \overline{\omega}_k (\hat{S}_k + \hat{T}_k) |M-n, n\rangle = \left(\sum_{k=1}^{M} \overline{\omega}_k \right) |M-n, n\rangle = 0. \tag{E.16}$$

From there we can conclude that

$$\hat{P}^{Q}_{M-2n} \sum_{k=1}^{M} \overline{\omega}_k \hat{\mathbf{u}}^z_k |E_{n-1}\rangle = \frac{-1}{\mathcal{N}} \left(\sum_{k=1}^{M} \hat{S}_k \overline{\omega}_k \right) |M-n, n\rangle = \frac{1}{\mathcal{N}} \left(\sum_{k=1}^{M} \hat{T}_k \overline{\omega}_k \right) |M-n, n\rangle \,. \tag{E.17}$$

Gathering the results of Eqs. (E.13) and (E.17) we find the same result as in Eq. (E.11).

As we have the exact wave-function for the scarred states of the second family, we can also compute their normalisation factor $\mathcal{N}_n$. It admits a simple expression

$$\mathcal{N}_n = \sqrt{\binom{M-2}{n-1}\left[\frac{1}{2}\sum_{k=1}^{M-1} J_{e,k}^2 + \sum_{k=1}^{M}\overline{\omega}_k^2\right]}. \tag{E.18}$$

This expression does not contain any cross-term $\overline{\omega}_k\overline{\omega}_j$ because all possible combinations of $k \neq j$ appear and we can then express them as

$$\sum_{k=1}^{M-1}\sum_{j=k+1}^{M}\overline{\omega}_k\overline{\omega}_j = -\frac{1}{2}\sum_{k=1}^{M}\overline{\omega}_k^2, \tag{E.19}$$

by using the fact that $\sum_{k=1}^{M}\overline{\omega}_k = 0$ and as such

$$0 = \left(\sum_{k=1}^{M}\overline{\omega}_k\right)^2 = \sum_{k=1}^{M}\overline{\omega}_k^2 + 2\sum_{k=1}^{M-1}\sum_{j=k+1}^{M}\overline{\omega}_k\overline{\omega}_j. \tag{E.20}$$

E.2 Proof that rainbow scars are eigenstates

Now that we have discussed the exact wave-function of both types of scarred states, we prove that they are actually eigenstates of the model in Eq. (6.12). We first address the straightforward cases of $n = 0$ and $n = M$. We then show the proof for the slightly more complicated $n = 1$ case and finally demonstrate that the same arguments generalise to arbitrary n.

E.2.1 $n = 0$ and $n = M$ scarred states

For $n = 0$, the only scarred state present belongs to the first family and is $|E_0\rangle = |SS\dots S\rangle$. From Eq. (6.18) we know that $|\mathbf{S}\rangle$ is an eigenstates of $\hat{h}_k^{\perp}$ with energy $-J_a$ and from Eq. (6.19) that $|\mathbf{SS}\rangle$ is an eigenstate of $\hat{h}_{k,k+1}^{\parallel}$ with energy 0. Thus, $|E_0\rangle$ must be an eigenstate of $\hat{H}$ with energy $-MJ_a$. Similarly, $|\mathbf{T}\rangle$ is an eigenstate of $\hat{h}_k^{\perp}$ with energy J_a and $|\mathbf{TT}\rangle$ is an eigenstate of $\hat{h}_{k,k+1}^{\parallel}$ with energy 0. Thus, $|E_M\rangle = |\mathbf{TT}\dots\mathbf{T}\rangle$ must be an eigenstate of $\hat{H}$ with energy MJ_a.

E.2.2 $n = 1$ scarred states

For $n = 1$ we will prove the eigenstate property by considering a 2×3 ladder and then show that the same holds for larger systems. Consider the state

$$|\psi\rangle = \beta_1\left(|\mathbf{HDS}\rangle + |\mathbf{DHS}\rangle\right) + \beta_2\left(|\mathbf{SHD}\rangle + |\mathbf{SDH}\rangle\right) + \alpha_1|\mathbf{TSS}\rangle + \alpha_2|\mathbf{STS}\rangle + \alpha_3|\mathbf{SST}\rangle. \tag{E.21}$$

Applying the Hamiltonian to this state and after some algebra, we obtain

$$\begin{aligned}\hat{H}\,|\psi\rangle = &-J_a\,|\psi\rangle + \left[2\beta_1\,(\omega_1-\omega_2)+J_{e,1}\,(\alpha_2-\alpha_1)\right](|\mathbf{DHS}\rangle - |\mathbf{HDS}\rangle)\\ &+\left[2\beta_2\,(\omega_2-\omega_3)+J_{e,2}\,(\alpha_3-\alpha_2)\right](|\mathbf{SDH}\rangle - |\mathbf{SHD}\rangle)\\ &+(J_{e,2}\beta_1 - J_{e,1}\beta_2)\,(|\mathbf{HTD}\rangle - |\mathbf{DTH}\rangle)\,.\end{aligned} \tag{E.22}$$

For $|\psi\rangle$ to be an eigenstate, all prefactors must cancel and so the coefficients must obey

$$2\beta_1\,(\omega_1-\omega_2)+J_{e,1}\,(\alpha_2-\alpha_1) = 0, \tag{E.23}$$

$$2\beta_2\,(\omega_2-\omega_3)+J_{e,2}\,(\alpha_3-\alpha_2) = 0, \tag{E.24}$$

$$J_{e,2}\beta_1 - J_{e,1}\beta_2 = 0. \tag{E.25}$$

In general, we have 5 unknowns but only 3 equations. The normalisation of the state provides a fourth equation, leaving room for two solutions. The first option is to set all α_j to be equal and all β_j to zero:

$$\alpha_j = 1, \quad \beta_j = 0. \tag{E.26}$$

From Eq. (E.21), it is straightforward to see that this corresponds to the scarred state of the first family, $|E_1\rangle$. The other solution is given by the scarred states of the second family that obey (up to a normalisation factor)

$$\alpha_j = \omega_j - \frac{1}{M}\sum_k \omega_k = \overline{\omega}_k, \quad \beta_j = \frac{J_{e,j}}{2}. \tag{E.27}$$

This is easy to see from Eqs. (E.23)-(E.25) as $\overline{\omega}_k - \overline{\omega}_{k+1} = \omega_k - \omega_{k+1}$. The reason why the $\overline{\omega}_k$ are used instead of the ω_k is to guarantee that the two families of scars are orthogonal as their overlap is given (up to their normalisation factors) by $\sum_j 1\times\overline{\omega}_j = 0$. This completes the proof for the special case of $M = 3$. However, generalising this to an arbitrary M is now straightforward. The general state is

$$\begin{aligned}|\psi\rangle = &\,\beta_1\,(|\mathbf{HDS}\ldots\mathbf{S}\rangle + |\mathbf{DHS}\ldots\mathbf{S}\rangle) + \beta_2\,(|\mathbf{S}\ldots\mathbf{SHDS}\rangle + |\mathbf{S}\ldots\mathbf{SDHS}\rangle)\\ &+\ldots+\beta_{M-2}\,(|\mathbf{S}\ldots\mathbf{SHD}\rangle + |\mathbf{S}\ldots\mathbf{SDH}\rangle) + \beta_{M-1}\,(|\mathbf{HDS}\ldots\mathbf{S}\rangle + |\mathbf{DHS}\ldots\mathbf{S}\rangle)\\ &+\alpha_1\,|\mathbf{TS}\ldots\mathbf{S}\rangle + \alpha_2\,|\mathbf{STS}\ldots\mathbf{S}\rangle + \ldots + \alpha_M\,|\mathbf{S}\ldots\mathbf{ST}\rangle - (M-2)J_a\,|\psi\rangle\,.\end{aligned} \tag{E.28}$$

Now we have M different α_j and $M-1$ different β_j, so $2M-1$ unknowns in total. For each block of 2×2 sites we get an equation similar to Eqs. (E.23) and (E.24). Thus, for $j = 1$ to $M-1$ we have

$$2\beta_j\,(\omega_j-\omega_{j+1})+J_{e,j}\,(\alpha_{j+1}-\alpha_j) = 0. \tag{E.29}$$

For each rectangular block of 2×3 sites we get an equation similar to Eq. (E.25). Hence, for $j = 1$ to $M-2$ we have

$$J_{e,j+1}\beta_j - J_{e,j}\beta_j + 1 = 0. \tag{E.30}$$

For a chain with $2M$ sites, this yields $(M-1)+(M-2) = 2M-3$ equations. Adding the constraint of normalisation, this always leaves us with two scarred states with energy $-(M-2)J_a$ (assuming the equations are linearly independent). It is straightforward to check that the two solutions given in Eqs. (E.26) and (E.27) are still valid.

E.2.3 Other values of n

While we treated the case $n = 1$ on its own to provide a simple example, the recipe is exactly the same for general n (except for $n = 0$ and $n = M$ that were already proven). We use the same Ansatz in which we only consider states with one $DH + HD$ pair in a background of $n - 1$ triplets and $M - n - 1$ singlets and states with n triplets and $M - n$ singlets.

We first restrict our investigation to an arbitrary location k, $k + 1$ for the hole-doublon pair.

$$|\psi\rangle = \beta_j \left(|\dots \mathbf{XHDY} \dots\rangle + |\dots \mathbf{XDHY} \dots\rangle\right) + \alpha_{TS} |\dots \mathbf{XTSY} \dots\rangle + \alpha_{ST} |\dots \mathbf{XSTY} \dots\rangle , \tag{E.31}$$

where $\mathbf{X}$ and $\mathbf{Y}$ denote either $\mathbf{S}$ or $\mathbf{T}$. For $\hat{h}^{\perp}$, the contribution on all other sites except k and $k + 1$ is diagonal and equal to $J_a(2n - M)$. Therefore, to prove that states are eigenstates with this energy, we need to prove that the action of the rest of the Hamiltonian annihilates the state. For $\hat{h}^{\parallel}_{k,k+1}$ we only have to care about the action on sites $k-1$ to $k+2$. Indeed, the rest of the state is composed of triplets and singlets. For any other pair, if it is $\mathbf{SS}$ or $\mathbf{TT}$, then it is annihilated by the action of the Hamiltonian. If, instead, it is $\mathbf{TS}$, then there exists another state in the superposition, with the same weight, that has $\mathbf{ST}$ instead. Therefore, their superposition is also annihilated by the Hamiltonian.

First, we can look at what happens if we act on the middle pair. This leads to

$$\begin{aligned} &2\beta_j \left(\omega_j - \omega_{j+1}\right) \left(|\dots \mathbf{XDHY} \dots\rangle - |\dots \mathbf{XHDY} \dots\rangle\right) \\ &+ J_{e,j} \left(\alpha_{ST} - \alpha_{TS}\right) \left(|\dots \mathbf{XDHY} \dots\rangle - |\dots \mathbf{XHDY} \dots\rangle\right) , \end{aligned} \tag{E.32}$$

and so

$$2\beta_j \left(\omega_j - \omega_{j+1}\right) + J_{e,j} \left(\alpha_{ST} - \alpha_{TS}\right) = 0. \tag{E.33}$$

We get a unique equation for every of the $M-1$ pair of sites and for every of the $\binom{M-2}{n-1}$ possible background configurations, where $n = 1$ to $M - 1$ is the index of the scarred states.

Now we still need to look at the effect of $\hat{h}^{\parallel}$ on $\mathbf{XD}$, $\mathbf{XH}$ (as well as $\mathbf{HY}$ and $\mathbf{DY}$). For that, we need to also consider the $\mathbf{DH}$ and $\mathbf{HD}$ pair placed one site to the left:

$$\beta_{j-1} \left(|\dots \mathbf{HDXY} \dots\rangle + |\dots \mathbf{DHXY} \dots\rangle\right) + \beta_j \left(|\dots \mathbf{XHDY} \dots\rangle + |\dots \mathbf{XDHY} \dots\rangle\right) . \tag{E.34}$$

Applying the Hamiltonian to these states leads to

$$\begin{aligned} &\beta_{j-1} J_{e,j} \left(|\dots H\bar{\mathbf{X}}\mathbf{DY} \dots\rangle - |\dots D\bar{\mathbf{X}}\mathbf{HY} \dots\rangle\right) \\ &- \beta_j J_{e,j-1} \left(|\dots H\bar{\mathbf{X}}\mathbf{DY} \dots\rangle + |\dots D\bar{\mathbf{X}}\mathbf{HY} \dots\rangle\right) , \end{aligned} \tag{E.35}$$

where $\bar{\mathbf{X}} = \mathbf{T}$ if $\mathbf{X} = \mathbf{S}$ and $\bar{\mathbf{X}} = \mathbf{S}$ if $\mathbf{X} = \mathbf{T}$. Hence we get an equation

$$\beta_{j-1} J_{e,j} - \beta_j J_{e,j-1} = 0, \tag{E.36}$$

for $j = 1$ to $M - 2$. Thus, for the β coefficients, we always have $M - 1$ unknown and $M - 2$ equations. Furthermore, these equations take the form of Eq. (E.36) and are *identical* for any value of n. Once again we recognise that setting all α equal and all β to 0 is a valid solution, and so the first family of scarred state is indeed an eigenstate. As for the $n = 1$, we also recognise that Eq. (E.36) admits $\beta_j = J_{e,j}/2$ as a solution.

For the α, if we add a contribution of $\overline{\omega}_j$ for each site that has a triplet on site j as in the second family of scars, we recognise that α_{ST} and α_{TS} have the same contributions outside of site k and $k+1$. It is then straightforward to see that $\alpha_{ST} - \alpha_{TS} = \overline{\omega}_{j+1} - \overline{\omega}_j$ and that Eq. (E.33) is satisfied, concluding our proof.

Appendix F

Entanglement entropy of rainbow scars

In this Appendix, we discuss the entanglement entropy of the two families of scarred eigenstates in the XY ladder of Sec. 6.3. Due to the su(2) algebra, the eigenstates of the first family have the structure of angular momentum eigenstates. As a result, they have entanglement entropy scaling as $\propto \ln(M)$. In fact, it is straightforward to compute their entanglement entropy analytically. Let us assume that M is even and equal to $2R$. For simplicity, we will concentrate on the state with $n = R$ which has exactly zero energy, as it has the highest entanglement entropy among all scarred states. We will make heavy use of the state $|a, b\rangle$, which as we recall denotes the superposition of all states with a singlets and b triplets. Using this notation, it is easy to decompose the state $|E_R\rangle$ as

$$|E_R\rangle = \frac{|R,R\rangle}{\sqrt{\binom{2R}{R}}} = \frac{1}{\sqrt{\binom{2R}{R}}} \sum_{k=0}^{R} |R-k,k\rangle \otimes |k,R-k\rangle = \sum_{k=0}^{R} \frac{\binom{R}{k}}{\sqrt{\binom{2R}{R}}} |\psi_{1,k}\rangle \otimes |\psi_{2,k}\rangle\,, \quad \text{(F.1)}$$

where $|\psi_{1,k}\rangle$, $|\psi_{2,k}\rangle$ are the normalised versions of $|R-k,k\rangle$ and $|k,R-k\rangle$, respectively. From the last expression, we recognise the prefactors as the Schmidt coefficients. Therefore, the entanglement spectrum has $R+1 = M/2+1$ non-zero values with

$$p_k = \frac{\binom{R}{k}^2}{\binom{2R}{R}}, \quad \text{(F.2)}$$

for $k = 0, 1, \ldots, R$. In the large-M limit, one can perform a saddle-point approximation to arrive at the result $S_{1,\perp} = 0.5 + 0.5\ln(\pi M/8)$, demonstrating the logarithmic scaling with system size.

For the second family of scars, the computation is more arduous as the entanglement entropy depends on the disorder realisation. Here we provide an exact computation for a few extremal cases. While we do not have proof that these are the cases with maximum and minimum entanglement entropy, they match with the results of our

numerical optimisations. First, we can focus on the $|J_{e,k}| \gg |\overline{\omega}_k|$ case, in which we assume that the $\overline{\omega}_k$ are negligible. Let us also set all $J_{e,k}$ equal to 1, except for the middle one which we set to $J_{e,R} = J_e$. We can then find the Schmidt decomposition of this state as

$$\begin{aligned}|E'_R\rangle =& \frac{J_e}{2\mathcal{N}_R}\sum_{k=0}^{R-1}|R{-}1{-}k,k\rangle\,|\mathbf{D}\rangle\otimes|\mathbf{H}\rangle\,|k,R{-}1{-}k\rangle+\frac{1}{2\mathcal{N}_R}\sum_{k=0}^{R-2}|\tilde{\psi}_{1,k}\rangle\otimes|k{+}1,R{-}1{-}k\rangle\\ &+\frac{J_e}{2\mathcal{N}_R}\sum_{k=0}^{R-1}|R{-}1{-}k,k\rangle\,|\mathbf{H}\rangle\otimes|\mathbf{D}\rangle\,|k,R{-}1{-}k\rangle+\frac{1}{2\mathcal{N}_R}\sum_{k=0}^{R-2}|k{+}1,R{-}1{-}k\rangle\otimes|\tilde{\psi}_{2,k}\rangle\,,\end{aligned} \tag{F.3}$$

with

$$\begin{aligned}|\tilde{\psi}_{1,k}\rangle =& \sum_{j=1}^{R-1}\Big(|\mathbf{DH}\rangle_{\Lambda_j}+|\mathbf{HD}\rangle_{\Lambda_j}\Big)\otimes|R{-}2{-}k,k\rangle_{\overline{\Lambda}_j},\\ |\tilde{\psi}_{2,k}\rangle =& \sum_{j=R+1}^{M-1}\Big(|\mathbf{DH}\rangle_{\Lambda_j}+|\mathbf{HD}\rangle_{\Lambda_j}\Big)\otimes|R{-}2{-}k,k\rangle_{\overline{\Lambda}_j}\,,\end{aligned} \tag{F.4}$$

where Λ_j denotes sites j and $j+1$ while $\overline{\Lambda}_j$ denote all other sites in the same half-system. To find the Schmidt coefficient the only step left is to normalise each ket in the decomposition. We already see that we have at most $4R-2 = 2M-2$ non-zero coefficients, showing that a state of this form can have, at most, entanglement growing as $\ln(M)$.

Let us first write down $\mathcal{N}_R$ from Eq. (E.18) as

$$\mathcal{N}_R = \frac{1}{\sqrt{2}}\sqrt{\binom{2R-2}{R-1}(J_e^2+M-2)}. \tag{F.5}$$

Consequently, the contribution to the entanglement spectrum in the first two sums are identical and given by

$$p_k^{DH} = p_k^{HD} = \frac{J_e^2}{2\,(J_e^2+M-2)}\frac{\binom{R-1}{k}^2}{\binom{2R-2}{R-1}}. \tag{F.6}$$

Similarly, the third and fourth sums have the same coefficients given by

$$p_k^1 = p_k^2 = \frac{(R-1)}{(J_e^2+M-2)}\frac{\binom{R-2}{k}\binom{R}{k+1}}{\binom{2R-2}{R-1}}. \tag{F.7}$$

The maximal entanglement entropy is obtained for $J_e = J_e^\star$ which scales as $\sqrt{M}$. In that case, we find numerically that $S_{2,\perp}^{\max} = S_{1,\perp} + \ln(4)$ in the large-M limit. It is easy to understand how this additive factor can appear. For the first family of scarred states, we have $R+1$ non-zero values in the entanglement spectrum, while in this case we have $4R-2$. For R very large, this is a fourfold increase of the number of non-zero

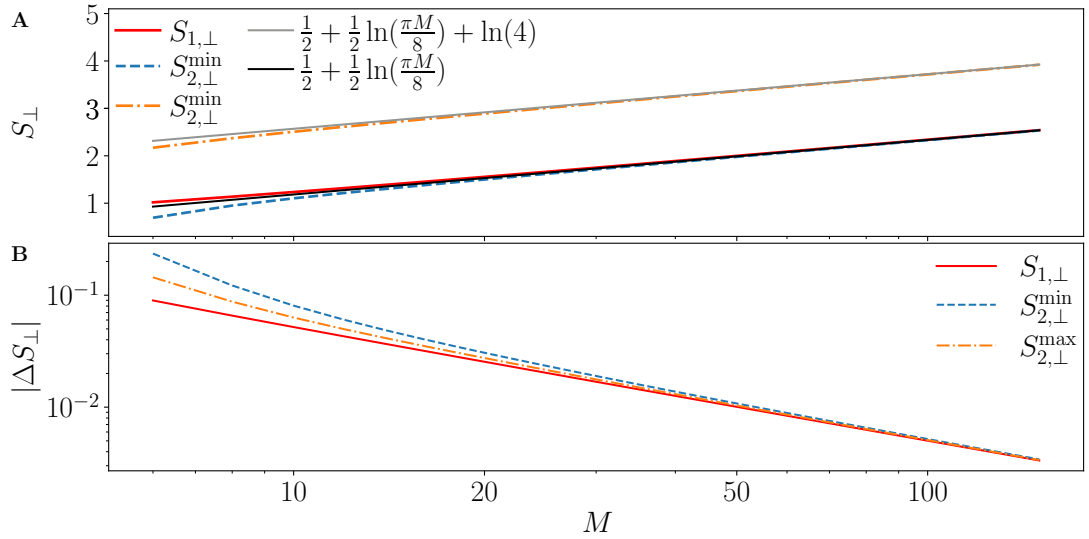

Figure F.1: **a** Entanglement entropy computed from the analytical formula of the entanglement spectrum. The gray and black lines represent the expected large-M limit and they are in good agreement with the data already for $M \approx 20$. **b** Difference between the data and the large-M prediction. For all three cases, the difference approximately decays as a power-law. We find that the slope is approximately -1, indicating a decay of $|\Delta S_\perp|$ as $\approx 1/M$.

values. As they have a similar distribution, this leads to a simple additive factor of 4 due to the log involved in the calculation.

The case with minimal entanglement entropy is in the limit of a single $J_{e,k}$ (with $k \neq R$) being much larger than all other ones. For simplicity, let us consider $J_{e,k} = \delta_{1,k}$. Then the state can be decomposed as

$$|E'_R\rangle = \frac{1}{\sqrt{2\binom{2R-2}{R-1}}} \sum_{k=0}^{R-2} \Big[(|\mathbf{DH}\rangle + |\mathbf{HD}\rangle) \otimes |R{-}2{-}k, k\rangle \Big] \otimes |k{+}1, R{-}1{-}k\rangle \,. \tag{F.8}$$

This gives us only $R-1$ Schmidt values, and the entanglement spectrum can be written down as

$$p_k = \frac{\binom{R-2}{k}\binom{R}{k+1}}{\binom{2R-2}{R-1}}. \tag{F.9}$$

In the limit of large M, we recover the same result as for scarred state of the first family $S^{\min}_{2,\perp} = S_{1,\perp} = 0.5{+}0.5\ln(\pi M/8)$. This can, once again, be understood simply from the number of nonzero values in the entanglement spectrum as their distribution is similar in both cases. As they have, respectively, $R-1$ and $R+1$ such values, they become identical at leading order in the large M limit. For all three cases, we can compute the entanglement entropy efficiently from the analytical form of the entanglement spectrum for systems with hundreds of sites. Fig. F.1 displays this along with the expected large-M behaviour. We find very good agreement between them already at $M \approx 20$, with the difference between them decreasing as $1/M$.

F. ENTANGLEMENT ENTROPY OF RAINBOW SCARS

While we do not have a proof that the cases treated are the true maximum and minimum of $S_{2,\perp}$ we now illustrate numerically that they provide excellent bounds in the large N limit. Fig. F.2**a** shows the entanglement entropy obtained for multiple random realisations with different ranges of parameters, and for numerical minimisation and maximisation over all $J_{e,k}$ and ω_k parameters. For the minimum we find exact agreement between our analytical and numerical results. For the maximum case, we find that in smaller systems, realisations with large disorder can have slightly higher entanglement entropy than our analytical Ansatz. Nonetheless, the difference between the numerical and analytical maxima quickly decreases as N gets larger. This is confirmed by looking at the entanglement spectrum. In all states obtained by numerical maximisation of entropy, there are exactly $N = 4R$ nonzero values in it. This precludes them from being volume-law states. Asymptotically, this will also be equivalent to the $4R-2$ nonzero values in our analytical Ansatz, up to $1/N$ corrections. For these reasons, we believe that the scarred states of the second family cannot be volume-law entangled and that our analytical Ansatz provides an upper-bound in the large N limit.

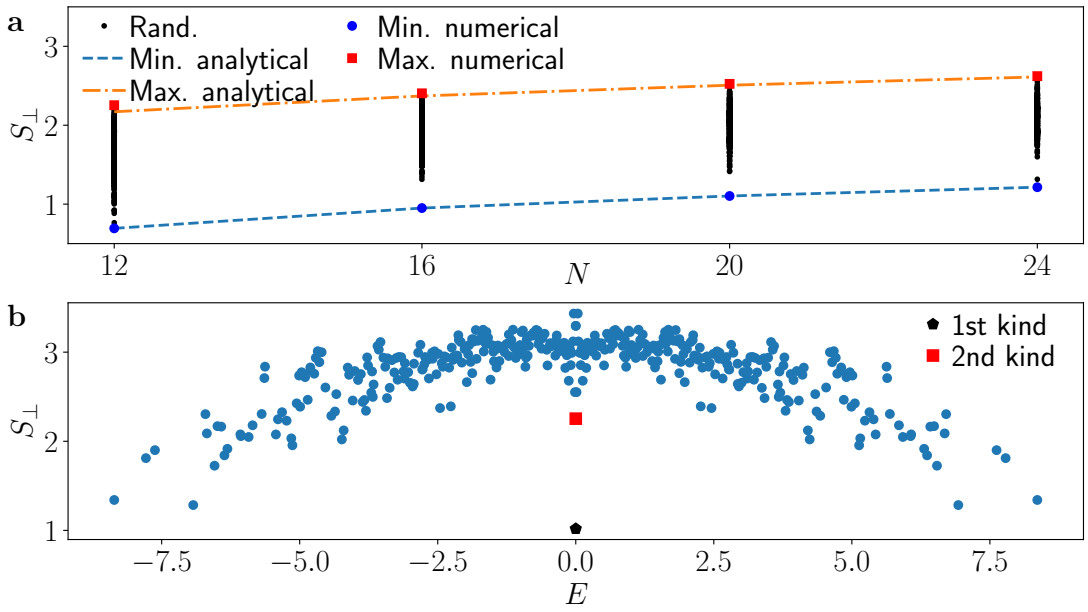

Figure F.2: **a** Entanglement entropy of the scarred state of the second family with $E = 0$ for random realisations, for the analytical formulas, and from numerical minimisation/maximisation. As N increases, the analytical and numerical results converge. **b** Entanglement entropy of eigenstates in the $Q = 0$ sector for $N = 12$ in the parameter regime found to maximise the entanglement entropy of the scarred state of the second family. The non-scarred eigenstates concentrate around an arc, as is typical from chaotic systems. This shows that high entanglement entropy can be obtained without getting close to a fine-tuned point where all parameters are identical.

The maxima of entanglement entropy obtained numerically are also useful to show

that it cannot only be reached by fine-tuned cases where many parameters are identical. As these case might be integrable or have additional symmetries, they are usually not trivially chaotic. Meanwhile, the numerical maxima do not have degenerate parameters and generically show characteristics of ergodic systems. This can be seen for example in the $N = 12$ case, for which the entanglement entropy of eigenstates is plotted in Fig. F.2**b**. The concentration of points around an arc is typical of systems obeying the ETH.

F. ENTANGLEMENT ENTROPY OF RAINBOW SCARS

References

[1] J.-Y. Desaules, F. Pietracaprina, Z. Papić, J. Goold and S. Pappalardi, Extensive multipartite entanglement from su(2) quantum many-body scars, *Phys. Rev. Lett.* **129**, 020601 (2022)

[2] M. Ljubotina, J.-Y. Desaules, M. Serbyn and Z. Papić, Superdiffusive energy transport in kinetically constrained models, *Phys. Rev. X* **13**, 011033 (2023)

[3] J.-Y. Desaules, G.-X. Su, I. P. McCulloch, B. Yang, Z. Papić et al., Ergodicity breaking under confinement in cold-atom quantum simulators, *arXiv eprints* **2301.07717** (2023)

[4] G.-X. Su, H. Sun, A. Hudomal, J.-Y. Desaules, Z.-Y. Zhou et al., Observation of many-body scarring in a Bose-Hubbard quantum simulator, *Phys. Rev. Res.* **5**, 023010 (2023)

[5] A. Daniel, A. Hallam, J.-Y. Desaules, A. Hudomal, G.-X. Su et al., Bridging quantum criticality via many-body scarring, *Phys. Rev. B* **107**, 235108 (2023)

[6] J.-Y. Desaules, A. Hudomal, C. J. Turner and Z. Papić, Proposal for realizing quantum scars in the tilted 1D Fermi-Hubbard model, *Phys. Rev. Lett.* **126**, 210601 (2021)

[7] P. Zhang, H. Dong, Y. Gao, L. Zhao, J. Hao et al., Many-body Hilbert space scarring on a superconducting processor, *Nature Physics* **19**, 120 (2023)

[8] H. Dong, J.-Y. Desaules, N. Gao Yu, Wang, Z. Guo, J. Chen et al., Robust rainbow entanglement in disordered quantum circuits at infinite temperature, In preparation

[9] L. Landau and E. Lifshitz, *Statistical Physics*, volume 5, Elsevier Science (2013)

[10] H. Muller-kirsten, *Basics Of Statistical Physics*, World Scientific Publishing Company, second edition (2013)

[11] L. D'Alessio, Y. Kafri, A. Polkovnikov and M. Rigol, From quantum chaos and eigenstate thermalization to statistical mechanics and thermodynamics, *Adv. Phys.* **65**, 239 (2016)

[12] M. Rigol, V. Dunjko and M. Olshanii, Thermalization and its mechanism for generic isolated quantum systems, *Nature* **452**, 854 (2008)

[13] M. Srednicki, Chaos and quantum thermalization, *Phys. Rev. E* **50**, 888 (1994)

[14] J. M. Deutsch, Eigenstate thermalization hypothesis, *Reports on Progress in Physics* **81**, 082001 (2018)

[15] M. Srednicki, The approach to thermal equilibrium in quantized chaotic systems, *Journal of Physics A: Mathematical and General* **32**, 1163 (1999)

[16] W. Beugeling, R. Moessner and M. Haque, Finite-size scaling of eigenstate thermalization, *Phys. Rev. E* **89**, 042112 (2014)

[17] M. A. Nielsen and I. L. Chuang, *Quantum computation and quantum information*, Cambridge university press (2010)

[18] D. N. Page, Average entropy of a subsystem, *Phys. Rev. Lett.* **71**, 1291 (1993)

[19] M. L. Mehta, *Random matrices*, Elsevier, third edition (2004)

[20] O. Bohigas, M. J. Giannoni and C. Schmit, Characterization of chaotic quantum spectra and universality of level fluctuation laws, *Phys. Rev. Lett.* **52**, 1 (1984)

[21] F. J. Dyson, A Brownian-motion model for the eigenvalues of a random matrix, *Journal of Mathematical Physics* **3**, 1191 (2004)

[22] E. P. Wigner, On the distribution of the roots of certain symmetric matrices, *Annals of Mathematics* **67**, 325 (1958)

[23] F. Haake, *Quantum Signatures of Chaos*, Springer Series in Synergetics, Springer, third edition (2010)

[24] V. Oganesyan and D. A. Huse, Localization of interacting fermions at high temperature, *Phys. Rev. B* **75**, 155111 (2007)

[25] Y. Y. Atas, E. Bogomolny, O. Giraud and G. Roux, Distribution of the ratio of consecutive level spacings in random matrix ensembles, *Phys. Rev. Lett.* **110**, 084101 (2013)

[26] B. Sutherland, *Beautiful models: 70 years of exactly solved quantum many-body problems*, World Scientific Publishing Company (2004)

[27] D. Basko, I. Aleiner and B. Altshuler, Metal–insulator transition in a weakly interacting many-electron system with localized single-particle states, *Annals of Physics* **321**, 1126 (2006)

[28] A. Pal and D. A. Huse, Many-body localization phase transition, *Phys. Rev. B* **82**, 174411 (2010)

[29] P. W. Anderson, Absence of diffusion in certain random lattices, *Phys. Rev.* **109**, 1492 (1958)

[30] R. Nandkishore and D. A. Huse, Many-body localization and thermalization in quantum statistical mechanics, *Annual Review of Condensed Matter Physics* **6**, 15 (2015)

[31] D. A. Abanin, E. Altman, I. Bloch and M. Serbyn, Colloquium: Many-body localization, thermalization, and entanglement, *Rev. Mod. Phys.* **91**, 021001 (2019)

[32] V. Khemani, M. Hermele and R. Nandkishore, Localization from Hilbert space shattering: From theory to physical realizations, *Phys. Rev. B* **101**, 174204 (2020)

[33] S. Pai and M. Pretko, Dynamical scar states in driven fracton systems, *Phys. Rev. Lett.* **123**, 136401 (2019)

[34] S. Moudgalya, A. Prem, R. Nandkishore, N. Regnault and B. A. Bernevig, Thermalization and its absence within Krylov subspaces of a constrained Hamiltonian, in *Memorial Volume for Shoucheng Zhang*, World Scientific, pp. 147–209 (2022)

[35] P. Sala, T. Rakovszky, R. Verresen, M. Knap and F. Pollmann, Ergodicity breaking arising from hilbert space fragmentation in dipole-conserving Hamiltonians, *Phys. Rev. X* **10**, 011047 (2020)

[36] E. J. Heller, Bound-state eigenfunctions of classically chaotic Hamiltonian systems: Scars of periodic orbits, *Phys. Rev. Lett.* **53**, 1515 (1984)

[37] E. J. Heller, Wavepacket dynamics and quantum chaology, in *Chaos and quantum physics*, North-Holland: Amsterdam, volume 52 (1991)

[38] G. G. de Polavieja, F. Borondo and R. M. Benito, Scars in groups of eigenstates in a classically chaotic system, *Phys. Rev. Lett.* **73**, 1613 (1994)

[39] D. A. Wisniacki, F. Borondo, E. Vergini and R. M. Benito, Localization properties of groups of eigenstates in chaotic systems, *Phys. Rev. E* **63**, 066220 (2001)

[40] S. Sridhar, Experimental observation of scarred eigenfunctions of chaotic microwave cavities, *Phys. Rev. Lett.* **67**, 785 (1991)

[41] P. B. Wilkinson, T. M. Fromhold, L. Eaves, F. W. Sheard, N. Miura et al., Observation of scarred wavefunctions in a quantum well with chaotic electron dynamics, *Nature* **380**, 608 (1996)

[42] D. Wintgen and A. Hönig, Irregular wave functions of a hydrogen atom in a uniform magnetic field, *Phys. Rev. Lett.* **63**, 1467 (1989)

[43] H. Bernien, S. Schwartz, A. Keesling, H. Levine, A. Omran et al., Probing many-body dynamics on a 51-atom quantum simulator, *Nature* **551**, 579 (2017)

[44] H. Labuhn, D. Barredo, S. Ravets, S. de Léséleuc, T. Macrì et al., Tunable two-dimensional arrays of single Rydberg atoms for realizing quantum Ising models, *Nature* **534**, 667 (2016)

[45] P. Fendley, K. Sengupta and S. Sachdev, Competing density-wave orders in a one-dimensional hard-boson model, *Phys. Rev. B* **69**, 075106 (2004)

[46] I. Lesanovsky and H. Katsura, Interacting Fibonacci anyons in a Rydberg gas, *Phys. Rev. A* **86**, 041601(R) (2012)

[47] S. Bravyi, D. P. DiVincenzo and D. Loss, Schrieffer-Wolff transformation for quantum many-body systems, *Annals of Physics* **326**, 2793 (2011)

[48] B. Olmos, M. Müller and I. Lesanovsky, Thermalization of a strongly interacting 1D Rydberg lattice gas, *New Journal of Physics* **12**, 013024 (2010)

[49] B. Sun and F. Robicheaux, Numerical study of two-body correlation in a 1D lattice with perfect blockade, *New Journal of Physics* **10**, 045032 (2008)

[50] C. J. Turner, A. A. Michailidis, D. A. Abanin, M. Serbyn and Z. Papić, Weak ergodicity breaking from quantum many-body scars, *Nature Physics* **14**, 745 (2018)

[51] A. Feiguin, S. Trebst, A. W. W. Ludwig, M. Troyer, A. Kitaev et al., Interacting anyons in topological quantum liquids: The golden chain, *Phys. Rev. Lett.* **98**, 160409 (2007)

[52] A. W. Sandvik, A. Avella and F. Mancini, Computational studies of quantum spin systems, in *AIP Conference Proceedings*, AIP (2010)

[53] M. Schecter and T. Iadecola, Many-body spectral reflection symmetry and protected infinite-temperature degeneracy, *Phys. Rev. B* **98**, 035139 (2018)

[54] C. J. Turner, A. A. Michailidis, D. A. Abanin, M. Serbyn and Z. Papić, Quantum scarred eigenstates in a Rydberg atom chain: Entanglement, breakdown of thermalization, and stability to perturbations, *Phys. Rev. B* **98**, 155134 (2018)

[55] S. Dooley and G. Kells, Extreme many-body scarring in a quantum spin chain via weak dynamical constraints, *Phys. Rev. B* **105**, 155127 (2022)

[56] J. Haegeman, J. I. Cirac, T. J. Osborne, I. Pižorn, H. Verschelde et al., Time-dependent variational principle for quantum lattices, *Phys. Rev. Lett.* **107**, 070601 (2011)

[57] P. A. M. Dirac, Note on exchange phenomena in the Thomas atom, *Mathematical Proceedings of the Cambridge Philosophical Society* **26**, 376 (1930)

[58] P. Kramer and M. Saraceno, *Geometry of the Time-Dependent Variational Principle in Quantum Mechanics*, Lecture Notes in Physics, Springer Berlin Heidelberg (1981)

[59] W. W. Ho, S. Choi, H. Pichler and M. D. Lukin, Periodic orbits, entanglement, and quantum many-body scars in constrained models: Matrix product state approach, *Phys. Rev. Lett.* **122**, 040603 (2019)

[60] D. Pérez-García, F. Verstraete, M. M. Wolf and J. I. Cirac, Matrix product state representations, *Quantum Inf. Comput.* **7**, 401 (2007)

[61] U. Schollwöck, The density-matrix renormalization group in the age of matrix product states, *Annals of Physics* **326**, 96 (2011)

[62] M. C. Gutzwiller, Correlation of electrons in a narrow s band, *Phys. Rev.* **137**, A1726 (1965)

[63] C. J. Turner, J.-Y. Desaules, K. Bull and Z. Papić, Correspondence principle for many-body scars in ultracold Rydberg atoms, *Phys. Rev. X* **11**, 021021 (2021)

[64] A. A. Michailidis, C. J. Turner, Z. Papić, D. A. Abanin and M. Serbyn, Slow quantum thermalization and many-body revivals from mixed phase space, *Phys. Rev. X* **10**, 011055 (2020)

[65] A. N. Kolmogorov, On the conservation of conditionally periodic motions under small perturbation of the Hamiltonian, in *Dokl. Akad. Nauk. SSR* (1954), volume 98, pp. 2–3

[66] V. I. Arnold, Proof of a theorem of A.N. Kolmogorov on the invariance of quasi-periodic motions under small perturbations of the Hamiltonian, *Russian Mathematical Surveys* **18**, 9 (1963)

[67] S. Choi, C. J. Turner, H. Pichler, W. W. Ho, A. A. Michailidis et al., Emergent SU(2) dynamics and perfect quantum many-body scars, *Phys. Rev. Lett.* **122**, 220603 (2019)

[68] K. Omiya and M. Müller, Quantum many-body scars in bipartite Rydberg arrays originating from hidden projector embedding, *Phys. Rev. A* **107**, 023318 (2023)

[69] K. Bull, J.-Y. Desaules and Z. Papić, Quantum scars as embeddings of weakly broken Lie algebra representations, *Phys. Rev. B* **101**, 165139 (2020)

[70] V. Khemani, C. R. Laumann and A. Chandran, Signatures of integrability in the dynamics of Rydberg-blockaded chains, *Phys. Rev. B* **99**, 161101(R) (2019)

[71] B. Windt and H. Pichler, Squeezing quantum many-body scars, *Phys. Rev. Lett.* **128**, 090606 (2022)

[72] C.-J. Lin and O. I. Motrunich, Exact quantum many-body scar states in the Rydberg-blockaded atom chain, *Phys. Rev. Lett.* **122**, 173401 (2019)

[73] T. Iadecola, M. Schecter and S. Xu, Quantum many-body scars from magnon condensation, *Phys. Rev. B* **100**, 184312 (2019)

[74] C.-J. Lin, A. Chandran and O. I. Motrunich, Slow thermalization of exact quantum many-body scar states under perturbations, *Phys. Rev. Research* **2**, 033044 (2020)

[75] I. Mondragon-Shem, M. G. Vavilov and I. Martin, Fate of quantum many-body scars in the presence of disorder, *PRX Quantum* **2**, 030349 (2021)

[76] A. A. Michailidis, C. J. Turner, Z. Papić, D. A. Abanin and M. Serbyn, Stabilizing two-dimensional quantum scars by deformation and synchronization, *Phys. Rev. Research* **2**, 022065(R) (2020)

[77] C.-J. Lin, V. Calvera and T. H. Hsieh, Quantum many-body scar states in two-dimensional Rydberg atom arrays, *Phys. Rev. B* **101**, 220304(R) (2020)

[78] D. Bluvstein, A. Omran, H. Levine, A. Keesling, G. Semeghini et al., Controlling quantum many-body dynamics in driven Rydberg atom arrays, *Science* **371**, 1355 (2021)

[79] K. Huang, Y. Wang and X. Li, Stability of scar states in the two-dimensional PXP model against random disorder, *Phys. Rev. B* **104**, 214305 (2021)

[80] F. M. Surace, P. P. Mazza, G. Giudici, A. Lerose, A. Gambassi et al., Lattice gauge theories and string dynamics in Rydberg atom quantum simulators, *Phys. Rev. X* **10**, 021041 (2020)

[81] J.-Y. Desaules, D. Banerjee, A. Hudomal, Z. Papić, A. Sen et al., Weak ergodicity breaking in the Schwinger model, *Phys. Rev. B* **107**, L201105 (2023)

[82] J.-Y. Desaules, A. Hudomal, D. Banerjee, A. Sen, Z. Papić et al., Prominent quantum many-body scars in a truncated Schwinger model, *Phys. Rev. B* **107**, 205112 (2023)

[83] A. Hudomal, J.-Y. Desaules, B. Mukherjee, G.-X. Su, J. C. Halimeh et al., Driving quantum many-body scars in the PXP model, *Phys. Rev. B* **106**, 104302 (2022)

[84] B. Mukherjee, S. Nandy, A. Sen, D. Sen and K. Sengupta, Collapse and revival of quantum many-body scars via Floquet engineering, *Phys. Rev. B* **101**, 245107 (2020)

[85] B. Mukherjee, A. Sen and K. Sengupta, Periodically driven Rydberg chains with staggered detuning, *Phys. Rev. B* **106**, 064305 (2022)

[86] N. Maskara, A. A. Michailidis, W. W. Ho, D. Bluvstein, S. Choi et al., Discrete time-crystalline order enabled by quantum many-body scars: Entanglement steering via periodic driving, *Phys. Rev. Lett.* **127**, 090602 (2021)

[87] H. K. Park and S. Lee, Subharmonic fidelity revival in a driven PXP model, *Phys. Rev. B* **107**, 205142 (2023)

[88] D. P. Arovas, Two exact excited states for the $S = 1$ AKLT chain, *Physics Letters A* **137**, 431 (1989)

[89] M. Serbyn, D. A. Abanin and Z. Papić, Quantum many-body scars and weak breaking of ergodicity, *Nature Physics* **17**, 675 (2021)

[90] A. Chandran, T. Iadecola, V. Khemani and R. Moessner, Quantum many-body scars: A quasiparticle perspective, *Annual Review of Condensed Matter Physics* **14**, 443 (2023)

[91] S. Moudgalya, B. A. Bernevig and N. Regnault, Quantum many-body scars and Hilbert space fragmentation: A review of exact results, *Reports on Progress in Physics* **85**, 086501 (2022)

[92] Z. Papić, Weak ergodicity breaking through the lens of quantum entanglement, in *Entanglement in Spin Chains: From Theory to Quantum Technology Applications*, Springer, pp. 341–395 (2022)

[93] N. Shiraishi and T. Mori, Systematic construction of counterexamples to the eigenstate thermalization hypothesis, *Phys. Rev. Lett.* **119**, 030601 (2017)

[94] F. M. Surace, G. Giudici and M. Dalmonte, Weak-ergodicity-breaking via lattice supersymmetry, *Quantum* **4**, 339 (2020)

[95] Y. Kuno, T. Mizoguchi and Y. Hatsugai, Flat band quantum scar, *Phys. Rev. B* **102**, 241115(R) (2020)

[96] P. A. McClarty, M. Haque, A. Sen and J. Richter, Disorder-free localization and many-body quantum scars from magnetic frustration, *Phys. Rev. B* **102**, 224303 (2020)

[97] J. Wildeboer, A. Seidel, N. S. Srivatsa, A. E. B. Nielsen and O. Erten, Topological quantum many-body scars in quantum dimer models on the kagome lattice, *Phys. Rev. B* **104**, L121103 (2021)

[98] S. Ok, K. Choo, C. Mudry, C. Castelnovo, C. Chamon et al., Topological many-body scar states in dimensions one, two, and three, *Phys. Rev. Res.* **1**, 033144 (2019)

[99] P.-G. Rozon and K. Agarwal, Broken unitary picture of dynamics in quantum many-body scars, *arXiv eprints* **2302.04885** (2023)

[100] L. Logarić, S. Dooley, S. Pappalardi and J. Goold, Quantum many-body scars in dual unitary circuits, *arXiv eprints* **2307.06755** (2023)

[101] C. N. Yang, η pairing and off-diagonal long-range order in a Hubbard model, *Phys. Rev. Lett.* **63**, 2144 (1989)

[102] D. K. Mark, C.-J. Lin and O. I. Motrunich, Unified structure for exact towers of scar states in the Affleck-Kennedy-Lieb-Tasaki and other models, *Phys. Rev. B* **101**, 195131 (2020)

[103] N. O'Dea, F. Burnell, A. Chandran and V. Khemani, From tunnels to towers: Quantum scars from Lie algebras and q-deformed Lie algebras, *Phys. Rev. Research* **2**, 043305 (2020)

[104] K. Pakrouski, P. N. Pallegar, F. K. Popov and I. R. Klebanov, Many-body scars as a group invariant sector of Hilbert space, *Phys. Rev. Lett.* **125**, 230602 (2020)

[105] J. Ren, C. Liang and C. Fang, Quasisymmetry groups and many-body scar dynamics, *Phys. Rev. Lett.* **126**, 120604 (2021)

[106] S. Moudgalya, N. Regnault and B. A. Bernevig, η-pairing in Hubbard models: From spectrum generating algebras to quantum many-body scars, *Phys. Rev. B* **102**, 085140 (2020)

[107] D. K. Mark and O. I. Motrunich, η-pairing states as true scars in an extended Hubbard model, *Phys. Rev. B* **102**, 075132 (2020)

[108] M. Schecter and T. Iadecola, Weak ergodicity breaking and quantum many-body scars in spin-1 XY magnets, *Phys. Rev. Lett.* **123**, 147201 (2019)

[109] S. Moudgalya, N. Regnault and B. A. Bernevig, Entanglement of exact excited states of Affleck-Kennedy-Lieb-Tasaki models: Exact results, many-body scars, and violation of the strong eigenstate thermalization hypothesis, *Phys. Rev. B* **98**, 235156 (2018)

[110] K. Omiya and M. Müller, Fractionalization paves the way to local projector embeddings of quantum many-body scars, *Phys. Rev. B* **108**, 054412 (2023)

[111] T. Iadecola and M. Schecter, Quantum many-body scar states with emergent kinetic constraints and finite-entanglement revivals, *Phys. Rev. B* **101**, 024306 (2020)

[112] N. Shibata, N. Yoshioka and H. Katsura, Onsager's scars in disordered spin chains, *Phys. Rev. Lett.* **124**, 180604 (2020)

[113] K. Lee, R. Melendrez, A. Pal and H. J. Changlani, Exact three-colored quantum scars from geometric frustration, *Phys. Rev. B* **101**, 241111(R) (2020)

[114] C. M. Langlett, Z.-C. Yang, J. Wildeboer, A. V. Gorshkov, T. Iadecola et al., Rainbow scars: From area to volume law, *Phys. Rev. B* **105**, L060301 (2022)

[115] J. Wildeboer, C. M. Langlett, Z.-C. Yang, A. V. Gorshkov, T. Iadecola et al., Quantum many-body scars from Einstein-Podolsky-Rosen states in bilayer systems, *Phys. Rev. B* **106**, 205142 (2022)

[116] P.-G. Rozon, M. J. Gullans and K. Agarwal, Constructing quantum many-body scar Hamiltonians from Floquet automata, *Phys. Rev. B* **106**, 184304 (2022)

[117] S. Moudgalya, E. O'Brien, B. A. Bernevig, P. Fendley and N. Regnault, Large classes of quantum scarred Hamiltonians from matrix product states, *Phys. Rev. B* **102**, 085120 (2020)

[118] S. Moudgalya and O. I. Motrunich, Hilbert space fragmentation and commutant algebras, *Phys. Rev. X* **12**, 011050 (2022)

[119] S. Moudgalya and O. I. Motrunich, Exhaustive characterization of quantum many-body scars using commutant algebras, *arXiv eprints* **2209.03377** (2022)

[120] S. Moudgalya and O. I. Motrunich, From symmetries to commutant algebras in standard Hamiltonians, *Annals of Physics* **455**, 169384 (2023)

[121] S. Moudgalya and O. I. Motrunich, Numerical methods for detecting symmetries and commutant algebras, *Phys. Rev. B* **107**, 224312 (2023)

[122] K. Bull, I. Martin and Z. Papić, Systematic construction of scarred many-body dynamics in 1D lattice models, *Phys. Rev. Lett.* **123**, 030601 (2019)

[123] S. Moudgalya, B. A. Bernevig and N. Regnault, Quantum many-body scars in a Landau level on a thin torus, *Phys. Rev. B* **102**, 195150 (2020)

[124] A. Hudomal, I. Vasić, N. Regnault and Z. Papić, Quantum scars of bosons with correlated hopping, *Commun. Phys.* **3**, 99 (2020)

[125] H. Zhao, J. Vovrosh, F. Mintert and J. Knolle, Quantum many-body scars in optical lattices, *Phys. Rev. Lett.* **124**, 160604 (2020)

[126] B. Buča, J. Tindall and D. Jaksch, Non-stationary coherent quantum many-body dynamics through dissipation, *Nat. Commun.* **10**, 1730 (2019)

[127] J. Tindall, B. Buča, J. R. Coulthard and D. Jaksch, Heating-induced long-range η pairing in the Hubbard model, *Phys. Rev. Lett.* **123**, 030603 (2019)

[128] S. Sugiura, T. Kuwahara and K. Saito, Many-body scar state intrinsic to periodically driven system, *Phys. Rev. Res.* **3**, L012010 (2021)

[129] K. Mizuta, K. Takasan and N. Kawakami, Exact Floquet quantum many-body scars under Rydberg blockade, *Phys. Rev. Research* **2**, 033284 (2020)

[130] N. S. Srivatsa, H. Yarloo, R. Moessner and A. E. B. Nielsen, Mobility edges through inverted quantum many-body scarring, *Phys. Rev. B* **108**, L100202 (2023)

[131] Q. Chen and Z. Zhu, Inverting multiple quantum many-body scars via disorder, *arXiv eprints* **2301.03405** (2023)

[132] M. Iversen and A. E. B. Nielsen, Tower of quantum scars in a partially many-body localized system, *Phys. Rev. B* **107**, 205140 (2023)

[133] V. Popkov, X. Zhang and A. Klümper, Phantom Bethe excitations and spin helix eigenstates in integrable periodic and open spin chains, *Phys. Rev. B* **104**, L081410 (2021)

[134] P. N. Jepsen, Y. K. E. Lee, H. Lin, I. Dimitrova, Y. Margalit et al., Long-lived phantom helix states in Heisenberg quantum magnets, *Nature Physics* **18**, 899 (2022)

[135] G. Zhang and Z. Song, Stable dynamic helix state in the nonintegrable XXZ Heisenberg model, *arXiv eprints* **2308.06146** (2023)

[136] W. Kao, K.-Y. Li, K.-Y. Lin, S. Gopalakrishnan and B. L. Lev, Topological pumping of a 1D dipolar gas into strongly correlated prethermal states, *Science* **371**, 296 (2021)

[137] I.-C. Chen, B. Burdick, Y. Yao, P. P. Orth and T. Iadecola, Error-mitigated simulation of quantum many-body scars on quantum computers with pulse-level control, *Phys. Rev. Res.* **4**, 043027 (2022)

[138] E. J. Gustafson, A. C. Y. Li, A. Khan, J. Kim, D. M. Kurkcuoglu et al., Preparing quantum many-body scar states on quantum computers, *arXiv eprints* **2301.08226** (2023)

[139] H. Zhou, H. Gao, N. T. Leitao, O. Makarova, I. Cong et al., Robust Hamiltonian engineering for interacting qudit systems, *arXiv eprints* **2305.09757** (2023)

[140] A. Omran, H. Levine, A. Keesling, G. Semeghini, T. T. Wang et al., Generation and manipulation of Schrödinger cat states in Rydberg atom arrays, *Science* **365**, 570 (2019)

[141] M. Ljubotina, B. Roos, D. A. Abanin and M. Serbyn, Optimal steering of matrix product states and quantum many-body scars, *PRX Quantum* **3**, 030343 (2022)

[142] A. Hallam, J.-Y. Desaules and Z. Papić, Embedding semiclassical periodic orbits into chaotic many-body Hamiltonians, *Phys. Rev. Lett.* **131**, 110401 (2023)

[143] S. Dooley, Robust quantum sensing in strongly interacting systems with many-body scars, *PRX Quantum* **2**, 020330 (2021)

[144] O. Gühne, G. Tóth and H. J. Briegel, Multipartite entanglement in spin chains, *New Journal of Physics* **7**, 229 (2005)

[145] C. W. Helstrom, Quantum detection and estimation theory, *Journal of Statistical Physics* **1**, 231 (1969)

[146] G. Tóth and I. Apellaniz, Quantum metrology from a quantum information science perspective, *Journal of Physics A: Mathematical and Theoretical* **47**, 424006 (2014)

[147] L. Pezzè and A. Smerzi, Quantum theory of phase estimation, in G. Tino and M. Kasevich, eds., *"Atom Interferometry", Proceedings of the International School of Physics "Enrico Fermi"*, IOS Press (2014), p. 691

[148] S. L. Braunstein and C. M. Caves, Statistical distance and the geometry of quantum states, *Phys. Rev. Lett.* **72**, 3439 (1994)

[149] D. Petz and C. Ghinea, Introduction to quantum Fisher information, in *Quantum Probability and Related Topics*, World Scientific (2011)

[150] L. Pezzè, A. Smerzi, M. K. Oberthaler, R. Schmied and P. Treutlein, Quantum metrology with nonclassical states of atomic ensembles, *Rev. Mod. Phys.* **90**, 035005 (2018)

[151] P. Hyllus, W. Laskowski, R. Krischek, C. Schwemmer, W. Wieczorek et al., Fisher information and multiparticle entanglement, *Phys. Rev. A* **85**, 022321 (2012)

[152] G. Tóth, Multipartite entanglement and high-precision metrology, *Phys. Rev. A* **85**, 022322 (2012)

[153] L. Pezzé and A. Smerzi, Entanglement, nonlinear dynamics, and the Heisenberg limit, *Phys. Rev. Lett.* **102**, 100401 (2009)

[154] P. Hauke, M. Heyl, L. Tagliacozzo and P. Zoller, Measuring multipartite entanglement through dynamic susceptibilities, *Nature Physics* **12**, 778 (2016)

[155] L. Pezzè, M. Gabbrielli, L. Lepori and A. Smerzi, Multipartite entanglement in topological quantum phases, *Phys. Rev. Lett.* **119**, 250401 (2017)

[156] J. M. Deutsch, Quantum statistical mechanics in a closed system, *Phys. Rev. A* **43**, 2046 (1991)

[157] H. Araki, Gibbs states of a one dimensional quantum lattice, *Communications in Mathematical Physics* **14**, 120 (1969)

[158] J. R. Garrison and T. Grover, Does a single eigenstate encode the full Hamiltonian?, *Phys. Rev. X* **8**, 021026 (2018)

[159] T. Kuwahara and K. Saito, Eigenstate thermalization from the clustering property of correlation, *Phys. Rev. Lett.* **124**, 200604 (2020)

[160] J. M. Deutsch, H. Li and A. Sharma, Microscopic origin of thermodynamic entropy in isolated systems, *Phys. Rev. E* **87**, 042135 (2013)

[161] L. Vidmar and M. Rigol, Entanglement entropy of eigenstates of quantum chaotic Hamiltonians, *Phys. Rev. Lett.* **119**, 220603 (2017)

[162] C. Murthy and M. Srednicki, Structure of chaotic eigenstates and their entanglement entropy, *Phys. Rev. E* **100**, 022131 (2019)

[163] M. Brenes, S. Pappalardi, J. Goold and A. Silva, Multipartite entanglement structure in the eigenstate thermalization hypothesis, *Phys. Rev. Lett.* **124**, 040605 (2020)

[164] P. Zanardi, M. G. Paris and L. C. Venuti, Quantum criticality as a resource for quantum estimation, *Physical Review A* **78**, 042105 (2008)

[165] M. Gabbrielli, A. Smerzi and L. Pezzè, Multipartite entanglement at finite temperature, *Scientific reports* **8**, 15663 (2018)

[166] I. Frérot and T. Roscilde, Quantum critical metrology, *Physical review letters* **121**, 020402 (2018)

[167] I. Frérot and T. Roscilde, Reconstructing the quantum critical fan of strongly correlated systems using quantum correlations, *Nature communications* **10**, 577 (2019)

[168] C. N. Yang, Concept of off-diagonal long-range order and the quantum phases of liquid He and of superconductors, *Rev. Mod. Phys.* **34**, 694 (1962)

[169] T. Prosen and M. Žnidarič, Diffusive high-temperature transport in the one-dimensional Hubbard model, *Phys. Rev. B* **86**, 125118 (2012)

[170] C. Karrasch, J. E. Moore and F. Heidrich-Meisner, Real-time and real-space spin and energy dynamics in one-dimensional spin-$\frac{1}{2}$ systems induced by local quantum quenches at finite temperatures, *Phys. Rev. B* **89**, 075139 (2014)

[171] M. Žnidarič, A. Scardicchio and V. K. Varma, Diffusive and subdiffusive spin transport in the ergodic phase of a many-body localizable system, *Phys. Rev. Lett.* **117**, 040601 (2016)

[172] A. J. Friedman, S. Gopalakrishnan and R. Vasseur, Diffusive hydrodynamics from integrability breaking, *Phys. Rev. B* **101**, 180302(R) (2020)

[173] J. De Nardis, M. Medenjak, C. Karrasch and E. Ilievski, Universality classes of spin transport in one-dimensional isotropic magnets: The onset of logarithmic anomalies, *Phys. Rev. Lett.* **124**, 210605 (2020)

[174] B. Bertini, F. Heidrich-Meisner, C. Karrasch, T. Prosen, R. Steinigeweg et al., Finite-temperature transport in one-dimensional quantum lattice models, *Rev. Mod. Phys.* **93**, 025003 (2021)

[175] D. Wei, A. Rubio-Abadal, B. Ye, F. Machado, J. Kemp et al., Quantum gas microscopy of Kardar-Parisi-Zhang superdiffusion, *Science* **376**, 716 (2022)

[176] J. Lux, J. Müller, A. Mitra and A. Rosch, Hydrodynamic long-time tails after a quantum quench, *Phys. Rev. A* **89**, 053608 (2014)

[177] Y. Gu, X.-L. Qi and D. Stanford, Local criticality, diffusion and chaos in generalized Sachdev-Ye-Kitaev models, *Journal of High Energy Physics* **2017**, 125 (2017)

[178] M. Blake, R. A. Davison and S. Sachdev, Thermal diffusivity and chaos in metals without quasiparticles, *Phys. Rev. D* **96**, 106008 (2017)

[179] K. Agarwal, S. Gopalakrishnan, M. Knap, M. Müller and E. Demler, Anomalous diffusion and Griffiths effects near the many-body localization transition, *Phys. Rev. Lett.* **114**, 160401 (2015)

[180] Y. Bar Lev, G. Cohen and D. R. Reichman, Absence of diffusion in an interacting system of spinless fermions on a one-dimensional disordered lattice, *Phys. Rev. Lett.* **114**, 100601 (2015)

[181] J. Z. Imbrie, On many-body localization for quantum spin chains, *Journal of Statistical Physics* **163**, 998 (2016)

[182] Y. B. Lev, D. M. Kennes, C. Klöckner, D. R. Reichman and C. Karrasch, Transport in quasiperiodic interacting systems: From superdiffusion to subdiffusion, *EPL (Europhysics Letters)* **119**, 37003 (2017)

[183] M. Žnidarič and M. Ljubotina, Interaction instability of localization in quasiperiodic systems, *Proceedings of the National Academy of Sciences* **115**, 4595 (2018)

[184] H. Singh, B. A. Ware, R. Vasseur and A. J. Friedman, Subdiffusion and many-body quantum chaos with kinetic constraints, *Phys. Rev. Lett.* **127**, 230602 (2021)

[185] J. Richter and A. Pal, Anomalous hydrodynamics in a class of scarred frustration-free Hamiltonians, *Phys. Rev. Research* **4**, L012003 (2022)

[186] G. Vidal, Classical simulation of infinite-size quantum lattice systems in one spatial dimension, *Phys. Rev. Lett.* **98**, 070201 (2007)

[187] M. Fishman, S. R. White and E. M. Stoudenmire, The ITensor software library for tensor network calculations, *arXiv eprints* **2007.14822** (2020)

[188] M. Žnidarič, Spin transport in a one-dimensional anisotropic Heisenberg model, *Phys. Rev. Lett.* **106**, 220601 (2011)

[189] M. Ljubotina, M. Žnidarič and T. Prosen, Spin diffusion from an inhomogeneous quench in an integrable system, *Nature Communications* **8**, 16117 (2017)

[190] E. Ilievski, J. De Nardis, M. Medenjak and T. Prosen, Superdiffusion in one-dimensional quantum lattice models, *Phys. Rev. Lett.* **121**, 230602 (2018)

[191] M. Ljubotina, M. Žnidarič and T. Prosen, Kardar-Parisi-Zhang physics in the quantum Heisenberg magnet, *Phys. Rev. Lett.* **122**, 210602 (2019)

[192] J. De Nardis, M. Medenjak, C. Karrasch and E. Ilievski, Anomalous spin diffusion in one-dimensional antiferromagnets, *Phys. Rev. Lett.* **123**, 186601 (2019)

[193] M. Dupont and J. E. Moore, Universal spin dynamics in infinite-temperature one-dimensional quantum magnets, *Phys. Rev. B* **101**, 121106(R) (2020)

[194] V. B. Bulchandani, C. Karrasch and J. E. Moore, Superdiffusive transport of energy in one-dimensional metals, *Proceedings of the National Academy of Sciences* **117**, 12713 (2020)

[195] V. B. Bulchandani, Kardar-Parisi-Zhang universality from soft gauge modes, *Phys. Rev. B* **101**, 041411(R) (2020)

[196] V. B. Bulchandani, S. Gopalakrishnan and E. Ilievski, Superdiffusion in spin chains, *Journal of Statistical Mechanics: Theory and Experiment* **2021**, 084001 (2021)

[197] A. Scheie, N. E. Sherman, M. Dupont, S. E. Nagler, M. B. Stone et al., Detection of Kardar–Parisi–Zhang hydrodynamics in a quantum Heisenberg spin-1/2 chain, *Nature Physics* **17**, 726 (2021)

[198] N. Keenan, N. F. Robertson, T. Murphy, S. Zhuk and J. Goold, Evidence of Kardar–Parisi–Zhang scaling on a digital quantum simulator, *npj Quantum Information* **9**, 72 (2023)

[199] A. Schuckert, I. Lovas and M. Knap, Nonlocal emergent hydrodynamics in a long-range quantum spin system, *Phys. Rev. B* **101**, 020416(R) (2020)

[200] M. K. Joshi, F. Kranzl, A. Schuckert, I. Lovas, C. Maier et al., Observing emergent hydrodynamics in a long-range quantum magnet, *Science* **376**, 720 (2022)

[201] J. a. S. Ferreira and M. Filippone, Ballistic-to-diffusive transition in spin chains with broken integrability, *Phys. Rev. B* **102**, 184304 (2020)

[202] J. Durnin, M. J. Bhaseen and B. Doyon, Nonequilibrium dynamics and weakly broken integrability, *Phys. Rev. Lett.* **127**, 130601 (2021)

[203] A. Bastianello, A. D. Luca and R. Vasseur, Hydrodynamics of weak integrability breaking, *Journal of Statistical Mechanics: Theory and Experiment* **2021**, 114003 (2021)

[204] Z. Yao, L. Pan, S. Liu and H. Zhai, Quantum many-body scars and quantum criticality, *Phys. Rev. B* **105**, 125123 (2022)

[205] H. Spohn, Nonlinear fluctuating hydrodynamics for anharmonic chains, *Journal of Statistical Physics* **154**, 1191 (2014)

[206] H. van Beijeren, Exact results for anomalous transport in one-dimensional Hamiltonian systems, *Phys. Rev. Lett.* **108**, 180601 (2012)

[207] D. Bluvstein, H. Levine, G. Semeghini, T. T. Wang, S. Ebadi et al., A quantum processor based on coherent transport of entangled atom arrays, *Nature* **604**, 451 (2022)

[208] S. Dooley, S. Pappalardi and J. Goold, Entanglement enhanced metrology with quantum many-body scars, *Phys. Rev. B* **107**, 035123 (2023)

[209] B. Yang, H. Sun, C.-J. Huang, H.-Y. Wang, Y. Deng et al., Cooling and entangling ultracold atoms in optical lattices, *Science* **369**, 550 (2020)

[210] B. Yang, H.-N. Dai, H. Sun, A. Reingruber, Z.-S. Yuan et al., Spin-dependent optical superlattice, *Phys. Rev. A* **96**, 011602 (2017)

[211] S. Sachdev, K. Sengupta and S. M. Girvin, Mott insulators in strong electric fields, *Phys. Rev. B* **66**, 075128 (2002)

[212] K. Sengupta, Phases and dynamics of ultracold bosons in a tilted optical lattice, in *Entanglement in Spin Chains: From Theory to Quantum Technology Applications*, Springer, pp. 425–458 (2022)

[213] F. Meinert, M. J. Mark, E. Kirilov, K. Lauber, P. Weinmann et al., Quantum quench in an atomic one-dimensional Ising chain, *Phys. Rev. Lett.* **111**, 053003 (2013)

[214] F. Meinert, M. J. Mark, E. Kirilov, K. Lauber, P. Weinmann et al., Observation of many-body dynamics in long-range tunneling after a quantum quench, *Science* **344**, 1259 (2014)

[215] J. Simon, W. S. Bakr, R. Ma, M. E. Tai, P. M. Preiss et al., Quantum simulation of antiferromagnetic spin chains in an optical lattice, *Nature* **472**, 307 (2011)

[216] B. Yang, H. Sun, R. Ott, H.-Y. Wang, T. V. Zache et al., Observation of gauge invariance in a 71-site Bose–Hubbard quantum simulator, *Nature* **587**, 392 (2020)

[217] J. Hauschild and F. Pollmann, Efficient numerical simulations with Tensor Networks: Tensor Network Python (TeNPy), *SciPost Phys. Lect. Notes* p. 5 (2018), code available from https://github.com/tenpy/tenpy

[218] A. M. Kaufman, M. C. Tichy, F. Mintert, A. M. Rey and C. A. Regal, The Hong-Ou-Mandel effect with atoms, in *Advances In Atomic, Molecular, and Optical Physics*, Elsevier, volume 67, pp. 377–427 (2018)

[219] R. Islam, R. Ma, P. M. Preiss, M. Eric Tai, A. Lukin et al., Measuring entanglement entropy in a quantum many-body system, *Nature* **528**, 77 (2015)

[220] W. S. Bakr, J. I. Gillen, A. Peng, S. Fölling and M. Greiner, A quantum gas microscope for detecting single atoms in a Hubbard-regime optical lattice, *Nature* **462**, 74 (2009)

[221] P. Jurcevic, H. Shen, P. Hauke, C. Maier, T. Brydges et al., Direct observation of dynamical quantum phase transitions in an interacting many-body system, *Phys. Rev. Lett.* **119**, 080501 (2017)

[222] S. Scherg, T. Kohlert, P. Sala, F. Pollmann, B. Hebbe Madhusudhana et al., Observing non-ergodicity due to kinetic constraints in tilted Fermi-Hubbard chains, *Nature Communications* **12**, 4490 (2021)

[223] M. Schulz, C. A. Hooley, R. Moessner and F. Pollmann, Stark many-body localization, *Phys. Rev. Lett.* **122**, 040606 (2019)

[224] E. van Nieuwenburg, Y. Baum and G. Refael, From Bloch oscillations to many-body localization in clean interacting systems, *PNAS* **116**, 9269 (2019)

[225] R. Yao and J. Zakrzewski, Many-body localization of bosons in an optical lattice: Dynamics in disorder-free potentials, *Phys. Rev. B* **102**, 104203 (2020)

[226] W. Buijsman, Number of zero-energy eigenstates in the PXP model, *Phys. Rev. B* **106**, 045104 (2022)

[227] F. H. L. Essler, H. Frahm, F. Göhmann, A. Klümper and V. E. Korepin, *The one-dimensional Hubbard model*, Cambridge University Press (2005)

[228] N. Pancotti, G. Giudice, J. I. Cirac, J. P. Garrahan and M. C. Bañuls, Quantum East model: Localization, nonthermal eigenstates, and slow dynamics, *Phys. Rev. X* **10**, 021051 (2020)

[229] J.-Y. Desaules, K. Bull, A. Daniel and Z. Papić, Hypergrid subgraphs and the origin of scarred quantum walks in many-body Hilbert space, *Phys. Rev. B* **105**, 245137 (2022)

[230] F. M. Surace, M. Dalmonte and A. Silva, Quantum local random networks and the statistical robustness of quantum scars, *SciPost Phys.* **14**, 174 (2023)

[231] F. Arute, K. Arya, R. Babbush, D. Bacon, J. C. Bardin et al., Quantum supremacy using a programmable superconducting processor, *Nature* **574**, 505 (2019)

[232] Y. Wu, W.-S. Bao, S. Cao, F. Chen, M.-C. Chen et al., Strong quantum computational advantage using a superconducting quantum processor, *Phys. Rev. Lett.* **127**, 180501 (2021)

[233] P. Krantz, M. Kjaergaard, F. Yan, T. P. Orlando, S. Gustavsson et al., A quantum engineer's guide to superconducting qubits, *Applied Physics Reviews* **6**, 021318 (2019)

[234] A. Blais, A. L. Grimsmo, S. M. Girvin and A. Wallraff, Circuit quantum electrodynamics, *Rev. Mod. Phys.* **93**, 025005 (2021)

[235] Y. Salathé, M. Mondal, M. Oppliger, J. Heinsoo, P. Kurpiers et al., Digital quantum simulation of spin models with circuit quantum electrodynamics, *Phys. Rev. X* **5**, 021027 (2015)

[236] K. Xu, J.-J. Chen, Y. Zeng, Y.-R. Zhang, C. Song et al., Emulating many-body localization with a superconducting quantum processor, *Phys. Rev. Lett.* **120**, 050507 (2018)

[237] K. A. Landsman, C. Figgatt, T. Schuster, N. M. Linke, B. Yoshida et al., Verified quantum information scrambling, *Nature* **567**, 61 (2019)

[238] X. Mi, P. Roushan, C. Quintana, S. Mandra, J. Marshall et al., Information scrambling in computationally complex quantum circuits, *Science* **374**, 1479 (2021)

[239] P. Roushan, C. Neill, J. Tangpanitanon, V. M. Bastidas, A. Megrant et al., Spectroscopic signatures of localization with interacting photons in superconducting qubits, *Science* **358**, 1175 (2017)

[240] W. P. Su, J. R. Schrieffer and A. J. Heeger, Solitons in polyacetylene, *Phys. Rev. Lett.* **42**, 1698 (1979)

[241] C. Neill, P. Roushan, K. Kechedzhi, S. Boixo, S. V. Isakov et al., A blueprint for demonstrating quantum supremacy with superconducting qubits, *Science* **360**, 195 (2018)

[242] R. Jafari and H. Johannesson, Loschmidt echo revivals: Critical and noncritical, *Phys. Rev. Lett.* **118**, 015701 (2017)

[243] K. Najafi, M. A. Rajabpour and J. Viti, Return amplitude after a quantum quench in the XY chain, *Journal of Statistical Mechanics: Theory and Experiment* **2019**, 083102 (2019)

[244] T. Iadecola and M. Žnidarič, Exact localized and ballistic eigenstates in disordered chaotic spin ladders and the Fermi-Hubbard model, *Phys. Rev. Lett.* **123**, 036403 (2019)

[245] B. van Voorden, M. Marcuzzi, K. Schoutens and J. c. v. Minář, Disorder enhanced quantum many-body scars in Hilbert hypercubes, *Phys. Rev. B* **103**, L220301 (2021)

[246] G. Zhang and Z. Song, Quantum scars in spin- isotropic Heisenberg clusters, *New Journal of Physics* **25**, 053025 (2023)

[247] N. Malvania, Y. Zhang, Y. Le, J. Dubail, M. Rigol et al., Generalized hydrodynamics in strongly interacting 1D Bose gases, *Science* **373**, 1129 (2021)

[248] J. Cotler and A. Y. Wei, Quantum scars in quantum field theory, *Phys. Rev. D* **107**, 125005 (2023)

[249] L. V. Delacrétaz, A. L. Fitzpatrick, E. Katz and M. T. Walters, Thermalization and chaos in a 1+1D QFT, *Journal of High Energy Physics* **2023**, 1 (2023)

[250] I.-C. Chen and T. Iadecola, Emergent symmetries and slow quantum dynamics in a Rydberg-atom chain with confinement, *Phys. Rev. B* **103**, 214304 (2021)